CRANFIELD UNIVERSITY

School of Engineering
Department of Aerospace Science
Applied Aerodynamics Group

MPhil Thesis

Academic Year 2011- 2012

Vassilis Michael Moraris

Experimental and Numerical investigation of Leading Edge Krueger Flaps at Low Reynolds Numbers

Supervisors: Dr N. J. Lawson and Prof. K. P. Garry

2012

This thesis is submitted in partial fulfilment of the requirements for the degree of MPhil

Abstract

Recent publications examining the flight of Eagles have shown that leading edge feather deflections occur on the lower surface of the wings in free flight to create a leading edge flap analogous to a Krueger flap system.

Such passive high lift devices may be adaptable to the lifting surfaces of unmanned air vehicles (UAVs). This work is aimed to an application of a passive leading edge Krueger device which will deploy during the landing and takeoff stages of a UAV flight.

A numerical and experimental study was performed on a Clark Y aerofoil with a 5% and 10% chord leading edge Krueger flap to examine its aerodynamic performance characteristics at Reynolds numbers of 0.6×10^6, 1×10^6 and 1.6×10^6, and to help identify the forces and moments acting on such configurations. A detailed account of the numerical and experimental analyses performed is included as well as an in depth examination and comparison of the results obtained. Increases of up to 18% and 14% of the C_L value where observed when the 10% and 5% flaps respectively, were deployed. In addition a delay of up to 3^o of the stall angle was also observed with the implementation of such a device. The forces and moments around the Krueger flap rotation point were calculated from the numerical analysis and are presented.

An initial stage in the design of a UAV passive flap system is also included. Different designs were considered and a brief description of each is put forward along with comments regarding their implementation.

Finally the potential benefits of the implementation of such a device are analysed and presented.

Acknowledgements

I would like to express my gratitude to my supervisors Dr. N. J. Lawson and Prof. K. P. Garry who have initiated me in this work and guided me in my times of need. In particular I would like to thank Dr. N. J. Lawson for his patience, his understanding and all his support throughout my deliberations until this stage.

My thanks to Cranfield University Aerodynamics and Wind Tunnel Laboratory staff in particular Mr. John Thrower and Mr. Lynton Banks-Davies for their cooperation, help and support during the experimental period of this work.

My thanks to Dr. Les Oswald and Mr. Billa Malhi of Cranfield University IT department for their support and back up for the occasions my computers gave up on me and I was fully immersed in thoughts of plain desperation.

My thanks also to those of my friends and colleagues who patiently offered rapport in my considerations, especially on the long days and nights of reading, result evaluation, writing up and proof reading.

As in all research I had my share of going over previously published literature, data, and documentation. Every effort has been made to refer to and identify my sources of information and a detailed list is included at the end of this work, however, thanks are due to all those I have referred to, as every new piece of knowledge is always a step forward from somewhere one, or someone else had previously finished.

Last but not least I would like to thank my parents and my family for the moral support and for standing firmly by me as always.

Vassilis M Moraris

Contents

List of Figures

List of Tables

Nomenclature

2D, 3D	Two dimensional, three-dimensional	
CFD	Computational Fluid Dynamics	
EWT	Enhanced Wall Treatment	
UAV	Unmanned aerial vehicle	
PDEs	Partial Differential Equations	
FVM	Finite Volume Method	
AOA	Angle of attack	
C_D, C_d	Drag coefficient	
Cf	Total skin friction coefficient	
Cf_x	Local skin friction coefficient	
C_L, C_a, C_l	Lift coefficient	
$C_{Llanding}$	Lift coefficient at Landing	
ΔC_{lmax} ΔC_{Lmax}	Increment of maximum section lift coefficient due to leading edge flap	
C_n, C_p	Pressure coefficient	
D	Total drag force	[N]
D_f	Drag due to skin friction and	[N]
D_p	Drag due to flow separation	[N]
L	Lift Force	[N]
A	Area	[m^{-2}]
F	Area of Reference	[m^2]
Λ	Aspect Ratio	[m]
V	Flow velocity	[m s^{-2}]
H	Height of Obstacle	[m]
L	Length of the channel	[m]
W	Takeoff weight	[kg]
S_r	Ground roll	[m]
V_{stall}	Stall Speed	[m s^{-1}]
V_α	Approach Speed	[m s^{-1}]

Re, Re_c	Reynolds number based on aerofoils chord and freestream velocity	
Re_L	Local Reynolds number based on distance from leading edge and freestream velocity	
$S_{landing}$	Landing distance	[m]
S_a	Obstacle clearance distance	[m]
σ	Density ratio	
α, α_o	Angle of attack	deg
γ	Glide angle	deg
$\Delta\alpha$	Increment of section angle of attack for maximum section lift coefficient due to leading edge flap deflection.	deg
b	Aerofoil span	[m]
μ	Dynamic coefficient of viscosity	[Pa s]
ν	Kinematic viscosity	[m^2/s]
u_τ	Friction velocity	[m/s]
τ	Shear stress	[N m^{-2}]
τ_w	Local shear stress	[N m^{-2}]
χ	Distance from aerofoil leading edge	[m]
l, c	Aerofoil chord length	[m]
l_n	Leading edge flap chord length	[m]
l_k	Trailing edge flap chord length	[m]
ρ	Density	[Kg m^{-3}]
p	Static pressure	[Pa]
q	Dynamic pressure	[Pa]
δ	Leading edge flap nose thickness, also boundary layer thickness	[m]
f_N	Camber of the leading edge flap	[m]
s	Slot length	[m]
$\eta_{N,}$, $\delta_{fL.E,}$ δ	Deflection of leading edge flap, measured in clockwise direction from the aerofoil chord (zero when flap lies along surface)	deg
y	Vertical Distance normal to wall direction	[m]
y^+	Dimensionless distance to the wall	

ω	Specific dissipation rate
ε	Dissipation rate

Chapter 1. Introduction

As environmental issues begin to dominate in the 21st century, there is a push for aircraft manufacturers to develop and implement ways of making their products more efficient. The design of an aircraft is driven by its mission requirements which include cruising, takeoff/landing speeds and distances, payload capacity and maximum velocity. The competitive nature of the industry demands simple, reliable designs with low maintenance and production costs.

A wing shape can be specifically tailored for certain Reynolds Number (Re), but will degrade in performance when operated under different conditions [1]-[8]. A wing therefore whose geometry is variable during operation, can offer numerous advantages such as increased efficiency or lift over drag ratio, higher stall angles through separation control, and greater manoeuvrability.

The aim of this project is to research and propose an adaptable wing configuration, with operating Reynolds numbers in the range of $0.6x10^6$ to $1.6x10^6$ where small and medium size UAVs (Tactical UAVs) operate [6]. This Reynolds number region is above the one of Mini UAV wings, which is highly characterised by strong viscous effects, but still belongs to the low Reynolds number regime. Within this low Re numbers separation, transition, and reattachment could all occur within a short distance and influence the performance of the lifting surface. The qualitative aerodynamic characteristics of such Re flows are significantly different than those normally seen in typical aerodynamic and aerospace applications. Slight changes in the flow speed can have large effects on the flow over a given aerofoil, most notably large changes in the L/D ratio.

The lift and drag of the wing are expected to be controlled without conventional control surfaces, but with a passive Krueger Device that will deploy to control the aerodynamic

behaviour of the configuration. A Krueger system offers a simple method of achieving high lift coefficient increments, by control of the leading edge curvature without the requirement for further leading edge modifications such as a slot device.

The complexity of the flow field generated by a Krueger flap arrangement, requires a joint experimental and CFD approach for evaluation. This is due to the fact that numerical solutions depend on the behaviour and set up of the turbulent model utilised, as well as the boundary and initial conditions. It is therefore essential to validate the numerical results against experimental data [9]. Successful comparison of the results, provides a better understanding of the problem and a higher degree of confidence which may lead to shorter test duration.

1.1 Report Structure

The project consists of the following sections:

Chapter 1. Introduction and Report Structure.

Chapter 2. High Lift Systems: A review of the development of mechanical high-lift flap systems and their applications to general aviation aircraft in recent years.

Chapter 3. Krueger flap History and Analysis: Presentation and analysis of Krueger flaps.

Chapter 4. Project definition: Description of the wing design considerations as well as the aims and objectives of this project.

Chapter 5. Computational Modelling: Description and presentation of the computational models used. Introduction to the concepts of CFD and detailed analysis of the turbulence models used for the purposes of this project. Description of the

boundary and inlet conditions, near wall modelling and mesh dependency tests, as well as methodology and comparison with the experimental data.

Chapter 6. Experimental Study: Description and details of the Experimental procedure followed. Focus on the model set up and experimental arrangements, the procedure followed to account for errors and the derivation of the lift and drag forces and their respective coefficients.

Chapter 7. High Lift Configurations – Computational and Experimental Study: The results obtained from the two processes for the baseline Clark Y are compared and analysed. Presentation of important information of the aerodynamic effect of the Krueger flap on the C_P distribution as well as the forces acting on such systems.

Chapter 8. Comparison of experimental and Numerical results for the leading edge flap: The experimental and numerical results for the two configurations examined are analysed and presented and their effect on L/D, $C_L^{3/2}/C_D$ is discussed. Presentation of the moments acting on such systems.

Chapter 9. UAV Performance Characteristics and Proposed Krueger flap design: A brief description of proposed Krueger flap systems designs applicable to a UAV type aircraft and outlines of the potential benefits from their implementation.

Chapter 10. Conclusions and Recommendations: Summary of the important findings and conclusions from the research program undertaken and recommendations for future work.

References

Appendices

Chapter 2. High Lift Systems

This chapter presents a review of the development of mechanical high-lift flap systems and their applications to general aviation aircraft in recent years. These flap systems include, leading edge slats, Krueger flaps and the more recently developed variable-camber high-lift mechanisms.

2.1 Introduction to High Lift Systems

The design of high-lift systems has a critical effect on the sizing, economics, and design of most aircraft configurations [10]. High-lift devices are small elements that are fitted at the leading and/or trailing edge of a wing. During cruise conditions they are retracted and stored in the contour of the aerofoil and at lower speeds (during landing and takeoff), they deflect increasing the camber of the aerofoil and therefore its lift. The complex flow phenomena observed in high lift systems as well as constrains in geometry, system integration, support and actuation, have led to a lengthy and intensive experimentation and development process over the years. Such devices are complex in construction, heavier, with higher part count, which makes them more maintenance intensive. Rapid development in computational software and hardware in the recent past, however, have changed significantly the engineering design process. Computational methods are gradually superseding empirical ones and engineers in aerodynamics, are devoting increasingly more time utilising such tools, to design and analyse the performance of high lift systems and aircraft schemes instead of conducting actual experimental tests.

High-lift systems have been in existence for years and their application in the civil sector can be referred to and used, as example and basis in the development of high-lift devices for UAVs. Currently, most civil transport airplanes use Krueger flaps or slats, to alter their lift characteristics during take-off and landing. The selection of the type of a high-lift device for a UAV and/or airplane, is based on issues of performance versus cost trade off, and past experience acquired. Considering examples from the civil sector, it can be seen that where early attention was mostly focused on the requirements of maximum lift, to satisfy the high

cruise wing loading needs of jet transport aircraft while retaining acceptable landing and takeoff distances, more recently the attention has shifted to the reduction of complexity and weight of such systems for given maximum lift levels. This is even more important in UAV designs, since the size of the wing and the aircraft in general is comparatively smaller, and thus provides a reduced amount of space to facilitate housing of high lift devices.

Rudolph [11] states in his work that, "an aircraft's high-lift system accounts for somewhere between 6% and 11% of the production cost of a typical jet transport which could potentially increase for more complex configurations". Additionally, work presented by Meredith [12] on the importance of high-lift systems on generic large twin engine transport suggests that:

- An increase of 1% in the maximum coefficient of lift, translates into an increase in payload of approximately 1995 kg or 22 passengers, for a fixed approach speed on landing.

- An increase in the payload of approximately 1270 kg or 14 passengers for a given range, can be achieved by a 1% improvement in the L/D value during takeoff.

Studies by Butter [13], describing the impact of the high-lift devices on the performance of the total aircraft, for a typical twin-engine jet transport aircraft showed that:

- An increase of 5% in the maximum lift, results to 12 to 15% increase in payload
- An increase of 5% in take off L/D, results to 20% increase in payload
- A 5% increase in the C_{Lmax} in landing configuration, results to 25% increase in payload

Even though such relationships are closely dependent upon the aircraft's overall design characteristics, such as the tail clearance angle, the above findings demonstrate that large payoffs in an airplane's weight and performance can be achieved, with relatively small changes in the aerodynamic characteristics of its high-lift system.

This sensitivity of an airplane's weight and performance characteristics to small changes in lift, in combination with the large impact of high-lift systems on an airplane's cost, explains why such systems and their aerodynamic behaviour remain in the forefront of aerospace

research [10]. Furthermore, smaller and more efficient wings are especially of interest to manufacturers of military and commercial transports, who are particularly concerned with the payload capability and operational costs of new aircraft. The potential benefits of increased performance capability could however, overshadow the manufacture, design and operational maintenance difficulties related with the design of a more complex high lift system. Manufacturers of the smaller general aviation aircraft are more interested in low initial costs, low maintenance requirements, and high reliability [14]. The market for new general aviation aircraft is highly competitive, and thus limits the consideration for more complex and more expensive high-lift systems.

The most commonly high lift leading edge devices used are slats (slotted leading-edge flaps) and Krueger flaps or combinations of both. Slats are normally deployed on circular tracks creating a slot between them and the main wing element, whereas Krueger flaps are deployed out of the pressure side of the wing and moved in front of its leading edge. Other possible solutions used are such as a droop-nose or a hinged nose. These devices deploy in a similar manner to a slat but do not create a slot to the main wing element.

Leading edge high lift devices such as slats increase the stall angle and maximum lift coefficient of the wing, whereas trailing edge devices such as Fowler flaps, produce an upward shift of the lift curve as shown in Figure 1 below, which illustrates the effects of multi-element high lift systems. This effect is achieved by increasing the camber and surface area of the wing and by keeping the flow attached at higher angles of attack.

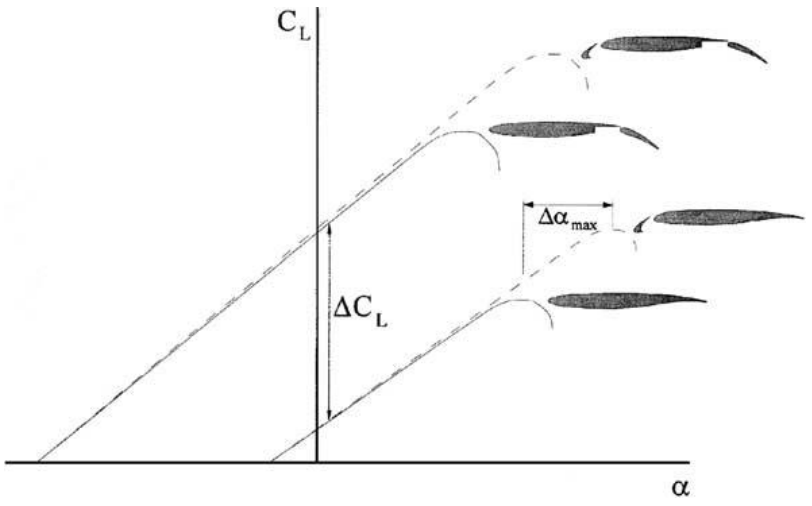

Figure 1: Effects of typical high-lift systems on lift coefficient value [10].

The field of high lift wing aerodynamics is influenced to a great degree by the effects and the requirements of other disciplines, particularly systems and structures. The support and actuation of high-lift systems may get quite complicated when the large aerodynamic loads generated by the various elements involved are considered. Additionally, multi element wings are required to demonstrate good performance for a wide range of flap settings, such as heavy and light takeoff and landing, and are sensitive to small variations in gap size and overlap between the different parts.

Aerodynamic characteristics such as: C_{Lmax}, cruise lift, drag and pitching moment in different deployment faces must be considered. The performance requirements of a configuration are defined by different constraints, such as takeoff weight, landing weight, runway length, climb gradient, approach and landing speed [15] with the final design solution being the best possible compromise between the requirements of the disciplines involved.

The layout of an aircraft is driven by the requirement for maximum efficiency which is measurable by the direct operating costs. Aerodynamic demands such as cruise speed and climb, altitude, and range capacity, directly affect the wing design characteristics such as area, sweep, aspect ratio, thickness, span loading and twist. Additionally, structural constraints such as for example manufacturability and weight must also be considered in the design process. In its turn the selected wing profile and shape will directly influence the design of the high-lift system, for instance a wing with small area might be of greater benefit for cruise performance, but it would require a more complex high-lift system to deliver sufficiently maximum lift during take-off and landing. The sweep angle, is another factor which influences the maximum performance of a high-lift system and subsequently its complexity. This dependency combined with the fact that slight changes in the lift characteristics can have significant effects on an aircraft's economics and performance, denote the importance and complexity of the design of such devices. Even though such systems are costly and complex, they are necessary in order to enable aircraft to take off and land on runways of adequate length, without significantly penalizing cruise efficiency.

A brief overview of the various high lift systems that are currently in use on civil transport jets is presented in the section which follows, as an introduction to the subject. The aim is not to give a detailed analysis of each system, but to provide a summary of the current configurations used. More in-depth analyses are provided by Niu [16] and Rudolph [11] .

2.2 Types of High Lift Systems

The maximum lift of an aerofoil may be increased by using four basic methods:

- Increase leading and trailing edge camber
- Extend the chord
- Delay boundary layer separation
- Energize the external flow field

The discussion in this section concentrates to those systems utilising the first three methods. The last method is more complex and costly to maintain since it involves boundary layer suction and/or blowing and might not be applicable for a simple UAV application.
Mechanical leading-edge devices are in use on many commercial and military aircraft. These devices assist in turning and accelerating the flow around the leading edge, thereby, keeping the flow attached at higher angles of attack and increasing the maximum lift coefficient of the configuration. The complexity of these devices ranges from the rather simple drooped leading edge device, with a single lower surface hinge point, to the very sophisticated variable-camber Krueger device actuated by complex four-bar linkage system [14].

It may be appropriate to first list possible high-lift devices before briefly describing them.

- Hinged leading edge (droop nose)
- Variable camber (VC) leading edge
- Fixed slot
- Simple Krueger flap
- Folding, bull nose Krueger flap
- Variable Camber Krueger flap
- Two position slat
- Three position slat

2.3 Hinged leading edge

Hinged leading edge or droop nose leading edge as might be called, have been used mainly on military supersonic fighter airplanes. The radius of curvature on the upper wing surface when this device is deployed is too tight which causes the flow to separate. At high speeds (supersonic) this is not a problem, since a much higher leading edge sweep angle can trigger the creation of a vortex on the upper surface of the wing which enhances lift [11].

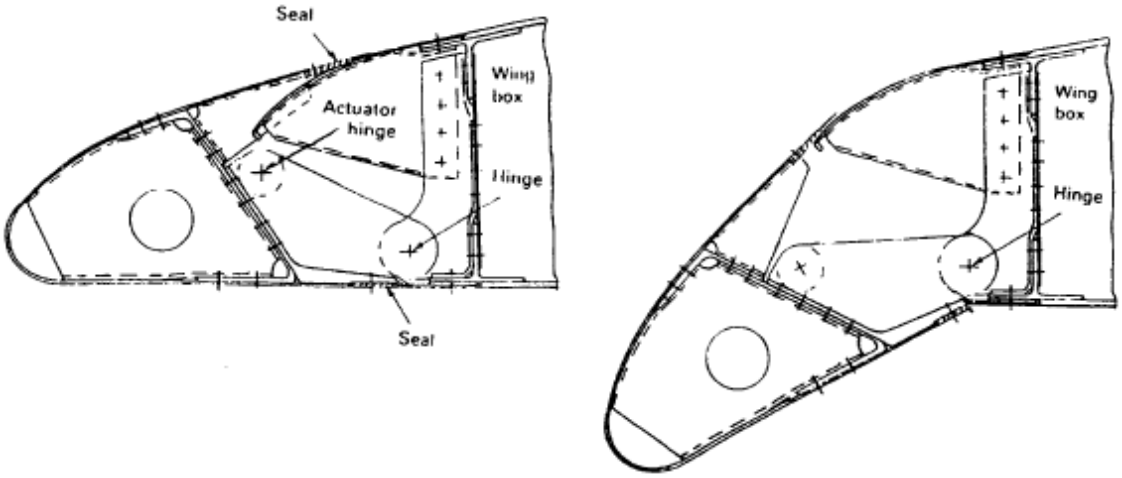

Figure 2: Hinged leading edge (droop nose) in retracted and deployed position [11].

2.4 Variable camber leading edge

Variable camber leading edge (VC) is a concept similar to that of a droop nose. The variable camber allows the deflection of the geometry on the suction side of the wing, thus creating a smoother leading edge radius when it is deployed see Figure 3, below. It works by utilising internal shape altering mechanisms, that deflect and smoothly reshape the leading edge of a wing, which optimises the wing camber during climb and descent. This device was tested successfully on NASA's Advanced Flight Technology Integration experimental airplane, (AFTI F-111) [17] shown in Figure 4, but was never used in the civil sector, due to its bad low-speed, high-lift characteristics [10]. A more detailed discussion of the development of this device is presented in reference [18].

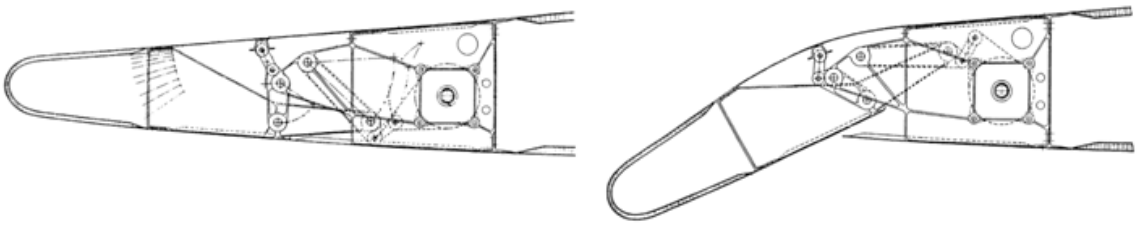

Figure 3: Variable camber leading edge flap in retracted and deployed position [11].

Figure 4: AFTI F-111 Mission Adaptive Wing (MAW) in flight [19].

2.5 Fixed slot

A fixed slot device as shown in Figure 5 is a device that has successfully been implemented on short takeoff and landing (STOL) airplanes, Figure 6, with low cruise speeds and this could lend its application on a UAV wing. It increases the C_L value, by allowing the wing to stall at higher angles of attack. The drag penalty of fixed slots however, is unacceptably high and would compromise the operational range of a UAV.

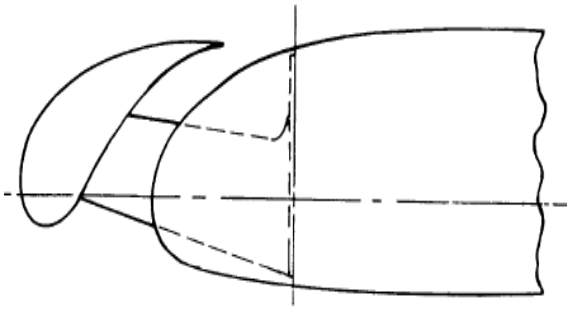

Figure 5: Schematic of a fixed slot [11].

Figure 6: STOL aircraft with a fix slot [11].

2.6 Krueger Flaps

There are three types of Krueger flaps:

- Simple Krueger flap
- Rigid bull nose Krueger flap and
- Variable camber Krueger flap

In the case of the simple Krueger flap, a panel on the pressure surface of the wing rotates first downwards and then forwards, with the help of a hinge located at the near end of the panel. When into the deployed position, its forward edge seals against the lower surface of the wing's leading edge as shown in Figure 7. Such flaps are used on the inboard wing of Boeing 707 and they are the simplest leading edge devices used in civil aircraft.

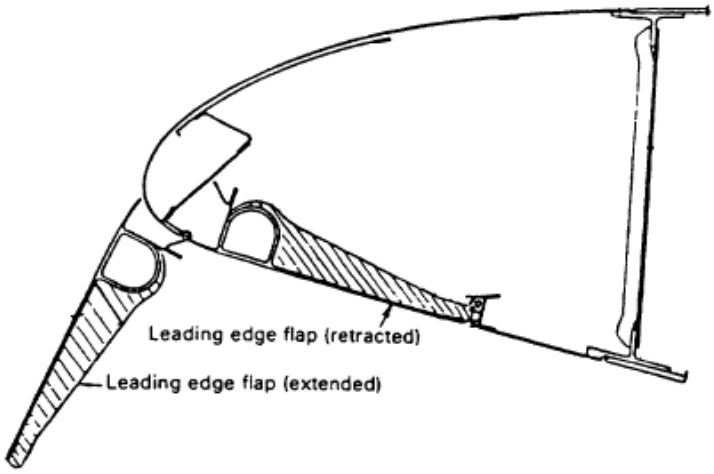

Figure 7: Simple Krueger flap in retracted and deployed position [11].

The deficiency of a simple Krueger flap lies in its inability to accommodate varying angles of attack. To address this problem a folding bull nose was added to the simple system decreasing the system's sensitivity to changes in angles of attack, and increasing its operational range. This bull nose, has a D-shaped cross section as illustrated in Figure 8 and deploys in parallel to the main Krueger element, enabling the flow on the suction side of the Krueger flap to stay attached over a wider range of angles of attack.

Further attempts to improve the aerodynamic performance of the leading edge Krueger flap, led to the development of the variable camber Krueger flap, as shown in Figure 9. In the previous configurations, the shape of the Krueger element was dictated by the shape of the aerofoil's leading edge pressure side. The rigid main Krueger flap panel was replaced with a flexible one, which improves the shape as well as the aerodynamic performance of the configuration. This performance gain, however, was achieved with an increase in complexity of the configuration, due to its more complex linkage system. Figure 10 illustrates the application of bull nose Krueger flaps in the inboard, and variable camber Krueger flaps in the outboard section of a Boeing 747.

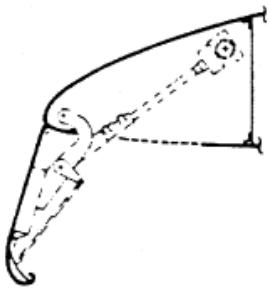

Figure 8: Folding, bull nose Krueger flap [21].

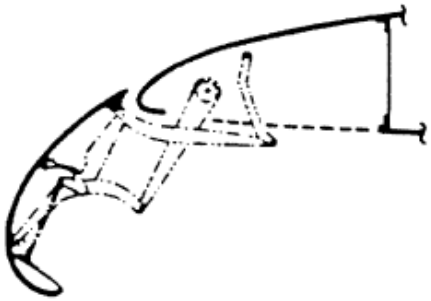

Figure 9: Variable camber Krueger flap [21].

Figure 10: Boeing 747 equipped with bull nose Krueger flaps in the inboard section and variable camber Krueger flaps on the outboard section [20].

Currently, Krueger flaps are used as two-position devices, biased towards an optimum landing configuration when deployed, therefore compromising the lift to drag ratio produced by the configuration during takeoff [22]. They tend to be lighter, and simpler than other high lift devices, and when retracted they can be stowed in the lower surface of the wing's leading edge, thus allowing a smooth suction surface. It should be noted, that irregularities on the suction side of the wing could cause premature transition, and a corresponding increase in trailing edge separation, which in turn could cause a loss in the maximum lift capability and an increase in the total drag. This lack of surface discontinuities has therefore, made the Krueger flap a more suitable device for laminar flow wing designs.

2.7 Leading edge slats

Leading edge slat design, is another type of high lift leading edge device that may be used. There are two types of slats: a) a two-position slat and b) a three position slat, which work in the same way. The two position slat, which lent its application on the F-84 fighter aircraft was mounted on a curved track, stowed with the force of a preloaded spring and deployed with the help of the aerodynamic forces. The leading-edge slat configuration is shown in Figure 11 below.

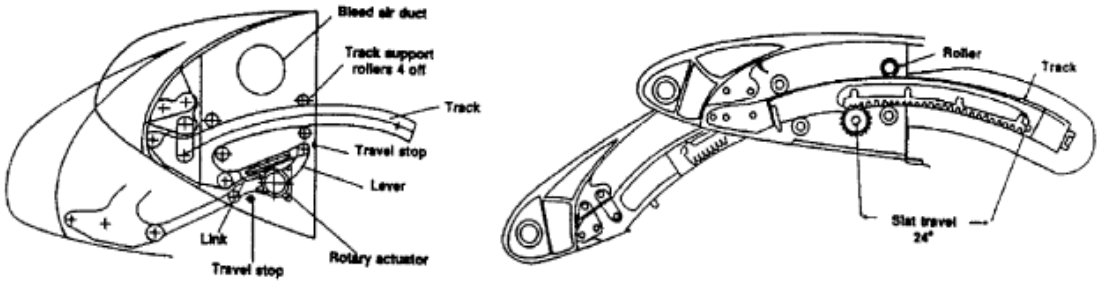

Figure 11: Slat mechanism used on A330/340 [10].

The three-position slat system, offers better characteristics and is the most frequently used leading edge device on current commercial aeroplanes. During landing, the slat is fully forward deployed to angles between 20^{o} and 38^{o}, and its trailing edge forms a slot with the leading edge whereas in its intermediate takeoff position, to enhance the L/D performance, the slat is at a shallow angle, with its trailing edge sealed against the upper surface of the

leading edge, see Figure 12. Examples of this device can be found on the Airbus A320 and Boeing 777. On the Airbus, the intermediate slat position used for takeoff allows for a shallow angle and a small slot, whereas on the Boeing, the fixed leading edge is shaped so that the slat trailing edge seals in the takeoff slat position.

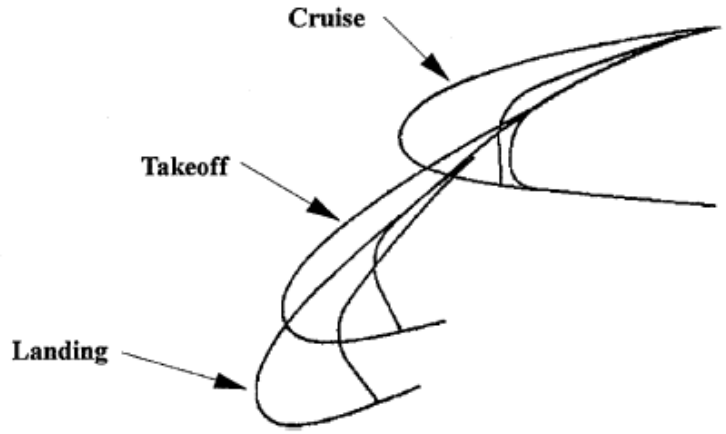

Figure 12: Landing, takeoff and cruise positions of a three position slat used on B777 [22].

Leading edge slats, can be used as three position devices in contrast to Krueger flaps. This enables the device to perform better during takeoff and landing, whereas the Krueger device is normally optimised for landing. This said however, the smoother surface provided on the suction side of a wing with the implementation of a Krueger flap instead of a slat, thus prolonging laminar flow, is a very important factor when considering wing designs for UAVs. UAVs operate at lower speeds than commercial aircraft, and keeping the flow laminar will significantly minimise the skin friction and total drag produced by the wing. A more efficient wing in its turn, will increase the operational range of a UAV. In the case of commercial aircraft, where the operational Reynolds number is significantly higher, transition takes place closer to the leading edge, therefore the implementation of a slat might not significantly alter the drag characteristics of the wing.

Chapter 3. Krueger Flap History and Analysis

3.1 Krueger flap overview

In the mid 1940s the first wind tunnel experiments were made by W. Krueger,[28]-[31] and subsequently Felicien F. Fullmer [32],[33] using different aerofoil sections equipped with a nose flap, with the aim to determine the effect that a nose flap would have when implemented on an aerofoil section. The following section attempts to summarise the important findings of these experimental studies as well to enhance knowledge on the subject.

The nose flaps, also since referred to as Krueger flaps, are small leading edge devices (see Figure 13) which help the aerofoil attain higher lift characteristics.

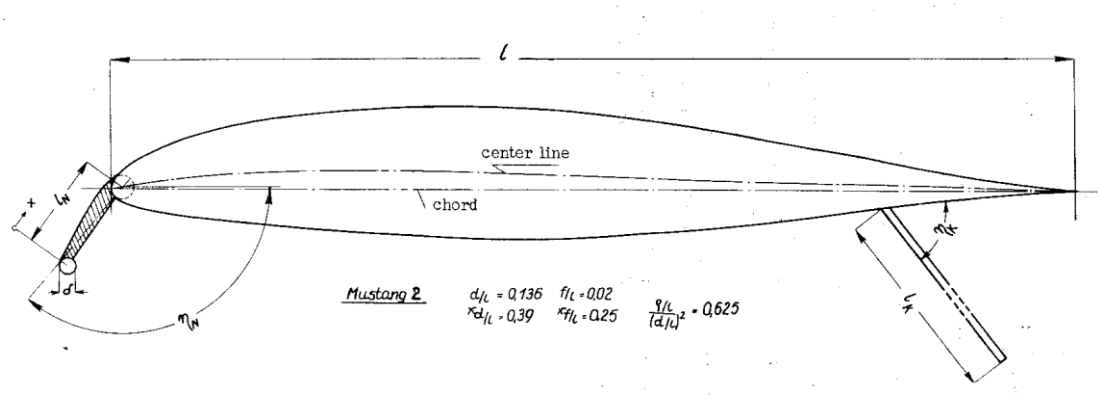

Figure 13: Mustang 2 profile used in Krueger's initial experiments [28].

More recent publications examining the flight of eagles, have shown that leading edge feather deflections occur on the lower surface of the wings in free flight to create a "leading edge flap" [23], analogous to the Krueger flap system. This phenomenon has been the subject of resent studies by Carruthers [24], by means of high speed video footage and was also briefly referred to by Hertel [25] and Azuma [26], [27] as an example of a high lift device. The high speed video by Carruthers [24], has shown that while the leading edge flap can deploy in segments, it ultimately spans most of the wing thus in flight the leading edge flap is essentially a two-dimensional device, also see Figure 14 below. Krueger flaps along with the

slats and nose flaps are mechanical high lift devices used in high Reynolds numbers to delay separation and increase the C_L value as mentioned earlier. Such passive high lift devices may be adaptable to the lifting surfaces of UAVs. Their utility however, has not been well documented in the low Reynolds number flows. Thus this project presents an experimental and numerical approach, to obtain the forces and moments acting on a Krueger flap configuration and their potential aerodynamic benefits, in the low Reynolds number region at which UAVs operate, where the aerodynamic characteristics of Krueger flaps are not well documented.

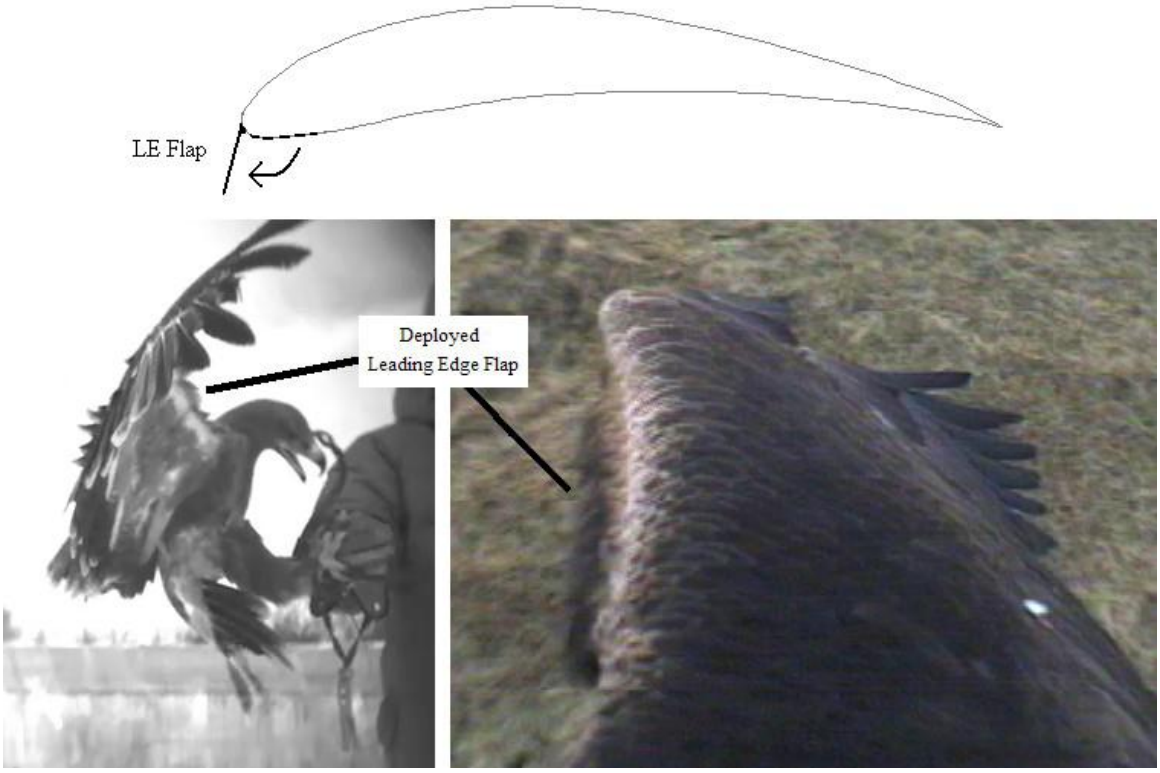

Figure 14: Deployment of flap as seen on the wing of an eagle photo from ref [23].

The work is aimed at an application of a passive leading edge Krueger device, which will deploy as required in the take-off and landing stages of a UAV flight. Experiments performed by Bakhtian and Babinsky [23], as well as Krueger [28]-[31] and Fullmer [32], [33] indicated that significant lift coefficient gains can be achieved, from the implementation of a Krueger high lift device, at Reynolds numbers based on chord length of $4x10^3$ to $1.4x10^4$ and $6x10^6$. Fulmer's experiments showed a 30% increase in maximum lift coefficient, when a Krueger flap was deployed from the lower surface of the aerofoil at Re = $6x10^6$. Numerical results indicate that, adjacent to the point of maximum flap curvature, an accelerated region generates a significant fall in C_P, followed by a substantial adverse pressure gradient resulting

in a region of separated flow. The extent of the separation is related to the degree of curvature in the leading edge region, as this leading edge geometry approximates an "ever-opening spiral", the less severe the separation will be thus removing the need for a slot, or a boundary layer control device to reattach the flow at a sharp corner or knee [34]. This simple arrangement, may also lend itself to application in a self deploying high lift device, such as is observed in the flight of an eagle.

The effect and efficiency of a Krueger flap design is influenced by a number of different factors, such as [28]:

- The angle of deflection of the nose flap
- The chord ratio
- The leading edge curvature
- The camber of the flap
- The influence of a slot
- The Position of the Krueger Flap
- The presence of a split – flap

The above design characteristics, have a great influence on the aerodynamic performance of a Krueger flap configuration and they are individually discussed, in more detail further on.

In addition to the above, however, another important factor which affects the performance of such configurations, is the magnitude of the nose radius coefficient $\boldsymbol{(r/l)/(d/l)^2}$ of the aerofoil, where d is the aerofoil's thickness, l is the aerofoil's chord and $\boldsymbol{r}$ is the aerofoils leading edge radius. According to Krueger [29] the lift increasing effect of the nose flap can be very important and its effect is larger the more pointed the profile used, that is, the smaller the nose radius coefficient $\boldsymbol{(r/l)/(d/l)^2}$. When an aerofoil with a small nose radius is used, the flow may begin to separate at low angles of attack directly behind the leading edge, due to the extremely steep pressure rise existing there. The effect of a Krueger flap can be explained, by the fact that at a suitable deflection angle the front stagnation point of the flow will be displaced quite near the leading edge of the flap. This will reduce the considerably high velocities observed near the leading edge of the aerofoil, thus decreasing the steep pressure rise behind the leading edge. Consequently, stalling will be delayed to higher angles of incidence [28].

Figure 15 clarifies this relationship. It can be seen that for a wing with a split – flap and without a Krueger flap, the pressure for C_{nmax} = 2.45 reaches the value p/q = -15.4 where p is the static and q is the dynamic pressures. For larger C_{nmax} = 2.65 the maximum negative pressure is reduced to p/q = -7.9 by the nose flap. Thus, the pressure increase in the flow immediately behind the profile nose is considerably reduced by the nose flap. The reason for this slight degree of improvement obtained in the maximum lift coefficient, is that for this profile, the point of turbulent separation travels with increasing angle of attack from the trailing edge to the front, whereas the flow of the aerofoil alone separates suddenly near the profile nose [30].

Krueger examined this effect, in 1946 [29] and the initial results obtained by his experiments for a typical laminar profile (1 5012 – 50 – 0,21), showed that a relatively high increase in the values of C_{amax} and α_{camax} is obtained by nose flaps of 5% of chord only. A more in-depth investigation of the effect of the leading edge flap (Krueger flap), was undertaken by W. Krueger and Felicien F. Fullmer, Jr in 1947 [28]-[33] and the results of their findings are subsequently summarized.

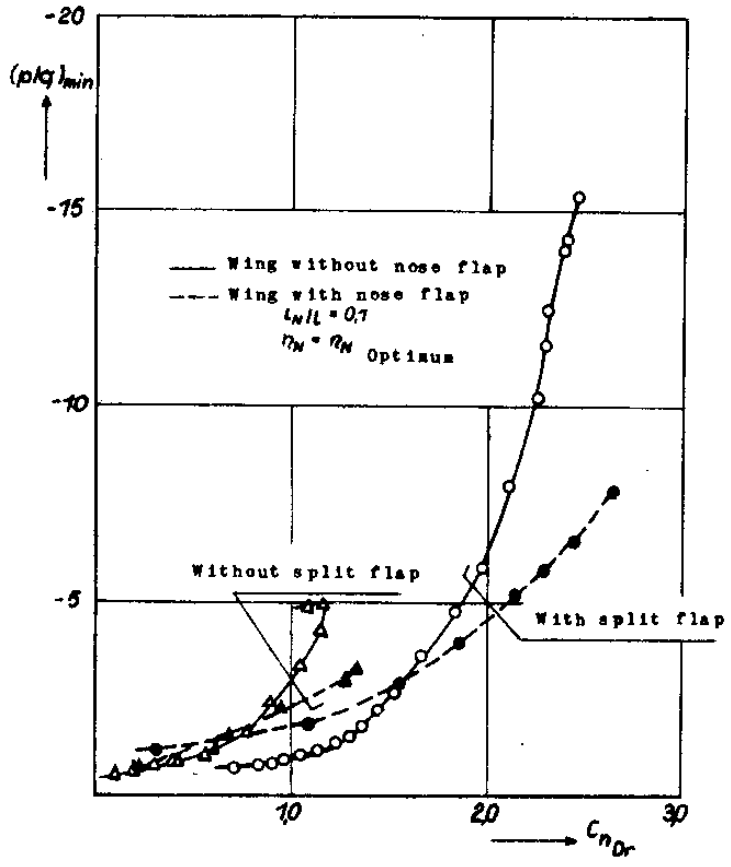

Figure 15: Represents the negative pressure pick at the nose of the profile as a function of the normal force coefficient (from pressure distribution measurements) [28].

The employment of a split – flap can additionally increase the aerodynamic efficiency of an aerofoil, however, it is very significant that this is positioned in the correct place so as not to eliminate the effect of the Krueger flap.

In order to complete his former tests, Krueger conducted further investigations on the Russian Laminar profile 2315 Bis (Figure 16). In these experiments Krueger altered the flap chord l_N flap camber f_N, and curvature of the entrance edge δ. In addition, Krueger investigated the influence of a slot between aerofoil and flap. The influence on the maximum lift of the magnitude and the form of the nose flap was recognizable from the results of his preliminary tests. Hence, systematic measurements were then made to investigate how the aerodynamic coefficients varied, in the process of employing these alternations. The effect of a split flap was also investigated.

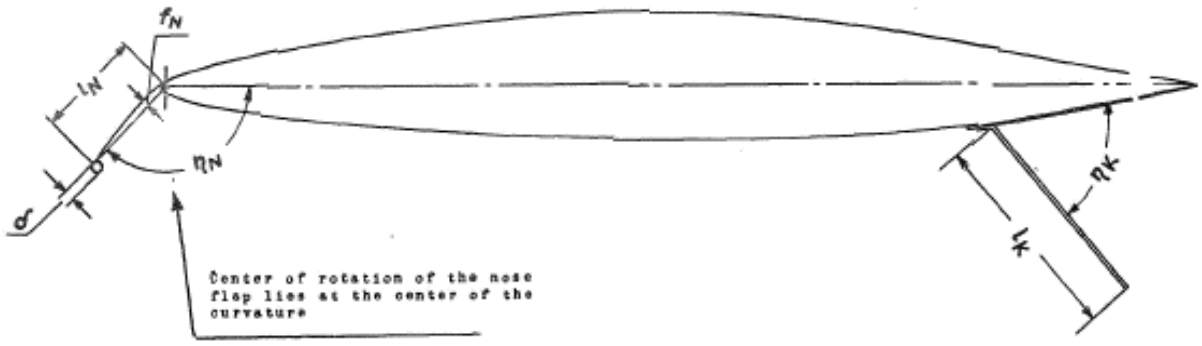

Figure 16: The 2315 Bis test profile [31].

The test wing platform used for the above experiments was rectangular and its dimensions are summarised and presented in Table 1:

Span:	b = 1.23 m
Chord:	l = 0.25 m
Area of Reference:	F = 0.3065 m^2
Aspect Ratio:	Λ= 4.94

Table 1: Summary of the model and experimental arrangements used by W. Krueger

All test measurements were made at a Reynolds number of 7.2 x 10^5 (40m/s wind speed). Air flow degree of turbulence considerations (factor of turbulence 1.13) led to an effective Re number of 8.2 x 10^5. The results were converted to infinite jet cross section as well as infinite aspect ratio [30],[31].

3.2 Influence of the nose angle deflection

Maximum lift, is highly dependent upon the flap angle. Figure 17 shows the effect of the nose flap on maximum lift increment ΔC_{amaxN} as a function of angle η_N for the wing with and without split flap [30].

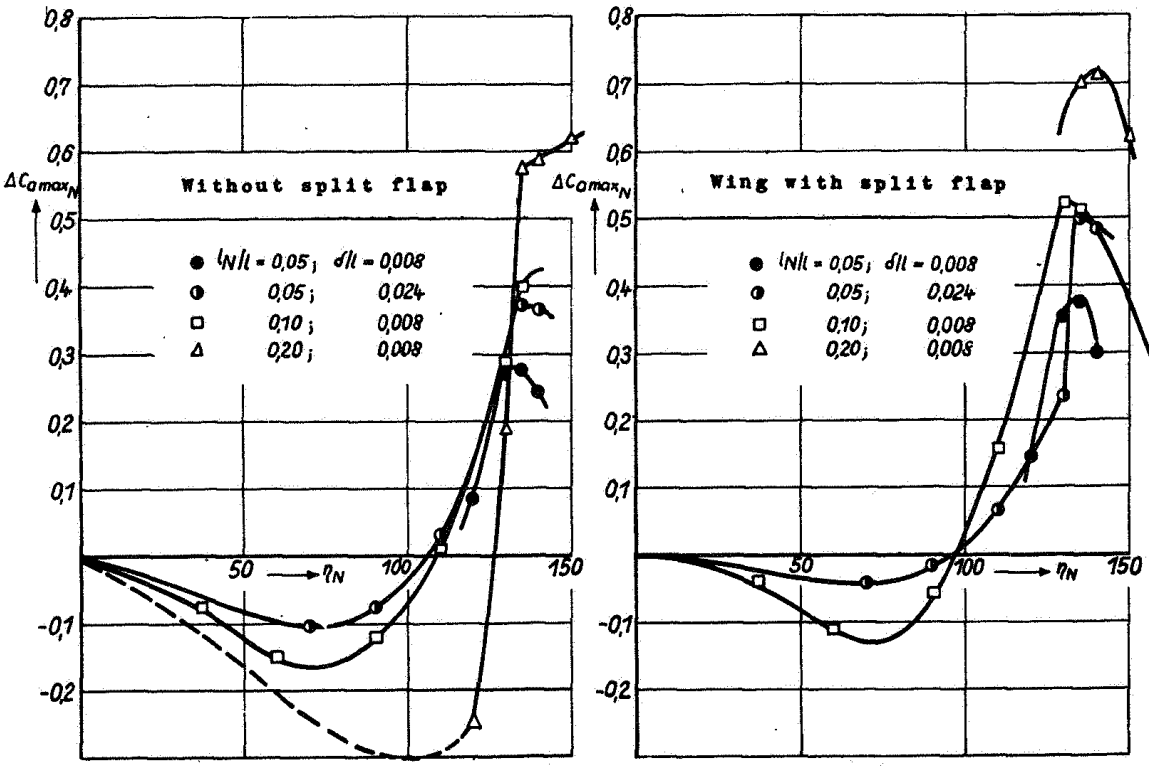

Figure 17: Increase of the maximum lift coefficient by the effect of the nose flap as a function of the angle of deflection η_N. Parameters: nose flap chord Ratio l_N / l and curvature of the leading edge δ / l_N. The camber of the nose flap corresponds to the pressure side contours of the smooth profile [31].

From the above graphs, it can be seen that the value of ΔC_{amaxN} decreases as the angle of the flap increases. As the Krueger flap deploys at small angles (η_N), it alters the geometry of the lower surface of the aerofoil hence increasing the lower camber. This in turn accelerates the flow around the lower surface, thus creating a pressure drop (Bernoulli's equation see APPENDIX A). As the angle η_N increases, an increase in the area of the aerofoil will be observed and a serious discontinuity of the flow will occur at the lower surface of the aerofoil thus reducing its lift and increasing its drag. During these low angles however, the Krueger flap can be used as a spoiler, thus deliberately reducing the lift and increasing the drag of the aerofoil. A further increase in the angle η_N, however, will start to align the flow approaching the leading edge with the flap, thus creating a substantial amount of lift without the presence of excessive pressure.

The flow over the rear portion of the aerofoil at flap deflections less than the optimum, becomes separated before the angle of attack is high enough for the load on the flap to substantially contribute to the lift [32].

3.3 Influence of the chord ratio

The results with three nose flaps of chord ratio l_N / l = 0.05, 0.10, 0.20 are represented in Figure 18.

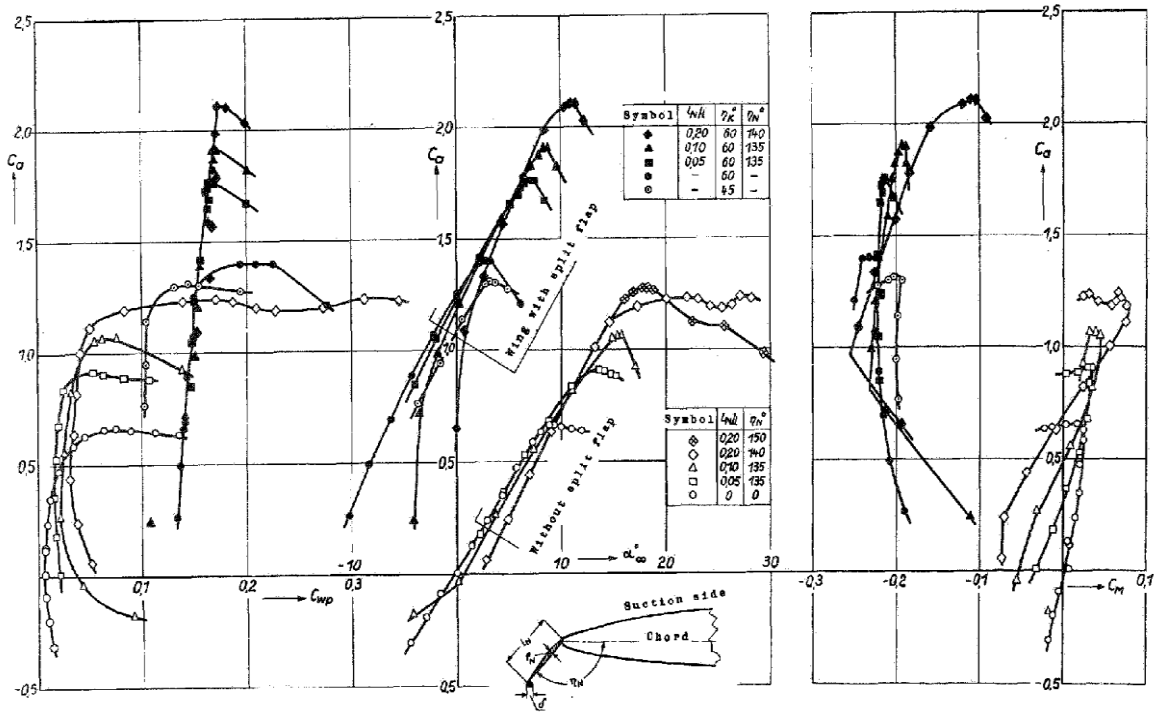

Figure 18: Influence of the chord of the nose flap upon the aerodynamic coefficients of the wing with and without split flap. Valid for the most favourable nose flap angle η_N and for $\delta / l_N = 0.008$. The camber of the nose flap is selected so that it coincides with the pressure side contour of the smooth profile when the flap is extended [31].

From the above graphs, it can be seen that as the value of the chord ratio increases a considerable increase is observed in the values of C_{amax}. The curves for each case represent the optimum value of η_N [30]. A considerable change in the value of C_{amax} can be produced by the implementation of a nose flap, and further improvements can be made as the value of the chord ratio increases as it can be seen from Figure 18 , however, the maximum result of such configurations can only be produced if the correct combination of η_N and l_N / l is made

3.4 Influence of the leading edge curvature

Further increase of the lift characteristics of such systems can be made possible by increasing the curvature of the leading edge of the flap as shown from Figure 19 and Figure 20 [31].

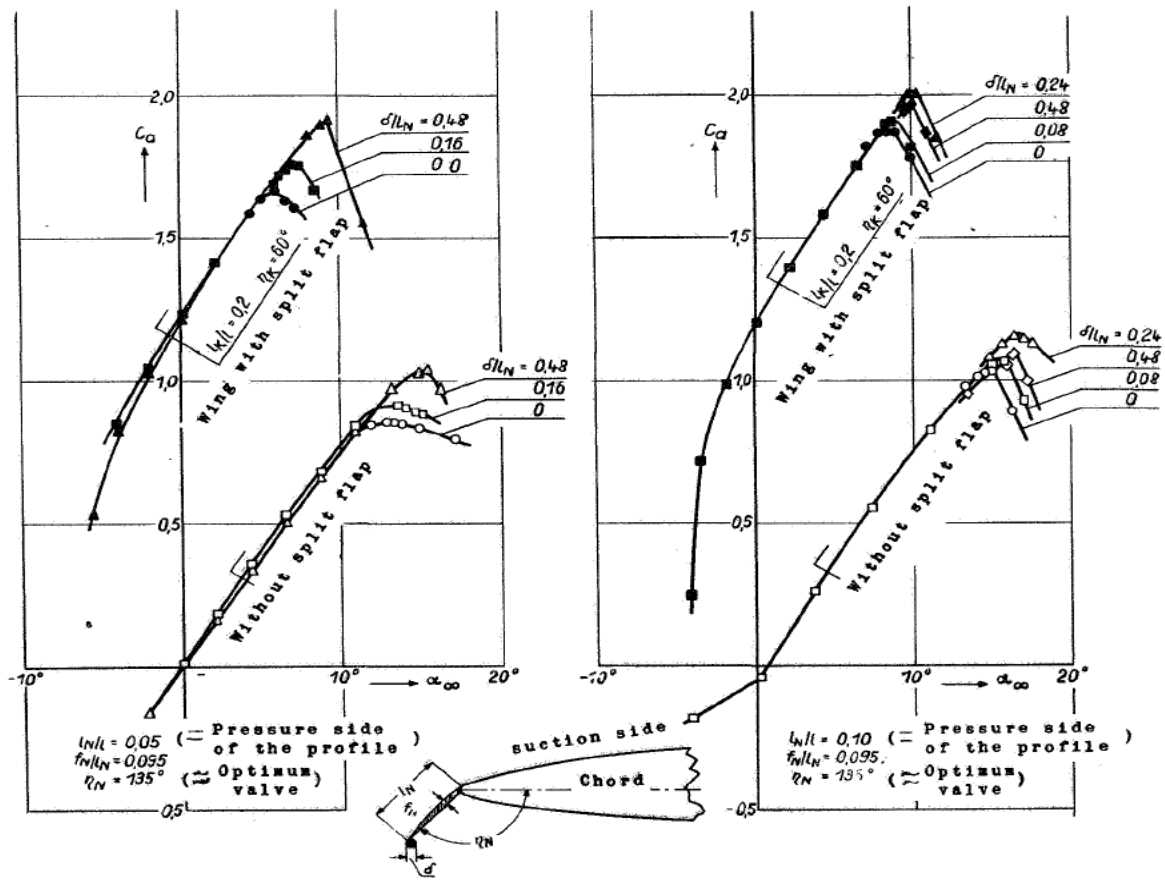

Figure 19: The Influence of curvature at the leading edge of the nose flap upon the lift [31].

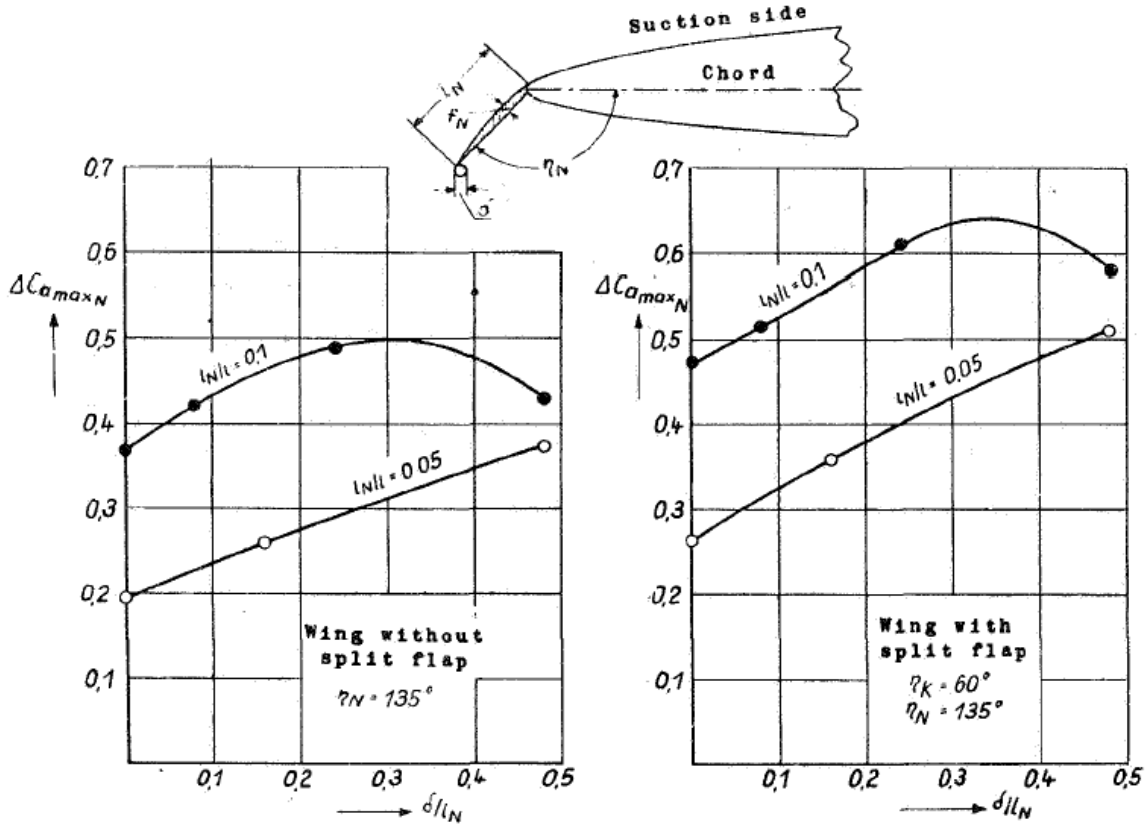

Figure 20: The increase of C_{amax} obtained by the nose flap as a function of the curvature of the leading edge of the flap. Parameter: flap chord ratio l_N / l [31].

As the value of δ / l_N increases a further increase of the value of ΔC_{amaxN} is observed. However, for very high curvatures a decrease in the value of ΔC_{amaxN} is obtained.

3.5 Influence of the camber of the flap

In most investigations in Krueger's experiments, the camber of the flap had been chosen so that the surface of the flap coincided with the lower side of the smooth profile when retracted, and with the contour of the pressure side when extended [30],[31]. As could be seen from Figure 21 no significant improvements could be obtained by an increase of the camber of the flap.

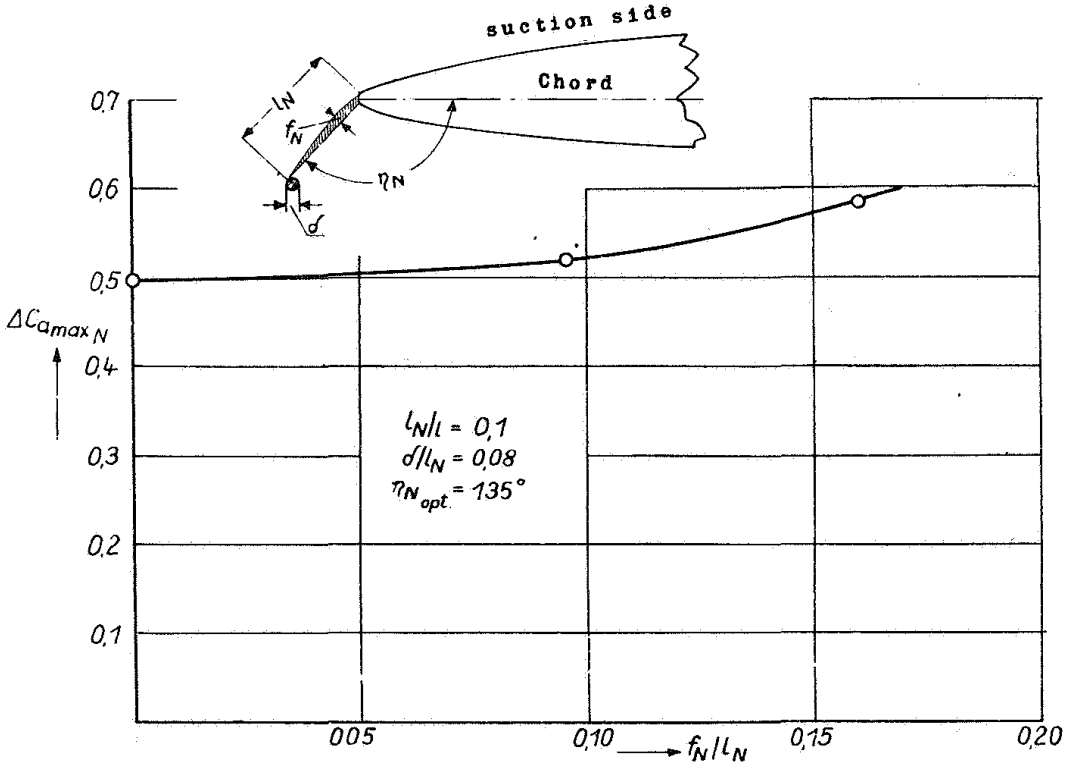

Figure 21: Represents the increase of Camax obtained by the nose flap as a function of the flap camber (f_N / l_N). Wing with split flap (l_N / l = 0.2; η_K = 60°). For f_N / l_N = 0.095 the camber of the nose flap corresponds to the pressure side contour of the smooth profile [31].

Recent developments and applications of the Krueger flap on aircraft however, show the importance of the camber of the flap. Boeing increased the performance of the Krueger flap by flexing the flap skin to approach an "ever – opening spiral" (Figure 22). This device is used both on the 747 with only a cove slot to encourage natural boundary layer control, and on the YC-14 where its effectiveness is enhanced by power blowing air at the cove slot to augment the air from below (Figure 23) [34]. This illustrates the need for a device having spiral geometry, with a reduction in the slope of curvature as the air moves back along the surface. According to Bernoulli's principle, the pressure is reduced as the speed of the air increases. The lower the pressure, the more easily the air can separate as it moves around the leading edge, due to the adverse pressure gradient. It is therefore, desirable for the curvature to be less abrupt as the air accelerates around it. The closer this geometry can approximate an "ever – opening spiral", the less need there is for cove slot or boundary layer control, to reattach the flow at a sharp corner or knee [34].

3.6 Influence of a slot

Figure 24 shows that the effect of a nose flap with a chord ratio $l_N / l = 0.10$ was nullified by a slot between the wing and the flap. However it is thought, as mentioned before in Krueger's experiments, that the camber of the flap had been chosen so that the surface of the flap coincided with the contour of the pressure side. Thus when extended, a smooth transition from the flap to the aerofoil was obtained. In cases where the transition is more abrupt such as in the case of the Krueger flap used in the 747, a slot between the aerofoil may have more favourable results.

3.7 Effect of the Position of the Krueger Flap

As mentioned earlier in addition to Krueger's experiments in the mid 1940s, subsequent experiments were carried out by Felicien F. Fullmer [32] and [33], using different aerofoil sections equipped with a nose flap, with the aim to determine the effect that a nose flap would have when implemented on an aerofoil section. Fullmer's experiments were conducted to

explore out the characteristics of leading edge flaps (Krueger flaps), used as high lift devices and to determine their effect on the maximum lift coefficient [32],[33]. In contrast with Krueger, Fullmer also examined how the position of the flap would influence its lift characteristics. Two similar NACA aerofoil sections were used for Fullmer's experiments. In his initial experiments a NACA 64_1-012 was used and in his subsequent experiments a NACA 64-009. Both investigations were conducted at a Reynolds number of 6.0×10^6, and included testing of two 10% chord leading edge flaps, one intended to slide forward along the upper surface and the other near the leading edge of the lower surface of the aerofoil. The aerofoil sections and the different leading edge configurations are shown in Figure 25 to Figure 28. The results of Fullmer's experiments are summarised and presented in two Parts. Part I describes his initial experiments and configurations using the NACA 64_1-012 (Figure 25 and Figure 26) and Part II describes his subsequent experiments using the NACA 64-009 section (Figure 27 and Figure 28).

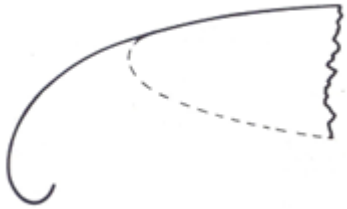

Figure 22: An Ever –Opening Spiral [34].

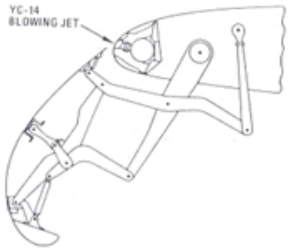

Figure 23: A Flexible fibreglass Krueger Flap similar to the one used on Boeing 747 and YC-14 [34].

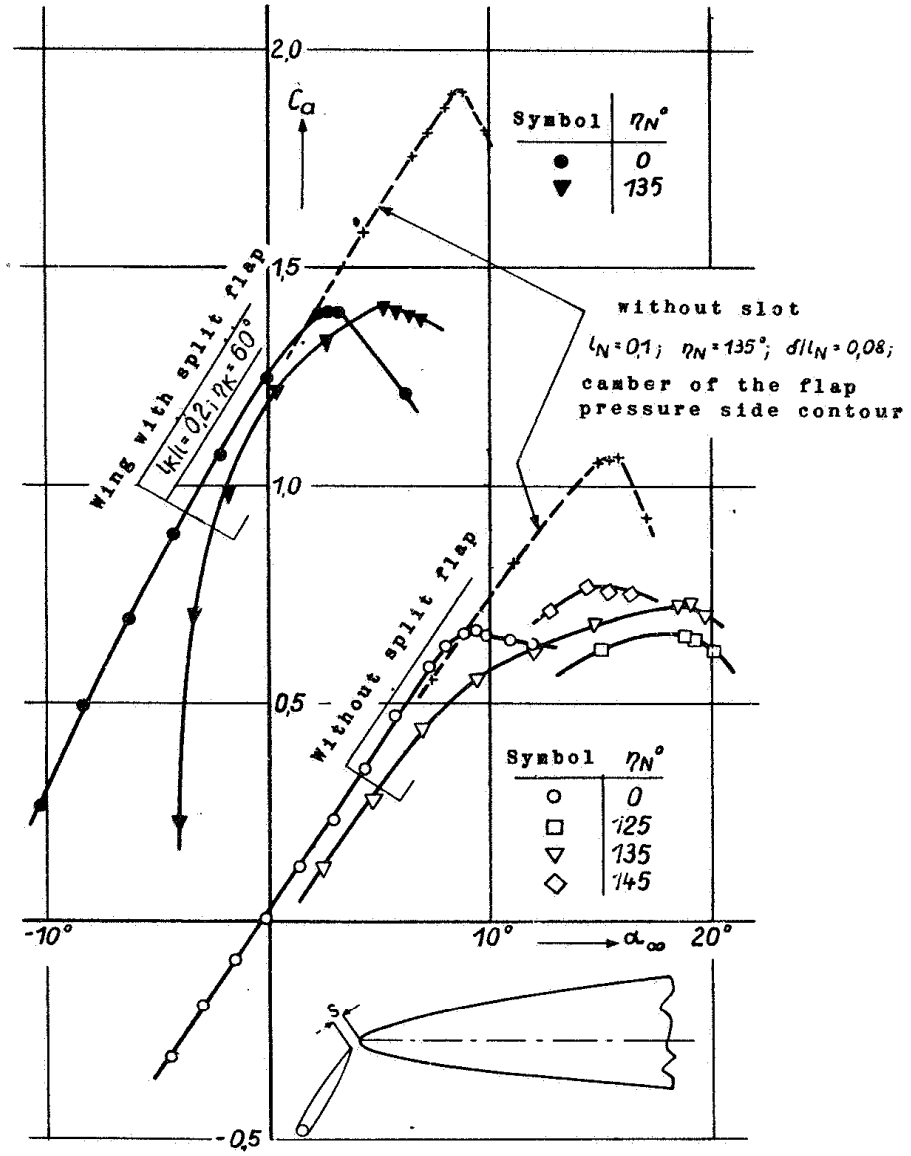

Figure 24: Illustrates the value of Ca Vs α_∞ for aerofoil with nose flap and slot. The case "without slot" is indicated by a dashed line for comparison [31]. Parameters: l_N / l = 0.1, δ / l_N = 0.12, s / l = 0.01.

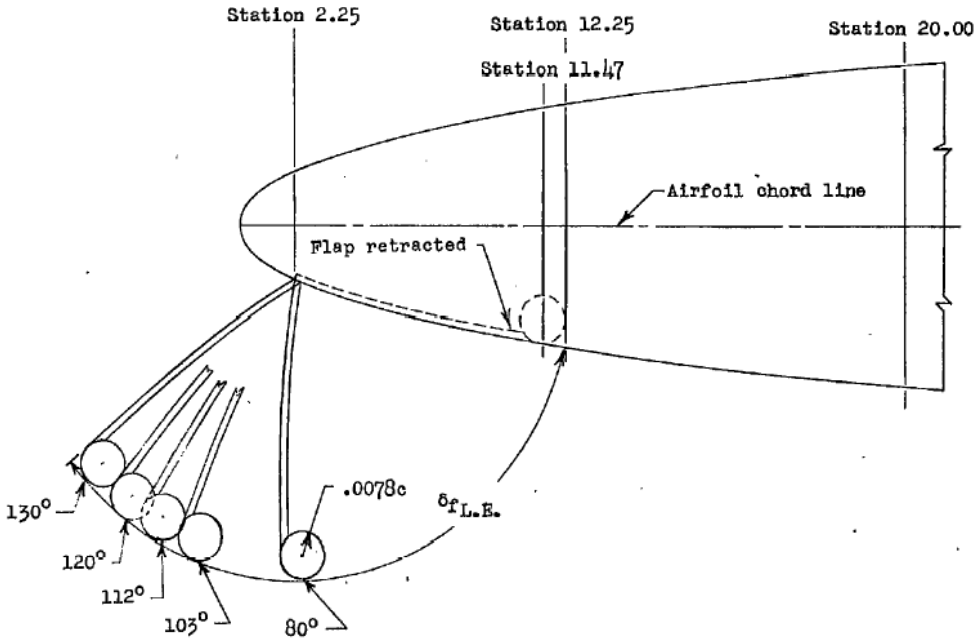

Figure 25: Leading edge lower - surface flap configuration (Station 2.25) on the NACA 64_1-012 aerofoil section [32].

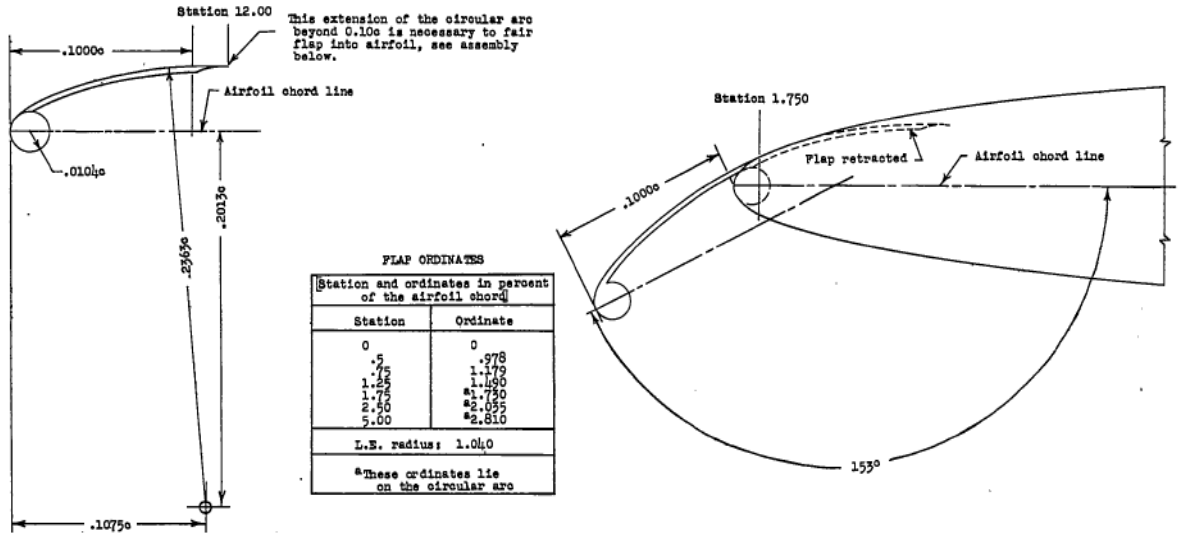

FLAP ORDINATES

Station and ordinates in percent of the airfoil chord	
Station	Ordinate
0	0
.5	.978
.75	1.179
1.25	1.490
1.75	[a]1.750
2.50	[a]2.055
5.00	[a]2.810
L.E. radius: 1.040	
[a]These ordinates lie on the circular arc	

Figure 26: Upper – surface leading edge flap, flap ordinates and the arrangement of the flap on the NACA 64_1-012 aerofoil section [32].

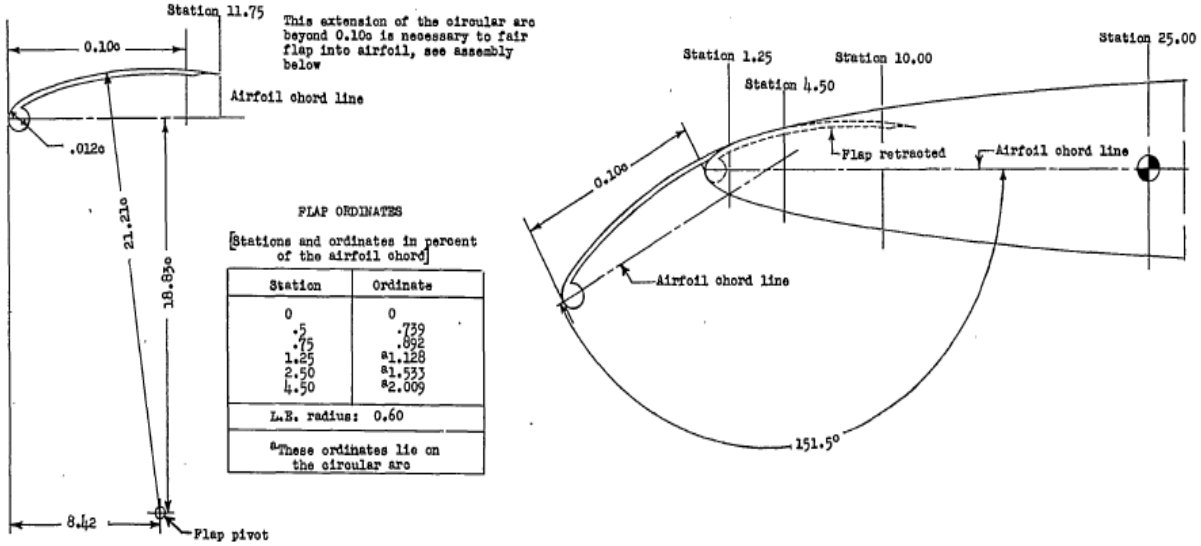

Figure 27: Upper – surface leading edge flap, flap ordinates and the arrangement of the flap on the NACA 64-009 aerofoil section [33].

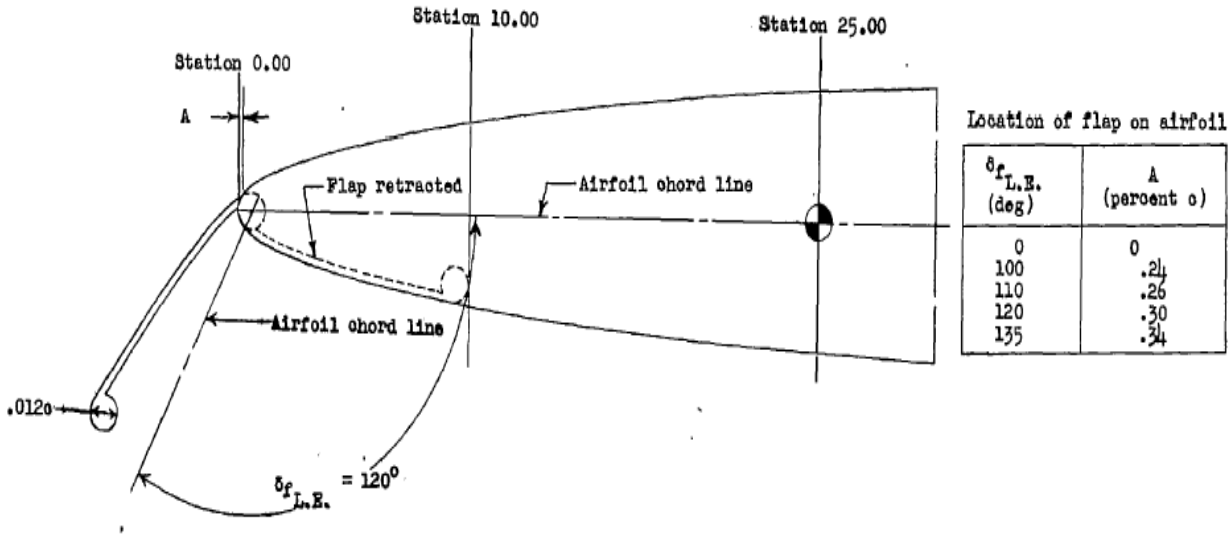

Figure 28: Leading edge lower - surface flap configuration (station 0.0) on the NACA 64-009 aerofoil section [33].

3.7.1 Fullmer's Part I Experiments

The lower surface leading edge flap was fixed to the surface of the aerofoil at a point 2.25% of the chord behind the leading edge, as illustrated in Figure 25. The l0% chord flap was shaped so as to conform to the aerofoil's lower surface contour between the, 2.25 and 11.47% aerofoil chord stations, and had a leading edge radius which equalled to 0.78% of the aerofoil's chord [32].

The upper surface flap design, shown in Figure 26, aimed to eliminate some of the more evident flaws exhibited by the lower surface flap, for instance the significant discontinuity occurring at the hinge point and the comparatively small area increase resulting with the flap at its optimum deployed position. Hence the upper surface flap was designed to assist smooth transition onto the aerofoil's upper surface with the flap at its fully deflected position while at the same time provide an increase in the aerofoil area.

Furthermore, the upper surface curvature near the leading edge is fairly large and smoothly decreases with distance while moving away from the leading edge [32].

The upper surface flap utilised in these tests simulated an extendable type flap which, in the retracted position, intentionally formed an integral part of the leading edge and upper surface of the aerofoil. The profile of the leading 50% of this 10 % flap was identical in contour with the original plain aerofoil from the leading edge to the 5% chord station, while the latter 50% of the flap was of true circular arc form.

The flap could hence extend by sliding along a circular arc track. The radius of this circular arc and its centre of curvature, were elected so that the arc conformed to the aerofoil's upper surface contour, between 1.75% and 5.00% chord stations. As the arc defined by this radius formed part of the original aerofoil surface, when extended, the flap merged smoothly with the aerofoil's upper surface, resulting to a highly cumbered aerofoil as illustrated in Figure 26. The details in Figure 26 also outline the ordinates, the flap to aerofoil relation, and how the effective 10% chord of the flap is measured [32].

Lower surface leading edge flap: An examination of the lift characteristic details of the NACA 64_1-012 aerofoil as illustrated in Figure 29, indicate that the lower surface leading edge flap when used in combination with the plain aerofoil, produces a maximum lift coefficient of 1.54 at an angle of attack of 15.7^o ($\delta_{fL.E} = 120^o$), corresponding to an increase in

the value of ΔC_{lmax} by 0.12 and $\Delta\alpha$ by 1.4^o above the values achieved by the aerofoil alone [32].

Upper surface leading edge flap: The upper surface leading edge flap appears to be more effective than the lower surface leading edge flap. As can be seen from Figure 31 when used in combination with the plain aerofoil it produces a maximum lift coefficient of 1.85 at an angle of attack of 18.3^o, which corresponds to an increase in the value of ΔC_{lmax} by 0.81 and $\Delta\alpha$ by 6.9^o above the values achieved by the aerofoil alone [32].

Thus results indicate that the increments in the values of ΔC_{lmax} and $\Delta\alpha$ are considerably greater in the case of the upper surface leading edge flap. This may be attributed mainly to the smooth contour of the upper surface leading edge flap and to the slightly greater profile area.

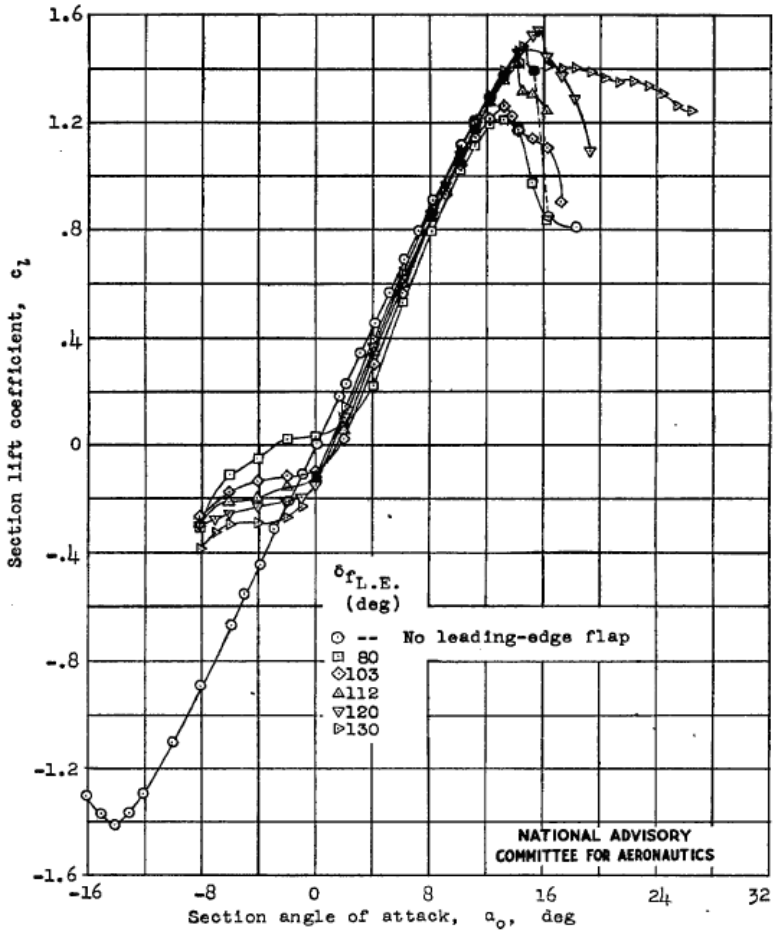

Figure 29: Lift detail for the NACA 64_1-012 aerofoil section incorporating 10% lower surface leading edge flap [32].

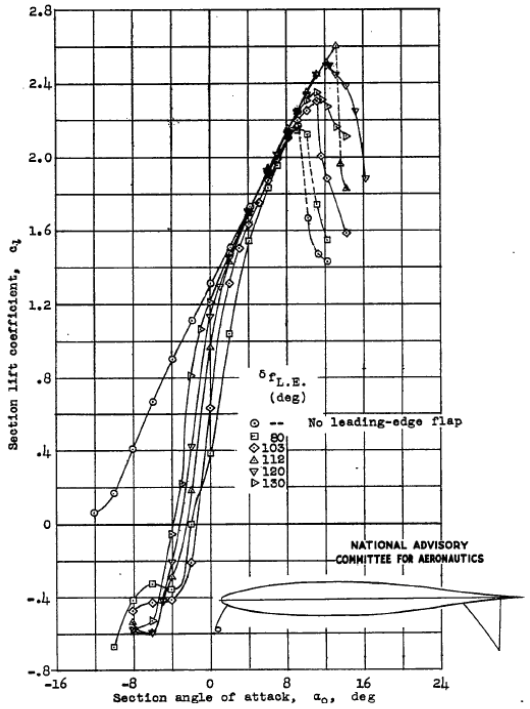

Figure 30: Lift details for NACA 64_1-012 aerofoil section incorporating a 10% lower surface leading edge flap and a 20% trailing edge split flap [32].

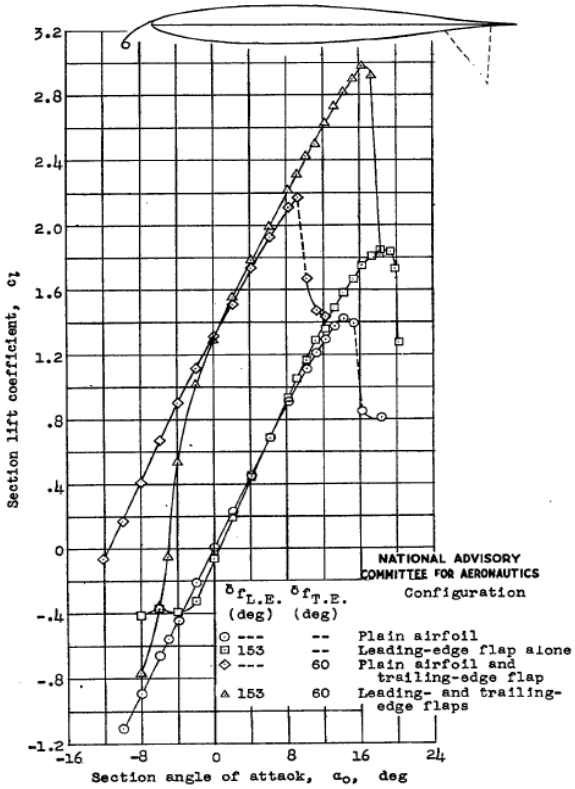

Figure 31: Lift curves for a NACA 64_1-012 aerofoil section incorporating: (a) a 10% upper surface leading edge flap only and (b) a 10% upper surface leading edge flap in combination with a 20% trailing edge split flap [32].

3.7.2 Fullmer's Part II Experiments

The l0% chord upper surface flap utilised in these tests simulated an extendable type flap which, in the retracted position intentionally formed an integral part of the aerofoil's leading edge and upper surface. The first 45% of flap profile was identical in contour to that of the original plain aerofoil from the leading edge to the 4.5% wing chord station, and the remaining 55% of the flap was of true circular arc contour. The flap could hence extend by sliding along a circular arc track. The radius defining this circular arc and its centre of curvature were such that the arc conformed to the contour of the aerofoil's upper surface between the 1.25% chord and 4.5% chord stations [33].

Because the arc defined by this radius formed a part of the original aerofoil surface, when the flap was extended its profile smoothly matched the aerofoil's upper surface, thus producing a highly cambered aerofoil as illustrated in Figure 27. The sketches in Figure 27 detail the ordinates, the flap to model relation, and how the effective 10% chord of the flap was measured [33].

The lower surface leading edge flap was designed to rotate about a single fixed pivot which was coincident with the location of the centre of the aerofoil's leading edge radius as illustrated in Figure 28. The flap had a chord equal to 10% of the aerofoil's chord, a shape which conformed to the contour of the aerofoil from the 0% chord to the 9.4% chord aerofoil stations, and a leading edge radius equal to 0.6% of the aerofoil's chord [33].

Upper surface leading edge flap: Comparing Figure 32 with Figure 31 and from the results summarised in Table 2, it can be seen that the value for the maximum lift coefficient produced by both aerofoils (9% thick in Part II and 12% thick in Part I respectively), without trailing edge flap, is essentially the same for approximately equal deflections of the leading edge flap. The value of ΔC_{lmax} however, for the 9% thick aerofoil is nearly twice as great as that obtained for the 12% thick aerofoil. This indicates that a greater increase in the value of C_l can be achieved when the aerofoil is thinner [33].

A difference of 0.33 is observed in the value of C_{lmax} between the 9 and 12% thick aerofoils. When a trailing edge flap was implemented only and in conjunction with a leading edge flap, in both NACA aerofoils, it was observed that above difference in C_{lmax} remained approximately the same (0.37 trailing edge flap only and 0.34 trailing and leading edge

flaps). Therefore it may be assumed that the leading edge flap was equally effective on both aerofoils.

Lower surface leading edge flap: The results of this configuration are summarised in Table 2. A direct comparison between the two NACA aerofoil configurations (9% thick in Part II and 12% thick in Part I respectively), cannot be made since in Part II the flap was located at a more favourable position. Therefore the aerofoil was compared with the 12% thick aerofoil with upper surface leading edge flap of Part II that had a more alike setting. The comparison shows that when the leading edge flap was used alone, or in conjunction with the trailing edge split flap, it was capable of producing increments in C_{lmax} and α_o slightly higher than those obtained with the upper surface leading edge flap used on the 12% thick aerofoil. Therefore as a high lift device, either the upper surface or the lower surface leading edge flap was more effective on the thinner aerofoil such as in Part II than the thicker aerofoil as in Part I [33].

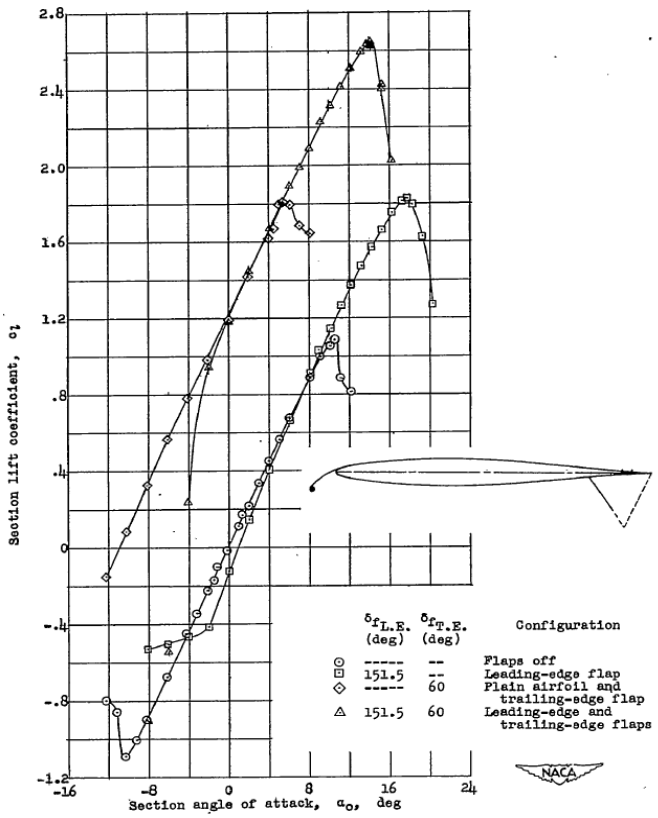

Figure 32: Lift graphs for the NACA 64-009 aerofoil section incorporating (a) a 10% upper surface leading edge flap only and (b) a 10% upper surface leading edge flap in combination with a 20% trailing edge split flap [33].

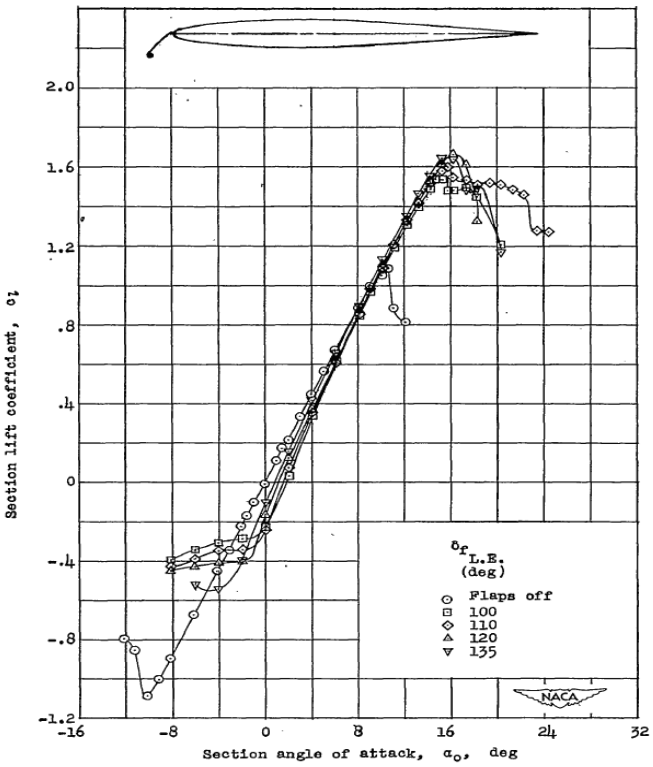

Figure 33: Lift graphs for the NACA 64-009 aerofoil section incorporating a 10% lower surface leading edge flap [33].

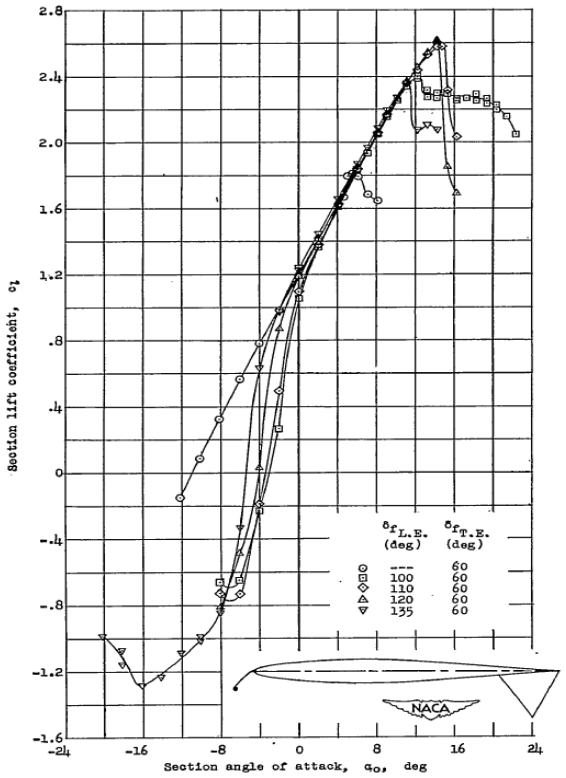

Figure 34: Lift graphs for the NACA 64-009 aerofoil section incorporating a 10% lower surface leading edge flap and a 20% trailing edge split flap [33].

Model configuration	$c_{l_{max}}$	α_o (deg)	$\Delta c_{l_{max}}$	$\Delta\alpha_o$ (deg)	$\delta_{f_{L.E.}}$ (deg)	$\delta_{f_{T.E.}}$ (deg)
NACA 64–009 airfoil						
Airfoil alone	1.09	10.6	------	-----	------	------
Airfoil and lower–surface leading–edge flap	1.66	16.2	0.57	5.6	120	------
Airfoil and upper–surface leading–edge flap	1.82	17.8	.73	7.2	151.5	------
Airfoil and trailing–edge flap alone	1.80	5.5	------	-----	------	60
Airfoil trailing–edge flap and lower–surface leading–edge flap	2.61	14.2	.81	8.7	120	60
Airfoil trailing–edge flap and upper–surface leading–edge flap	2.64	14.2	.84	8.7	151.5	60
NACA 64_1–012 airfoil						
Airfoil alone	1.42	14.3	------	-----	------	------
Airfoil and lower–surface leading–edge flap	1.54	15.7	0.12	1.4	120	------
Airfoil and upper–surface leading–edge flap	1.85	18.3	.43	4.0	153	------
Airfoil and trailing–edge flap alone	2.17	9.3	------	-----	------	60
Airfoil trailing–edge flap and lower–surface leading leading–edge flap	2.60	13.2	.43	3.9	112	60
Airfoil trailing–edge flap and upper–surface leading–edge flap	2.98	16.2	.81	6.9	153	60

Table 2: Summary of results obtained from tests of the NACA 64 – 009 and the NACA 641 – 012 Aerofoils incorporating two types of leading edge flaps [33].

3.7.3 Discussion of the results

According to Fullmer and Krueger, the leading-edge flap is supposed to produce increases in C_{lmax} and in the angle of attack for C_{lmax}, by in effect reducing the magnitude of the pressure peaks and the magnitude of the adverse pressure gradient, which are usually associated with the flow conditions near maximum lift of the plain aerofoil section. At the optimum deflection stage, the flap is aligned with the flow approaching the leading edge so that a significant amount of lift is produced by the flap, without the presence of extreme pressure peaks. Of course, some increase in lift is also due to the effective increase in area produced by the flap deflection. At flap deflections less that optimum the flow over the rear portion of the aerofoil separates, before the angle of attack is high enough for the load on the flap to substantially contribute to the lift. At flap deflections greater than the optimum, large pressure peaks form at the leading edge of the flap at low angles of attack [32] .

As the angle of attack reduces, the flow becomes less aligned with the flap [32]. At low angles of attack therefore, the leading edge flap can act as a spoiler on the lower surface of the aerofoil, with a resultant large reduction in lift and a large increase in drag.

3.8 The effect of split-flap application

Comparing the data presented in Figure 29 to Figure 33 indicates that sufficient increase in the performance of the aerofoil is achieved, when a trailing edge split flap is employed in conjunction with the leading edge flap. In addition Table 2 indicates that an increase in C_{lmax} of the order of 0.7 can be accomplished by implementing the trailing edge split flap, and a further increase of around 0.3 can be attained when used in combination with the leading edge flap. According to Fullmer however, when the trailing edge split flap was deflected on the NACA 64 – 009 aerofoil, the effectiveness of the leading edge flap was not so extensive as it was in the test for the NACA 64_1- 012 aerofoil section.

3.9 Conclusions

1. The upper surface leading edge flap was, in general, a more effective high-lift device than the lower surface leading edge flap, especially when used alone on the plain aerofoil.

2. Slightly larger increments in the C_{lmax} were produced when a leading edge flap (with approximately equal amounts of effective camber) was attached to the 9% thick aerofoil rather than to the 12% thick aerofoil.

3. At high angles of attack a forward movement of the aerodynamic centre was observed as a consequence of the deflection of either type of leading edge flap.

4. The addition of a split-flap shifts the C_L values upwards in the C_LVs graph

Chapter 4. Project Definition

4.1 Aims and Objectives

The primary aim for a given wing is to maximize its lift and reduce its drag thus increasing the overall L/D ratio. This factor is often regarded as the measure of the overall efficiency of a configuration and it is often highly dependent upon not only the wing's geometry but also on the given flow conditions as well. These flow conditions can be expressed in typical dimensionless parameters such as Mach number M and Reynolds number Re. For a given aerofoil section, a large range of lift and drag characteristics can be observed over the possible operational Re and M ranges for a given aircraft. Aerofoils are therefore designed to achieve optimum performance, for a narrow range of flow conditions and in general maximum efficiency is achieved during the cruising phase of a flight envelop. Alternatively, one could design an aerofoil that adequately operates over a wider range of flow conditions.

The object of this project is to use an experimental and theoretical approach, to demonstrate a design of a Krueger flap high lift configuration that would deploy during landing and takeoff such that the parameter V^2C_L will remain constant. Given this parameter originates from the lift equation, $L = \frac{\rho \cdot V^2 S \cdot C_L}{2}$, this system will thus allow a typical, low thickness to chord ratio wing to configure at decreasing airspeeds during an approach to provide for a lower landing speed and distance. This design has inspiration from examples in nature such as bird wings which self configure over a wide range of flight speeds.

For a passive high lift system design to be a viable design option, some of the following criteria must be as good as or better than those of a conventional wing:

1. Efficiency
2. Manoeuvrability
3. Control
4. Weight
5. Cost

It is believed that a primary benefit of utilising a passive system would be improved efficiency, with a minimal increase in design complexity. This project aims to examine the validity of this statement

As well as examining the aerodynamic characteristics of such configurations the project aims to quantify the magnitude of the forces and moments exerted in such systems. By knowing this, a design can be proposed for a passive high lift system, that will be efficient as well as weight and cost effective.

The joined experimental and numerical approach, is used to present a Krueger flap design directly applicable to a tactical unmanned aerial vehicle (UAV) application.

The research program was also designed so as to investigate the effects of flap size and positioning, as well as the influence of a transition strip and geometry discontinuity on the aerodynamic behaviour of the configuration. In addition, using validated CFD models the forces and moments acting on such systems are determined and presented.

The experimental and numerical investigations were performed in the Reynolds number range of $0.6x10^6$-$1.6x10^6$, which is representative of the ranges expected on a wide range of UAVs as illustrated in Figure 35 and coincides with the operational range of small and medium size UAVs, see reference [5].

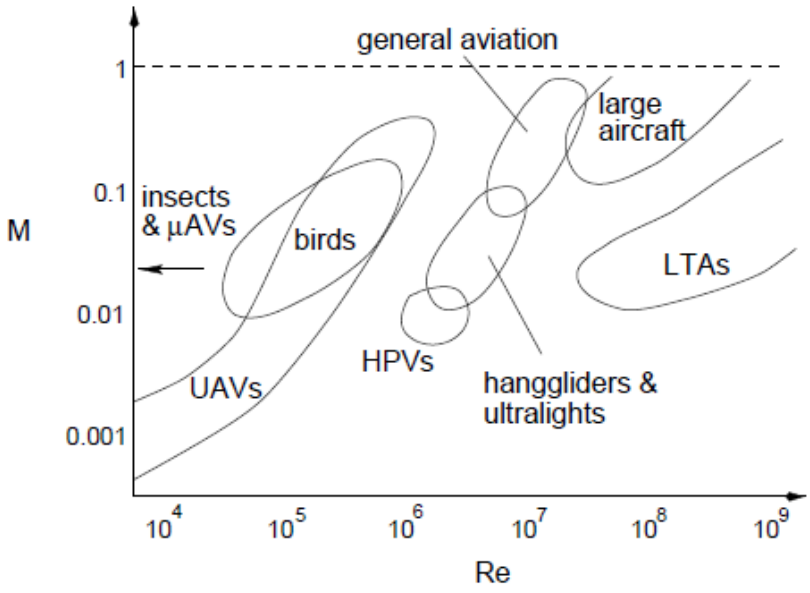

Figure 35: Mach number versus Re for various ranges of operation for man-made and natural flyers [35],[36].

4.2 Wing Design Considerations

Recent advancements in CFD tools, allow the development of more sophisticated and advanced wing designs. This is especially relevant for UAVs, where different design specifications and mission requirements, as well as imposed non aerodynamic constraints might make impractical the use of single element aerofoils. These methods in combination with experimental tests, allow the design of radical configurations which should provide improvements on the UAV characteristics and provide answers to different mission requirements.

Special interest is observed for the development of high lift wings for the cases of small and medium size UAVs (Tactical UAVs 50 kg $\leq$ W $\leq$ 500 kg), due to the low Reynolds numbers that may be encountered during the flight envelope. For conventional wing body tail configurations with unswept wings, the typical chord Reynolds number range expected close to stall speeds, is between $0.3x10^6$ and $1x10^6$ [6]. This range still belongs in the domain of low Reynolds number aerodynamics even though it is much higher than that of mini UAVs the characteristics of which are strongly dominated by viscous flow effects [6].

For the aerodynamic development of wings used on Tactical UAVs the following design objectives may be formulated:

- Increased high lift capabilities at reduced Reynolds numbers and flight safety at speeds close to stall

- Capability to fly and recover from post stall angles

- Extension of usable range of the lift up to C_{Lmax} and elimination of the safety speed margin ($V_{flight} \geq 1.2V_{stall}$)

- Reduced sensitivity to contamination effects and capability to continue the mission of cruising/loitering flight in unfavourable weather conditions

- Improved endurance performance of configurations with moderate aspect ratio wings and increased level of parasite drag

- Enhanced takeoff and landing performance

- Capability to increase the glide angles at approach to landing and to perform the landing at stall / post-stall angles of attack

- Enhanced manoeuvrability and maximum turn performance

Configurations with enhanced lift carrying capabilities are especially attractive for development for UAV wings because of their potential to provide an answer to most desirable UAV characteristics [6]. The concept of high-lift, loitering flight was adopted by Israel Aircraft Industries for the development of long endurance subsonic and transonic UAVs [5], [35]-[38] which is relevant for design of configurations with high aspect ratio wings and increased level of parasite drag. In the case of sailplanes with high aspect ratio wings, and low levels of parasite drag, moderate values of lift coefficient (0.8-1) and C_{Lmax} (1.3-1.5), are sufficient for the realization of best endurance performance. Due to the required speed safety margin ($V_{flight} \geq 1.2V_{stall}$) and limited wing span, it might be hard to achieve the maximum lift coefficient required for a UAV case, using a single element wing section. Adding a leading edge flap however, will increase the lift capacities of the configuration appointing it as a potential solution for matching such challenging requirements. For cases of small and medium size UAVs with moderate aspect ratio wings, the high lift configurations could produce significant advantages in loitering performance as well as takeoff and landing, relative to conventional wings with moderate maximum lift [39].

In the last decade an effort has been made to develop high lift configurations, using trailing edge slats. Such configurations were developed and examined and more detailed analyses can be found in references [5],[37] and [38]-[53]. Purpose of this work is not to examine such designs but to provide evidence, that leading edge Krueger flaps can also be used to enhance the lift characteristics of a wing making them suitable for implementation on a Tactical UAV.

As well as understanding how the leading edge Krueger flaps work, this project also aimed to investigate whether the implementation of such devices could enhance, the already attractive features of mild stall aerofoils, for their use on small and medium size UAVs. The above requirements defined the operating Reynolds number range for this project.

4.3 Aerofoil Selection

While much of the current speculation regarding low Re aerofoil performance is centred around newer aerofoil sections, there are older designs about which a great detail is already known. One such aerofoil which is known to be a good performer at low speeds is the Clark Y. The Clark Y is a widely studied aerofoil, that has showed very favourable lift and drag characteristics in experiments made at various facilities [42]-[50]. Its mild stall characteristics might be considered as a beneficial factor for the flight of small UAVs, in gusty air and for relaxation of speed margins during the flight and takeoff/landing [6]. Mild stall arises when the boundary layer separation occurs near the trailing edge of the aerofoil, and moves progressively upstream with increasing angle of attack [52]. This results to a gradual loss in lift. After stall, the lift does not drop abruptly but decreases gradually hence the term mild stall. In addition it was noted that the best Reynolds number range for mild stall aerofoils is between Re = $0.5x10^6$ - $1x10^6$ [12], which coincides with the operational range of small and medium size UAVs ($0.3x10^6$ - $1x10^6$)[2]. At higher Reynolds numbers, it seems that there is a gradual deviation from the mild stall characteristics, and at values of Re below $0.5x10^6$ a special alteration of the aerofoil's upper surface might be required, for a better integration with the laminar separation bubble and for prevention of laminar stall. For UAV configurations with such wings no significant rolling moments are expected at stall angles, which will improve the aircraft's responses to asymmetric stall and prevent the drop of the wing and development of spin modes [5].

Furthermore at close to stalling speeds, mild stall wings such as the Clark Y, are expected to produce beneficial nosedown moments for conventional wing body tail configurations [54]. This is attributed to the deviation from linear lift build-up on the wing and to the gradual loss of wing downwash on horizontal tail surface. These effects provide the feature of "passive self-recovery in pitch plane" (build-in safety mechanism that protects a UAV from

unintended stall). The concept should be supported by adequate design of the tail and sufficient power of the elevator for trimming negative pitching moments [5].

According to Alexander et al., the standard speed safety margin ($V_{flight} \geq 1.2\ V_{stall}$) may be revised and relaxed for mild stall wings, allowing better exploitation of available maximum lift [5],[54]. As previously mentioned this may improve take off/landing characteristics and allow loitering at higher lift coefficients. The reduced sensitivity of mild stall wings to contamination effects, could provide the possibility of maintaining a safe flight in hard weather conditions.

The cases of typical mild and abrupt stall aerofoils were outlined by McMasters and Henderson, showing the characteristics of aerofoils with concave and highly cambered upper surface [55]. It was shown by Liebeck that mild stall aerofoils produce moderate values of C_{Lmax}, while high lift front loaded aerofoils have a tendency for abrupt stall [2]. The behaviour of mild stall aerofoils is illustrated in Figure 36, showing the lift curves of two well known mild stall aerofoils, such as the NACA 4415 and FX61-184. It was suggested however, that the maximum lift coefficient of mild stall aerofoils may be enhanced, by delaying the formation of a sharp suction peak at their leading edge, which might be achieved by reshaping the forward portion of the aerofoil or by the implementation of a leading edge flap [56],[57].

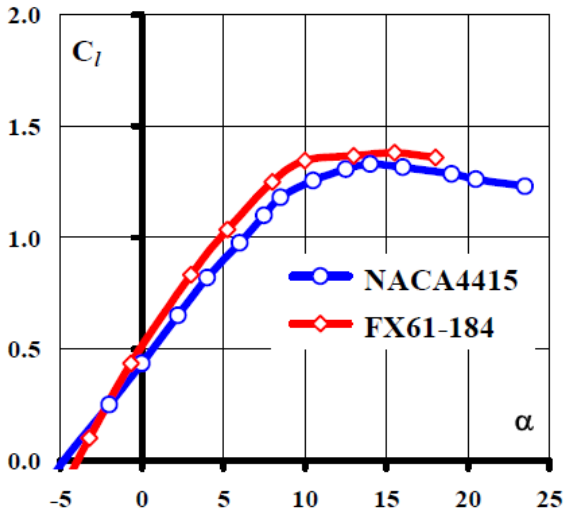

Figure 36: Wind tunnel results of NACA4415 and FX61-184 at Re 1x10^6[39]

Other aerofoils such as the above mentioned NACA4415 and FX61-184 as well as NACA$63_3$618 and NFL1015 [2], [56]-[57], have similar characteristics to the Clark Y. The Clark Y however, has been a favourite, because of its good aerodynamic performance, its ease of construction and its availability. In addition, the thickness of the Clark Y section, could permit the installation of standard sized servo motors within the wing, for actuation of ailerons, flaps etc. All the above characteristics, make the Clark Y aerofoil a suitable candidate for implementation on small UAVs, hence its selection and use for the purposes of this project.

Chapter 5. Computational Modelling

This chapter provides an overview on CFD and identifies the methods used to generate the models examined. Description of the assumptions and models used as well as of errors that might arise from unsatisfactory modelling criteria are also presented.

In brief, Computational Fluid Dynamics or CFD is a computational technology which enables the user to study the analysis of systems involving fluid flow, heat transfer and other associated phenomena as for example chemical reactions [59].

5.1 CFD Overview

The computational analysis undertaken within this project is concerned with the performance and the flow characteristics of a two dimensional wing and flap configuration. The commercial CFD package FLUENT 6.3 solver and GAMBIT 2.4 pre-processor were utilised to develop and analyse the models examined and also determine the forces acting on such configurations.

5.1.1 Pre-Processor / Gambit

The Gambit [59] pre-processor is the interface used to enter the characteristics of a particular flow problem into the CFD solver. The pre-processing stage involved six steps:

a). Definition of region geometry: i.e. definition of computational domain.
b). Mesh / Grid generation. A very important step in the CFD analysis since the density and the quality of the mesh will specify the accuracy of the results and the time taken until the solution will converge.
c). Selection of the physical and chemical properties which need to be modelled.

d). Definition of the fluid's physical properties
e). Application of boundary conditions at the extremity of the solution domain.
f). Mesh export from pre-processor.

With respect to the creation of the mesh, generally the finer the mesh the more accurate the results. However, time and cost must be taken into account for the development of the grid. A finer mesh will need more time to be solved thus increasing the computational cost. This limitation is best met using unstructured or hybrid grids [60],[61]. In regions, where large variations arise from point to point, a finer structured mesh may be used to achieve higher accuracy whereas in areas with relatively little change, a more coarse unstructured mesh can be utilised.

5.1.2 Solver/Fluent

There are three distinct ways of formulating a numerical approximation to solve one, or a set of partial differential equations governing the motion of fluid:

a). Finite Difference
b). Finite Element
c). Finite Volume

For the purposes of this project the finite volume method was used which is centred on the use of a control volume of fluid (see APPENDIX B), which is subjected to property changes caused by convection, diffusion and source generation [62].

FLUENT, solves the Reynolds Average Navier-Stokes (RANS) equations by means of the finite volume method (FVM) to arrive at converged solutions [63]. The FVM provides a clearer relationship between the numerical algorithm and the underlying physical conservation principle which makes its concepts much simpler to understand than the finite element and finite difference methods [62].

The finite volume method is a numerical method used for solving partial differential equations that calculates the values of the conserved variables average across the volume. Finite volume refers to the small volume surrounding each node point on a mesh. (It views space as being broken down into a set of volumes each of which surrounds one of the points).

By this method, volume integrals in a partial differential equation that contain a divergence term are converted to surface integrals using the divergence theorem. These terms are then evaluated as fluxes at the surface of each finite volume. To attain a solution the solver performs an approximation of the unknown variables by means of simple functions, it then converts the resulting integral equation into a system of algebraic equations by approximating the terms therein and finally solves the algebraic equations.

The finite volume method has the advantage over the finite difference method in that it does not require a structured mesh (even though a structured mesh may be used). Since the values of the conserved variables are located within the volume element, and not as nodes or surfaces, the boundary conditions can be applied non-invasively thus making the finite volume method preferred to other methods.

Finite volume methods are particularly powerful cases of calculations where the mesh moves to track interfaces or shocks and on coarse non-uniform grids.

The steps which the finite volume method utilises are [62]:

a) Formal integration of the governing equation(s) of fluid flow over the (finite) cells/control volumes making up the solution domain.
b) Converting the resulting integral equations into a system of algebraic equations by approximating the terms therein, for processes such as convective and diffusive transport by interpolation functions for the face values of the cells/control volumes written in terms of local nodal values.
c) Solution of the algebraic equations.

5.2 Procedure

The CFD procedure followed the steps outlined in the simulation process Flow chart below (Figure 37).

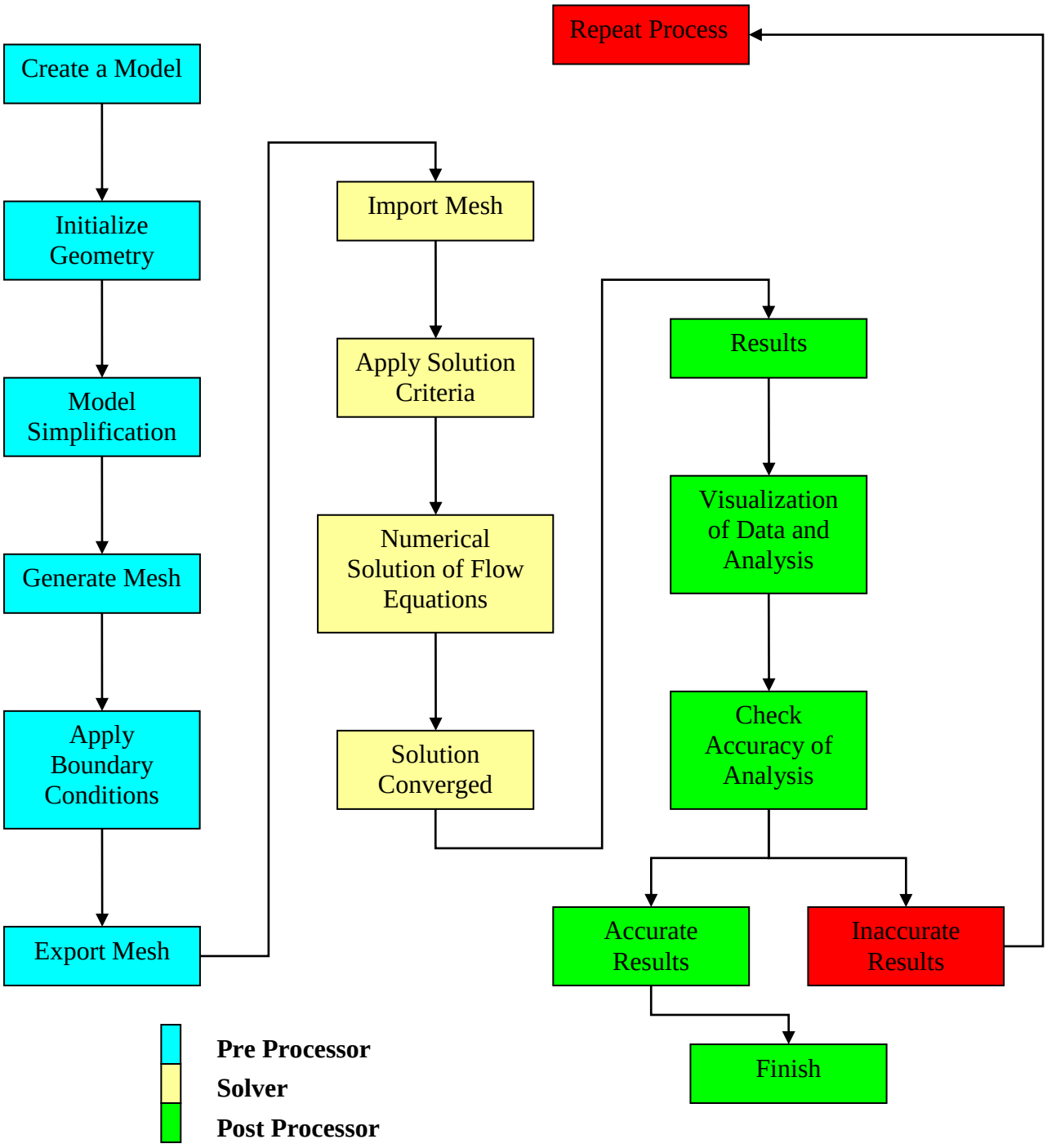

Figure 37: Simulation process Flow chart.

5.3 Modelling

For the creation of the 2D model, vertex data were imported in Gambit of the coordinates of the Clark Y aerofoil, setting up an array of vertices. These vertices were then connected using a smooth curve, defining the surface of the aerofoil. A flow domain surrounding the aerofoil was also formed using a similar method. To see if the flow around the aerofoil interferes with the domain walls two types of domains were examined, a small and a larger one. Results showed no significant difference in the C_L and C_D values between the two domains. For precautionary purposes however, the larger of the two domains was used since the domain must be large enough to accommodate the flow behaviour and to allow a stable solution. The dimensions used for the creation of the domain and aerofoil are shown in Figure 38.

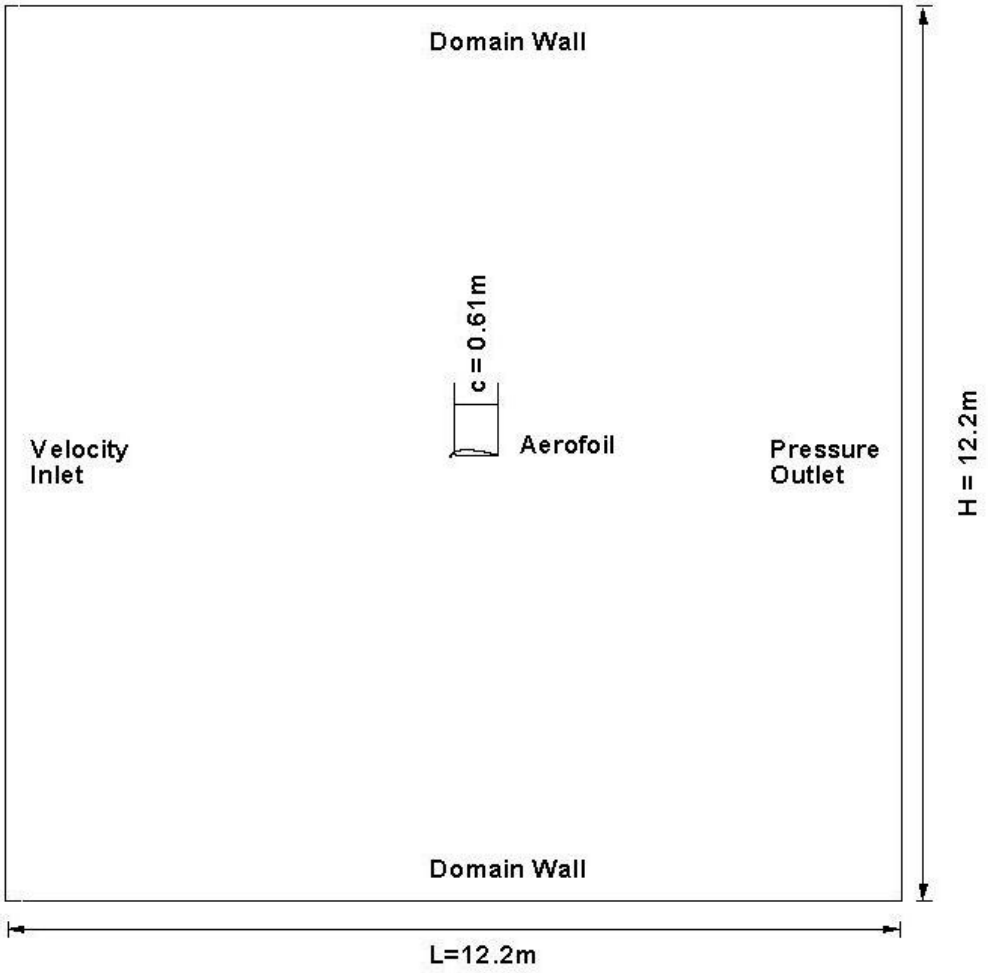

Figure 38: Dimensions and arrangement used for the creation of the initial domain and aerofoil.

The boundary conditions were kept similar to those of the experiment with air as the flow medium. The walls around the 2-D aerofoil were assigned as moving walls [64] with the same velocity as the incoming flow, to avoid the formation of a boundary layer and the inlet velocities were set to achieve the same Reynolds number as the experiments. Fluent recommends the used of moving walls for incompressible flows. Finally an examination of the test cases in references [65]-[72] showed that the far-field boundary appears to be located between six and twelve chords on either side of the aerofoil, a distance often farther than the location of the walls of the test section in which experiments are performed [71]. The computational domain extended to 10 chord lengths from the body in all directions as in ref [72]. The relevant domain dimensions used in this study in terms aerofoil chord are: H = 20C, L = 20C, C= 0.61m.

Gambit only meshes faces. Therefore the relevant edges were grouped in an appropriate manner so that the geometry remained retained. Subsequently the aerofoil face was subtracted from the domain face thus creating only one face. The new face was then meshed and the boundary conditions were applied by highlighting specific edges with various settings such as velocity inlet, wall, and pressure outlet. Once the model was completed it was exported to the solver.

5.4 Grid Generation

The grid generation is one of the most important steps during the overall analysis since the density and quality of the elements determines how accurate the results obtained will be. Grid or Mesh generation is achieved by sub-dividing the domain into a number of smaller sub-domains.

The flow is described by Partial Differential Equations (PDEs) which are derived from the fundamental parameters. The PDEs need to be solved on a discrete subspace of physical continuous space or on some sort of mesh or grid, which ideally (but not essentially) should be regular. It is at the points of intersections of the grid which are known as mesh points, that the solution is sought. In the finite volume method these PDEs are represented by a system of

algebraic equations, which are subsequently solved by the computer. The grid generation is an important and time consuming task of the CFD analysis as its density and quality affect the computational time and accuracy of the results. If the grid is coarse computational time will be less but the solution will not be as accurate. If the grid is too fine (more dense), then the solution may be more accurate but it will take more computational time for the solution to converge. It is of great importance to achieve a grid independent solution, as this will establish a greater level of confidence in the results, and will provide a better understanding of the model accuracy. Sufficiently large number of elements must be utilised to achieve adequate modelling of the boundary layer region near the wall. If this is not realised the results will be of limited use.

The process of finding the optimum grid is a major part of the verification process. Generally, the optimum grid is achieved when no significant change in the solution variables is observed with a further increase in the grid density. The choice of grid depends on the degree of accuracy required and the shape of the computational domain. There are three types of mesh, structured, unstructured and hybrid. In the case of a simple external flow a structured mesh can be used giving relatively accurate results. However, for complicated geometries, an unstructured or hybrid mesh is more appropriate since it can fit complex geometries and permits a local increase in the mesh density, without the penalty of increasing the density in other locations, thus producing more accurate results and consequently optimising computational time [61]. Hybrid grids combine the capability of unstructured grids in handling complex geometries and of structured grids in resolving viscous boundary layers therefore enabling high quality, efficient meshes to be formed for a wide range of problems [60]. A structured grid is utilised in the vicinity of the bodies and an unstructured grid is used to fill the rest of the domain. For the purposes of this project, all of the CFD configurations used hybrid meshes, with structured quadrilateral cells in the aerofoil and flap near wall regions (see Figure 39, Figure 40 and Figure 41) dense enough to have the boundary layer resolved and pave triangular cells in the remainder of the domain. These meshes inevitably take longer to form and require greater expertise than totally unstructured grids. However, the potential efficiency and modelling gains that these grids offer are such, that the total elapsed time and cost to achieve the end result the engineer aims for justifies the required investment [61]. Hybrid grids are in particular suitable for use with the finite volume solvers such as Fluent since different element types do not limit the solver [73],[74]. Examining Figure 39 is seen that in areas where large variations occur from point to point (near the aerofoil walls),

the grid is finer and in regions with relatively little change (domain) coarser. This arrangement enables a good representation of the complex surface of the aerofoil and flap configuration geometry, as well as a better interpretation of the complex flow phenomena one would expect to observe in such a flow. The stretching ratio(SR) used for the creation of the unstructured mesh, was adjusted in such a way so as to eliminate any skewed elements and/or any discontinuities around the aerofoil's boundary layer mesh and to provide a smooth transition from the structured boundary mesh to the unstructured surface mesh. This value was kept below 1.2 corresponding to a maximum change in grid spacing of less than 20%, which is less than the maximum allowed value of 1.3 in accordance to references [74] and [75].

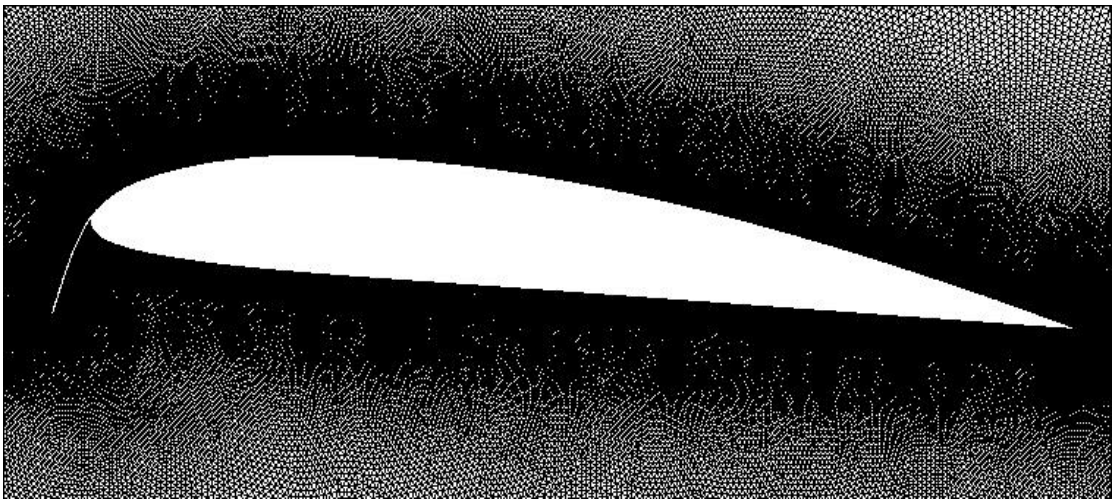

Figure 39: Hybrid grid used for the CFD analysis

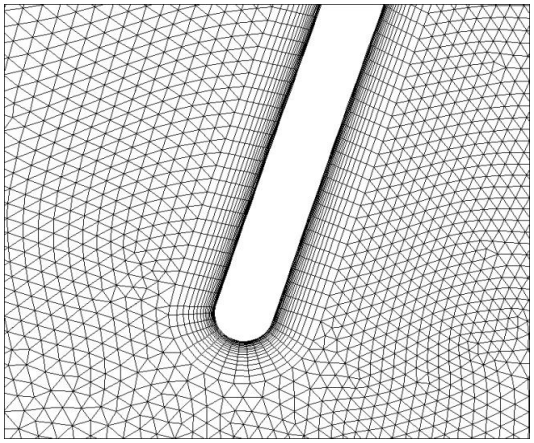

Figure 40: Magnification of the grid on the leading edge.

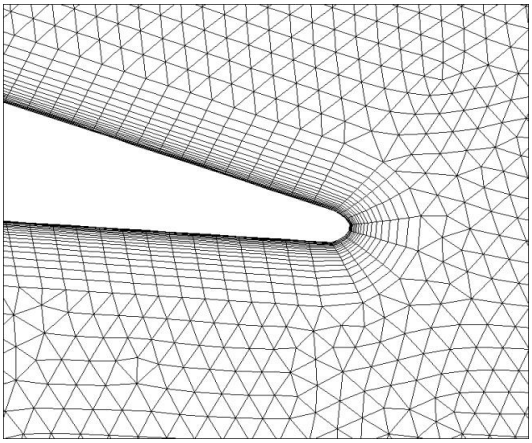

Figure 41: Magnification of the grid on the trailing edge.

5.5 Near wall modelling

A structured grid was used to accurately model the complicated near wall flow around the aerofoil, which represents the portion of the domain of most interest due to its high variable gradients. The flow in this area comprises of a viscous sublayer, a buffer layer or blending region where the flow is in a transitional state and a fully turbulent region, see Figure 42.

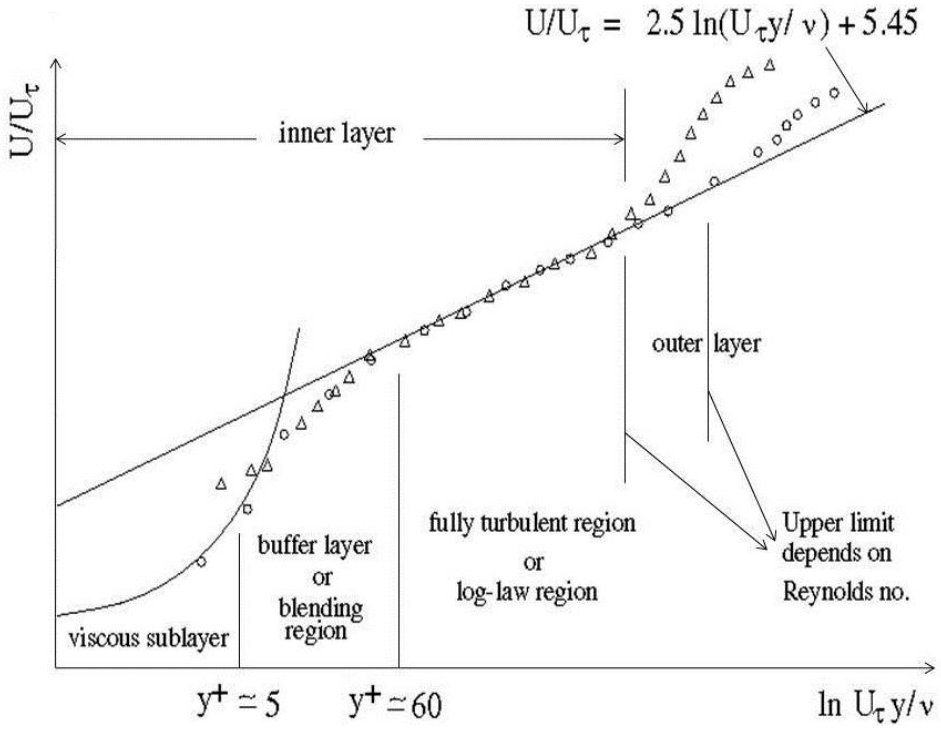

Figure 42: Subdivision of the Near-Wall region [79].

Three variables are of great importance for the construction of the structured boundary layer grid:

- the viscous scale y^+
- the boundary layer thickness δ_β
- and the geometric stretching ratio SR

Depending on the mesh quality, two ways for boundary layer resolution of turbulent flows in Fluent RANS modelling may be considered:

1. Enhanced Wall Treatment. Resolves the near wall region using the two-layer zonal model if the first point is located at $y^+ = 1$.

2. Standard Wall Function. The first grid point must be located within the log-law layer $30 < y^+ < 300$.

For the use of any of the above methods the value of the y^+must be specified and the value of y calculated. This can be done using equation [1] below, which is derived from the correlation formula for the flat plate skin friction coefficient see APPENDIX A for derivation.

$$y = 5.2 \cdot y^+ \cdot Re_C^{-0.9} \cdot C \qquad [1]$$

Substituting the values of y^+, C and Re_C in the above equation the coordinate of the first grid point can be defined.

The next step in the creation of the boundary layer mesh is to calculate the thickness of the boundary layer. Analysis was performed using equations obtained from flat plate theory to give an initial estimate about the boundary layer thickness δ_β around the aerofoil. For turbulent incompressible boundary layer on a flat plate the value of the boundary layer thickness was obtained using [81]:

$$\delta_\beta = \frac{0.37x}{Re_x^{0.2}} \qquad [2]$$

Where Re_x is the local Reynolds number as it is based on the local coordinate x. For the purposes of this work $x = C = 0.61m$ hence $Re_x = Re_C$ the Reynolds number in terms of the chord length.

Once the above values for y^+ and δ_β were obtained a mesh was generated using a geometric stretching ratio (SR) not exceeding 1.2 for the boundary layer mesh, which according to the analysis performed by Spalart [82] provides the optimal grid distribution. Smaller values could be used which would enable a higher resolution of the boundary but at the cost of a sharp increase in the number of grid points and computational points. Initial runs were then performed to enable the actual distribution of y^+ on the aerofoil to be determined and conclusions to be drawn on its suitability. The mesh was refined or coarsened so as to obtain the suitable value of y^+. The manual of Fluent recommends that ''the value of y^+ should not exceed the value of 5 when solving the viscous sub-layers of the boundary layer''. However, Menter [83] states that ''the first grid point should be no further than $y^+ = 3$''. For the purposes of this project therefore, the mesh was clustered in a manner so as to generate a value for $y^+ \approx 1$, thus resolving explicitly the near wall region using the two-layer zonal model which was more appropriate. Even though y^+ is a geometric characteristic, it is also flow dependent since it changes in relation to the frictional velocity, which in turn is interrelated to the wall shear stress thus making it dependable on the velocity gradient near the wall. In areas of high velocity, where the gradient is more severe the y^+ value increases. Additionally in points of separation where the shear wall stress reduces to zero the value of y^+ also reduces to zero. Considering the value of y^+ could therefore give an indication of the separation point. The values assumed for the boundary layer mesh creation are tabulated and summarised in Table 3 below:

Re	$0.6x10^6$	$1x10^6$	$1.6x10^6$
y	0.02mm	0.012mm	0.0083mm
SR	1.2	1.2	1.2
δ_β	0.016m	0.014m	0.012m

Table 3: Values used as guidance for the creation of the boundary layer mesh

5.6 Grid Skewness

In addition to grid independence, the cell quality also plays an important factor on the accuracy of the numerical solution. The quality of a cell is defined by its skewness which is

the difference of the cell's shape compared with that of an equilateral cell of equivalent area. The accuracy and stability of the solution, can increase or decrease on the basis of the overall skewness of the grid. Fluent is capable of solving the flow equations in cells with skewness level up to 0.91, with 0 indicating the best case of an equiangular cell and the value of 1 for that of a completely degenerate cell. Optimal triangular cells should have vertex angles preferably close to 60^{o}, while quadrilateral cells should have vertex angles closer to 90 degrees. For the simple aerofoil cases, the skewness of 97% of the cells was in the range of 0 - 0.1 and for the remaining 3% between 0.1- 0.51 with just one element having the worst skewness of 0.52. In the aerofoil and flap configuration, for cases with a flap deflection angle in excess of 80 degrees, 95% of the cells were within 0 - 0.1. Remaining 5% was between 0.1 and 0.771 out of which only 0.14% exceeded 0.5 levels, with one or two elements approaching maximum value of 0.771. Similarly for cases with less than 80 degrees flap deflection, 92% of the cells were within 0 - 0.1. Remaining 8% was between 0.1 and 0.88 out of which only 0.2% exceeded 0.5 levels and just one element reaching the maximum value of 0.88. Skewness levels above 0.88 or the maximum recommended value of 0.91 were not observed in any case.

Given the low percentage of cells with high skewness, the inaccuracy introduced in the computation due to their presence was assumed negligible [59],[84].

5.7 Solving

When the model was finished, it was then exported from Gambit and imported to Fluent 6.3, where further additions could be made to the boundary conditions as required and a way of solution specified from the options available. The following procedure was repeated each time a model was solved using the steps below:

- Smooth nodes in mesh. This step checks that the mesh imported is free from defective elements and if any are found ensures they are made smooth.
- Select a viscous model from the ones available (k-ω SST in this case).
- Edit boundary conditions. Values are assigned to the boundary conditions set-up from Gambit.

- Deselect auto-convergence checks.
- Initialise. Each time a new model is to be solved the program must be initialised so that all old data is discarded and a new solution process can take place.
- Iterate. This is the final command that sets the solution running by choosing the number of iterations. If the solution set does not converge in the given number of iterations then it is feasible to run any number of additional iterations, as long as the model is not initialised again.

5.8 Boundary Conditions.

CFD problems are defined in terms of initial and boundary conditions and it is important to understand their role in the numerical algorithm. For the purposes of this project, the boundary conditions were set up as follows:

- Inlet: The front face of the domain was set as a velocity inlet. The velocity varies in accordance with the case examined.
- Outlet: The rear face of the domain was set as a pressure outlet in the model, so that all flow would pass the entire length of the domain. (This is simply a continuum from the inlet and has no specified pressure, velocity or temperature).
- Domain walls: The domain walls were set as moving walls moving at the same rate as the velocity inlet, to simulate an aerofoil travelling in an open environment.
- Aerofoil and flap setting: The aerofoil and flap, were set as no slip walls and the angle of attack and flap deflection varied according to the case.

5.9 Analysis

The analysis in Fluent can be both qualitative and quantitative. By utilising the various display functions, an image of the selected quantity can be shown thus giving a broader idea of the processes occurring. Furthermore, the geometry of the grid with the solution of the flow behaviour can be observed and can be used to visualise domain geometry, and vector plots. By combining the raw data taken directly from CFD results and further quantities that

can be then calculated such as C_L and C_D, a complete interpretation can be undertaken and conclusion on the performance of the aerofoil and flap configuration can be drawn. Details of the FLUENT running conditions used are summarised and presented in Table 4.

The RANS equations were solved using the finite volume method. Second order upwind discretisation in space was used and the resulting equations solved using the SIMPLE coupled solution procedure until the convergence criteria were satisfied. The free stream turbulent intensity and hydraulic diameter where set at 0.9% and 1.829 (m) respectively, to represent the running conditions of the wind tunnel.

Velocities (m/s)	14.4, 24, 38.3
Chord (m)	0.61
Re ($x10^6$)	0.6, 1, 1.6
Angle of attack (deg)	0 ~ 17
Flap Deflection angle (δ) of 10%C (deg)	70-120
Flap Deflection angle (δ) of 5%C (deg)	50-90
Turbulence Models Used	k-ω SST
Solution	Second Order
Mesh Density ($x10^5$)	0.66, 2.7, 88
Domain	(20x20)C

Table 4: Summary of FLUENT Running conditions.

5.10 Convergence Criteria

During the iteration process the convergence rate was monitored by means of the dependent variables of the governing differential equations.

Convergence criteria, are the pre-set conditions on the residuals which indicate that a certain level of convergence has been achieved. The residual history, provides a convenient indication of the state of numerical convergence of the model. In general, diminution of the

residual sums to small values which do not change significantly during the iteration process, should be regarded as a necessary-though not sufficient-basis for judging model convergence. Often the difference between successive iterates is used as a measure of the error in the converged solution, although this in itself is inadequate. A small relaxation factor can always give false indication of convergence [77]. If all the problem variable residuals fall below the convergence criteria but are still in decline, it is a sign that the solution is still changing to a greater or lesser degree. Residual plots can reveal when the residual values have reached the specified tolerance.

In general:

1. Convergence is reached when:
    a. Changes in solution variables from one iteration to the next are negligible (residuals provide a mechanism to help monitor this trend)
    b. Overall property conservation is achieved.
2. The accuracy of a converged solution is dependent upon:
    a. Appropriateness and accuracy of physical models.
    b. Grid resolution and independence.
    c. Problem setup.

A particular trait of the FLUENT software package is that it includes a feature to automatically terminate the solution of individual variables if their residual sum falls below a prescribed limit. This feature is active by default and is intended to speed up model run times by concentrating the computational resource on variables that are less well converged. However, as this feature effectively terminates the iteration procedure for the respective variables based on the value of the corresponding residual sum alone, it should be disabled [77]. This then allows the solution procedure to be applied to all the variables, for each iteration, enabling better observations of the behaviour of the residual sums. A better indication is considered when the residuals flatten in a traditional residual plot (a plot of residual value versus iteration). The plots of the residuals and lift and drag coefficients versus iteration number are monitored and the solution is assumed complete when the residuals drop at least four orders of magnitude and have zero gradient. The convergence was based on the behaviour of the discrete solution and the error (E) of the solution was referred to as the difference between the discrete solution $f(\Delta)$ and the exact continuum solution f^{exact} of the

model equations [76]. Discretisation errors (E), arise due to the difference between the exact continuum solution f^{exact} of the model equations and the discrete solution $f(\Delta)$ [76]. If the flow solution is represented through a Taylor series, the exact continuum solution occurs when the truncation error is effectively zero, which is a function of the grid size. Convergence was monitored through plots of the residuals and lift and drag coefficient versus iteration number and the solution was assumed converged, when the residuals dropped to at least four orders of magnitude and had zero gradient, see Figure 43 and Figure 44. Figure 44, shows the residuals of the mean flow equations versus the iteration number and it can be seen that there are numerous oscillations occurring as the residuals converge. These oscillations are due to unsteady flow at the trailing edge of the aerofoil as well as to the characteristics of the zonal interfaces when the information travels between the zones. The above mentioned unsteadiness of the flow, causes high frequency oscillations on the C_L and C_D curve (see Figure 43) as they try to converge. The solutions are deemed converged when the residuals have dropped over five orders of magnitude and the values of C_L and C_D have converged to four significant digits [94]. Lift and drag forces were obtained using near-field integration of the pressure and viscous forces around the aerofoil with a function provided by Fluent. From these forces, the drag and lift coefficients C_D and C_L were calculated for different angles of attack.

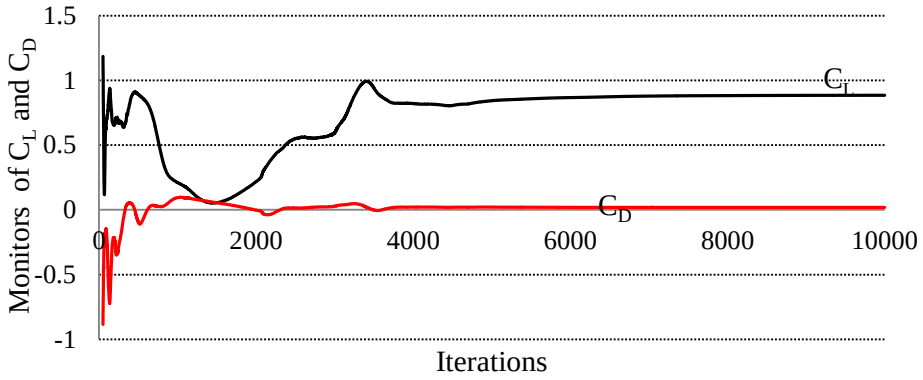

Figure 43: Monitors of C_L and C_D Vs Iteration number.

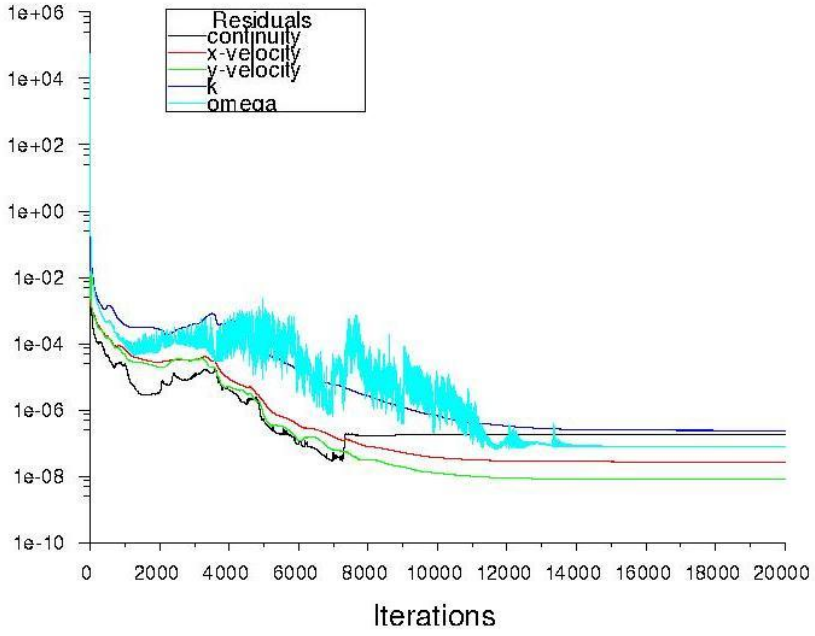

Figure 44: Residual monitors Vs Iteration number.

5.11 Mesh density sensitivity

The mesh density and the selection of a turbulence model influence the accuracy of the solution but also its cost, in terms of necessary computer hardware and calculation time. For this reason, in this project, analysis was performed on three turbulence models, with a common geometry, in order to investigate the effect of mesh density and to demonstrate the grid-independence of the solution. The most common way to demonstrate grid independence, is to repeat a computation on a grid with twice as many grid points, and compare the two solutions [76]. If computer resources are unavailable to facilitate grid doubling, a grid halving is also appropriate, although the error bounds will not be as sharp [77]. Using results from two different grids, techniques such as Richardson extrapolation can be used to determine discretization error [77].

Three cases were examined with different mesh densities and the values of C_D and C_L were compared with data derived from literature including flat plate theory, dimensionless analysis, current published experiment data as well as data obtained from corresponding wind tunnel tests. The mesh was refined in the regions where high adverse pressure and flow separation was expected. Table 5 shows the total number of cells used in each case examined.

	Case 1	Case 2	Case 3
Total no. Cells	66000	270000	880000

Table 5: Grid size for each case examined

Figure 45 quantifies the variation of C_L of a plane Clark Y aerofoil for each case examined at the respective Re. The initial CFD run was performed in 2^o intervals from 0^o – 18^o to establish the stall angle. Further studies for Cases 2 and 3, used the same increment up until $\alpha = 12^o$ and 1^o increments until $\alpha = 16^o$. This was performed so as to accurately predict the stall angle. In addition it was documented by Rumsey and Ying [78] that the turbulent models do not perform very well at post stall angles and as a UAV would not fly at angles higher than stall it was not deemed necessary to run simulations for such cases. The C_L plots reveal an increase in the lift coefficient of 7.5% between Case 1 and Case2 at Re = $0.6x10^5$, and a further increase of 0.15% between Case 2 and Case 3 at $\alpha = 0^o$. Similarly, for Re = $1x10^6$ and $1.6x10^6$ the respective increases were 1.3% and 0.72% between Case 1 and Case 2 and 1.8% and 0.55% between Case 2 and Case 3, see Figure 45. The mesh of Case 3 was therefore deemed more accurate for the purpose of this project. Going through these results however, the question might arise, as to why Case 3 was selected and not Case 2 since the difference in C_L is relatively small and it would require more computational time to be solved? The answer is found in Figure 46 below, which illustrates the average % error between the CFD and Experimental results (the average % error was calculated for values from 0^o – 16^o). Overall one can see, that Case 3 predicts the lift coefficient better through the angles of attack range than the other two Cases. The errors occurring in Cases 2 and 3 are mainly due to the inability to compute the correct C_L at high angles of attack (see also Figure 47 and Figure 49).

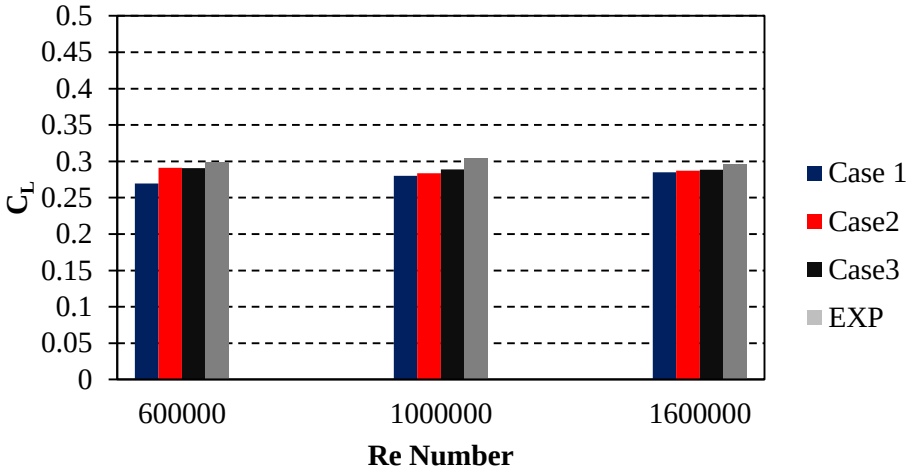

Figure 45: Variation of C_L for the three grid cases and experimental results against Re numbers

Even thought all three cases reasonably predict the lift coefficient in the linear region, it seems that the mesh in Cases 1 and 2 is not dense enough to capture the flow phenomena that one would expect to observe at high angles of attack. Additionally, Figure 46, illustrates the importance of the mesh density as the Reynolds number decreases.

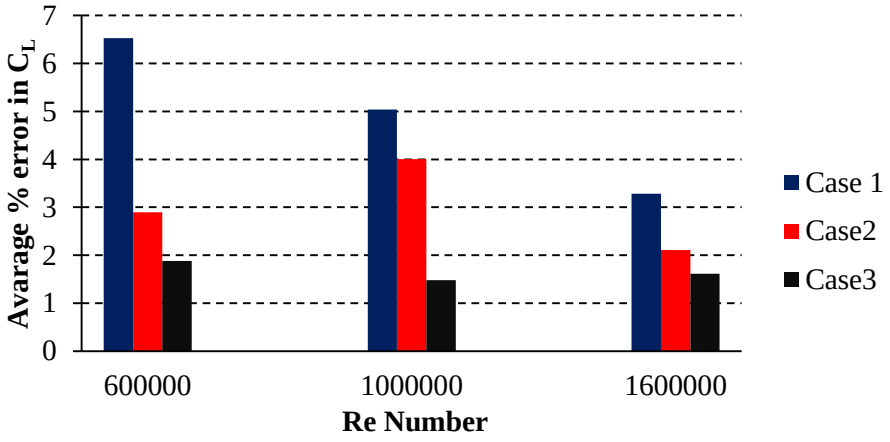

Figure 46: Average percentage error in C_L for the three grid densities examined Vs Re number.

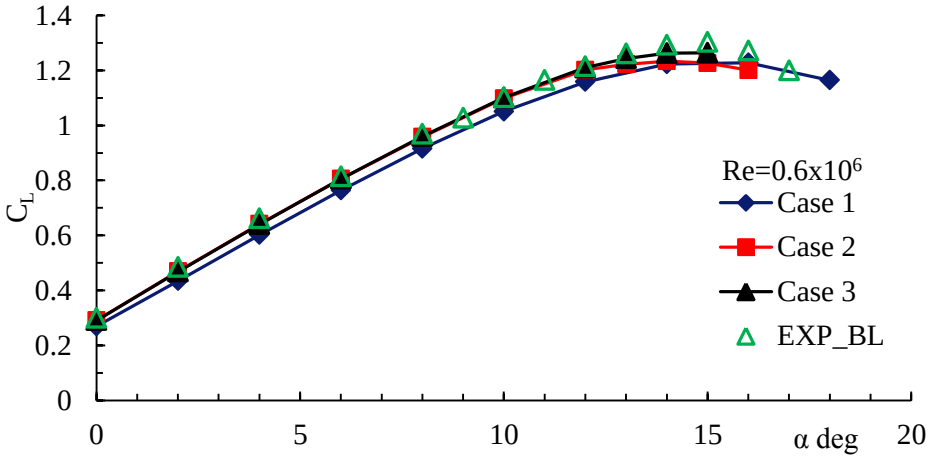

Figure 47: C_L Vs angle of attack for Re = 0.6x10^6 for the three mesh cases.

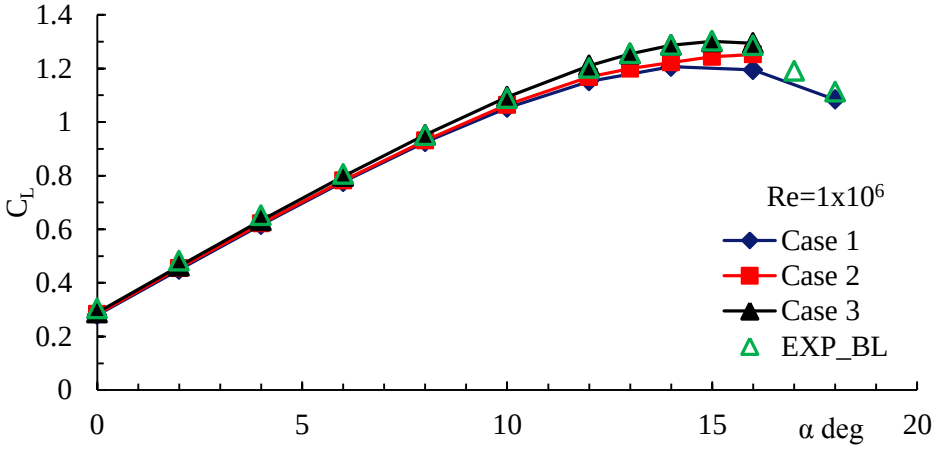

Figure 48: C_L Vs angle of attack for Re = 1x10^6 for the three mesh cases.

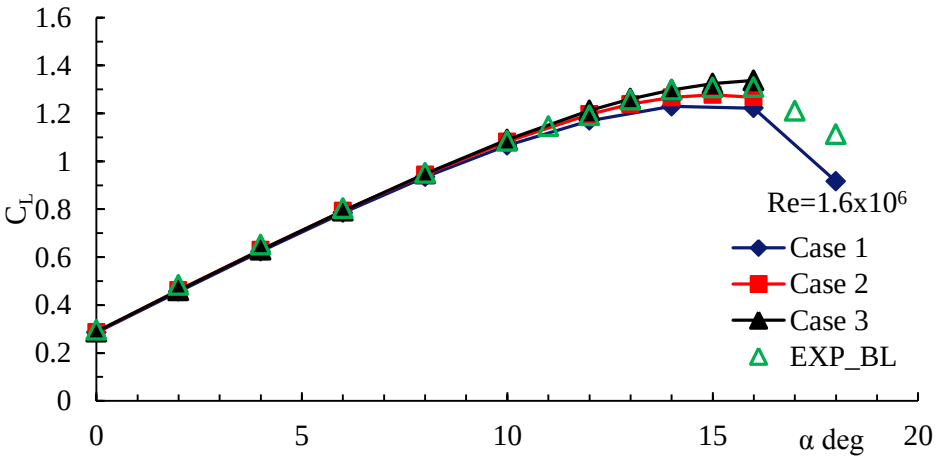

Figure 49: C_L Vs angle of attack for Re = 1.6x10^6 for the three mesh cases.

5.12 Turbulence model selection procedure

From literature for flows past aerofoils it was noted that the critical Reynolds number, Re_{xcr}, for transition determined from experience, is approximately $Re_{xcr} = 5x10^5$ [81]. The initial wind tunnel test which used surface flow visualisation, however, indicated turbulent transition to occur at the leading edge region of the aerofoil. This early transition was thought to be caused by the leading edge flap mounting system, as outlined in the experimental chapter in section 6. Therefore, a turbulent model was used throughout the mesh for all subsequent modelling with no laminar transition.

A very important aspect of a turbulence model, is its ability to predict accurately adverse pressure gradient boundary-layer flows. Also, it is of great importance for the model, to accurately predict the location of the flow separation as well as the displacement effect associated with it, since the pressure distribution and the aerodynamic performance of a body are greatly influenced by the viscous-inviscid interaction [85].

An ideal turbulence model according to Wilcox, should "introduce the minimum amount of complexity while capturing the essence of the relevant physics" [86]. A range of turbulence models are available in Fluent some of which are [59]:

1. Spalart-Allmaras (S-A) model (1 equation)

2. k-ε models (2 equations)
    a. Standard k-ε model
    b. Renormalization-group (RNG) k-ε model
    c. Realizable k-ε model

3. k-ω models (2 equations)
    a. Standard k-ω model
    b. Shear-stress transport (SST) k-ω model

Unfortunately, there is no single turbulence model which is universally acceptable as superior for general application and for all classes of problems. The selection of a turbulence model

depends on such considerations as the physics involved in the flow, the so far established practice for the particular class of the problem, the required level of accuracy, the computational resources available and last but not least the amount of time available for the simulation. To make therefore the most appropriate selection of the model for an application, it is necessary to understand fully the capabilities as well as the limitations of each option.

In the one-equation turbulence model, e.g. Spalart-Allmaras [87] only one combination of the turbulent scales is computed by solving the transport equation for the kinematic eddy viscosity. Similarly to the k-ω, the Spalart-Allmaras model uses a derivation of the Enhanced Wall Treatment (EWT) for meshes with $y^+ \approx 1$ or a standard wall function when $30 < y^+ < 300$, while the buffer region $5 < y^+ < 30$ should be avoided. According to Yang [88], the Spalart-Allmaras model demonstrates good behaviour in boundary layers which are subjected to adverse pressure gradients.

The two-equation turbulence models such as Wilcox's k-ω [89], Laurent and Sharma's k-ε [90], and their variations, are in a sense more complete in that two transport equations are solved for both the turbulent scales, and the Reynolds stress tensor can be determined completely from the local state mean flow and from the mean turbulent quantities. Such models however require more time and computational resources to achieve convergence since two equations must be solved. More details and information in this subject can be found in APPENDIX D.

5.13 Turbulence model study

The two most suitable models obtained from theory, the k-ω SST and S-A have been studied and compared with each other and with the experimental results. The models were evaluated by comparing their resulting C_L and C_D coefficients with the experimental results. Figure 50 and Figure 51, illustrate that both models reasonably predict the coefficients of lift and drag. For low angles of attack, both models are comparable for predicting the value of C_L within 2% of the experimental results. However, as the angle of attack increases, the S-A model under predicts the value of C_L, whereas the k-ω SST shows results comparable with the experiment. On average the S-A shows a 4% deprivation from the experimental results, whereas the k-ω SST shows 1.5 % deprivation. Examining Figure 51 it can be seen, that the

turbulence models are not as good in predicting the value for the drag coefficient. The S-A model shows higher results for C_D with an average difference of 35% from the experimental and the k-ω SST displays lower values than the experimental of an order of 21% on average. In general, the k-ω SST took more time per iteration to reach solution than the S-A since it solves two differential equations.

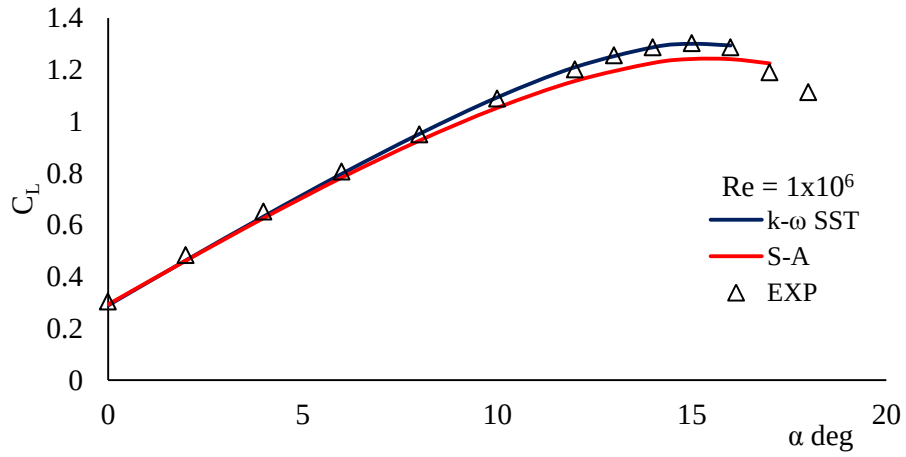

Figure 50: C_L Vs angle of attack for k-ω SST and Spalart-Allmaras models.

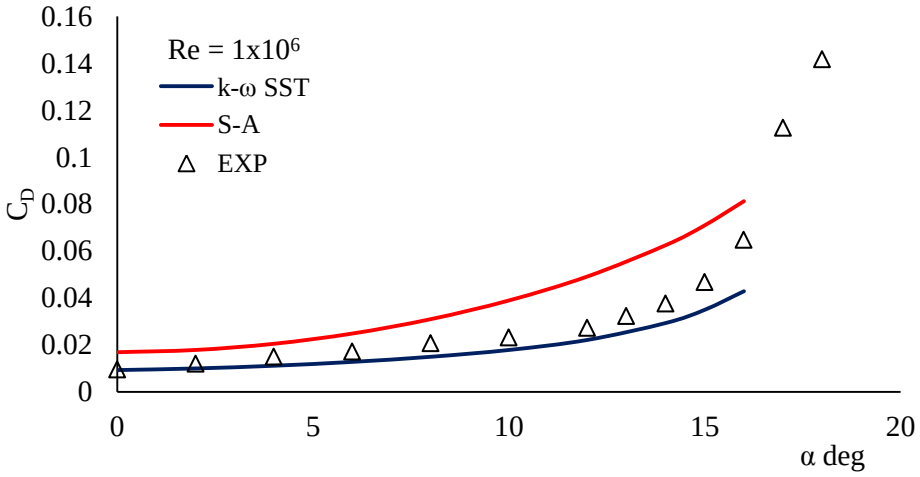

Figure 51: C_D Vs angle of attack for k-ω SST and Spalart-Allmaras models.

Since the k-ω SST model produced superior results than the S-A, it was used in the computational analysis. This model is described in detail in APPENDIX E

Chapter 6. Experimental Study

6.1 The 2.4m x 1.8m Wind Tunnel

An experimental investigation was carried out in the 2.4m x 1.8m general purpose wind tunnel at Cranfield University. This facility has a closed return layout with a closed rectangular working section providing test section flow velocities in the range 5 – 55 m/sec with a freestream longitudinal turbulence intensity of 0.9% at nominally 45 m/sec [104]. Two-dimensional aerofoil testing was carried out using rectangular platform wing sections with AR = 2, mounted horizontally, at mid test section height, between circular end-plates (see Figure 52). The end-plates serve to ensure nominally 2D flow conditions on the wing and provide fairings for the struts connecting the section model to the overhead six component weighbeam mechanical balance. Incidence adjustment was by means of a tail wire and conventional pitch-strut assembly. Measurements of aerodynamic force, moment and Cp were made over the same range of aerofoil incidence and Reynolds numbers as used in the CFD study.

The 0.61m chord aerofoil was fitted with a 10% chord composite Krueger flap element which was manually adjusted by means of end-plate mounted set screws. The flap was initially secured to the leading edge of the main aerofoil. During the initial tests, however, it was established that the spanwise rigidity of the flap was not sufficient and therefore a series of formers at five equally spaced spanwise locations were added to maintain the required flap cove geometry at each flap deflection (see Figure 52).

Test runs were carried out at operating Reynolds number Re based on chord in the range of $Re = 0.6x10^6$ to $Re = 1.6x10^6$ where small and medium size UAVs (Tactical UAVs) operate [6]. However, initial surface flow visualisation of the aerofoil, using fluorescent pigment suspended in paraffin, indicated turbulent transition near the leading edge of the aerofoil due to surface condition of the leading edge which contained the flap mounting points. A similar

leading edge transition location was also found with the flap fitted, due to the joint between the flap and the leading edge.

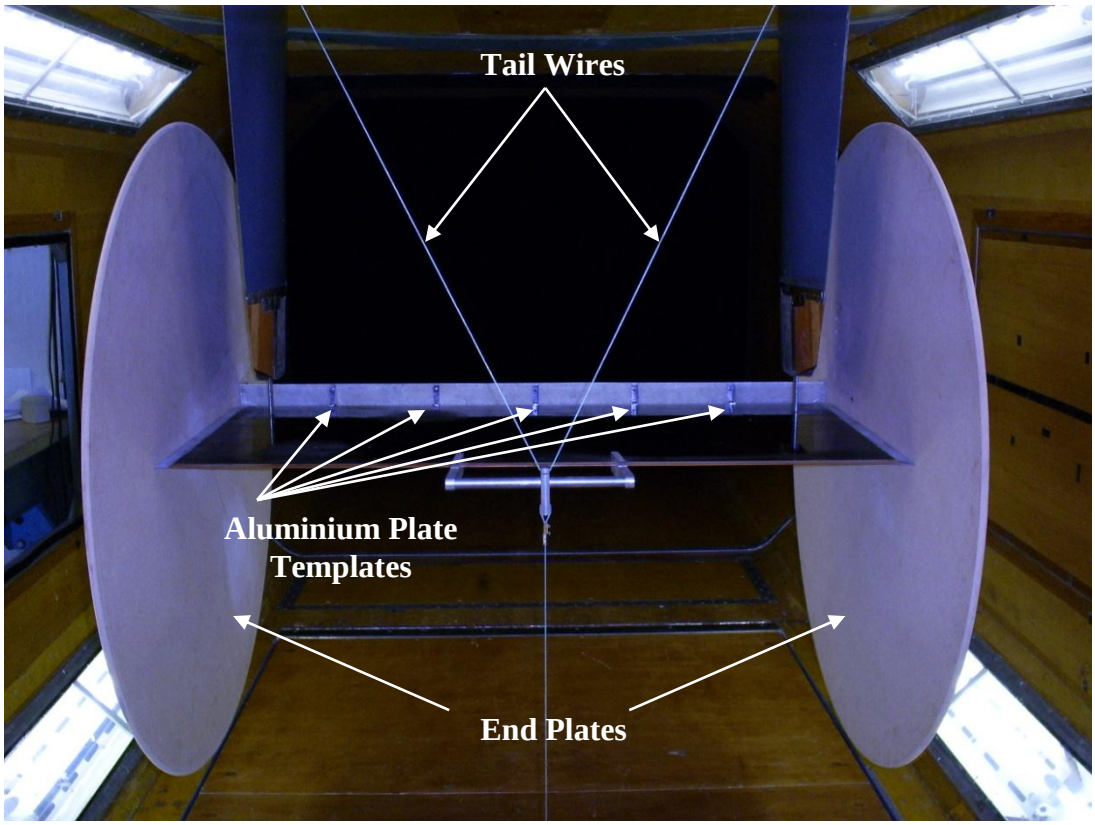

Figure 52: Rear view of the wing and flap experimental apparatus used. Wing is in inverted position.

6.2 Model Description

The experimental program was based on a Clark Y aerofoil section as historic data was readily available for this aerofoil section [42]-[50]. More recent aerofoil sections such as the ONERA M6 was also considered, but the Clark Y was selected based on its mild stall characteristics and good low Re performance (See Aerofoil Selection appraisal, Section 4.3 above). The main wing element (Clark Y) was constructed from wood and had a reference chord of 0.61m excluding the leading edge devices.

Made from fibre glass the Krueger flap elements were designed in such a way as, in their retracted position to produce a smooth contour at the surface of the aerofoil thus minimizing any protuberances and hence the drag produced by the configuration.

The Clark Y aerofoil was pressure tapped with a set of chordwise tapings at mid-span of the model. Such tapping was not possible on the flap itself due to its limited thickness. The following section describes the experimental program.

6.2.1 Clean Clark Y

The first case examined was that of a plain Clark Y aerofoil. Based upon the previously described tail wire and conventional pitch-strut assembly the angle of attack was varied from 0 – 18 degrees in two degree interval steps for Reynolds number values of $0.6x10^6$, $1x10^6$ and $1.6x10^6$. This enabled the comparison of the data obtained from the Cranfield wind-tunnel experiments with other published experimental data thus providing a baseline configuration to which the performance of the flap could be related to.

6.2.2 Clark Y and Flap configuration

Made from fibreglass with a mean thickness of 2mm, the aerodynamic characteristics of two flaps were examined with chord lengths of 61mm and 30.5mm representing 10% and 5% of the aerofoil's chord length respectively. Figure 53 shows a schematic of the two flaps used.

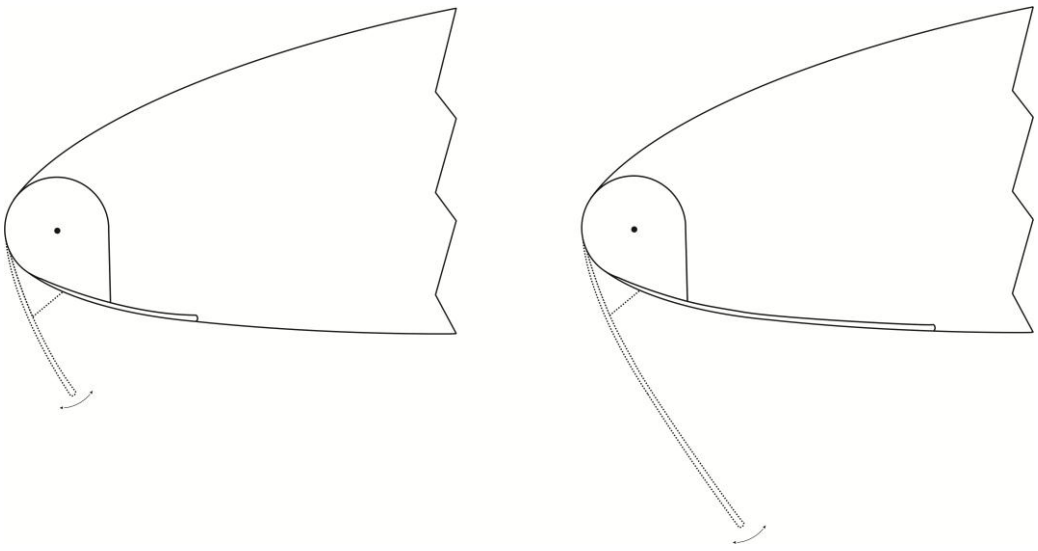

Figure 53: Cross- sectional schematics of the 5% and 10% flaps.

Each flap was mounted separately and examined over the range of angles of attack and Reynolds numbers with and without an emery transition strip, as illustrated in Figure 54. Even though initial flow visualization showed that transition occurred near the leading edge of the flap the transition strip was used to verify such occurrence. For this purpose, 20mm wide emery strips were applied to the upper surface of the flap (see Figure 54 and Figure 56) so as to purposely trip the flow. The strips spanned the flap and were applied 2mm back from its leading edge.

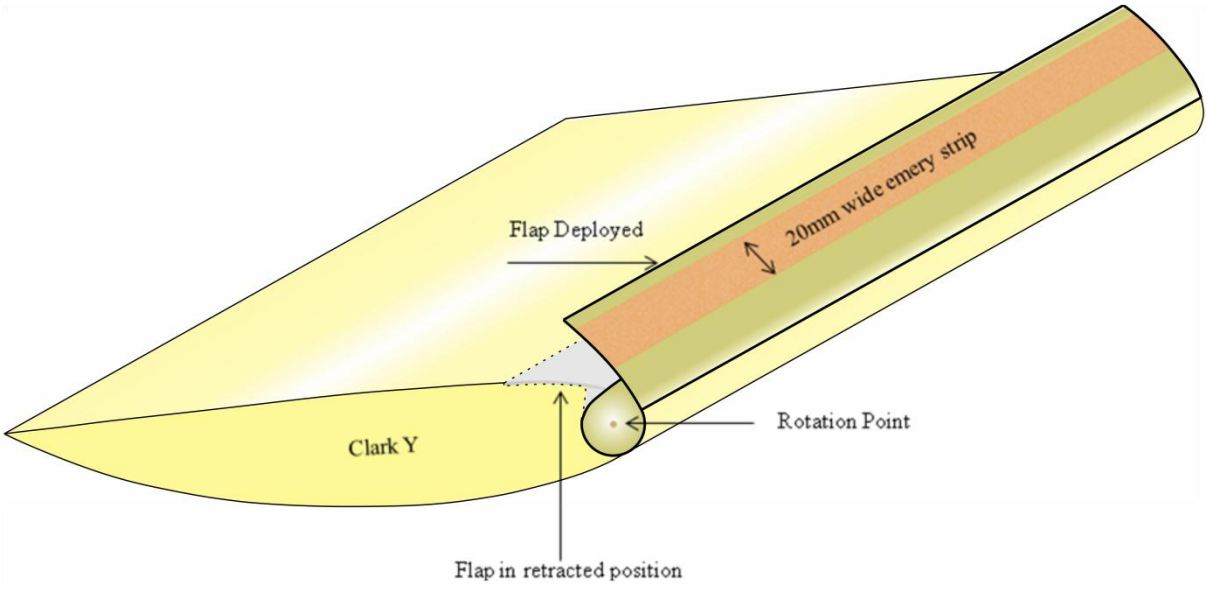

Figure 54: Schematic of the wing and flap configuration in an inverted position illustrating the 20mm emery stip.

To ensure accurate measurement and setting of the deflection angles for the leading edge flap, holes were drilled on the end-plates which provided a guide for each configuration. Due to wind-tunnel availability and time limitations the flaps could not be examined in all possible deflection settings. Based on results obtained from published data [28] - [33], optimum deflection angles were defined to minimise wind tunnel time requirements. The wind tunnel running conditions are thus summarised and presented in Table 6 below where each flap was examined at three deflection angles (δ) over a range of angles of attack (α) and at three different Reynolds numbers.

With the leading edge flap deployed, a gap formed along the geometry between the flap and aerofoil as shown in Figure 55, which produced a discontinuity in the flow. As the gap was close to the leading edge where any discontinuities could have an effect on the total aerodynamic characteristics of the configuration, it was deemed necessary that its effects should be examined and quantified. Experimentation was therefore performed with and without smoothing this gap with the aim to investigate this disparity in the geometry.

Configuration	Re number $x10^6$	α deg	δ deg
10% Flap	0.6, 1, 1.6	0 – 18	70, 100, 110
5% Flap	0.6, 1, 1.6	0 – 18	50, 70, 80

Table 6: Summary of experimental running conditions.

To provide a smooth course over the aerofoil and the flap the gap was first filled and shaped with plasticine filler, with a thin aluminium tape then applied on top thus ensuring a smooth and continuous transition between the two elements. In addition, however, aluminium tape was used alone without first filling and shaping the gap, thus examining the effect of the "step" left between the flap and main element, as shown in Figure 56.

Plasticine filler was also used to fill the gap between the flap and the aerofoil on the lower surface thus ensuring the flap was not deformed or deflected through the runs.

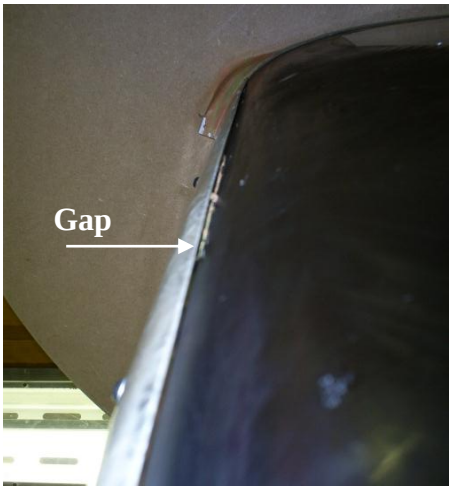

Figure 55: The gap formed between flap and main element.

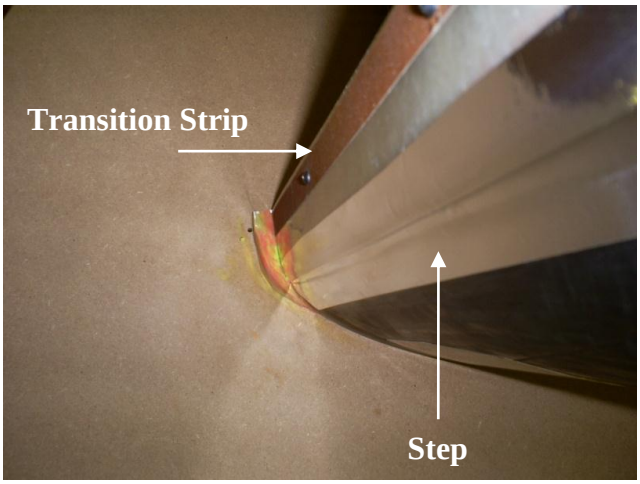

Figure 56: Illustrates the step formed with only aluminium tape applied (10% flap with transition strip).

6.3 Freestream Measurements

The mean freestream dynamic pressure q was measured simultaneously with each surface static pressure measurement. A mean voltage representative of the freestream dynamic pressure was recorded and electrical offsets were subtracted from it. The value was multiplied by the digital manometer calibration factor and wind tunnel calibration factor and converted into SI units to produce the dynamic pressure of the working section.

In addition measurements of temperature (T) and atmospheric pressure (P) were recorded in parallel with the experimental procedure and were used to calculate the value for density using the ideal gas law:

$$P = \rho RT \qquad [3]$$

Where R is the universal gas constant 287 $JKg^{-1}K^{-1}$ and T is the temperature in degrees Kelvin.

Using the calculated values for dynamic pressure and density and assuming incompressible flow due to the low Mach numbers examined (M<0.3), the working-section velocity was calculated from:

$$q = \frac{1}{2}\rho V^2 \qquad [4]$$

6.4 Balance Analysis of Aerodynamic Forces

During a run for any given configuration the axial, normal, side and yaw forces exerted on the model were displayed on four dial encoders which were manually balanced. The measurements were made using the six-component balance situated above the tunnel's working section. In addition the atmospheric pressure, temperature and freestream dynamic pressure were also displayed and logged for each configuration. The offset of each of the four aerodynamic forces was recorded before each test with the wind off and the values were then used for the calculation of the lift and drag forces from the equations below. Equations [5] and [6] were derived using a pre-defined calibration. No hysteresis effects were evident in the experimental procedure, however, as a precaution the balance measurements were always conducted for increasing incidence at any specified wind speed and for increasing Reynolds number. The results were recorded on a PC and normalised by the working section's dynamic pressure to give the non dimensional lift and drag coefficients. At the end of each run the non – dimensional coefficients of C_L and C_D were plotted against angle of attack α to ensure sufficient accuracy and continuity.

$$L = 4.448\{(5.16(N_f - N_{offset})) - 0.004(A_f - A_{offset})\} \qquad [5]$$

$$D = 4.448\{\left(0.0046\left(N_f - N_{offset}\right)\right) + 0.416(A_f - A_{offset})\} \qquad [6]$$

In contrast to the C_P measurements, the total drag of the wing (Pressure drag and Skin friction drag) was measured when the overhead six component weighbeam mechanical balance was used for the estimation of the aerodynamic forces. The disadvantage of the above procedure is however, that the interference between wing and end plates is also included in the measurement. Muller and Jansen [102] suggested that a three-dimensional flow regime exists in this region which is dominated by flow separation and a formation of a corner vortex. Experiments that they performed showed that the effect of an end plate at each end of the

model was to increase the value of C_{Dmin} by 10%. Additional experiments performed by Pelletier and Muller [103] as well as Render [104] showed similar results. In addition to the above and due to the small magnitude of the expected C_D values, even small errors or variations and differences in balance readings could affect in greater extend the total accuracy of the C_D in comparison to C_L.

6.5 Surface Static Pressure Measurements

The wing static pressure measurements were obtained using a combination of a Furness Controls FC0318 differential pressure system and a PX139 0.3psi Series pressure transducer which were connected sequentially to the surface pressure tapings using equal length pressure tubes. Each measurement was sampled over a 10 second time period and a sample rate of 300Hz. Investigation of the damping effects of the pressure tubes connecting the tapings with the pressure transducer revealed a 5 second settling time was sufficient to overcome any damping errors. Tunnel velocity was calculated using the pressure output from a static ring set connected to the FC0318 pressure system.

The value of C_P was obtained from:

$$C_P = \frac{P - P_r}{q_w} \quad [7]$$

In the above equation, P is the mean surface static pressure, P_r is the reference static pressure taken upstream of the model and q_w is the working section dynamic pressure.

The pressure coefficients over the upper and lower surfaces of the aerofoil against x/c were then plotted. This expresses an important quantity since the distribution of C_P over the aerofoil leads directly to an estimate of the value of C_L. The normal (C_N) and axial force (C_A) acting perpendicular and parallel to the aerofoil's chord respectively can then be calculated by integrating the mean surface static pressure.

The normal force coefficient C_N can be calculated from:

$$C_N = \frac{N}{qc} = \int_0^1 \left(C_{p,l} - C_{p,u}\right) d\left(\frac{x}{c}\right) \quad [8]$$

where $C_{p,l}$ and $C_{p,u}$ are the pressure coefficients on the lower and upper surface of aerofoil respectively.

In a similar manner the axial force coefficient C_A can be calculated from:

$$C_A = \frac{A}{qc} = \int_{\left(\frac{t}{c}\right)min}^{\left(\frac{t}{c}\right)max} \left(C_{p,f} - C_{p,a}\right) d\left(\frac{y}{c}\right) \quad [9]$$

Where $C_{p,f}$ and $C_{p,a}$ are the pressure coefficients on the fore and aft sections of aerofoil respectively.

The lift and drag coefficients can therefore be determined from equations:

$$C_L = C_N cos\alpha - C_A sin\alpha \quad [10]$$

$$C_D = C_N sin\alpha - C_A cos\alpha \quad [11]$$

The above lift and drag coefficients are purely depended upon the pressure distribution over the aerofoil and do not include the effect of shear stresses acting on its surface. Shear stresses contribute very little to the normal force and hence to the coefficient of lift but they have a more significant impact on the value of total C_D since they account for the skin friction drag. The drag coefficient provided from Equation [11] does only therefore provide an estimate of the pressure drag and does not account for the effect of the skin friction drag.

The values of C_L obtained from C_P as well as the values obtained using the balance, are presented in Figure 57 to Figure 59 (Section 6.7).

6.6 Blockage Corrections

The presence of solid boundaries within the wind tunnel's working section, as well as the wind tunnel walls, will produce a wake and solid blockages thus altering the aerodynamic forces calculated during the experimental procedure. The results obtained therefore might be unrepresentative of those arising in an unbounded flow field such as the free atmosphere. Standard two-dimensional low Reynolds number corrections as detailed by Barlow, Rae and Pope [105] and Pankhurst and Holden [106] for wake and solid blockages, were thus applied to the aerodynamic coefficients of lift and drag as well as to the freestream quantities and pressure coefficients, for both the direct measurements from the overhead external balance and the surface pressure distributions.

The effect on the aerodynamic forces by each of the other components in the wind tunnel such as tail wires, endplates, connection wires and struts were obtained individually by running the model without the wing. Using this approach however, does not account for the interference between the different elements such as the endplates and the wing or for phenomena such as corner vortex flow.

6.7 Errors and Repeatability

Various factors may influence experiments and introduce errors to the results, in this case, variability of the measured flow field as well as model positioning and instrumentation.

Measurements of the ambient temperature were constantly monitored as significant variation could have an effect on the pressure readings. It was observed that the ambient temperature did not deviate more than $3^{o}C$ during each run therefore, it was assumed it did not contribute any significant error to the measured values.

The accuracy of the lift and drag measurements through a static load calibration was estimated to be ±1.02N and ±0.88N respectively. This corresponded to full scale errors of ±0.068% and ±3.1% in lift and drag, which translated to ±0.26% and ±3.2% errors in estimates of C_L and C_D respectively. Pressure coefficient, C_p, measurements were expected to

be better than ±1.44% based on a ±0.25% and ±1% full scale error in pressure from the FC0318 and PX139 pressure systems respectively.

As the model was removed from the wind tunnel between the balance measurement program and Cp measurement program, it was essential to check the consistency in setting and measurement of the wing angles of attack. As previously stated, angles were determined each time by a digital inclinometer in a wind off condition and the process was repeated periodically to check that no deviation occurred.

Additional tests were conducted in regular intervals to establish the repeatability of the results and the effect of slight variations in Reynolds number, caused by possible ambient temperature and atmospheric pressure fluctuations. The results were tabulated and compared against each other and conclusions were drawn upon their repeatability. It was observed that the values of the lift coefficient varied within a range of ±2%, while the range of difference in drag coefficient was slightly higher reaching values of ±5%. Similar results were also obtained with the pressure measurements.

Figure 57, Figure 58 and Figure 59 illustrate the repeatability of the C_L results, a comparison between the lift coefficients obtained from the balance (BL) measurements and the C_p measurements. Both procedures predicted stall at the same locations and produced similar results for the values of C_L with a difference of less than ±2% between them.

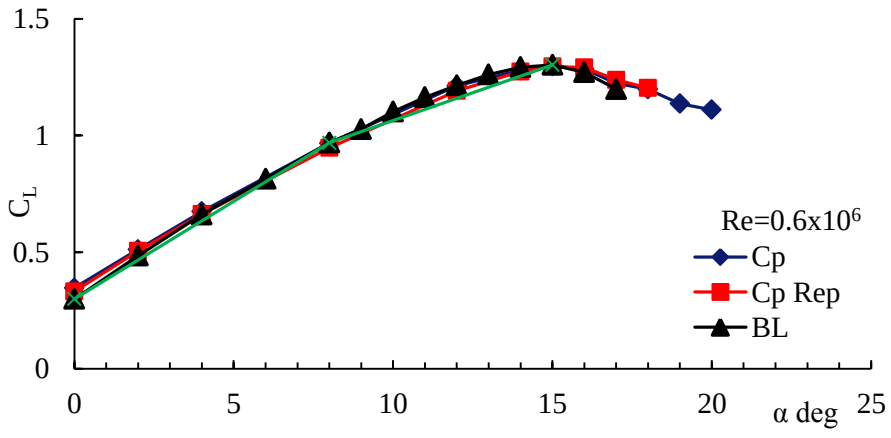

Figure 57: Illustrates the value of C_L derived from C_p and balance measurements (BL) for a range of angles of attack α at Reynolds number $0.6x10^6$.

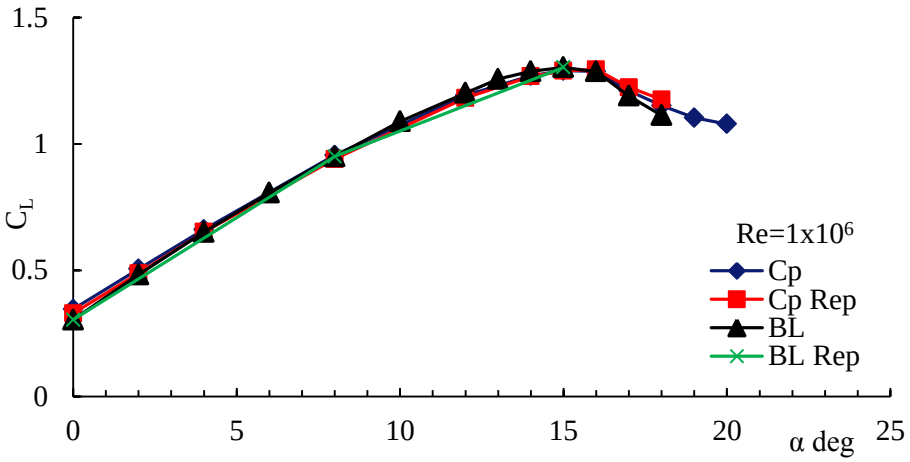

Figure 58: Illustrates the value of C_L derived from C_p and balance measurements (BL) for a range of angles of attack α at Reynolds number $1x10^6$.

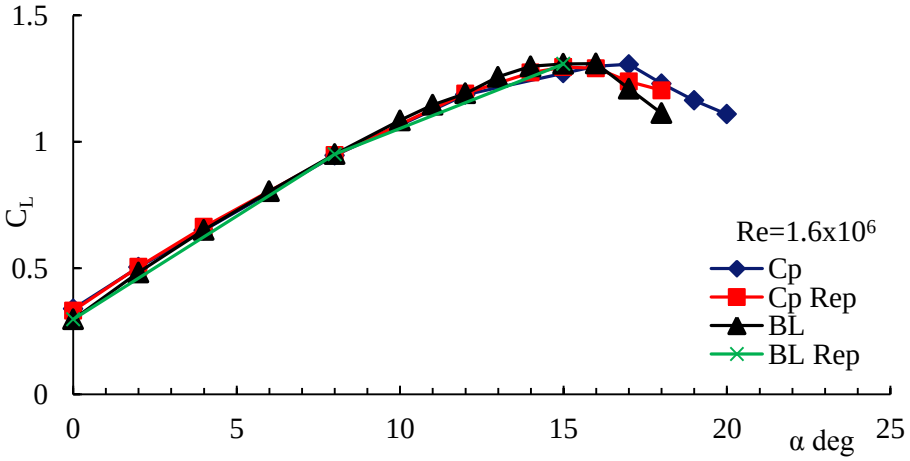

Figure 59: Illustrates the value of C_L derived from C_p and balance measurements (BL) for a range of angles of attack α at Reynolds number $1.6x10^6$.

6.8 Summary of test Cases

From the available published data (See Chapter 3) a relationship was established between flap deflection angle and force, from which an estimated optimum flap deflection angle range was extracted. The Reynolds number range was selected such as to coincide with the one observed in the flight of tactical UAVs. A summary of the experimental test parameters is presented here below:

Case 1: Plain aerofoil (no flaps)

Operating Reynolds Numbers $0.6x10^6$, $1x10^6$, $1.6x10^6$

Angles of attack α range: 0-18 deg.

Case 2: Aerofoil with 10% chord flap

Flap deflection angles δ: 70, 100, 110 deg.

Operating Reynolds Numbers: $0.6x10^6$, $1x10^6$, $1.6x10^6$

Angles of attack α range: 0-18 deg.

Case 3: Aerofoil with 5% chord flap

Flap deflection angles δ: 50, 70, 80 deg.

Operating Reynolds Numbers: $0.6x10^6$, $1x10^6$, $1.6x10^6$

Angles of attack α range: 0-18 deg.

Case 2 and Case 3 were examined with and without transition fixing. In addition the discontinuity observed in the aerofoil-flap surface contour and its effect on the aerodynamic performance characteristics of the aerofoil and flap configuration was also investigated.

Chapter 7. High Lift Configurations – Computational and Experimental Study

This chapter presents an analysis, comparison and discussion of the numerical and experimental results obtained in this work.

Important conclusions are drawn upon the characteristics and performance of the high lift configurations under the various different conditions and arrangements examined.

7.1 Baseline Results

The following results portray and analyse the performance of the plain Clark Y aerofoil over the range of Reynolds numbers examined. For the experimental procedure the flow field around the aerofoil was analysed by means of surface static pressure distributions which were then compared with analogous results obtained from the corresponding CFD analysis. As previously stated no significant differences were observed in the values of C_L obtained between the balance measurements and the surface static pressure distribution. The direct comparison of the experimental and numerical results enables a more detailed analysis and evaluation of the flow field behaviour around the aerofoil and subsequently the aerofoil and flap configuration to be made. In addition it enables the calculation of the loads acting on each element individually and/or collectively.

Figure 60, to Figure 62 illustrate C_L Vs α data for the baseline cases at the three Reynolds numbers examined. By comparing the graphs it can be seen that the C_L values obtained from CFD analysis are predicted to within 5% of the experiments, follow the same trends and stall at $\alpha=15^o$.

The corresponding C_D graphs are shown in Figure 63 to Figure 65. Even though the experimental C_D is slightly higher than the numerical one, a good agreement is observed noticeably at low angles of attack and a similar/comparable trend is followed throughout the angle of attack range.

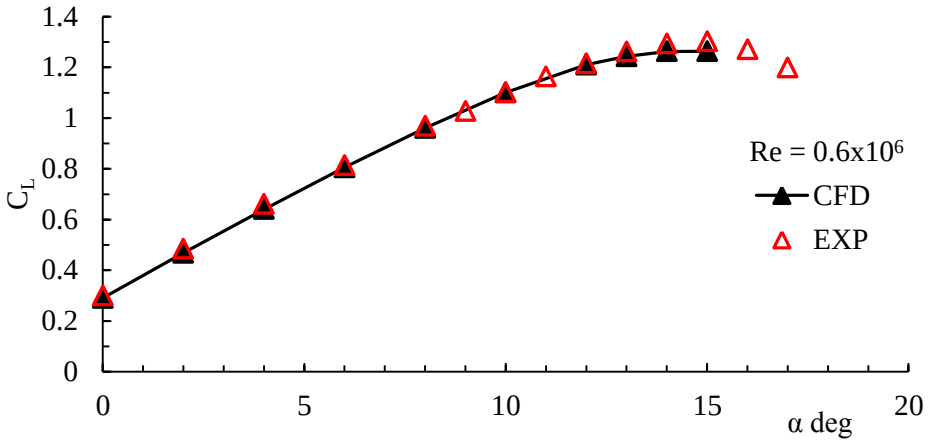

Figure 60: C_L plots over a range of angles of attack of the numerical and experimental results for a baseline Clark Y at Re=0.6x10^6.

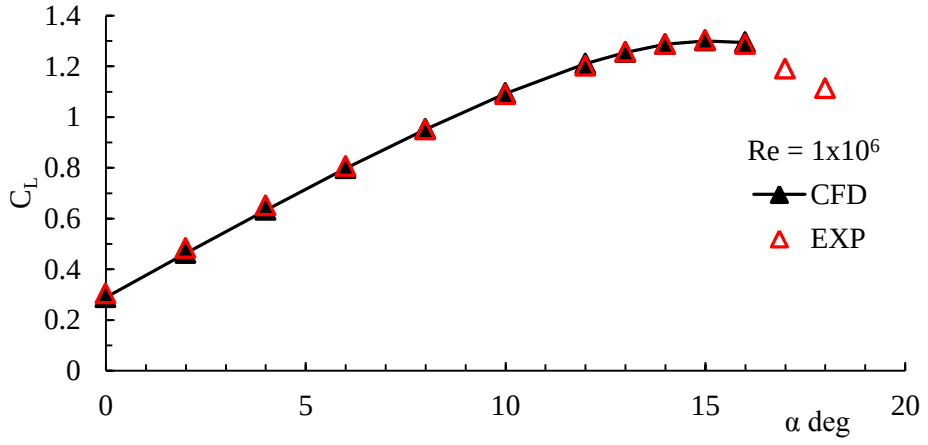

Figure 61: C_L plots over a range of angles of attack of the numerical and experimental results for a baseline Clark Y at Re=1x10^6.

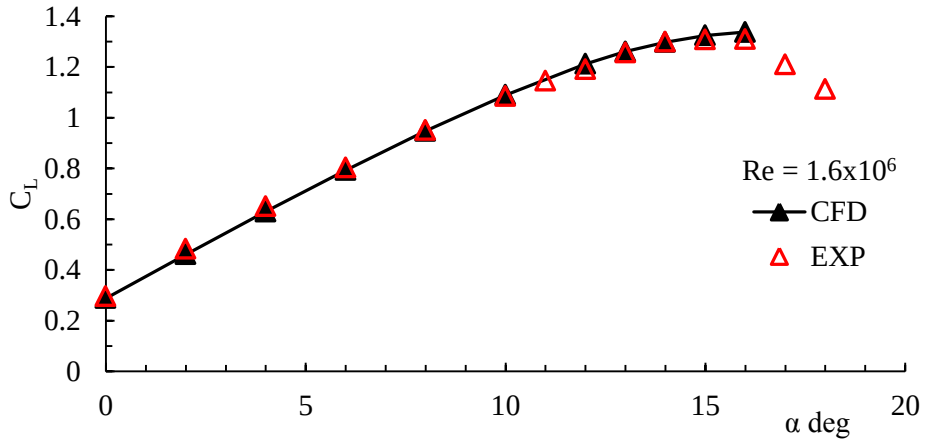

Figure 62: C_L plots over a range of angles of attack of the numerical and experimental results for a baseline Clark Y at Re=1.6x10^6.

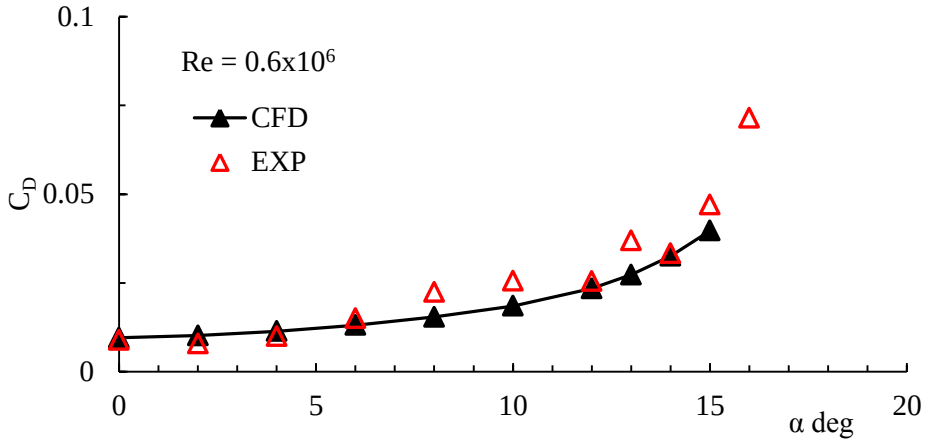

Figure 63: C_D plots over a range of angles of attack of the numerical and experimental results for a baseline Clark Y at Re=0.6x10^6.

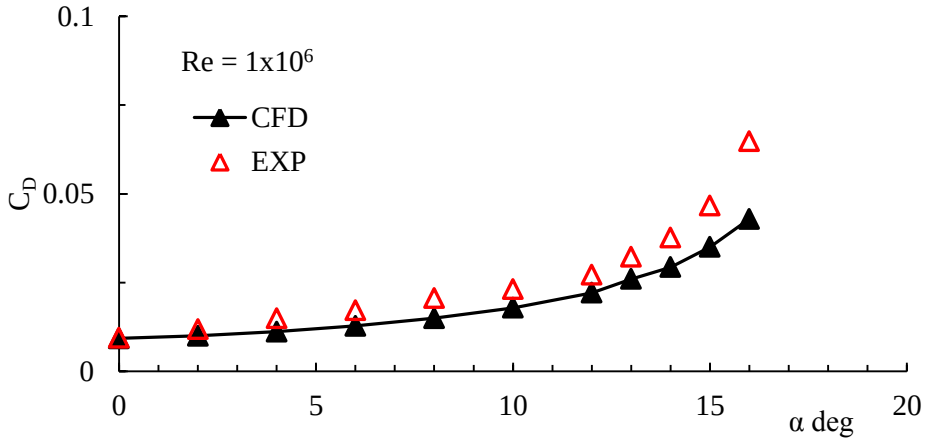

Figure 64: C_D plots over a range of angles of attack of the numerical and experimental results for a baseline Clark Y at Re=1x10^6.

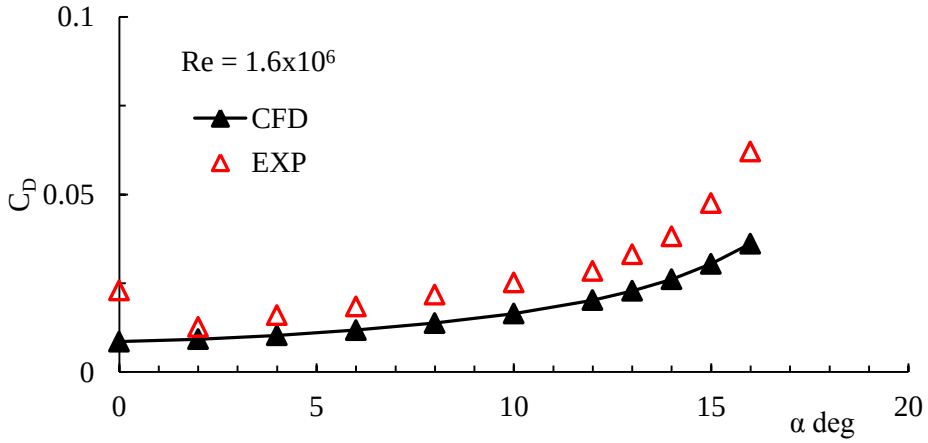

Figure 65: C_D plots over a range of angles of attack of the numerical and experimental results for a baseline Clark Y at Re=1.6x10^6.

Figure 66a and 7b illustrate comparisons of the results for the minimum and maximum C_L as well as the minimum and maximum C_D for the numerical and experimental analyses, respectively, at the different Reynolds numbers examined. It can be seen, that the variation in the lift coefficient between the experimental and numerical results, is less than 0.05 which translates to a difference of less than 3%. The numerical C_D values are in good agreement with the experimental values at low angles of attack for all three conditions examined, with a variation ranging between 5% and 10%. At high angles of attack, however, this difference increases reaching values of approximately 24%.

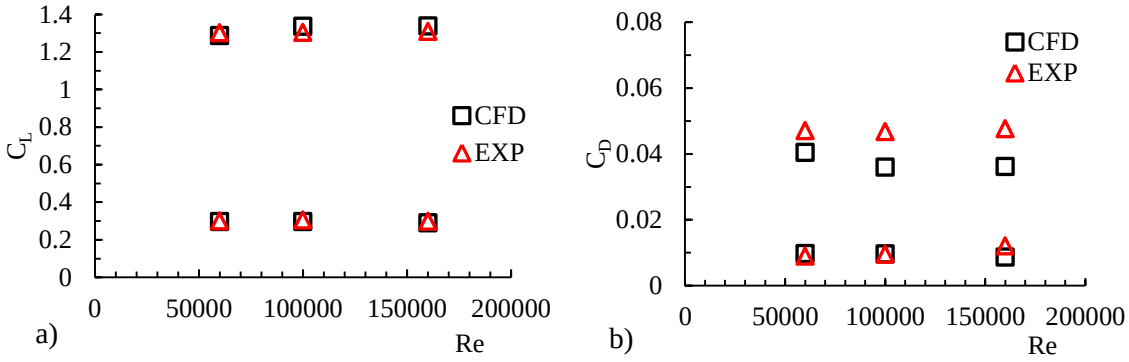

Figure 66: Comparison between numerical and experimental C_L and C_D results against Re number.

7.2 Examination of Cp Distribution around the Clark Y

The maximum amount of lift produced by an aerofoil is limited by the flow separation on its upper surface. Highest pressure is obtained at the leading edge of the aerofoil (stagnation region). As the flow expands around the suction side an adverse pressure gradient region is observed downstream the maximum thickness of the aerofoil. If the adverse pressure gradient is small the flow remains attached. As the angle of attack of the aerofoil increases though, the pressure difference between the upper and lower surfaces also increases, thus resulting to an increase in the net lift force. The adverse pressure gradient along the suction side of the aerofoil, however, intensifies and trailing edge separation gradually develops. This separation in turn, results to the increase in the thickness of the wake flow, and a reduction in the pressure rise that occurs near the trailing edge.

Figure 67 to Figure 73 show plotted the numerical and experimental C_P values over a range of angles of attack, AOA, and Re = $1x10^6$. Results for Re = $0.6x10^6$ and $1.6x10^6$ are of similar nature and are presented in APPENDIX F. The agreement between the two sets of data is good especially at low AOA ($\alpha < 4^o$), where it can be observed, that the plots follow similar trends.

At higher AOA, the shape of the C_P curve is captured quite well by the numerical methods and the deviations are minor. The position of the stagnation point (C_P=1) is in good agreement with the experimental results and it is predicted with reasonable accuracy (between 3% to 5% in most cases).

A good agreement is also observed for the location of the suction peak but the numerical analysis predicts slightly higher values for C_P. This could be caused by possible small anomalies between the actual tested and the assumed theoretical model geometries at the leading edge. Since the deviation is less than 5% and localized in this area, it can be assumed that it does not influence the accuracy of the aerodynamic load calculations. Apart from the above difference in the suction peak values the pressure coefficients are in very good agreement over the full aerofoil surface.

Similar trends in the C_P plots are also observed when comparing results from the experimental and numerical analyses performed in the course of this work in Cranfield, with results from published literature (see Figure 180 APPENDIX F). A suction peak near the leading edge of the aerofoil starts to become evident for values of $\alpha>4^o$ and trailing edge separation gradually develops at $\alpha>12^o$. This separation becomes more noticeable as the AOA increases and the effect gradually moves towards the leading edge until $\alpha = 15^o$ where the aerofoil stalls.

The effect of the stall can also be seen by observing the contours of Velocity magnitude (See Figures in APPENDIX H. By observing and comparing the baseline aerofoil performance at the different Reynolds numbers considered, it can be seen that the effect of the trailing edge separation slightly decreases with increasing Reynolds number. Although this effect does not influence the stall angle, it gives however, a small increase in the value of C_{Lmax}.

A direct comparison between the experimental, numerical and published data is presented in Figure 74 and Figure 75 at $\alpha=4^o$. It can be seen that the C_P trends obtained from this analysis closely follow the ones obtained from published literature.

Cp plots for a baseline Clark Y at Re = 1x10^6 and AOA range of α=0^o to 15^o.

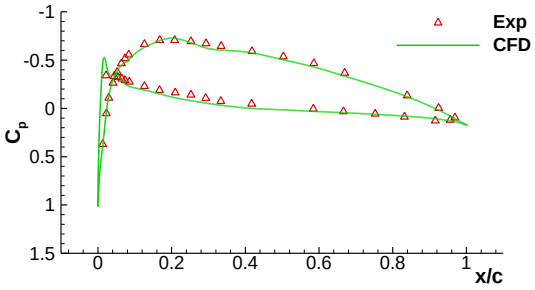

Figure 67. Experimental and numerical C_p plots for a baseline Clark Y at Re=1x10^6 and α=0^o.

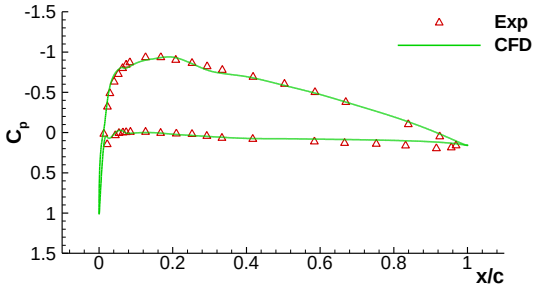

Figure 68. Experimental and numerical C_p plots for a baseline Clark Y at Re=1x10^6 and α=2^o.

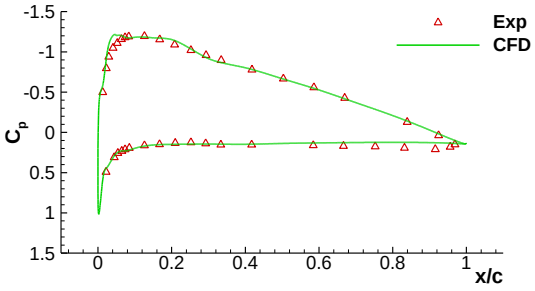

Figure 69. Experimental and numerical C_p plots for a baseline Clark Y at Re=1x10^6 and α=4^o.

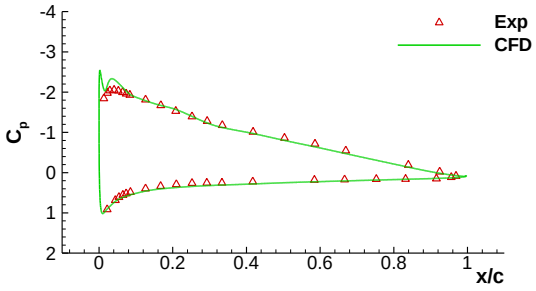

Figure 70. Experimental and numerical C_p plots for a baseline Clark Y at Re=1x10^6 and α=8^o.

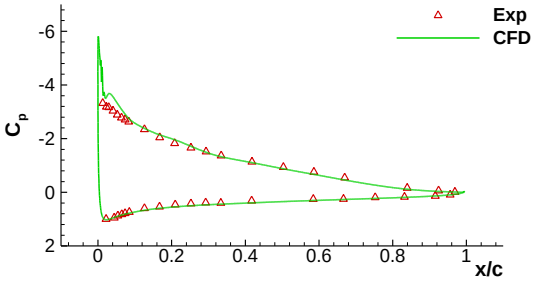

Figure 71. Experimental and numerical C_p plots for a baseline Clark Y at Re=1x10^6 and α=12^o.

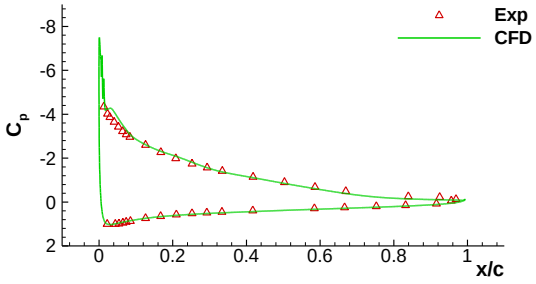

Figure 72. Experimental and numerical C_p plots for a baseline Clark Y at Re=1x10^6 and α=14^o.

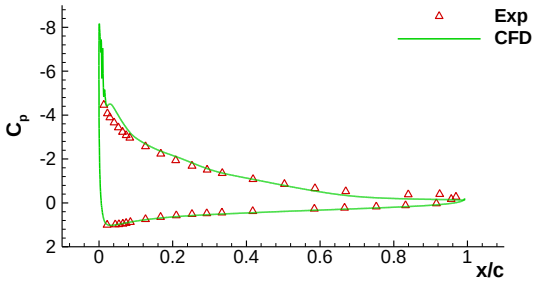

Figure 73. Experimental and numerical C_p plots for a baseline Clark Y at Re=1x10^6 and α=15^o.

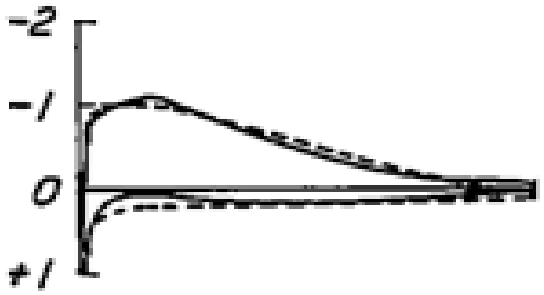

Figure 74. C_p plots obtained from theory for a baseline Clark Y at Re=0.356x10^6 (doted), Re=6.7x10^6 (straight) and α=4^o [107].

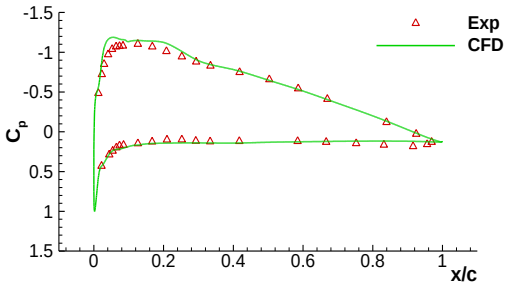

Figure 75. Experimental and numerical C_p plots for a baseline Clark Y at Re=0.6x10^6 and α=4^o.

7.2.1 Reynolds number effect on the plain Clark Y aerofoil

The effect of Reynolds number on the maximum and minimum aerodynamic characteristics of the baseline aerofoil can also be seen from Figure 66a and 67b (page 85). A slight increase in the value of C_{Lmax} is observed (approximately 3%) with increasing Reynolds number, whereas the values of C_{Lmin} and C_{Dmin} do not show any significant variation.
The streamlines obtained from the numerical analysis at Re=0.6x10^6 and 1.6x10^6 and α=15^o are compared in Figure 76 and Figure 77 respectively. The flow at Re=1.6x10^6 shows a reduced separation region (approximately 10%) compared to that at Re=0.6x10^6.

The presence and character of the boundary layer around the aerofoil can affect its performance characteristics by altering its effective shape through development of boundary layer displacement and through flow separation.

As the angle of attack and the section lift coefficient increases, the negative Cp increases (suction peak). This results in an increasing adverse pressure gradient as the flow decelerates towards the trailing edge. If the pressure gradient is too high then the pressure forces overcome the fluid's inertial forces and the flow separates. The location of the separation depends on the character of the boundary layer (laminar/turbulent) and its thickness, and therefore the Reynolds number. In the case of the numerical analysis performed in this project the flow was assumed to be fully turbulent for all three Re numbers examined.

Comparing the C_P graphs for the low and high Re number cases (see Figure 166 to Figure 179 APPENDIX F) it can be observed that they follow similar trends. The change in the effective shape of the aerofoil can therefore be assumed negligible for the three baseline cases. As the Reynolds number increases however, the inertial forces in the boundary layer increase delaying the separation point when under an adverse pressure gradient (see Figure 76 and Figure 77).

Following flow separation, the boundary layer thickens thus increasing the thickness of the wake flow. This results in C_P divergence at the trailing edge with a resultant increase in pressure drag. Any increase in the pressure drag affects the total drag produced by the aerofoil. Thus observing Figure 63 to Figure 65 (page 84), it can be seen that the result of the higher pressure drag is to slightly increase the value of the total drag and hence increase C_D with decreasing Re. In addition, increase in the separation area for the low Re case could lead to a slight decrease in lift (3% as stated before). This effect is somewhat more evident in the numerical results as can be seen in Figure 66b page 85.

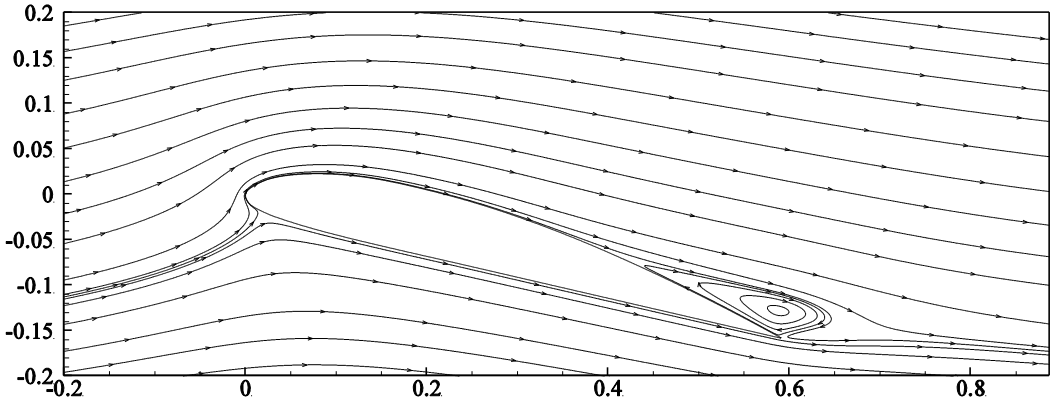

Figure 76: Streamlines of aerofoil and flap configuration at α=15^o and Re=0.6x10^6.

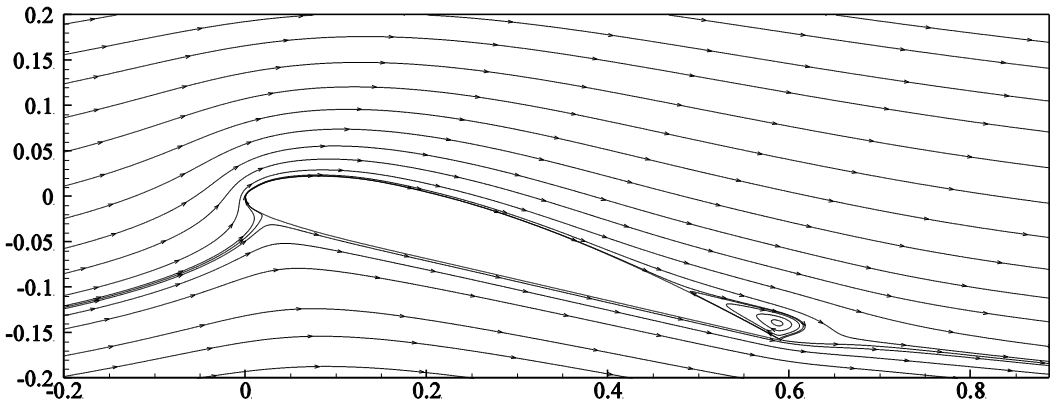

Figure 77: Streamlines of aerofoil and flap configuration at α=15^o and Re=1.6x10^6.

7.3 Flap-aerofoil configurations

Two different flap-aerofoil configurations, one with a 10% flap and another with a 5% flap, were investigated under different conditions. Each configuration was examined at different flap deflection, angle of attack and at three different Reynolds numbers. In the experimental study emphasis was also given in the investigation of the flap-aerofoil transition and the step created between the flap and aerofoil, with the aim to examine their effect and influence on the overall configuration performance. Each case is presented and discussed in detail here below.

7.4 10% Flap Smooth with no transition

Ideally, the purpose of a high lift device is to generate as much lift as possible without causing separation to the flow [115] [116] . Without the presence of external devices, such as wall suction, the use of flaps and slats is recognised as the most effective way to achieve this goal. With the use of such devices, the inviscid pressure distribution may be manipulated to reduce the pressure rise over the elements [115],[118]. The flap used for this study had a length of 61mm and thickness of 2mm, see Figure 78. It was designed and applied in such a manner so as to eliminate as much as possible the discontinuity which might occur between flap and main element. The application of plasticine fillet and aluminium tape, as described earlier, further enabled a smooth transition of the flow from the flap onto the aerofoil's upper surface when the flap was deployed. The flap was designed to rotate about a single fixed pivot point which was coincident with the location of the centre of the aerofoil's leading edge radius as shown in Figure 78. This arrangement enables a smooth surface contour between the flap and the main element when the flap is nested but also at low flap deflection angles.

High speed video observing the flight of eagles, [117] has shown that while such leading edge flaps can deploy in segments they ultimately span most of the wing, which essentially establishes the leading edge flap as a two-dimensional device. A joint experimental and numerical analysis was thus performed to obtain the aerodynamic performance characteristics and loads acting on such devices. The CFD analysis enabled the calculation of the loads acting on each part of the configuration (flap and aerofoil), individually and/or collectively

and gives a better understanding of the contribution of each element to the aerodynamic characteristics of the configuration.

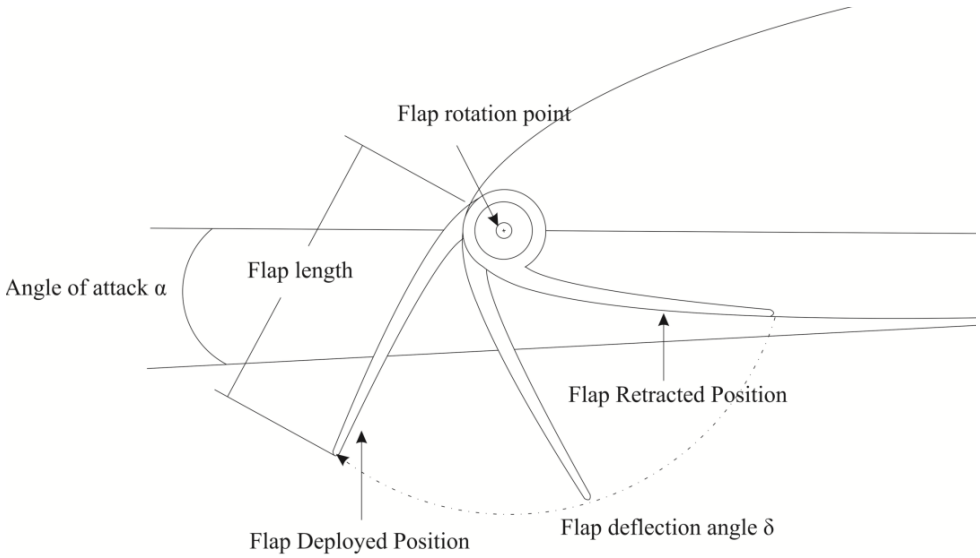

Figure 78: Clark Y and 10% flap configuration schematic used for the experimental procedure.

The maximum lift coefficient (C_{Lmax}) determines the stalling speed and approach angle of an aircraft, a UAV for the purposes of this work. In addition, values such as C_{Lmax} and C_{Dmin} are critical in defining takeoff and landing speeds and runway lengths, as well as maximum range and endurance (this is discussed in more detail further on). It is important therefore, to determine the influence and effect that leading edge flaps have on these coefficients, on an aerofoil-flap configuration and in comparison to a plain aerofoil.

The experimental results obtained from Cranfield wind tunnel tests, as part of this work, are summarised and presented in Figure 79 to Figure 81. These figures demonstrate, the effect that the 10% flap has on the C_L in comparison to the baseline Clark Y aerofoil, at the three flap deflection angles and Reynolds numbers examined.

The results of the experiments, for configurations with 10% flap, show, that as α and/or δ increase the flap aligns with the approaching flow and an increase in C_L is achieved. The angle α, at which the aerofoil and flap configuration start to produce more lift than the baseline model, depends on δ and it decreases as δ increases. The benefits of utilizing a leading edge flap start to become evident at angles of attack between, $\alpha=5^o$ - 6^o for $\delta = 100^o$ and $\alpha=3^o$ - 5^o for $\delta = 110^o$. As the flap deployment angle decreases, the angle of attack at

which the device becomes effective increases. At δ less than the optimum, the flap serves only to increase the drag as the flow separates before the angle of attack is high enough for any contribution of the flap to be evident. A trailing edge stall is observed in all configurations which is characterised by a gradual decrease in the value of C_L.

For the 10% flap the C_L plots reveal an increase in the maximum lift coefficient between 15% - 18% at a stall angle of $\alpha = 16^o$ -17^o and flap deflection angle of $\delta = 110^o$ and 11% and 12% at $\delta = 100^o$. At $\delta = 70^o$ however, the flap does not offer any benefits in the value of C_L, on the contrary rather, it seems to decrease the efficiency of the configuration.

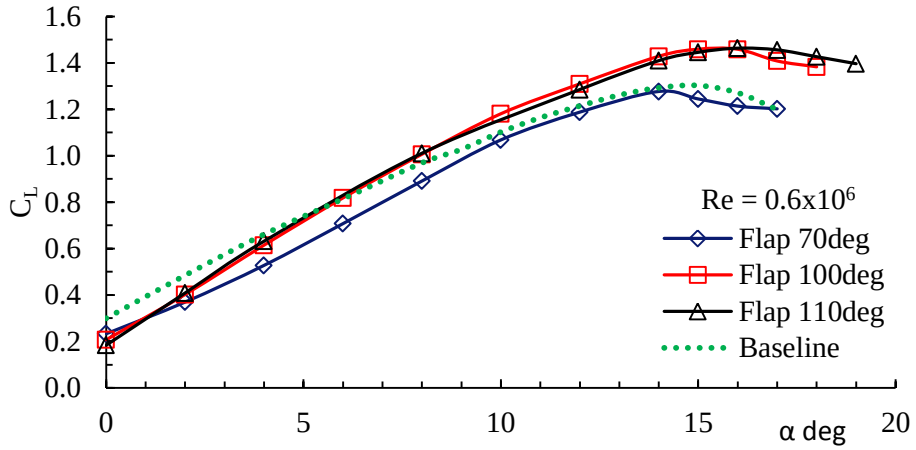

Figure 79: C_L plots for Re = 0.6x10^6 over the range of angles of attack of the experimental results for an aerofoil and flap configuration with $\delta = 70^o$, 100^o and 110^o.

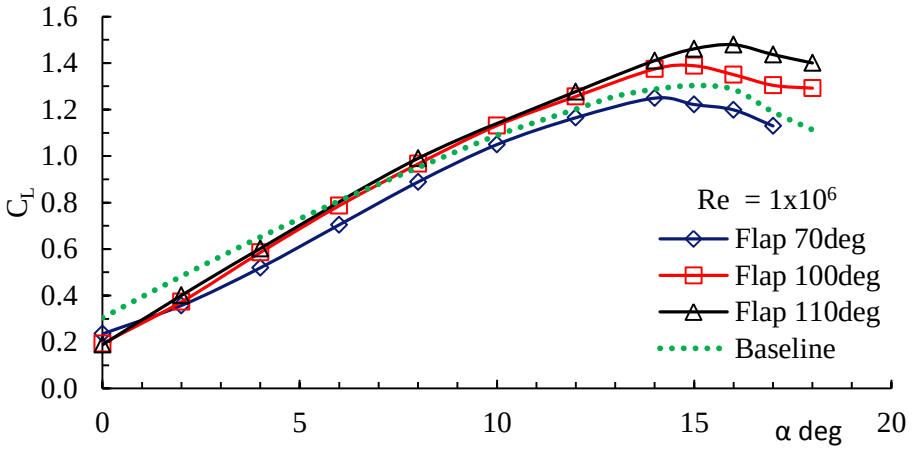

Figure 80: C_L plots for Re = 1x10^6 over the range of angles of attack of the experimental results for an aerofoil and flap configuration with $\delta = 70^o$, 100^o and 110^o.

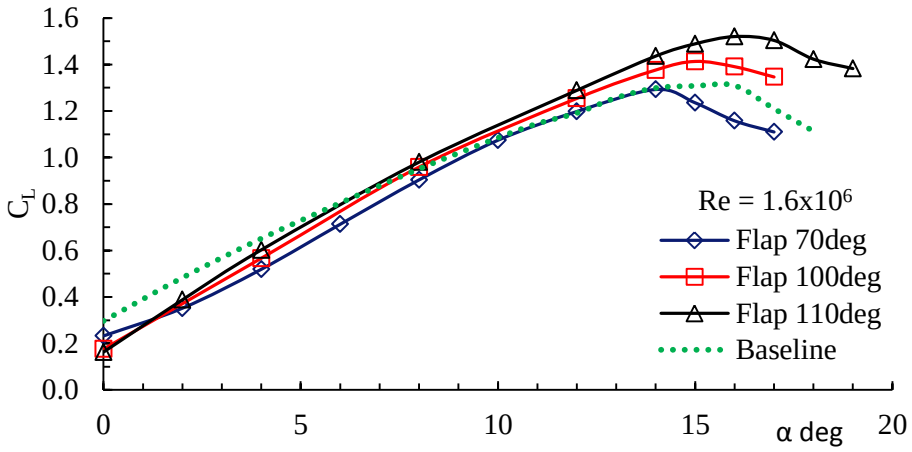

Figure 81: C_L plots for Re = 1.6x10^6 over the range of angles of attack of the experimental results for an aerofoil and flap configuration with δ = 70^o, 100^o and 110^o.

7.5 5% Flap Smooth with no transition

The previously described experimental and analytical process was similarly repeated with a 5% flap. This enabled the comparison of the two different size flaps and helped draw important data pertaining to length and relative performance characteristics for each device. The 5% flap had 30.5mm length and 2mm thickness and was applied in a similar manner as the 10% case, to ensure a smooth surface contour and to eliminate any discontinuities in/to the flow. Due to time limitations it was not possible however, to examine both flaps for all possible δ's. The 5% flap was examined at δ = 50^o, 80^o, and 90^o and the results are summarised in Figure 82 to Figure 84.

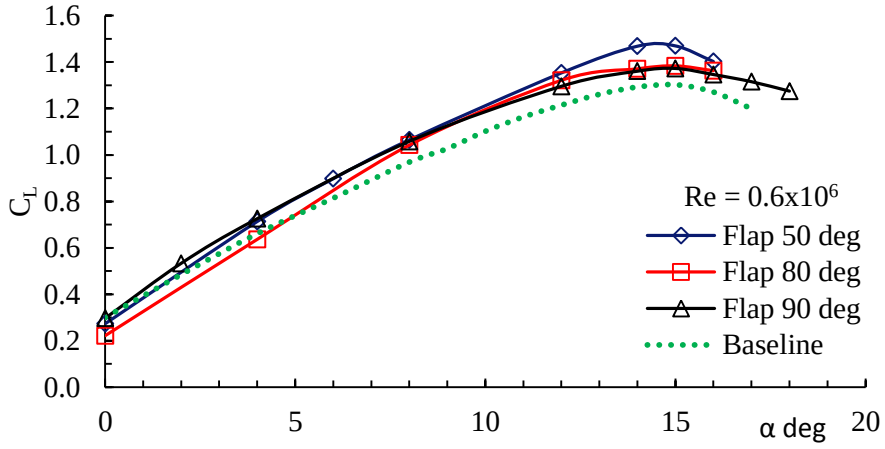

Figure 82: C_L plots for Re = 0.6x10^6 over the range of angles of attack of the experimental results for an aerofoil and flap (5%) configuration with δ = 50^o, 80^o and 90^o.

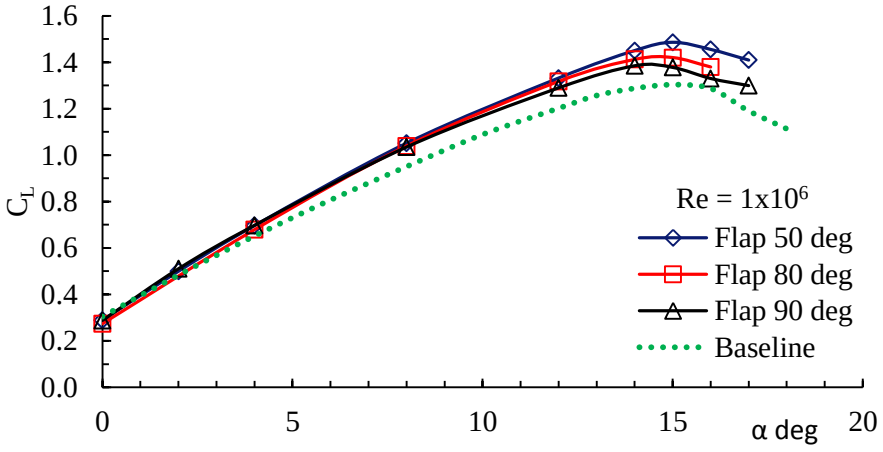

Figure 83: C_L plots for Re = 1x10^6 over the range of angles of attack of the experimental results for an aerofoil and flap (5%) configuration with δ = 50^o, 80^o and 90^o.

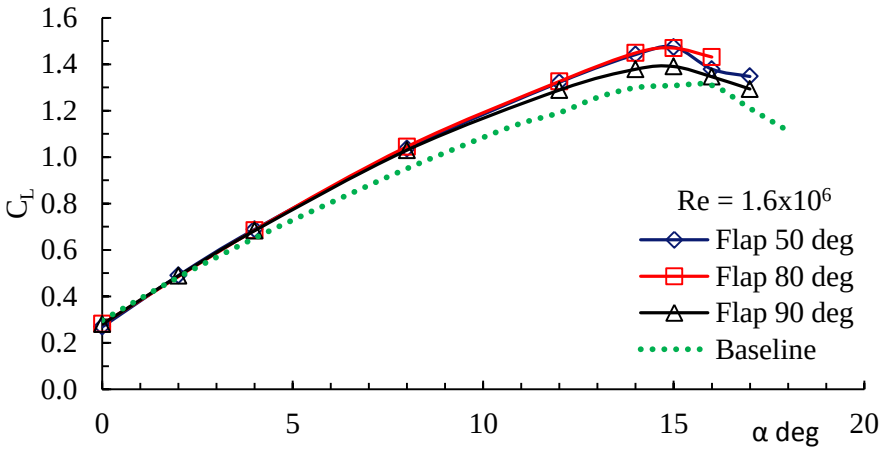

Figure 84: C_L plots for Re = 1.6x10^6 over the range of angles of attack of the experimental results for an aerofoil and flap (5%) configuration with δ = 50^o, 80^o and 90^o.

The results of the 5% flap case show that as α and/or δ decrease an increase in C_L is attained. The angle α, at which the aerofoil and flap configuration start to generate more lift than the baseline model, depends on δ and it decreases as δ increases, likewise to the 10% flap case. Due to the smaller geometry of the 5% flap, however, the flow aligns with the configuration at lower angles of attack and the benefits of utilizing the 5% flap start to become evident between α= 1^o - 5^o for all flap deflection angles. Similarly, as in the case of the 10% flap a trailing edge stall is observed in all configurations which leads to a gradual loss in C_L.

The C_{Lmax} value achieved for the 5% flap is slightly lower than the one observed for the 10% flap. The C_L graph is, however, more elevated in the lower range of angles of attack and

especially for $\delta = 50^o$. In contrast to the 10% flap, the 5% flap performs better at lower flap deflection angles δ and its performance slightly decreases as δ increases (whereas, the opposite is the case for the 10% flap). This is shown in Figure 82 to Figure 84 which show that the lift characteristics of a configuration with a 5% flap at $\delta=50^o$ are slightly better. It is believed, that the introduction of the flap at $\delta=50^o$ increases the camber and the leading edge thickness of the aerofoil thus increasing its lift slope characteristics.

In the case of the 5% flap configuration, the corresponding increase in the C_{Lmax} values was between 14% - 16% at a stall angle $\alpha=15^o$ to 17^o and flap deflection angle $\delta = 50^o$ between 11% - 12% for $\delta = 80^o$ and close to 8% at $\delta = 90^o$.

A more detailed analysis for each individual configuration is presented in the following section.

7.6 Variation of ΔC_L for the 10% flap cases

Considering Figure 85, which illustrates the ΔC_L between the baseline aerofoil and the aerofoil and flap configuration at $\delta=70^o$, a decrease in the value of C_L can be observed as earlier mentioned. The decrease is noted throughout the investigated range of the angles of attack. Examining the flow characteristics of the configuration from the numerical analysis, it can be seen that the flow separates as it moves around the leading edge of the flap and a recirculation area is produced on the pressure side of the aerofoil, which reattaches at x/c = 0.62, as can be seen in Figure 86. The implementation of the flap results in a slight decrease in the magnitude of the suction peak forming on the main aerofoil. The recirculation area which develops behind the flap at low angles of attack (see Figure 86), gives rise to a pressure difference between the fore and aft of the wing thus increasing the value of the pressure drag. As a consequence therefore, the total value of the drag increases (the Cp curves are presented later on in Figure 181 to Figure 198). As the angle of attack increases, the recirculation area becomes smaller and approaches the leading edge thus minimising its effect. The aerofoil however, stalls before any contribution to the lift can be achieved by the load acting on the flap.

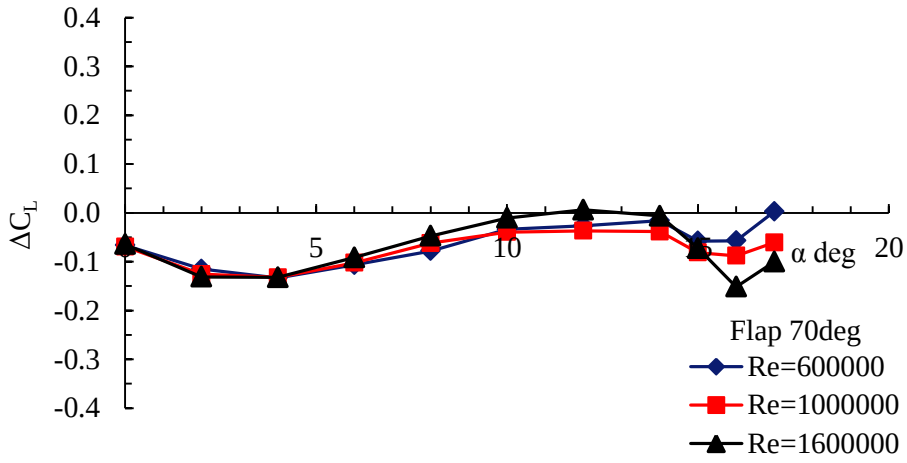

Figure 85: ΔC_L Vs α between baseline and aerofoil and flap smooth configuration with no transition strip. Flap deflection angle δ=70° over the range of Reynolds numbers.

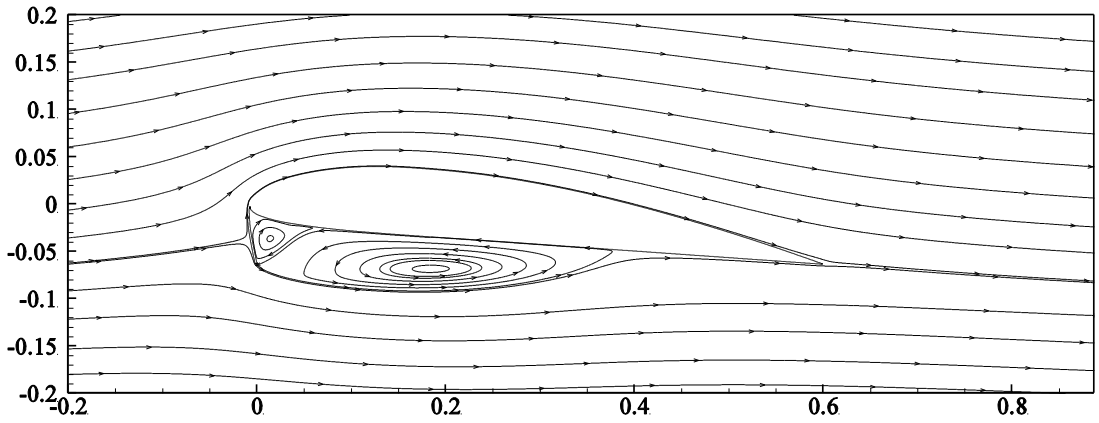

Figure 86: Streamlines of aerofoil and flap configuration at δ=70° and Re=0.6x10^6.

Similarly, the ΔC_L between the baseline aerofoil and a 10% flap configuration at δ=100° is summarised in Figure 87. In contrast to the configuration with the 10% flap at δ=70°, an almost linear increasing relationship is observed in this case. At low angles of attack, the ΔC_L is negative since the incoming flow is not yet aligned with the flap. A similar separation region is observed behind the flap in this case as with δ=70°, see Figure 88. However, the magnitude of the recirculation area is smaller than before (δ=70°) and the flow reattaches at approximately x/c = 0.34. The flow starts to align for α between 7° and 8° and at higher angles of attack the ΔC_L starts to become positive and follows an increasing trend. On average the flap in this case performs slightly better in the lower Reynolds number regime.

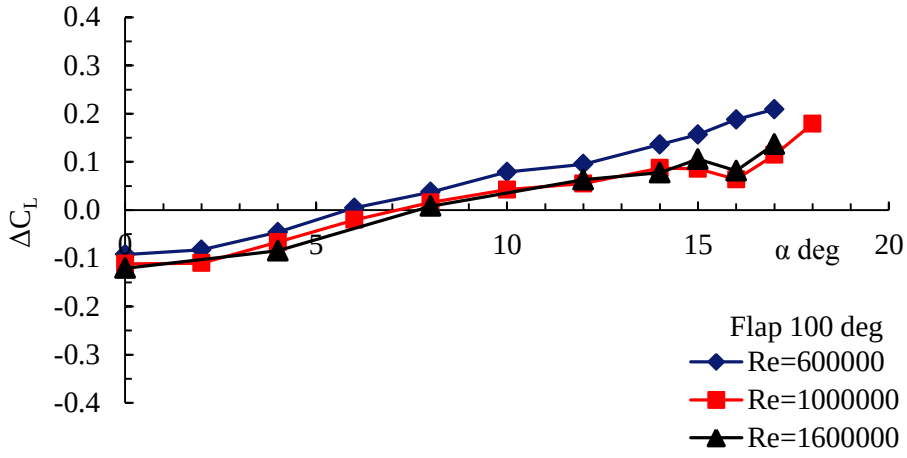

Figure 87: ΔC_L Vs α between baseline and aerofoil and flap smooth configuration with no transition strip and flap deflection angle δ=100° over the range of Reynolds numbers.

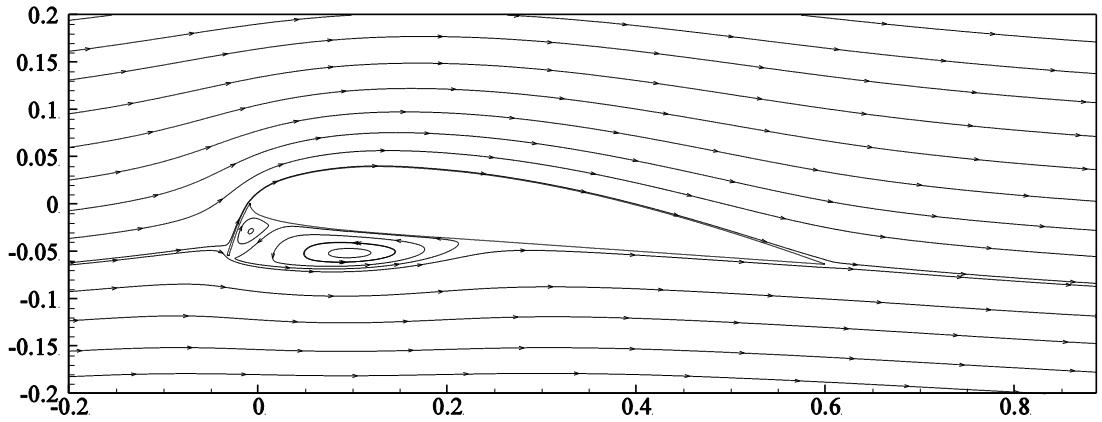

Figure 88: Streamlines of aerofoil and flap configuration at δ=100° and Re=0.6x10^6.

The ΔC_L behaviour between the baseline aerofoil and the 10% flap configuration at δ=110°, is comparable to the one observed at δ=100°, however, the flap seems to perform similarly at all Reynolds numbers with no significant difference between them, see Figure 89. The angle α, at which the flap starts to positively influence the configuration's performance occurs slightly earlier in this case and it is observed closer to 6°. Likewise, as before, a separation region with a recirculation area is observed behind the flap, which compromises the effect of the configuration at low angles of attack, see Figure 90. This region is smaller than the previously examined cases and reattaches in the region of x/c= 0.25. This enables the configuration to achieve slightly better lift and drag characteristics under these conditions.

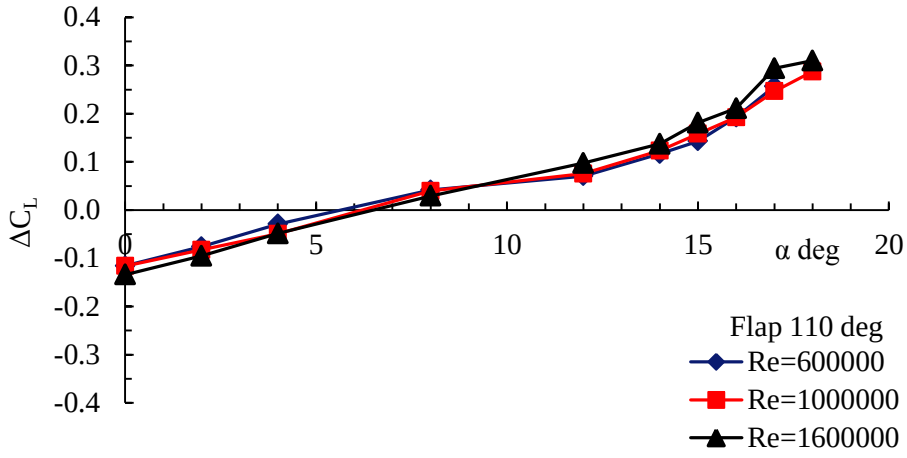

Figure 89: ΔC_L α between baseline and aerofoil and flap smooth configuration with no transition strip and flap deflection angle δ=110° over the range of Reynolds numbers (for 10% flap).

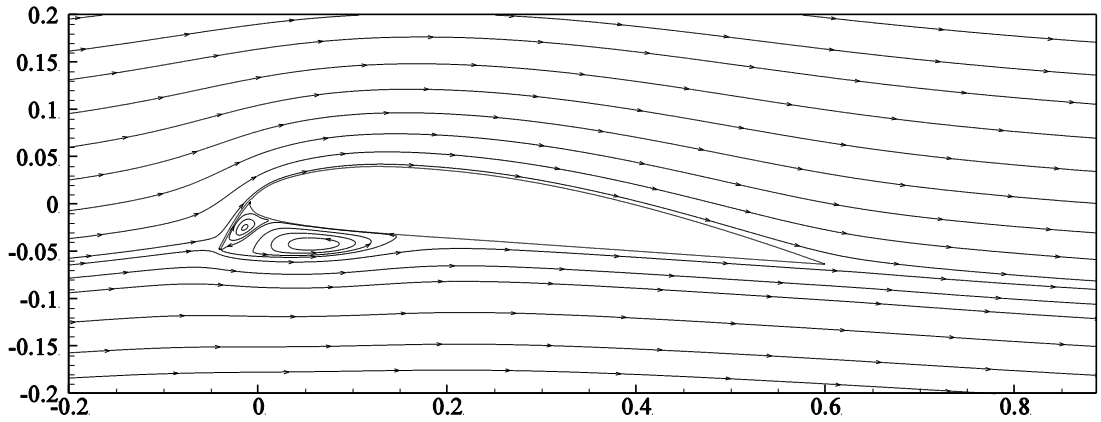

Figure 90: Streamlines of aerofoil and flap configuration at δ=110° and Re=0.6x10^6.

7.6.1 Summary 10% flap case

Implementation of a 10% flap results to an increase in the lift produced by the aerofoil at high angles of attack α. The crucial interaction between the main aerofoil and the flap brought about by their positions relative to each other contributes in the creation of up to 18% increase in lift by modifying the airflow around the main aerofoil element. At low flap deflection angles δ and low angles of attack α, a discontinuity of flow occurs at the lower surface of the aerofoil which reduces the total lift produced by the configuration and increases its drag. Comparing Figure 76, page 89 and Figure 91 which illustrate the streamlines around the baseline model and an aerofoil with a 10% flap at δ=100° both at Re=0.6x10^6 and angle of attack α=15° it can be seen, that the flow remains attached for

approximately 25% more when the flap is in fact deployed. This increase in the attached region helps the aerofoil-flap configuration to achieve higher lift values and stall at higher angles of attack.

Figure 86, Figure 88 and Figure 90 show instantaneous captions of the flow and are used to illustrate the effect that δ has on the magnitude of the recirculation area. This effect can also be seen by observing the C_P characteristics of the three cases illustrated in Figure 92. In addition Figure 92 shows a decrease in the magnitude of the suction peak with increasing δ, which leads to a decrease in magnitude of the slope after the peak. This can result to a decrease of the adverse pressure gradient in comparison to the baseline aerofoil thus reducing the separation region at high angles of attack.

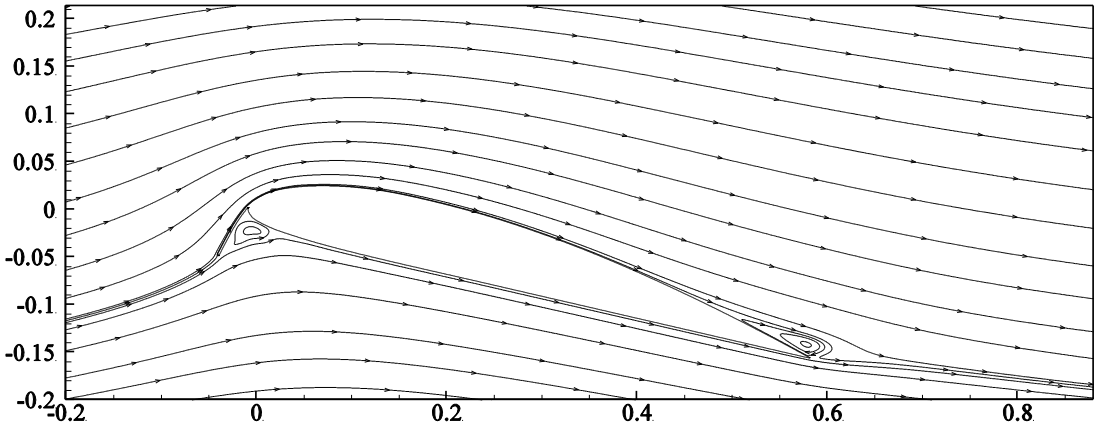

Figure 91: Streamlines of aerofoil and flap configuration at α=15°, δ=100° and Re=0.6x10^6

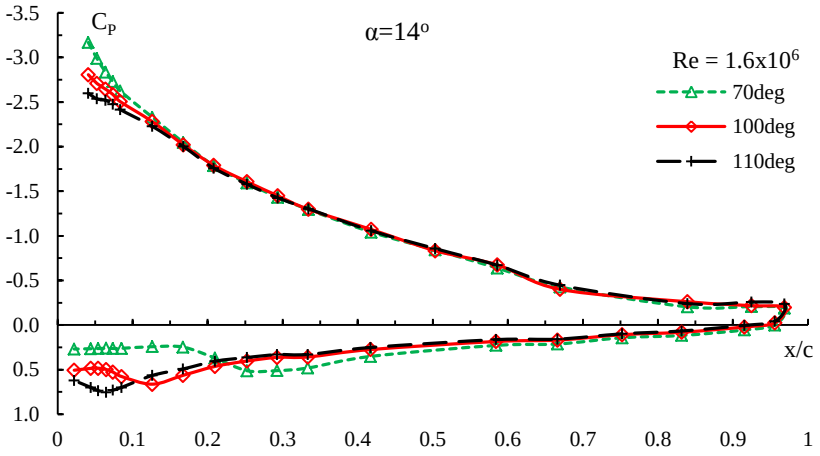

Figure 92: C_P plots for the 10% flap at δ=70°, 100°, 110°, α=14° and Re=1.6x10^6

7.7 Variation of ΔC_L for the 5% flap cases

In contrast to the 10% flap it can be observed that the 5% flap starts to positively affect the performance of C_L at lower angles of attack (see Figure 93). An almost linear increasing trend in the ΔC_L can be observed for the 5% flap at $\delta=50^o$. The effect starts to become more evident as the angle of attack increases and the Reynolds number decreases reaching a value of approximately 0.3 at $\alpha = 17^o$ and $Re = 0.6x10^6$, 0.2 at $\alpha = 17^o$ and $Re = 1x10^6$ and 0.17 at $\alpha = 18^o$ and $Re = 1.6x10^6$.

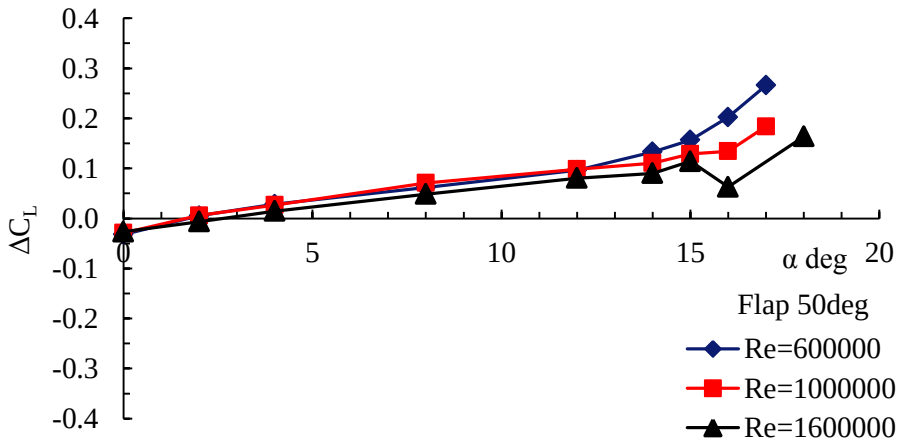

Figure 93: ΔC_L Vs α between the baseline and aerofoil-flap smooth configuration with no transition strip. Flap deflection angle $\delta=50^o$ over the range of Reynolds numbers.

Examining the flow characteristics of the configuration from the numerical analysis it can be seen that a similar separated region is observed behind the 5% flap as the 10% flap case. The magnitude of the recirculation area is however, smaller and the flow reattaches at approximately x/c = 0.2 as can be observed in Figure 93. This effect increases the leading edge thickness and the camber of the aerofoil leading to an increase in its C_{Lmax}. As the angle of attack increases the recirculation area becomes slightly smaller. This increase in camber and leading edge thickness enables the configuration to achieve better C_L characteristics than a plain aerofoil especially at lower Reynolds numbers and high angles of attack.

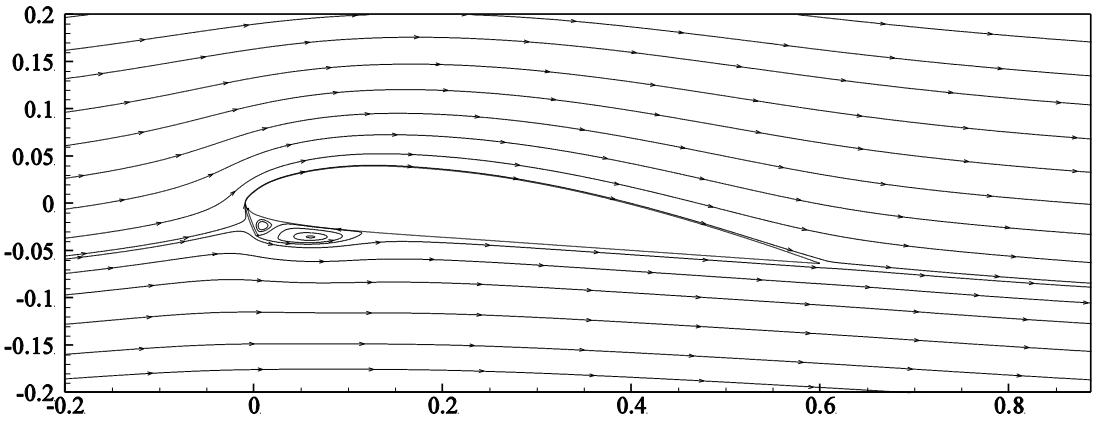

Figure 94: Streamlines of aerofoil and flap configuration at δ=50° and Re=0.6x10^6

Figure 95 summarises the ΔC_L between the baseline aerofoil and a configuration with a 5% flap at δ=80°. The trend followed is similar with what observed in the δ=50° case with the maximum values of ΔC_L slightly lower. During this deployment face, increases in the ΔC_{Lmax} value of 0.10 at α = 16° and Re = 0.6x10^6, 0.13 at α = 14° and Re = 1x10^6 and 0.15 at α = 18° and Re = 1.6x10^6 are noted. The angle of attack at which the flap starts to positively influence the C_L value for this configuration is approximately at α=5° for Re = 0.6x10^6 and between α=1° and α=2° for the other two cases. The magnitude of the recirculation area is slightly smaller in this case and the flow reattaches at approximately x/c = 0.12 (See Figure 96).

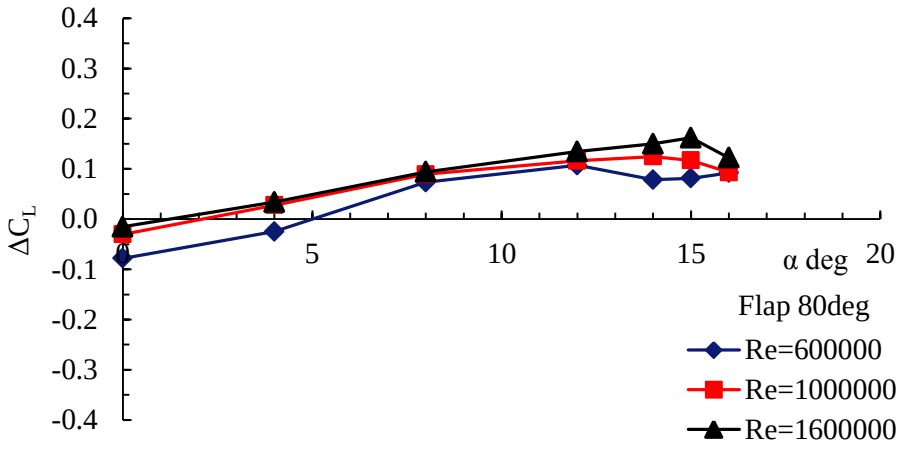

Figure 95: ΔC_L Vs α between the baseline and aerofoil-flap smooth configuration with no transition strip. Flap deflection angle δ=80° over the range of Reynolds numbers.

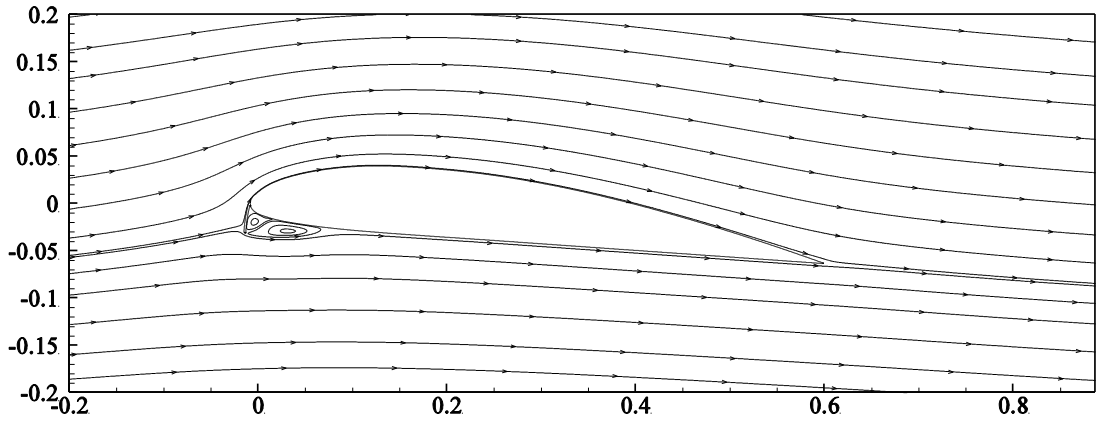

Figure 96: Streamlines of aerofoil and flap configuration at δ=80^o and Re=0.6x10^6.

The ΔC_L behaviour between the baseline aerofoil and the configuration with 5% flap at δ=90^o is outlined in Figure 97. The flap seems to behave in a similar manner at all Reynolds numbers with no significant difference between them. The angle α at which the flap starts to positively affect the configuration performance occurs slightly earlier in this case and it is observed closer to α=1^o. During this deployment phase increases in the ΔC_{Lmax} value of 0.11 at α = 17^o and Re = 0.6x10^6, 0.11 at α = 17^o and Re = 1x10^6 and 0.1 at α = 12^o and Re = 1.6x10^6 are noted.

A further decrease in the recirculation area is observed in comparison to the two previous cases and the flow reattaches at approximately x/c= 0.08.

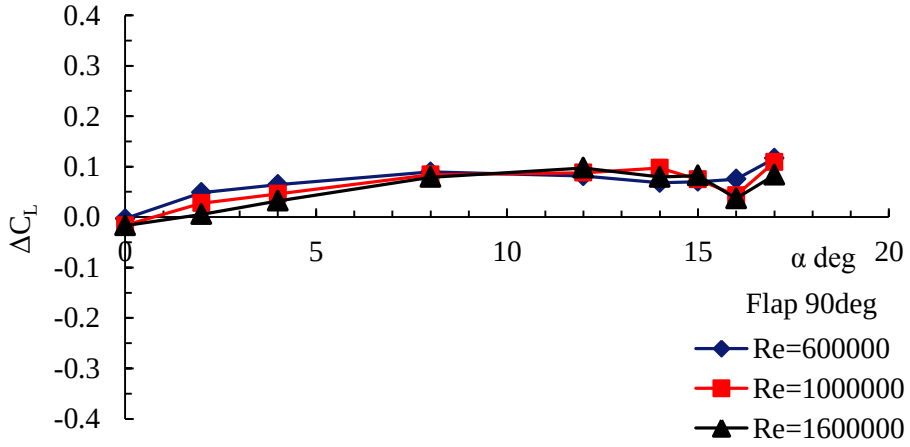

Figure 97: ΔC_L Vs α between the baseline and aerofoil-flap smooth configuration with no transition strip. Flap deflection angle δ=90^o over the range of Reynolds numbers.

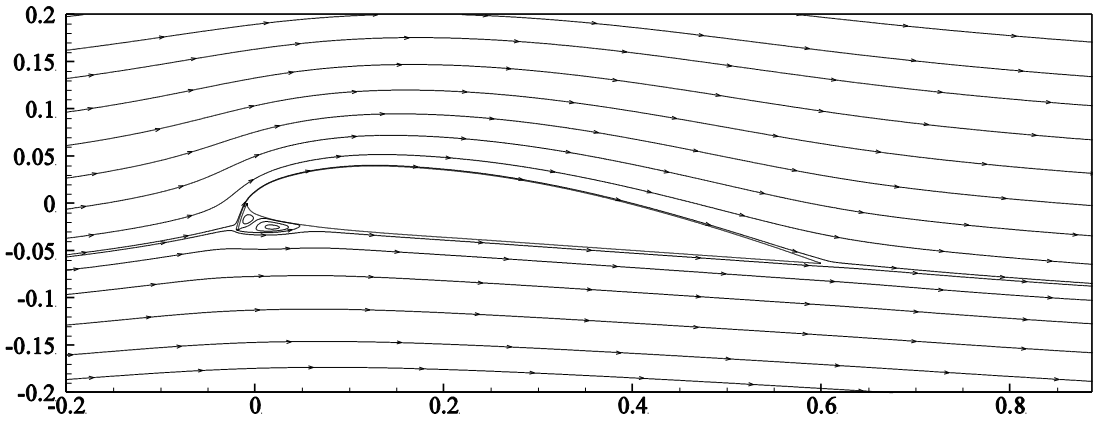

Figure 98: Streamlines of aerofoil and flap configuration at δ=90^o and Re=0.6x10^6.

7.7.1 Summary 5% flap case

In general, the implementation of the 5 % flap seems to increase the thickness and camber of the aerofoil thus allowing the configuration to stall at a later stage. This is more evident at δ=50^o. In addition, the gradient of the C_L graph increases resulting to a higher C_L for a given angle of attack. The increase in the camber also positively contributes in the configurations achieving higher C_{Lmax}.

Figure 99 presents the C_P for the three 5% flap configurations at α=14^o and Re =1.6x10^6. It can be seen that the magnitude of the recirculation area at the pressure side behind the leading edge flap is significantly smaller for the 5% flap than the 10% flap and barely noticeable for δ=80^o and 90^o. In addition, for the configuration with δ=80^o slightly larger separation area is observed at the trailing edge.

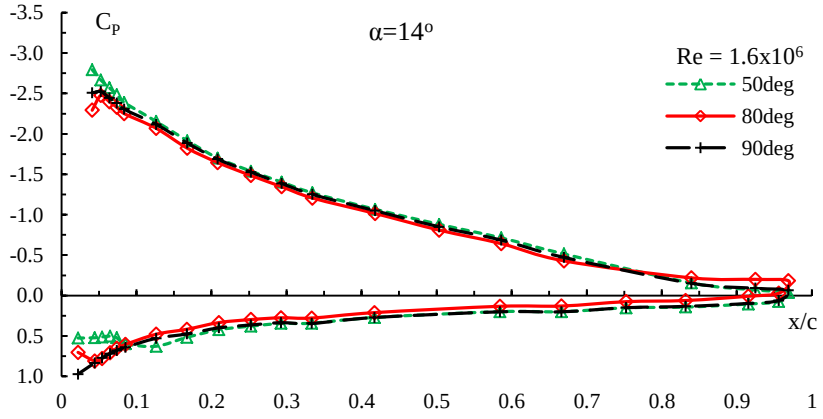

Figure 99: C_P plots for the 5% flap at δ=50^o, 80^o, 90^o, α=14^o and Re=1.6x10^6

7.8 Step and Transition strip Characteristics of the 10% and 5% flaps

The introduction of a Krueger flap alters significantly the aerodynamic behaviour of a baseline aerofoil. Results from published literature [28] to [108], but also from this study show that at high angles of attack, the aerofoil and flap configuration produces more lift and the flow remains attached longer when the flap is actually deployed, which also leads to an increase in the stall angle.

The characteristics of the configuration were observed with and without a smooth surface between the flap and aerofoil as well as with and without step. Figure 100, to Figure 102 summarise the experimental results obtained for the aerofoil and flap configuration at flap deflection angle $\delta = 110^o$ (this was selected as it is the angle at which best performance was found to be achieved by the 10% flap) for smooth (SM), smooth and transition (SM_TR), step and transition (ST_TR) and step with no transition (ST) surface conditions. This particular work helped to draw important information and data on how the specific surface discontinuity and transition strip affect the aerodynamic characteristics of the configurations examined.

The results are of great interest and are presented in the form of C_L plots. It can actually be seen that when the plasticine fillet is not utilised the configuration is not quite as efficient. It is observed, that at low angles of attack (in the linear region of the C_L graph), all configurations produce similar results. Close to stall angles, however, an increase in C_L of approximately 0.12 which translates to 12% can be obtained for configurations with smooth surface at $\alpha=16^o$. The respective increase at $Re=1x10^6$ and $Re=1.6x10^6$ is approximately the same (12%). Further observations show, that at low angles of attack this effect becomes less significant especially at higher Reynolds numbers. It was observed that the loss of lift was repeatable in all flap deflection angles for the 10% flap. The plots did not show any significant deviation between each other when a transition strip was used which can show that the flow is fully turbulent.

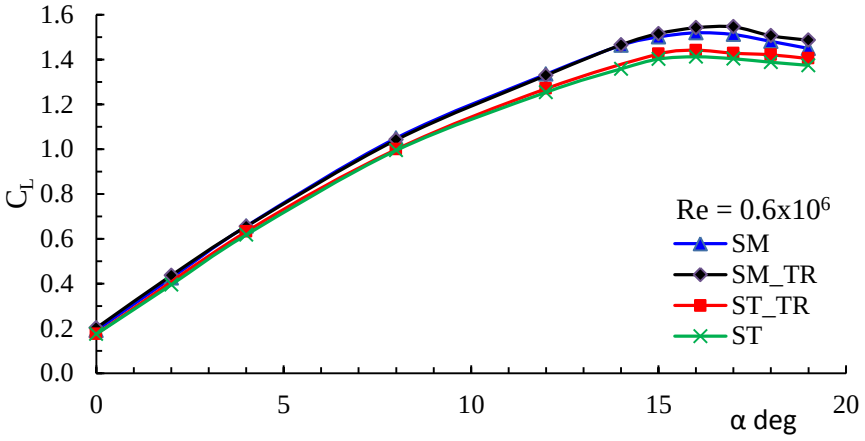

Figure 100: C_L plots of 10% flap at δ=110° and Re =0.6x10^6 for the four different configurations examined: Smooth (SM), smooth with transition (SM_TR), step with transition (ST_TR) and baseline

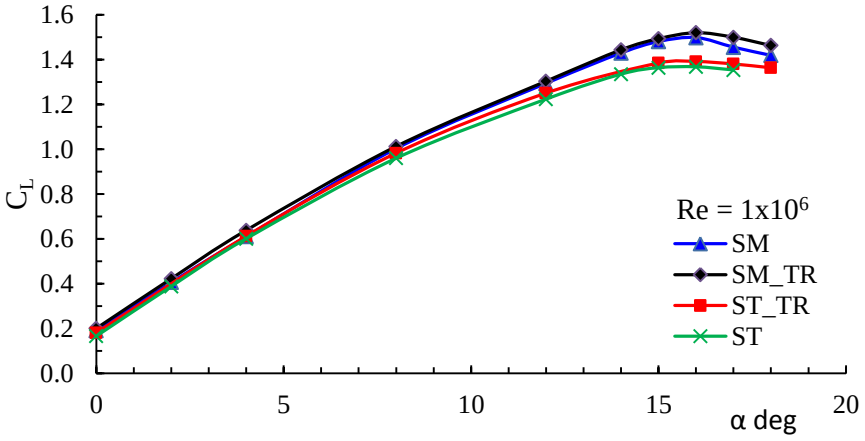

Figure 101: C_L plots of 10% flap at δ=110° and Re =1x10^6 for the four different configurations examined: Smooth (SM), smooth with transition (SM_TR), step with transition (ST_TR) and baseline.

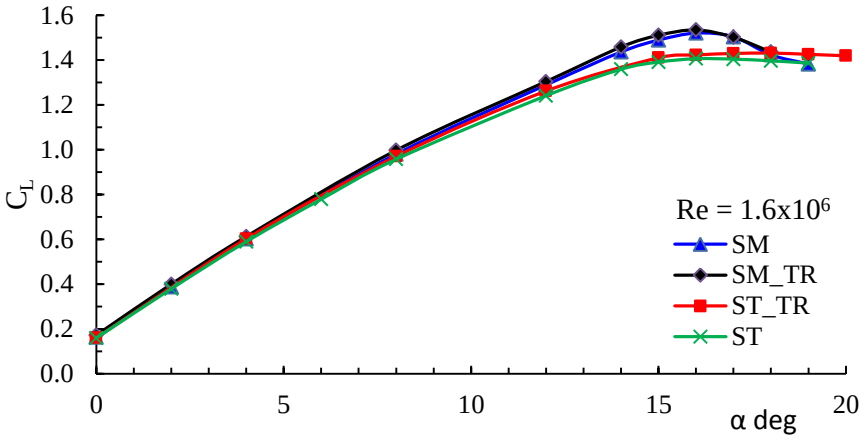

Figure 102: C_L plots of 10% flap at δ=110° and Re =1.6x10^6 for the four different configurations examined: Smooth (SM), smooth with transition (SM_TR), step with transition (ST_TR) and baseline.

The respective results for the 5% flap at $\delta = 50^o$ are presented in Figure 103 to Figure 105. It can be observed, that the effect of the step is not as significant as in the cases previously examined with the 10% flap. This is mainly due to fact, that at low flap deflection angles the surface contour between the flap and the main aerofoil element is already smooth and the discontinuity observed is not as significant as in the 10% flap case. An increase in the gradient of the graphs is observed in contrast to the baseline aerofoil which enables the configuration to produce better lift characteristics through most of the angles of attack for all 5% flap configurations. It seems that at low flap deflection angles, the step between the flap and the aerofoil is not as significant. The discontinuity in the geometry is not as severe and the lift is not affected to the same extend as in the case of the 10% flap.

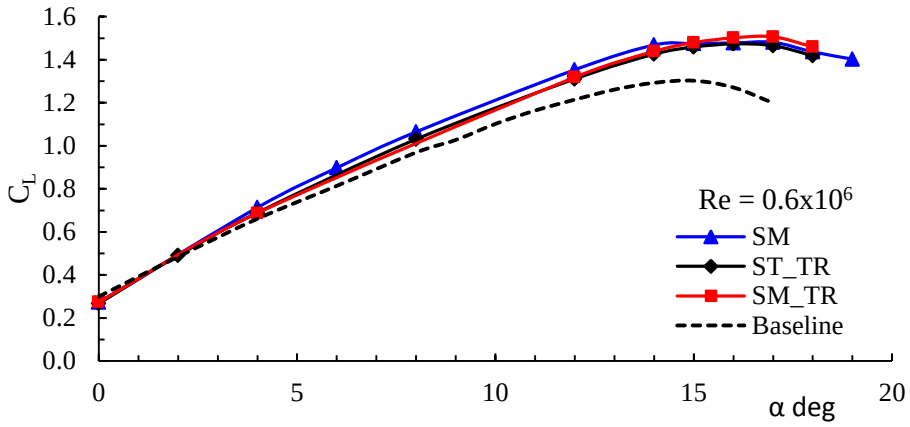

Figure 103: C_L plots of 5% flap at $\delta=50^o$ and Re =0.6x10^6 for the four different configurations examined: Smooth (SM), smooth with transition (SM_TR), step with transition (ST_TR) and baseline.

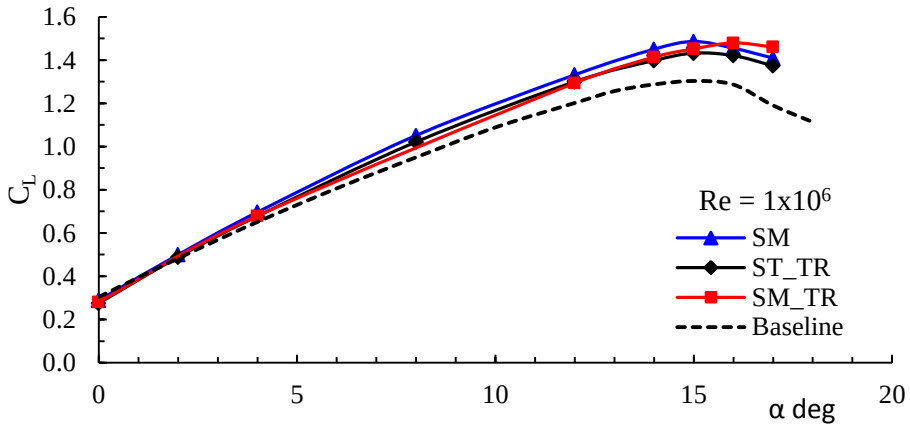

Figure 104: C_L plots of 5% flap at $\delta=50^o$ and Re = 1x10^6 for the four different configurations examined: Smooth (SM), smooth with transition (SM_TR), step with transition (ST_TR) and baseline.

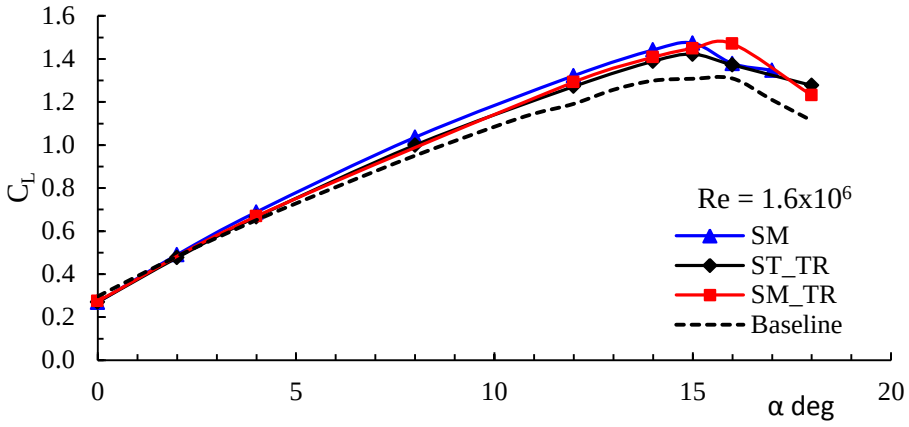

Figure 105: C_L plots of 5% flap at δ=50° at Re = 1.6x10^6 for the four different configurations examined: Smooth (SM), smooth with transition (SM_TR), step with transition (ST_TR) and baseline.

7.9 Effect of Reynolds Number, step and transition on the value of ΔC_{Lmax}

The effect of the Reynolds number, step and transition on the ΔC_{Lmax} are summarised and presented in Figure 106 to Figure 111 for all the configurations examined. These figures show the variation of ΔC_{Lmax} with Reynolds numbers for the different cases examined.

No significant difference in the value of ΔC_{Lmax} is observed with increasing Reynolds number for the 5% and 10% flap cases.

It can be seen however, that over the examined Reynolds number range, the configurations with a smooth geometry performed better and attained higher C_{Lmax}. This effect amounts to an increase between 8% - 12% in the value of C_{Lmax} in the case of the 10% flap, in contrast to a not as significant (2%-5%) effect with the 5% flap.

Assessing the results a trend is observed. It can in fact be seen that maximum lift coefficient is produced by the SM_TR case followed by the SM, ST_TR and then TR. The difference between the SM_TR and SM, is not as significant as the difference between SM_TR and ST_TR especially for the 10% flap.

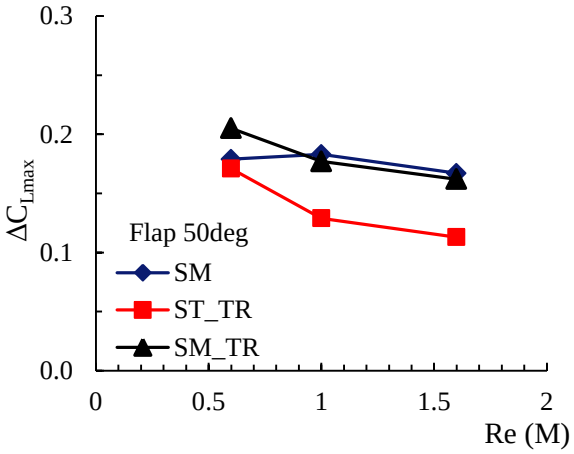

Figure 106: ΔC_L Vs Re number for the various cases examined at $\delta = 50^o$ for the 5% flap.

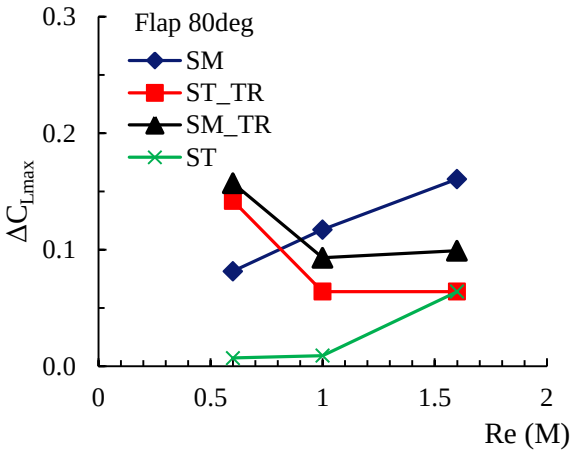

Figure 107: ΔC_L Vs Re number for the various cases examined at $\delta = 80^o$ for the 5% flap.

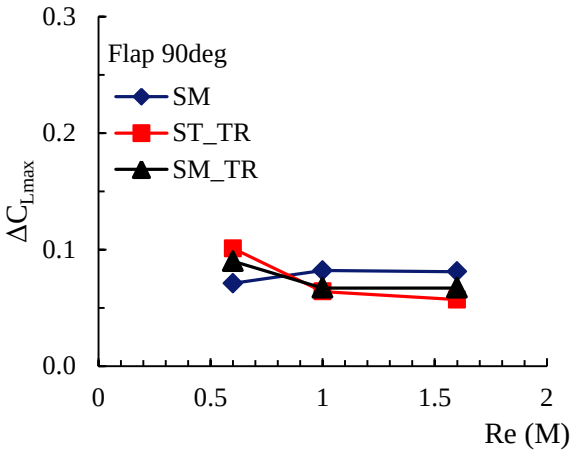

Figure 108: ΔC_L Vs Re number for the various cases examined at $\delta = 90^o$ for the 5% flap.

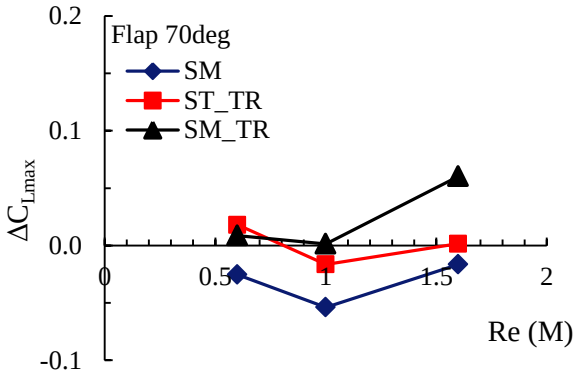

Figure 109: ΔC_L Vs Re number for the various cases examined at $\delta = 70^o$ for the 10% flap.

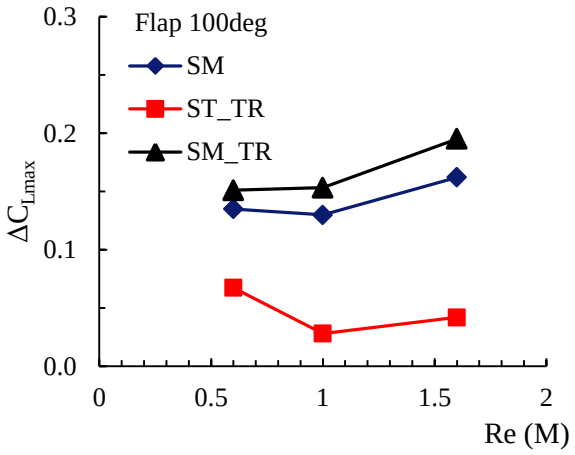

Figure 110: ΔC_L Vs Re number for the various cases examined at $\delta = 100^o$ for the 10% flap.

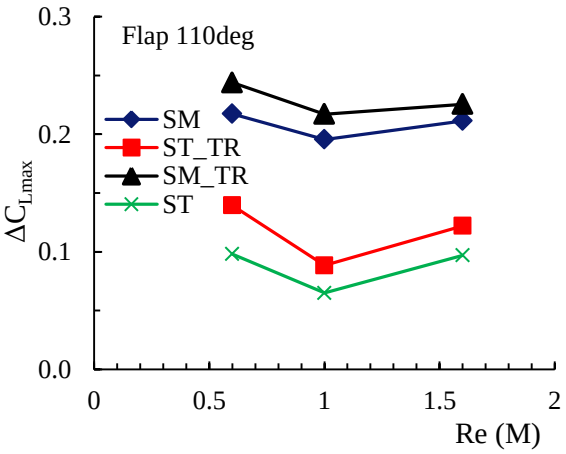

Figure 111: ΔC_L Vs Re number for the various cases examined at $\delta = 110^o$ for the 10% flap.

7.10 Analysis of C_P plots

Figure 181 to Figure 216 in APPENDIX G exhibit the full set of C_P plots obtained from the experimental analysis for the two most favourable cases with flap deflection angle $\delta = 110^o$ and 50^o for the 10% and 5% flap configurations respectively.

From these plots it can be seen that at low angles of attack, the C_P curves are almost identical and overlap for all cases (ST, ST_TR, SM, SM_TR). As the angle of attack increases, the SM_TR and SM configurations show more elevated C_P values in the suction side and a trailing edge separation is evident which however, gradually starts to propagate further upstream. In the case of the configurations with step, this separation is observed at lower angles of attack and propagates upstream faster thus reducing the lift produced, as well as the stall angle.

A direct comparison of the SM_TR and SM cases (see Figure 112 to Figure 114) shows that there is no significant difference in the two C_P plots. This identifies that there is no transition region on the main element of the configuration. The flow can therefore be assumed fully turbulent and thus a fully turbulent CFD model can be used for the prediction of the aerodynamic forces.

Comparing the plots in Figure 115 it can be seen that the 10% flap configuration with flap deflection angle $\delta = 110^o$ at $\alpha=14^o$ shows a trailing edge separation at x/c=0.6 for the ST_TR case and $Re=0.6x10^6$. For the same α, δ and Re this separation is evident at x/c=0.85 for SM_TR which corresponds to a 30% increase in the attached region. This value increases to 33% for $\alpha = 16^o$ (just before stall). Similar results obtained for the ST and SM cases, show separation points at x/c = 0.58 and 0.84 respectively, which correspond to an increase of 30% of the attached region. This behaviour is repeatable for all Reynolds numbers.

It is believed that as air passes above the leading edge it accelerates resulting in a loss of pressure. At lower pressures the air can separate more easily as it moves around the leading edge and it is therefore desirable for the curvature to be as less abrupt as possible. Similar observations were made by Williams in Ref [34]. The presence of the step can therefore, increase the possibility for separation, by introducing disturbances in the flow, which will propagate downstream and help the flow to separate at a point where the energy is not sufficient to keep the boundary layer attached. The fact that as the Reynolds number increases the effect of the step becomes less noticeable can provide evidence to sustain such statement.

It is noted that such differences are not evident for the configurations with the 5% flap, and this is mainly due to the fact that no similar discontinuities in the geometry contour are observed. In this case, all the graphs follow the same trends, with only minor deviations.

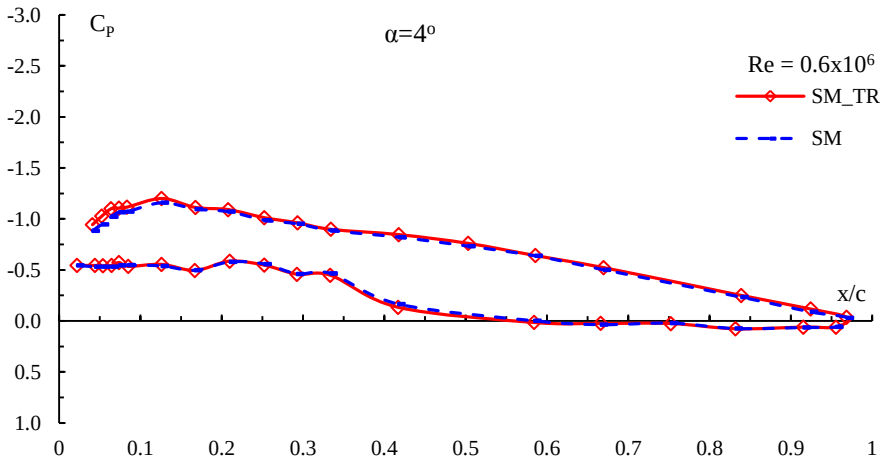

Figure 112. Exp C_p plots for SM_TR and SM, with $\delta = 110^o$ at Re=0.6x10^6 and $\alpha=4^o$.

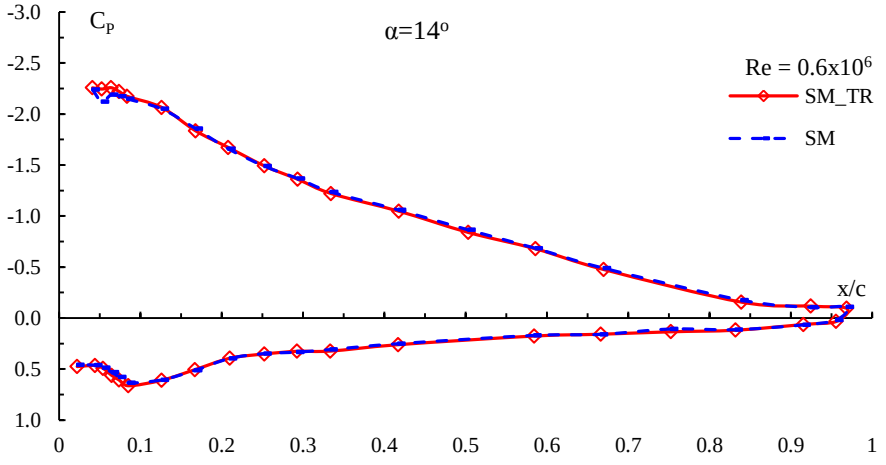

Figure 113. Exp C_p plots for SM_TR and SM, with $\delta = 110^o$ at Re=0.6x10^6 and $\alpha=14^o$.

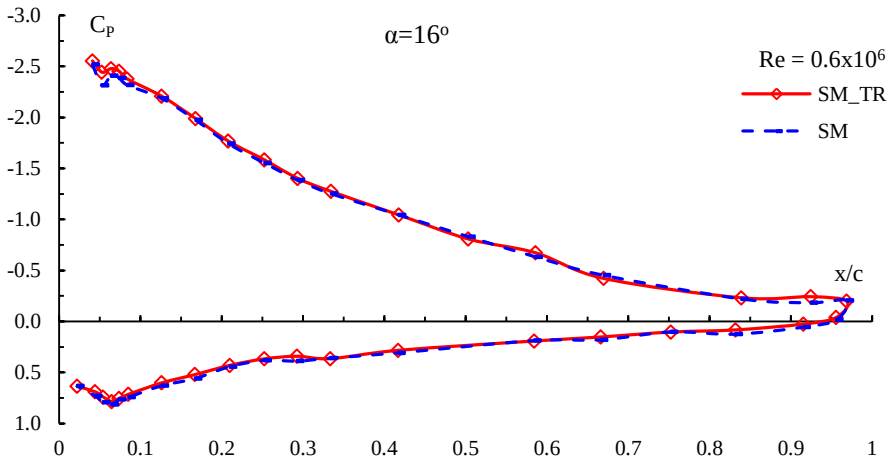

Figure 114. Exp C_p plots for SM_TR and SM, with δ = 110° at Re=0.6x10^6 and α=16°.

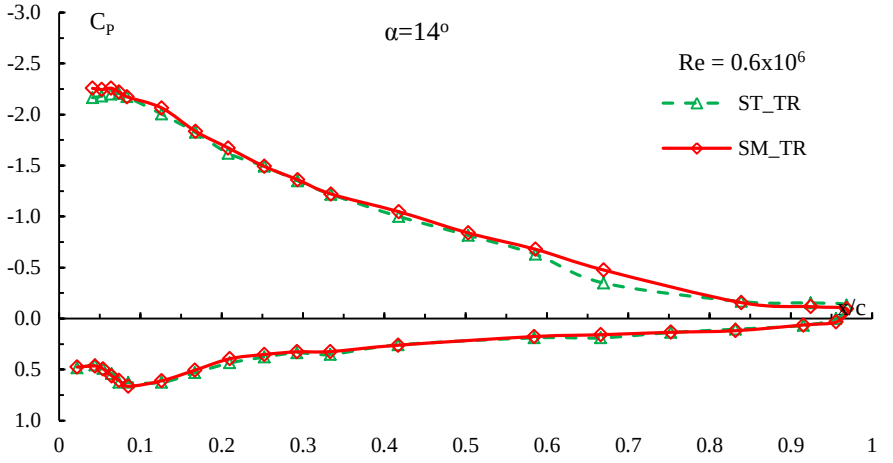

Figure 115. Exp C_p plots for ST_TR and SM_TR, with δ = 110° at Re=0.6x10^6 and α=14°.

7.11 The effect of step on Drag polar

The increase in the trailing edge separation area results in a slight increase in the drag coefficient as well as decrease in the lift coefficient. Analysis of the drag polar for the 10% flap (Figure 116 to Figure 118), shows higher lift coefficients and lower drag values at high angles of attack for the configurations with no step. It can be seen, that the maximum lift coefficient decreases and the minimum drag increases for the configurations where the step is obvious. This effect is repeatable for all Reynolds numbers for the 10% flap. No significant differences are observed between the different cases at low angles of attack, where the flow is attached over the suction side and the value of pressure drag is small.

For the 5% flap the effect of the step is almost non noticeable. This is mainly due to the fact that at flap deflection angles below $\delta=90^o$ the step between the two surfaces is barely evident. Furthermore, as the flap deflection angle decreases, the contour of the geometry between the flap and the aerofoil becomes even smoother. The polar drags for the 5% flap at $\delta = 50^o$, at which the C_{Lmax} is achieved, are shown in Figure 119 to Figure 121 where it can be seen that no significant difference is observed between the different cases examined.

In addition, by comparing the Cp graphs of the 5% and 10% flap configurations (see Figure 181 to Figure 216 in APPENDIX G), it can be seen that the recirculation area formed behind the flap (in the pressure side) is smaller for the 5% case. This effect as previously stated, decreases the value of the pressure drag thus justifying the slightly smaller values of total drag obtained for the 5% case, at low angles of attack. As the angle of attack increases, this area becomes smaller and the drag decreases. Observing Figure 116 to Figure 121 a sharper decrease in the C_D of the 10% flap is obtained in comparison to the 5% flap.

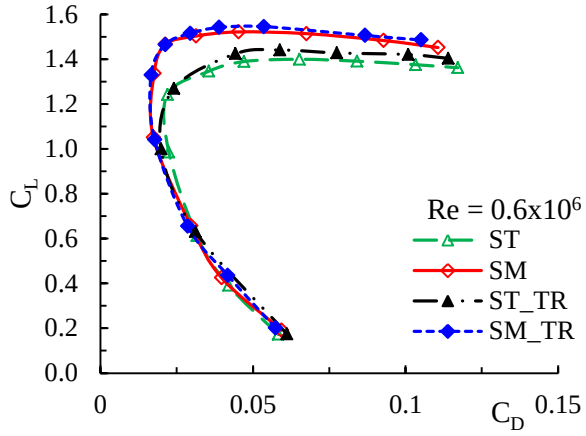

Figure 116. C_L Vs C_D plots for the four configurations examined with $\delta = 110^o$ at Re=0.6x10^6.

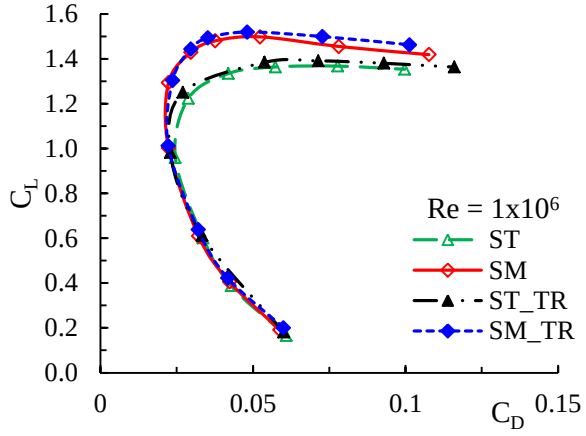

Figure 117. C_L Vs C_D plots for the four configurations examined with $\delta = 110^o$ at Re=1x10^6.

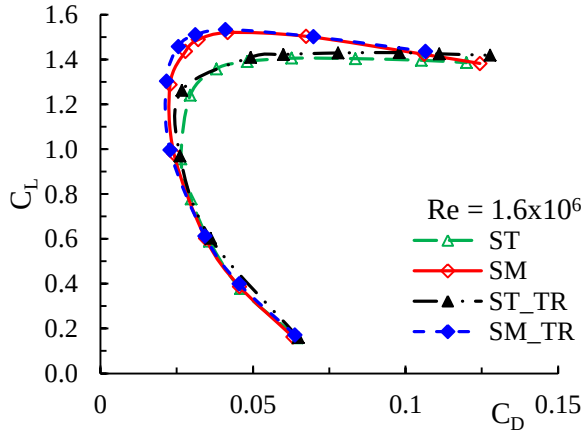

Figure 118. C_L Vs C_D plots for the four configurations examined with $\delta = 110^o$ at Re=1.6x10^6.

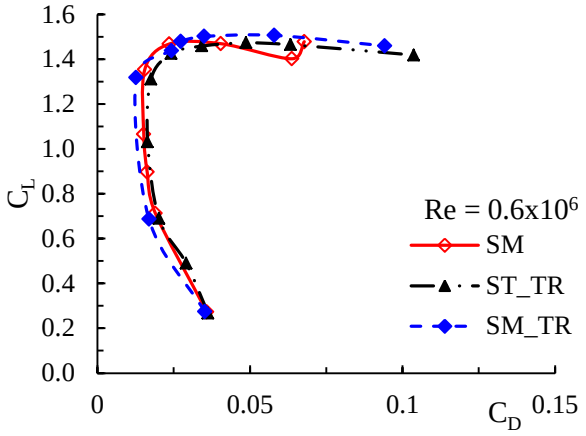

Figure 119. C_L Vs C_D plots for the four configurations examined with $\delta = 50^o$ at Re=0.6x10^6.

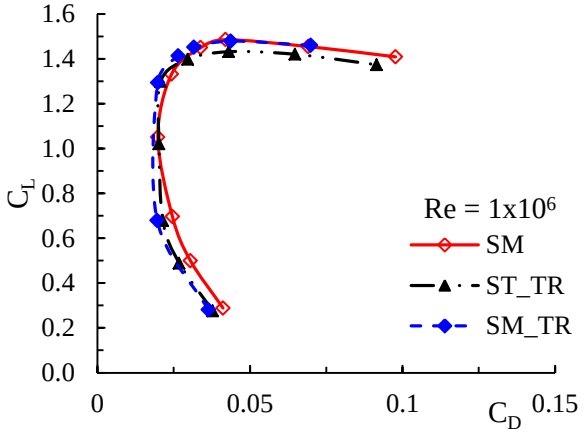

Figure 120. C_L Vs C_D plots for the four configurations examined with $\delta = 50^o$ at Re=1x10^6.

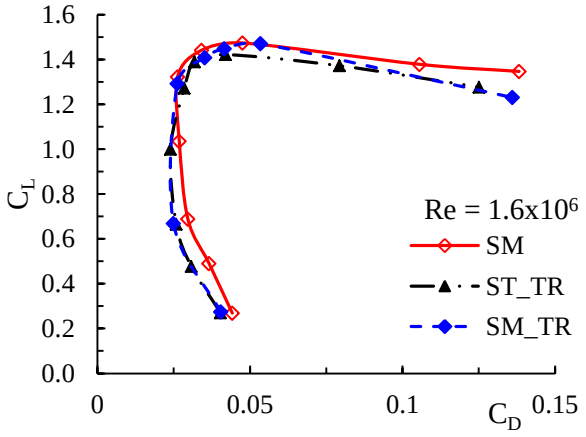

Figure 121. C_L Vs C_D plots for the four configurations examined with $\delta = 50^o$ at Re=1.6x10^6.

Figure 122 and Figure 123 illustrate the effect of the step and transition strip on the maximum and minimum value of C_L for the 10% and 5% flap respectively.

This analysis demonstrates the importance of the correct positioning of the flap. Even slight discontinuities in the profile contour can significantly alter the value of the maximum lift coefficient as well as the C_D and $(L/D)_{max}$ thus reducing the overall efficiency of the system. A decrease in the C_{Lmax} of 12% and an increase of C_D at C_{Lmax} of 14% can be observed in the results of the configurations with step. This translates to a 24% decrease in the value of $(L/D)_{max}$ between configurations with and without step.

In the 5% flap configuration the values of C_{Lmax} and C_D at C_{Lmax} show smaller variations and are in the range of 2-3%. The value of C_{Lmin} is approximately the same for all cases for both configurations.

The speed range ratio C_{Lmax}/C_{Dmin} and the efficiency of the configuration thus increase, when the step is not evident

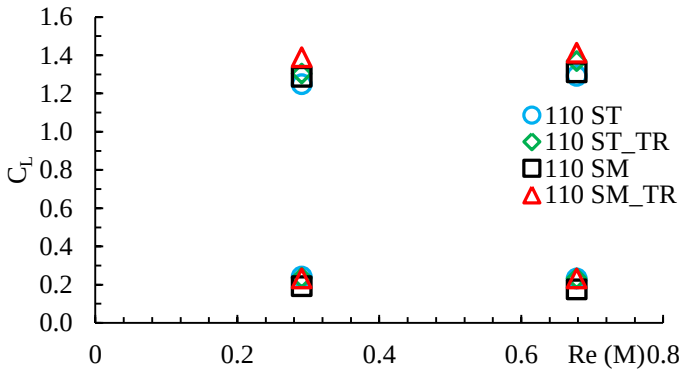

Figure 122: Comparison of C_{Lmax} and C_{Lmin} between the different configurations against Re number for the 10% flap.

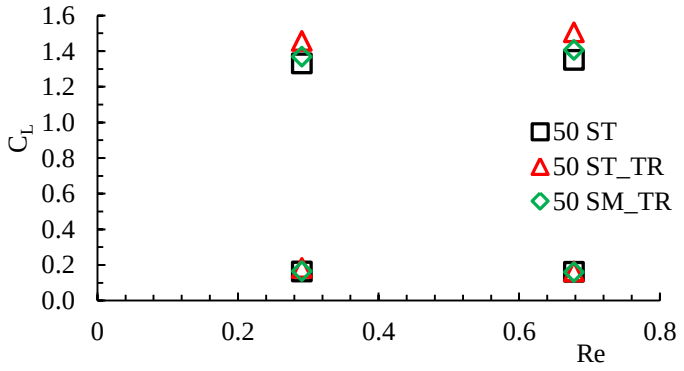

Figure 123: Comparison of C_{Lmax} and C_{Lmin} between the different configurations against Re number for the 5% flap.

7.12 Pitching moment Coefficient

A comparison of the section pitching moment data obtained from the experimental analysis performed in this work with and without the leading edge flap, illustrate that the addition of the flap causes the pitching moment coefficient to increase negatively with increasing angle of attack up until the point where the angle is high enough for the flap to become effective. Further increase to the angle α, results to a positive increase of the pitching moment coefficient until stall (see Figure 124 and Figure 125). This corresponds to the forward position of the aerodynamic centre with respect to the quarter chord point of the baseline aerofoil and is consistent with the fact that area has been added ahead of the leading edge of the baseline aerofoil due to the implementation of the flap.

The development of trailing edge separation at high angles of attack produces favourable nose down moments which could provide a build-in mechanism for passive self-recovery of a UAV.

A comparison of the results between the 10% flap and 5% flap configurations are illustrated in Figure 124 and Figure 125. It can be seen that the character of the pitching moment curves with the 5% flap and 10% flap deployed is about the same for both configurations. In general the graphs show that the magnitudes and the slopes of the curves of the 10% flap are slightly greater than those obtained for either the baseline aerofoil or the 5% flap.

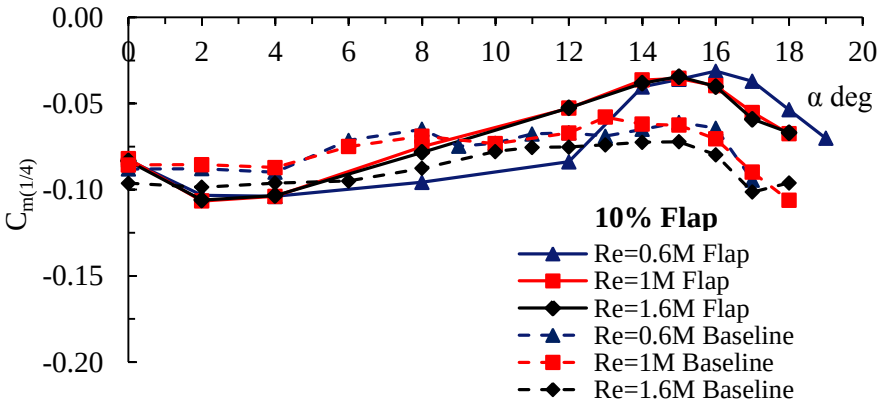

Figure 124: Comparison of $C_{m(1/4)}$ between the baseline Clark Y and a 10% flap configuration.

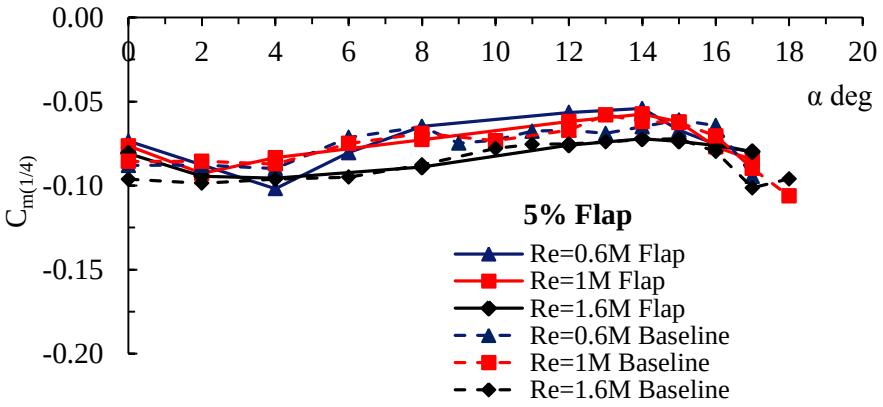

Figure 125: Comparison of $C_{m(1/4)}$ between the baseline Clark Y and a 5% flap configuration.

Chapter 8. Comparison of Experimental and Numerical Results for Leading Edge Flap

8.1 Aerodynamic characteristics 10% Flap

The requirement to establish detailed aerodynamic force and moment characteristics of the Krueger flap for use in a subsequent design, led to the development of a two-dimensional CFD model of the aerofoil-flap system. The following study aims to identify and quantify the forces and moments acting on a basic Krueger flap configuration, as schematically represented in Figure 126 below, and further to establish the deployment load (in the form of flap hinge moment) for either a shape alloy or passive design proposal.

Following the baseline CFD studies, a further set of 2D numerical studies were completed for a range of angles of attack α from 0^o to 18^o and a range of Krueger flap deflection angles δ range from 70^o to 110^o for each angle of attack case. A similar mesh and domain were used as for the baseline model investigation. The mesh was modified slightly and it was clustered in such a manner so as to accommodate the flow phenomena around the aerofoil. The Clark Y aerofoil and Krueger flap configuration shown in Figure 126 was used throughout this part of the investigation at Reynolds numbers of $0.6x10^6$, $1x10^6$ and $1.6x10^6$.

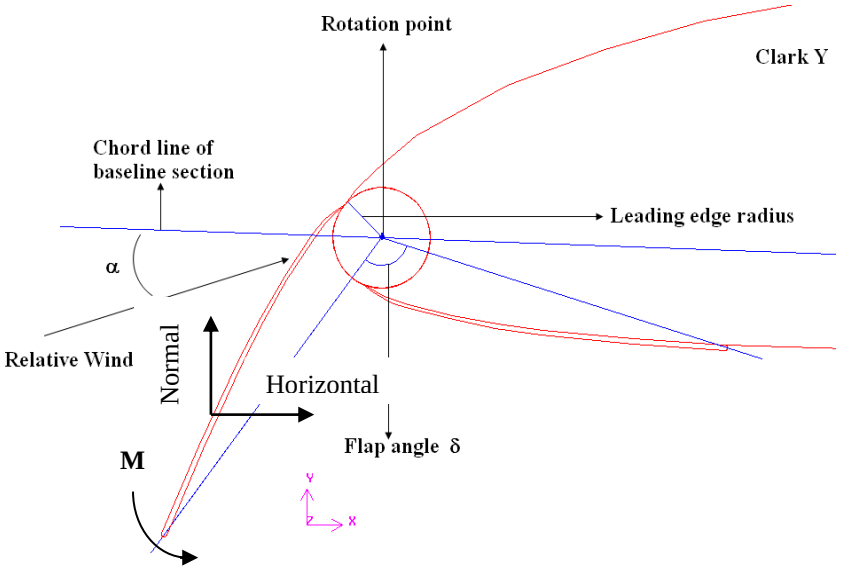

Figure 126: Schematic representation of the leading edge of the Clark Y aerofoil incorporating a leading edge Krueger flap.

A good agreement was observed for all the cases examined, between the experimental and numerical results, especially in the linear region. Results obtained from the numerical analysis of the aerofoil and flap configuration, were summarized and plotted against equivalent experimental results obtained from the Cranfield wind tunnel investigation as well as the baseline results for a plain Clark Y.

Figure 127 and Figure 128 represent a comparison between the experimental and numerical results as well as with the baseline Clark Y data, for the two most effective flap deflection angles δ, at two Reynolds numbers. Results indicate that the turbulence model k-ω SST does well in predicting the values of C_L and stall angle of the aerofoil-flap configuration. The experimental and numerical values are within 5% of each other and both demonstrate an increase in the lift coefficient of approximately 18%.

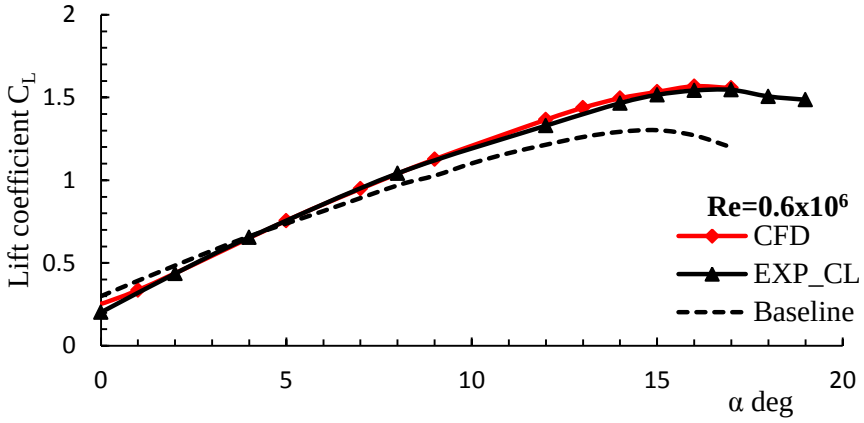

Figure 127: Experimental and numerical lift coefficient data for an aerofoil and flap configuration with δ = 110 at Re = 0.6x10⁶.

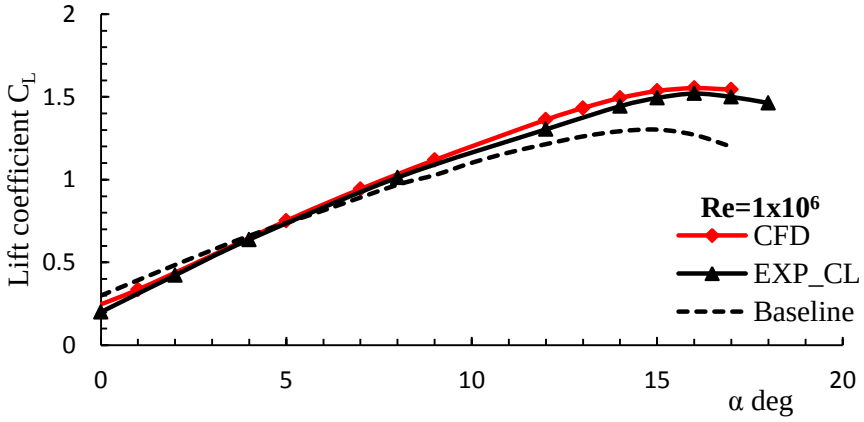

Figure 128: Experimental and numerical lift coefficient data for an aerofoil and flap configuration with δ = 110° at Re = 1x10⁶.

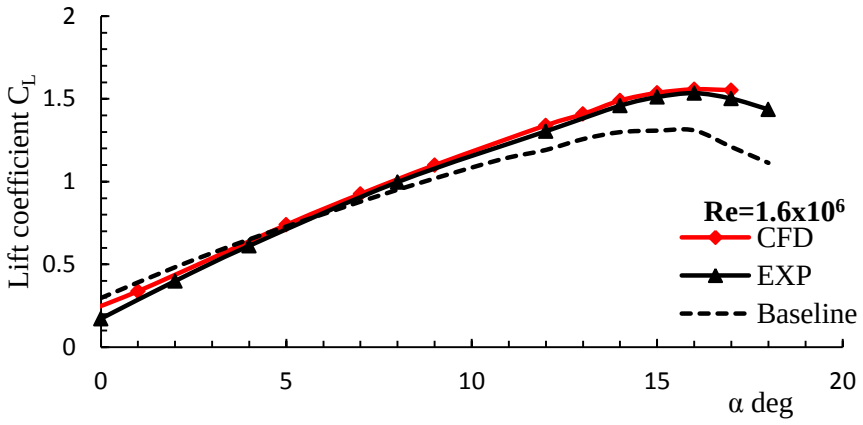

Figure 129: Experimental and numerical lift coefficient data for an aerofoil and flap configuration with $\delta = 110^o$ at Re = $1.6x10^6$.

Considering L/D from the CFD data, indicates an increasing trend between $0^o < \alpha < 12^o$ for $\delta = 70^o$ and 100^o, reaching $(L/D)_{max}$ of 50 and 58 respectively at $\alpha = 12^o$ and a progressive decrease in magnitude thereafter. A similar trend is observed for $\delta = 110^o$ reaching $(L/D)_{max}$ at of 61.5 at $\alpha = 9^o$. The numerical and experimental data are summarized and presented in Figure 132. The increment in C_L due to the introduction of the flap was predicted to within 5% by the computational simulation for the majorly of any given α and it is consistent with the trend identified from the wind-tunnel data.

Observing Figure 130 and Figure 131 which illustrate the coefficient of drag C_D versus the angle of attack α, it can be seen that in contrast with C_L higher differences are detected between the experimental and numerical results which affect the calculated values of L/D. The results follow a similar relationship with the experimental and are closely matched when the flow is aligned with the flap. Due to these higher discrepancies of the C_D value the L/D ratio produces differences of up to 35% between the experimental and numerical data.

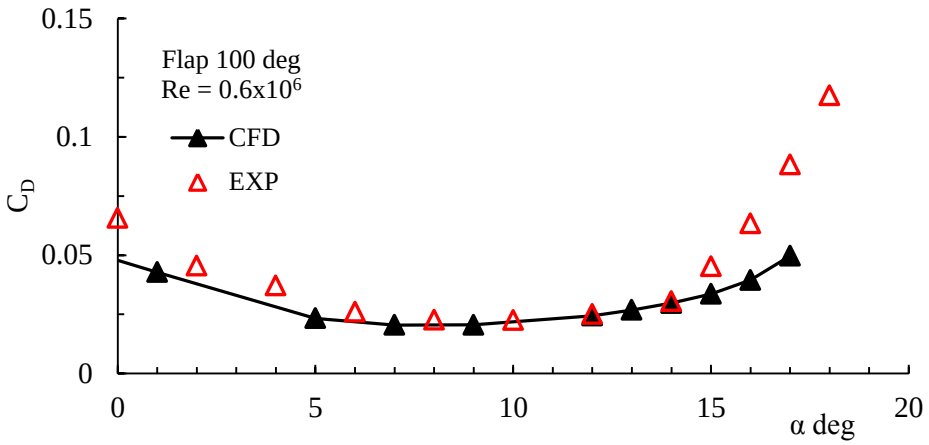

Figure 130: Experimental and Numerical drag coefficient data for an aerofoil and flap configuration at δ= 100° and Re = 0.6x10^6.

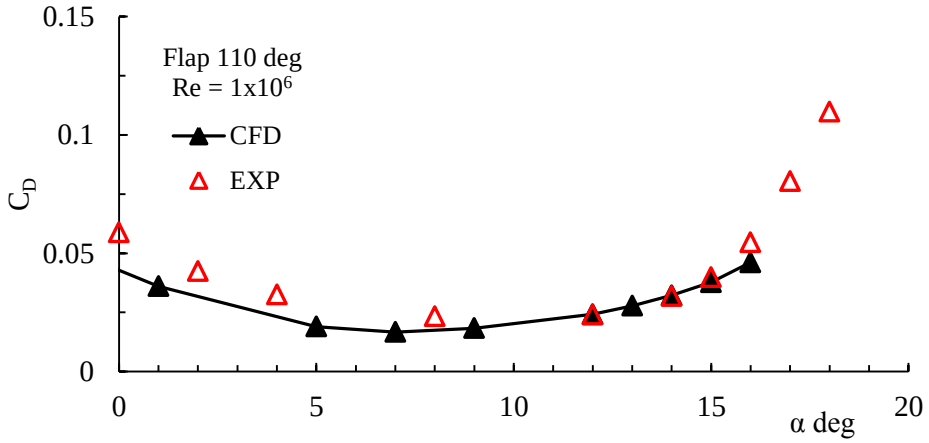

Figure 131: Experimental and Numerical drag coefficient data for an aerofoil and flap configuration at δ= 110° and Re = 1x10^6.

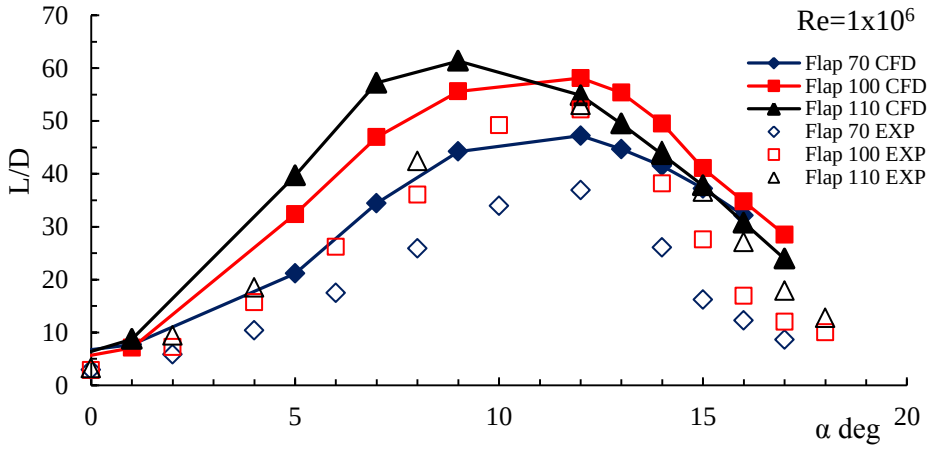

Figure 132: L/D plots for Re= 1x10^6 over the range of flap angle and angles of attack (in all flap configurations a smooth surface is assumed, for 10% flap).

8.2 Aerodynamic characteristics 5% Flap

A similar comparison was carried out for the 5% flap case. The studies were completed for a range of angles of attack α from 0^o to 18^o and a range of Krueger flap deflection angles δ varying from 50^o to 90^o for each angle of attack case. A similar mesh and domain were used as in the baseline models and the 10% flap cases. The mesh was modified to accommodate the slight difference in the leading edge geometry. Reynolds numbers of $0.6x10^6$, $1x10^6$, and $1.6x10^6$ were again used as previously.

Figure 133 to Figure 135 represent a comparison between the experimental and numerical lift coefficient values for the maximum flap deflection angle ($\delta = 90^o$) of the 5% flap configuration. The results indicate a good agreement and comparison between the experimental and numerical results. Again on average, the CFD solver (k-ω SST model) does well in predictions of C_L and stall angle of the configuration with the results within 5% of each other. The results obtained for the rest of the cases are of similar accuracy.

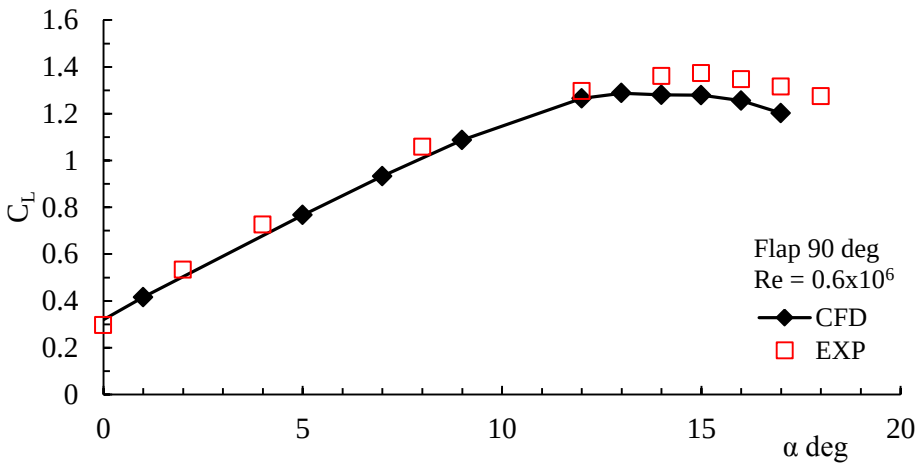

Figure 133: Experimental and Numerical C_L Vs α for the 5% flap configuration with $\delta = 90^o$ and Re = $0.6x10^6$.

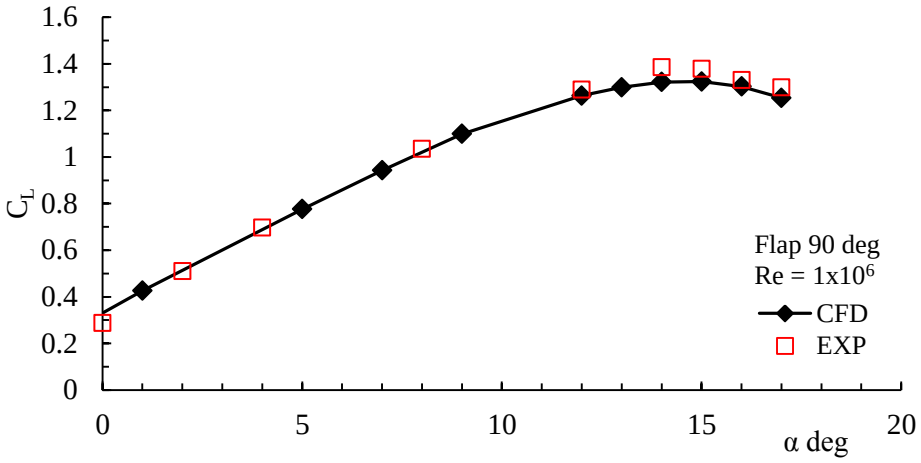

Figure 134: Experimental and Numerical C_L Vs α for the 5% flap configuration with δ = 90° and Re = 1x10⁶.

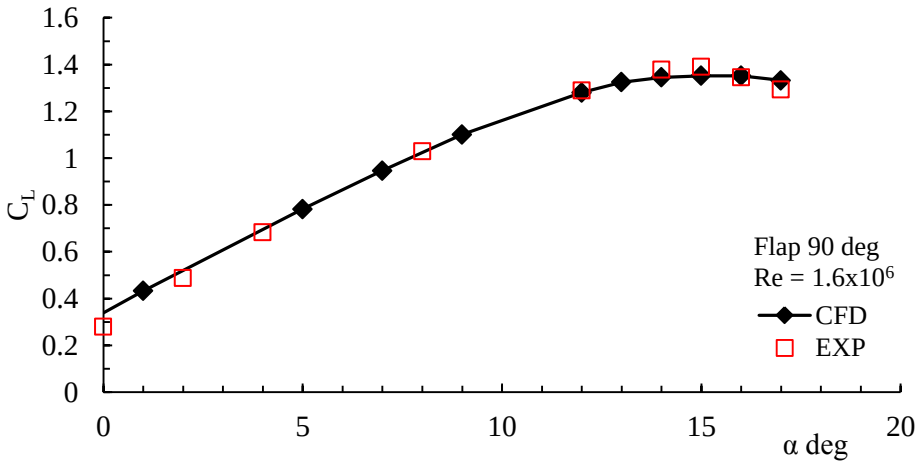

Figure 135: Experimental and Numerical C_L Vs α for the 5% flap configuration with δ = 90° and Re = 1.6x10⁶.

Considering L/D for the CFD data indicates an increasing trend for L/D between $0 < \alpha < 9$ for $\delta = 50^o$, 80^o and 90^o, reaching $(L/D)_{max}$ of 64, 61 and 56 respectively at $\alpha = 9^o$ and a progressive decrease in magnitude thereafter. The numerical and experimental data are summarized and presented in Figure 136. Similarly, as in the case of the 10% flap considerations, the increment in C_L attributed to the introduction of the flap was predicted to within 5% by the computational simulation for the majority of any given α and was found consistent with the trend identified from the wind-tunnel data. The values of L/D ratio exhibit a variation of ≈15% - 20% between the experimental and numerical data.

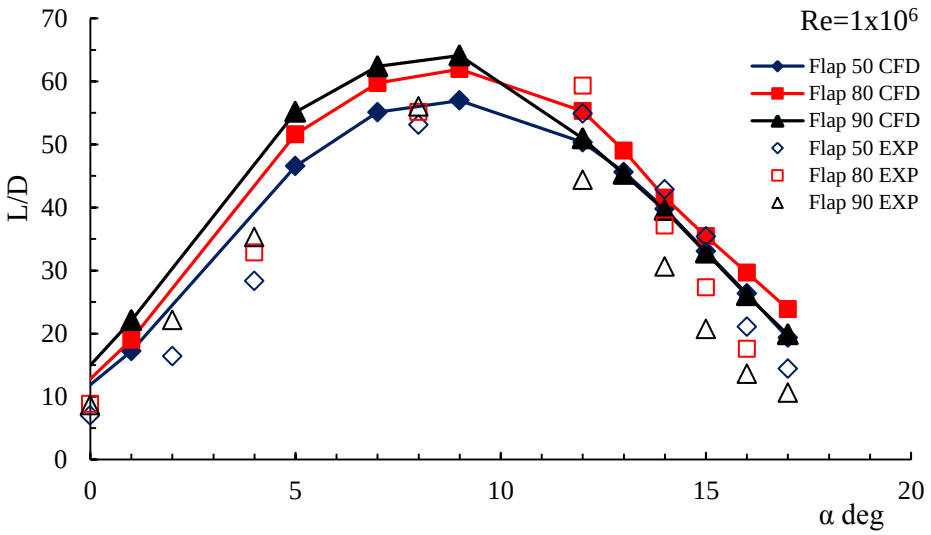

Figure 136: L/D Vs α plots over a range of flap angles and Re= 1x10^6 (5% flap and assuming a smooth surface in all flap configurations).

8.3 Drag Errors

Even though the numerical C_L value was predicted to within 5% of the experimental outcome it was noted that the C_D values exhibited higher deviations.

This can be attributed to:

a) The turbulence models which may under predict the values for C_D [109] and

b) Even with the presence of end-plates in the experimental procedure the flow may not be truly two dimensional [104], [111].

Palletier [111], showed that the presence of endplates for two dimensional aerodynamic testing could lead to errors in C_D. In his work he stated that an increase in C_D was caused by the presence of a corner flow and boundary layers growing on the end plates. Mueller and Jansen [102] also showed that even by accounting for the drag produced by the end plates, the interaction between the wing and the end plates can result in a 20% increase in C_D at low Reynolds numbers for an 18% thick aerofoil. These factors could justify the higher values of C_D obtained from the experimental tests as well as the differences observed in L/D and $C_L^{3/2}/C_D$. In addition, the effect of the aluminium blocks utilised to connect the flap with the end plates and to adjust the flap deflection angle was not accounted for. Also it must be noted that it is sometimes difficult to measure drag accurately because of the difficulty involved in measuring the very small in magnitude drag forces [112].

Finally, improvements in the relation between the numerical and experimental values of C_L for the different cases examined could be achieved, by creating and using a different mesh tailor-made for each angle of attack.

8.4 Forces 10% Flap

The individual components of the force acting on the Krueger flap were deduced and calculated from the numerical analysis and are presented in Figure 137 and Figure 138. These figures illustrate the Normal and Horizontal force components (also Figure 126) acting on the flap. It can be observed that both trends have similar but opposite characteristics. A pseudo-linear relationship describes the behaviour of the forces. The gradient of the graphs increases with the Reynolds number indicating a dependency of the behaviour of the force on the value of Re. Observing more closely, an increase of up to 90% of the force acting on the flap can be realized between Re=0.6x10^6 and 1x10^6 in each direction. Figure 138, illustrates the dependency of force F on the flap deflection angle δ from which it can be seen that with increasing α, ΔF is positive for the normal force and negative for the horizontal. Maximum forces are attained at high angles of attack and reach values of approximately 40 N at δ = 110^o and Re 1x10^6. A design envelop can thus be obtained from the graphs, to provide a working frame for the development of a passive design. The point of intersection between the two lines is where the flap actually starts to act positively in the value of C_L.

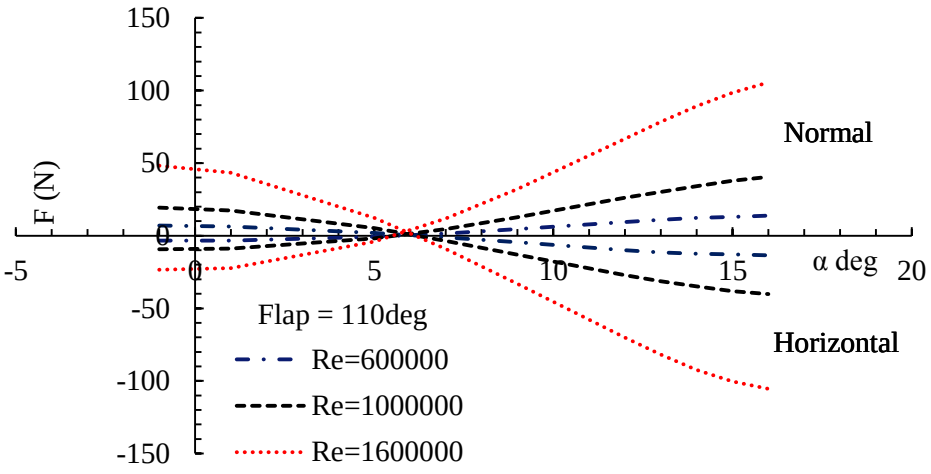

Figure 137: Normal and Horizontal Force components acting on a 10% flap with δ=110^o at three Reynolds numbers.

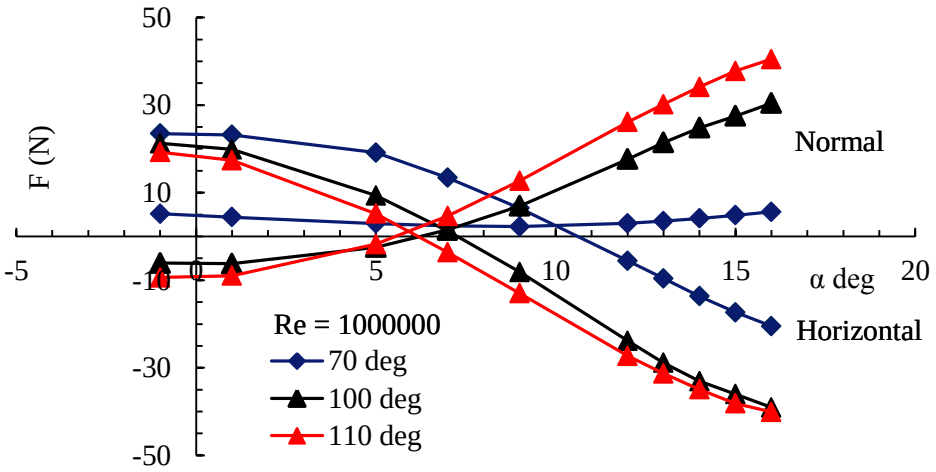

Figure 138: Normal and Horizontal Force on a 10% flap at various δ and Re = 1x10^6.

By isolating the normal force acting on the flap its effect can be assessed. This helps to identify how the flap influences and contributes to the creation of the overall aerofoil-flap configuration lift.

8.5 Moments 10% flap

The moments around the Krueger flap rotation point were also considered and calculated from the numerical analysis as an initial stage towards the design of a passive flap system. These moments are illustrated in Figure 139 and Figure 140 . It can be observed that ΔM with increasing α is negative in all cases where the magnitude of the ΔM/α gradient increases with increasing δ. Given that a moment still exists at zero lift conditions, this results in a number of α points where the moment is zero. Figure 141 shows a further plot of M vs δ for a series of α. Given this pseudo-linear relationship, in principle, it should be possible to design a simple passive flap deployment system based on a conventional speed loaded pulley and lever arrangement providing the angle of attack could be used to baseline load of the spring. Further design work is presented in the following chapter.

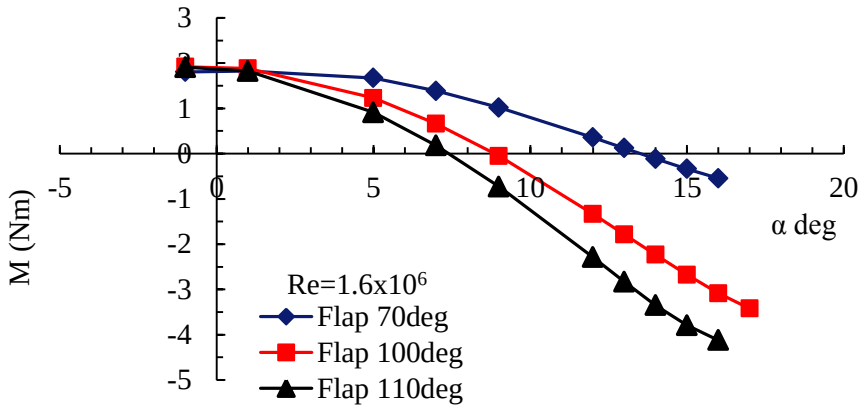

Figure 139: Moment (M) plots for Re = 1.6x10^6 over the range of flap angles and angles of attack.

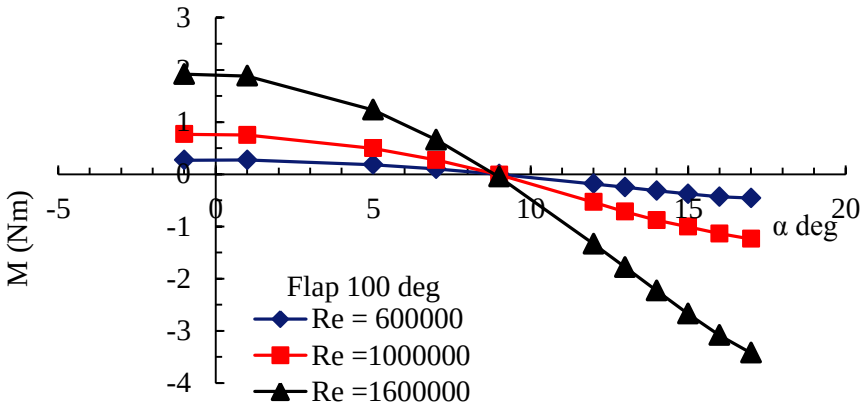

Figure 140: Moment (M) over a range of Re numbers for δ=100^o.

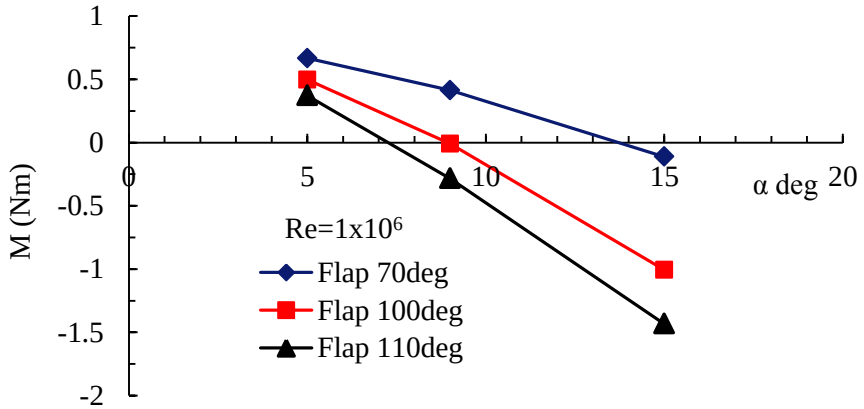

Figure 141: Moment (M) for δ =70^o, 100^o and 110^o for Re number 1x10^6 and fixed α.

A similar analysis was performed for the 5% flap also. Due to the similarity of the results with the 10% flap case however, the results and analysis are exhibited in APPENDIX I and only a direct comparison between the 5% flap and 10% flap is presented in this chapter.

8.6 Comparison of Moments between the 5% and 10% flap configurations

A more in depth comparison of the moments exerted on the two configurations was accomplished by comparing Figure 142 to Figure 144 which illustrate further plots of M vs δ for a series of angles of attack α and Reynolds numbers. It appears that both flaps exhibit the same trend with the 10% flap relatively being subjected to higher values of moments through the deployment phase. The value of ΔM is negative for all cases with increasing α. Also, it was observed that the magnitude of the ΔM/α gradient increases with increasing δ as well as increasing Reynolds number. The magnitude of the moment acting on the 10% flap configuration is significantly higher than that of the 5% flap. This is due mainly to the increase in length and flap deflection angle. The magnitude of moment is therefore depended on flap length. At higher δ's the normal force acting on the flap is significantly higher than the horizontal force thus producing higher moment values. As δ decreases the horizontal component of the force increases which has a reducing effect on the value of the moment.

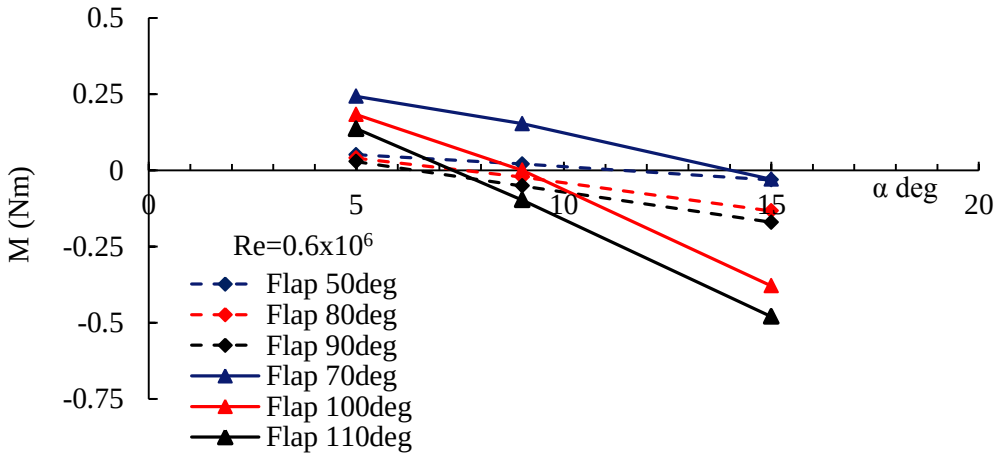

Figure 142: Moment (M) for the 10% flap at δ = 70°, 100° and 110° and for the 5% flap at δ = 50°, 80° and 90° at Re number 0.6x10^6 and fixed α.

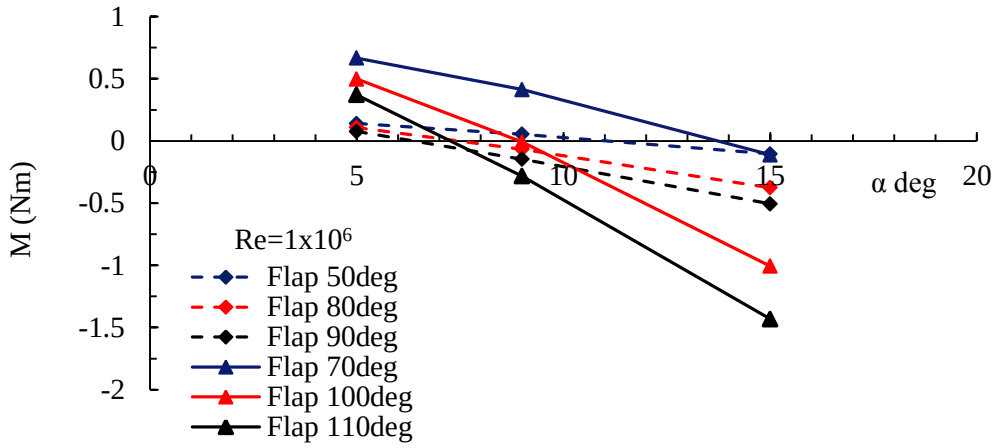

Figure 143: Moment (M) for δ = 70°, 100° and 110° for the 10% flap and δ = 50°, 80° and 90° for the 5% flap at Re number 1x10⁶ and fixed α.

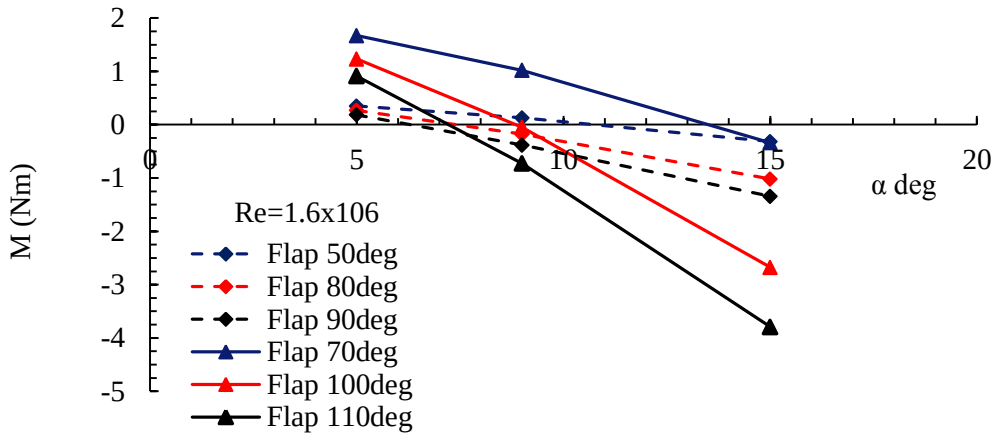

Figure 144: Moment (M) for δ = 70°, 100° and 110° for the 10% flap and δ = 50°, 80° and 90° for the 5% flap at Re number 1.6x10⁶ and fixed α.

8.7 Performance Comparison between 5% and 10% flaps

Figure 145 illustrates a comparison of the maximum lift coefficient obtained from each of the 5% and 10% flaps against flap deflection angle δ, at the three Reynolds numbers examined, for a smooth configuration with transition strip (SM_TS - doted lines) and smooth configurations with no transition strip (SM - continuous lines). It can be seen that the flaps behave in an opposite manner. The 5% flap achieves its maximum lift coefficient at low flap deflection angles whereas the 10% flap achieves its maximum lift coefficient at high flap

deflection angles. In general, it is observed that the configurations with transition strips achieve higher lift characteristics.

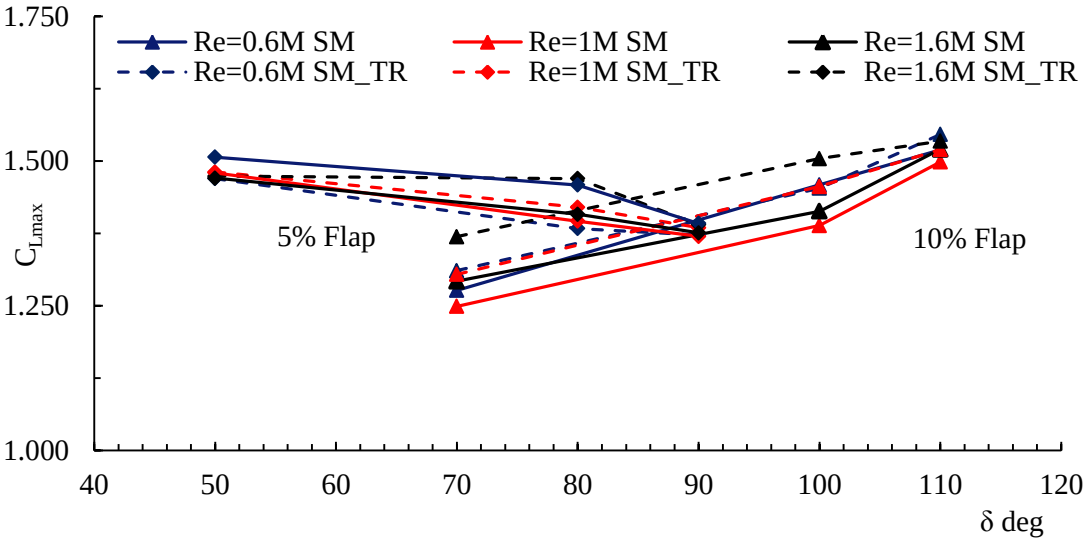

Figure 145: Maximum lift coefficient for the 5% and 10% flaps vs flap deflection angle δ at the three Reynolds numbers examined.

8.8 Evaluation of ΔC_{Lmax} and comparison with published data.

The plots in Figure 146 illustrate the expected increase in C_{Lmax} achieved as a result of implementing a leading edge Krueger flap versus the flap deflection angle, for both the 5% and 10% flaps. These plots can be compared with analogous results obtained from Fullmers experimental investigations (Figure 148) [113]. Even though the tests performed in Cranfield for this work and the ones from theory are at different Reynolds numbers and for different aerofoil sections their results can be compared and conclusions can be drawn on the outcome of each case. In both cases (Fulmer's and Cranfield) the aerofoils are equipped with a 10% flap and similar trends can be seen after observing the two figures (Figure 146 and Figure 148). An exponential increase in the ΔC_{Lmax} up to approximately $\delta=110^o$ for the Clark Y, and $\delta=120^o$ for the NACA 64_1-012 can be seen. The maximum ΔC_{Lmax} ranges between 0.23 to 0.26 at $\delta=110^o$ for the three Reynolds numbers examined and the corresponding value for the NACA case is approximately 0.175 at $\delta=120^o$. A decrease in the values is observed thereafter for both sets of results. The similarity of the two sets of data provides confidence for the

accuracy of the results. In contrast to the 10% case a decrease in the ΔC_{Lmax} with increasing δ is observed for the 5% flap. In this case maximum ΔC_{Lmax} is achieved at lower flap defection angles ($\delta=50^o$) and the values range between 0.16 to 0.2 for the three Reynolds numbers examined. There are no available results in published literature for the 5% flap for a similar comparison to be made. It should be noted however, that for both flaps studied, the maximum ΔC_{Lmax} is achieved for the lower Reynolds number conditions examined.

8.9 Effect of Flap on Stall angle

The increments of the stall angle have been plotted versus the flap deflection angle and compared against results from published literature. Figure 147 shows maximum increase in stall angle of 2^o and this is achieved for the 5% and 10% flap at $\delta = 50^o$ and 110^o respectively at $Re = 0.6x10^6$. Comparing these results with values obtained from published literature (Figure 146 and Figure 147 with Figure 148) it can be seen that they follow similar trends. An increase from zero to two is observed for the 10% flap for $\delta=70^o$ to 110^o and a decrease thereafter. In contrast an opposite trend is observed for the 5% flap with the configuration achieving maximum values at δ=50%. Results from this work, however, show a more positive increase in the stall angle of 2^o, whereas the results from published literature show an increase of approximately 1^o at $\delta = 120^o$.

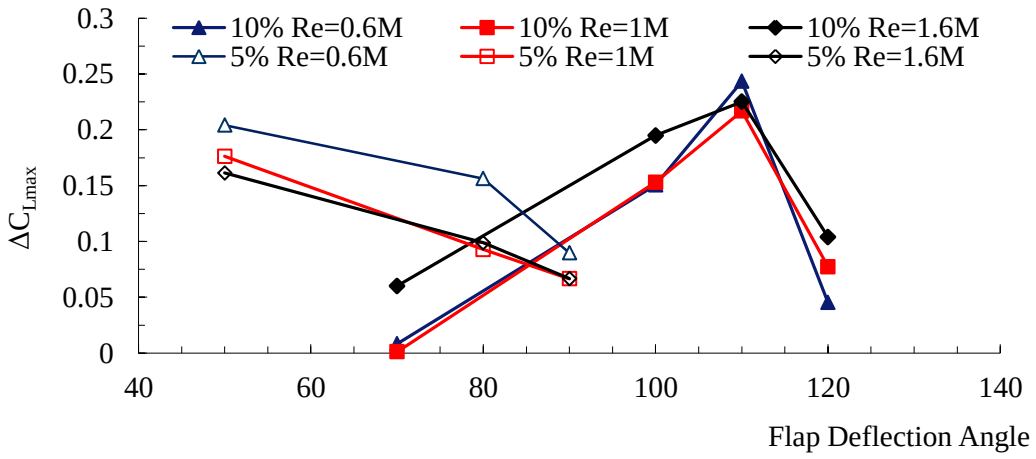

Figure 146: ΔC_{Lmax} for the 5% and 10% flaps vs flap deflection angle δ at the three Reynolds numbers examined.

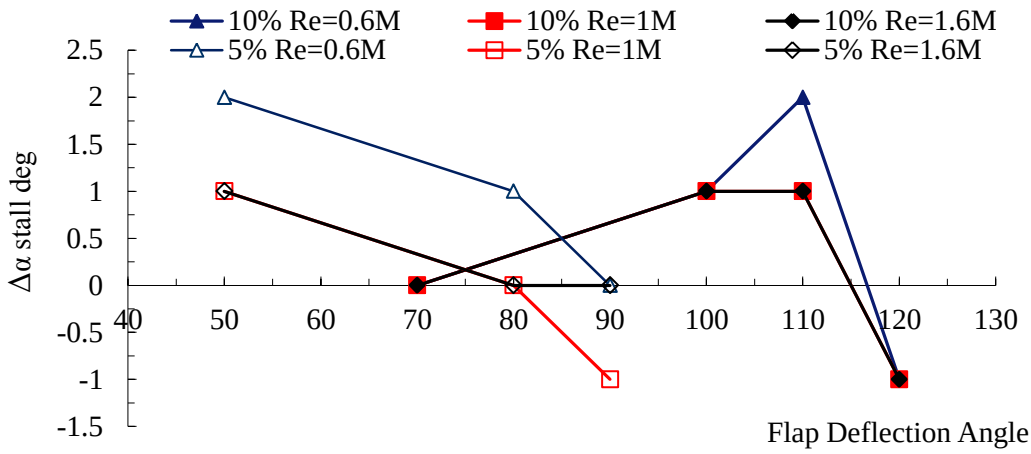

Figure 147: Δα stall for the 5% and 10% flaps vs flap deflection angle δ at the three Reynolds numbers examined.

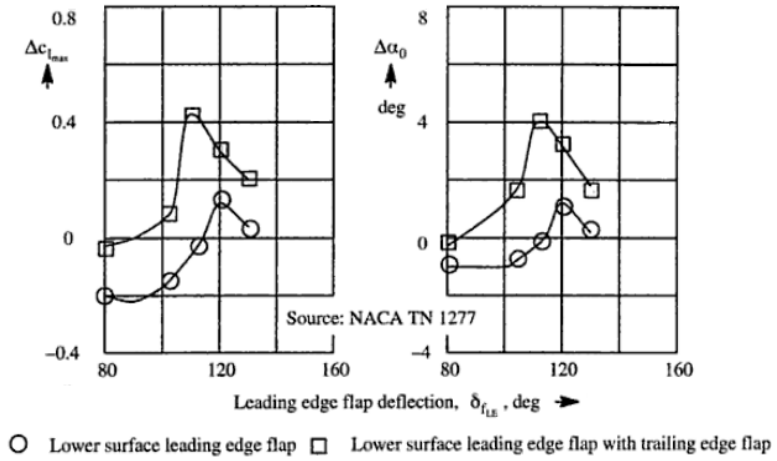

Figure 148: Published results of ΔC_{Lmax} and Δα stall for a 10% flap vs flap deflection angle δ.

8.10 Effect on UAV performance

Assuming that a UAV only loses weight via fuel consumption, there are defined takeoff and landing weights, with corresponding coefficients of lift. Using the Braguet equations [81] for propeller powered aircraft that assumed steady level flight, the Range and Endurance equations are:

$$R = \frac{\eta}{c}\frac{C_L}{C_D}\ln\left(\frac{W_0}{w_1}\right)$$

$$E = \frac{\eta}{c}\frac{C_L^{3/2}}{C_D}\frac{\sqrt{2\rho_\infty S}}{\sqrt{W_1}-\sqrt{W_0}}$$

These equations serve well for estimates for the true range or endurance of a UAV and even though they include certain assumptions, they do provide a good basis for reference [114].

For a given mission, the parameters of the above equations are constant, apart from the lift and drag. It can therefore be seen that the range is directly related to (C_L/C_D) and the endurance to $C_L^{3/2}/C_D$. In addition, the landing distance is related to C_{Lmax} and C_{Lmin} (see Chapter 9 for a more detailed analysis). It is therefore important to determine how these values vary with Reynolds numbers. Figure 149 to Figure 152 show the behaviour of C_{Lmax}, C_{Lmin}, and $(C_L^{3/2}/ C_D)_{max}$ as a function of Reynolds number for configurations with different flap angles.

Figure 149 presents a comparison of the C_{Lmax} for the 5% and 10% flap configurations at different flap deflection angles in relation to the C_{Lmax} obtained from the plain Clark Y. Apart from only one case (10% flap at $\delta = 70^o$) the results show a significant increase in the lift coefficient and its noted, that the higher values of C_{Lmax} are observed at lower Reynolds numbers.

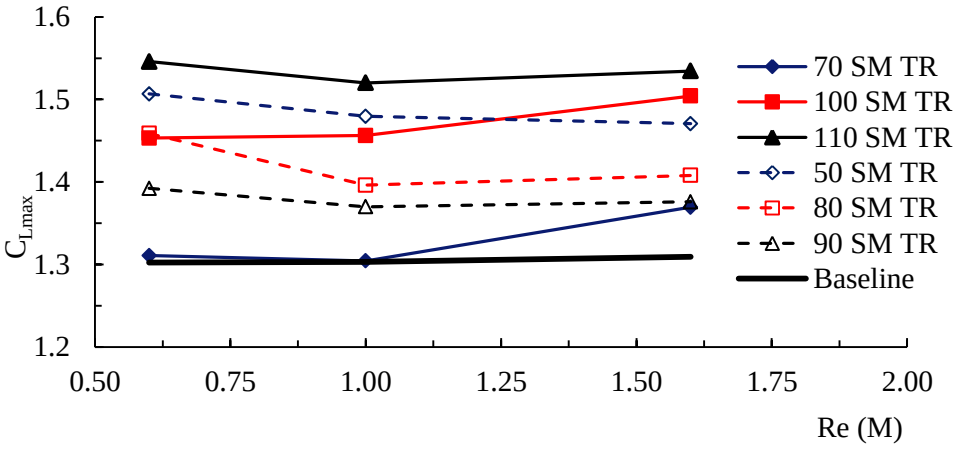

Figure 149: Behaviour of the C_{Lmax} Vs Reynolds number for the different configurations in relation to the baseline aerofoil.

Figure 150 presents a similar comparison but for the C_{Lmin}. All configurations produce lower values of C_{Lmin} with the 10% flap performing the worst. These values however, are achieved at low angles of attack at which point the flap will still be in the nested position during flight. The C_{Lmin} of the configuration will thus be comparable to the C_{Lmin} of the plain Clark Y aerofoil.

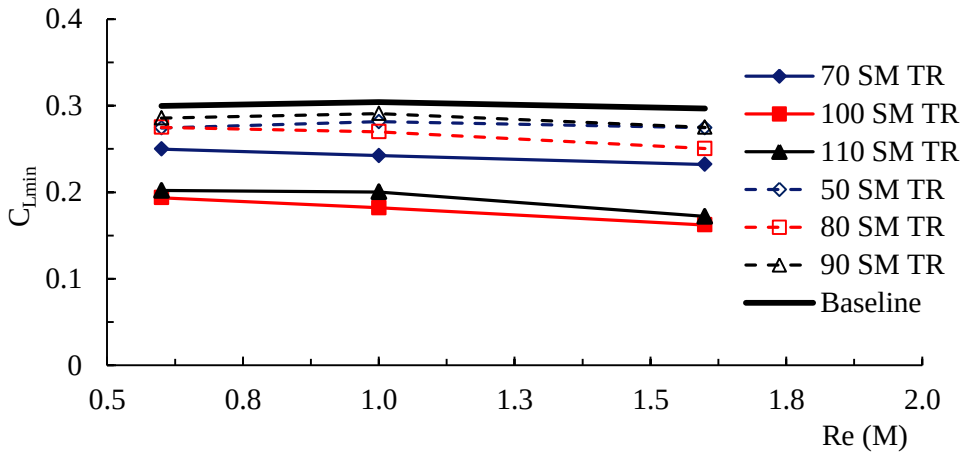

Figure 150: Behaviour of the C_{Lmin} Vs Reynolds number for the different configurations in relation to the baseline aerofoil.

The values of C_{Dmin} for the baseline configuration are lower than those of aerofoil and flap. Not surprisingly the C_{Dmin} for the configurations with a flap is not observed at $\alpha = 0^o$ but at the angle where the incoming flow aligns with the leading edge flap (that is, between 7^o to 8^o and 11^o to 13^o for the 5% and 10% flap, respectively). As however stated before, the flap will not be deployed at low angles of attack, it follows that C_{Dmin}(aerofoil-flap)= C_{Dmin} (Clark Y). Keeping this in mind thus shows, that the implementation of the flap enhances and increases the speed range ratio (C_{Lmax}/C_{Dmin}).

Figure 151 illustrates, experimental values of $(C_L^{3/2}/ C_D)_{max}$ for the 10% flap configuration and baseline model versus flap deflection angle for the different Reynolds number examined while Figure 152, similarly illustrates the numerical results.

From these figures, it is evident that implementation of the flap significantly increases the $(C_L^{3/2}/C_D)_{max}$ of an aerofoil-flap configuration, thus increasing its endurance. Results from the experimental analysis indicate a max increase of 61% is achieved at $\delta=110^o$ and Re $=0.6x10^6$

between the baseline model and the aerofoil-flap configurations. Likewise CFD results show an analogous increase of 66% while both sets of results follow similar trends.

This effect can therefore result to an increase of the load capacity and flight time as well as enable the UAV to fly at higher altitudes and to achieve better fuel consumption.

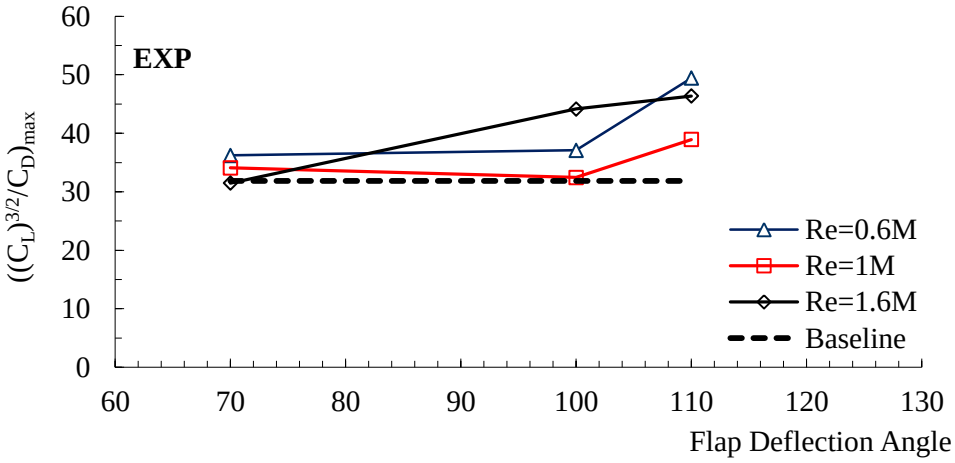

Figure 151: Experimental values of $(C_L^{3/2}/C_D)_{max}$ for 10% flap versus flap deflection angle for the different Reynolds numbers examined.

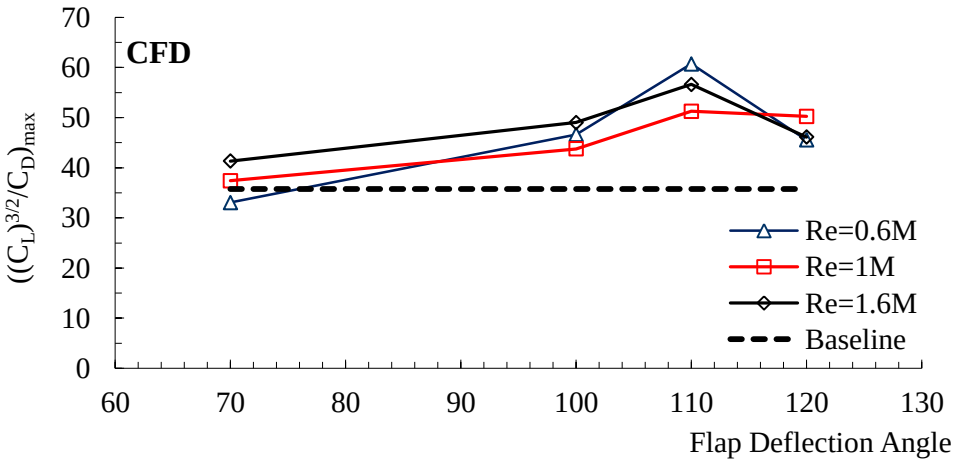

Figure 152: Numerical values of $(C_L^{3/2}/C_D)_{max}$ for 10% flap versus flap deflection angle for the different Reynolds numbers examined.

8.11 Concluding Remarks

Analysis of the experimental and numerical results indicates that the aerodynamic characteristics of aerofoil and leading edge flap configurations are superior to those of a plain aerofoil, especially the values of lift to drag ratio and maximum lift coefficient. The ΔC_{Lmax} shows a slight increase at low Reynolds number conditions. The same behaviour was obtained for $(L/D)_{max}$ and $(C_L^{3/2}/ C_D)_{max}$. On the other hand, C_{Dmin} showed a slight increase with decreasing Reynolds number. The maximum L / D generally occurred at $\alpha = 7^o$ to 8^o for the 5% flap and $\alpha = 11^o$ to 13^o for the 10% apart for $\delta=110^o$ where it was observed close to $\alpha = 9^o$. The values of $(C_L^{3/2}/ C_D)_{max}$ were observed at similar ranges.

In general the 10% flap attains higher C_L values than the 5% flap with the exception of the configuration with $\delta=70^o$. At low angles of attack between $\alpha=0^o$ and 12^o the 5% flap has slightly better lift and lift to drag (L/D) characteristics. This behaviour could lead to a combined deployment design arrangement with the 5% flap deploying first followed by the 10% flap, or an adjustable flap subject to the angle of attack and L / D requirements.

Configurations without step produced significantly superior results for C_L and C_D in comparison to configurations with step, especially for the 10% flap.

Chapter 9. UAV Performance Characteristics and Proposed Krueger Flap Design

The aim of this chapter is to look into the benefits and propose a simple design for a leading edge flap configuration, for application on a UAV, simpler than the current available designs used on commercial aircraft, which were reviewed in Chapter 1.

Aerofoils have design points which are related to the given aircraft application. Any given aerofoil profile also has optimum design points at one particular phase of the flight. Altering the aerofoils physical geometry, i.e., their camber and chord length, make it possible to achieve optimum aerodynamic performance for a number of different flight conditions.

9.1 General Design Considerations

The lift produced by an aerofoil depends on lift coefficient C_L, its area S, and to the square of its velocity V. The lift coefficient and wing area required to maintain the aircraft's altitude during cruising however, is less than what is required during takeoff or landing. Given the take-off and landing conditions exist for only a relatively brief period during a flight, optimising the aerofoil for these phases of flight would result in compromising the cruise efficiency thus compromising payload and fuel consumption.

To improve the efficiency of the aerofoil and in general the aircraft design, critical consideration of the aircraft's primary mission i.e., conditions to which the aircraft will be subjected to over the major portion of the flight must be made. Since for most cases this is the cruising portion, a considerably smaller aerofoil area would be adequate than what takeoff distance and landing speed would seem to demand. Optimising the wing for cruising conditions would on the other hand, compromise the aircraft's landing and takeoff capabilities. This problem is addressed by incorporating into the aerofoil a high lift device

such as a Krueger flap or other form of flap, which when extended would increase the range of angles of attack α, stall angle, speeds, and the resulting lift coefficient available. The Krueger system has an additional advantage over a conventional trailing edge flap device in that it provides a substantial increase in drag under certain conditions which results in a wider range of lift to drag ratio thus allowing a greater range of approach angles. As the following will demonstrate, this greater range of lift to drag can be achieved with a relatively simple Krueger flap device which, for approach and landing, permit a better range of final approach angles, therefore improving obstacle clearance and landing distances, as well as providing an improved view of the runway.

9.2 UAV Hermes 450 performance characteristics

To put theory into practice, the results obtained from the experimental and numerical analysis, are considered and here below theoretically implemented on a current UAV configuration.

The UAV configuration selected for this purpose is the Hermes 450 shown in Figure 153 below.

Figure 153: The UAV Hermes 450 [119].

The Hermes 450 is powered by a 52 hp rotary engine and its characteristics are summarised in Table 7 to Table 9 below [119], [120]. This aircraft has been selected because its approach,

stalling and cruising speeds are within the Reynolds number range investigated within this work. Also, its wing is a plain aerofoil section with no flaps, which allows ground for discussion and such development with leading edge flaps as is the present aim.

A summary of the Hermes 450 characteristics are as follows [120]:

Table 7: Dimensional:

Wing span	10.51 m
Wing chord	0.69 m
Wing area	6.90 m^2
Length overall	6.10 m

Table 8: Loadings:

Weight empty	200 kg
Max payload	150 kg
Max usable fuel	105 kg
Max Takeoff weight	450 kg

Table 9: Operating Performance:

Max level speed	176 km/h (48.8 m/s)
Cruising speed	130 km/h (36.1 m/s)
Stalling speed	78 km/h (21.6 m/s)
Takeoff	350 m

9.3 Effect of Krueger Flap on UAV performance

It has been shown within this work, that implementation of a Krueger flap on a plain Clark Y aerofoil results to an increase of the maximum lift coefficient by 18% and 14%, with the 10% flap and 5% flap configurations respectively.

9.3.1 Landing distance estimate

The landing distance of an aircraft is generally determined by the wing loading, $\frac{W}{S}$, which in turn directly determines the approach speed. Depending on the aircraft, the approach speed must be a certain multiple of the stall speed (usually, 1.3 for civil aircraft, 1.2 for military aircraft) [121]. Also it is expected for an aircraft to meet its landing requirements at or close to the takeoff design weight. The landing distance for most jet aircraft, is calculated on the basis of approximately 85% of maximum takeoff weight. Full payload and 50% remaining fuel are usually the required landing requirements for military design purposes [121].

The increase in lift coefficient can be translated into landing distance for a UAV, using the equation for landing distance $S_{landing}$ obtained from Raymer [121].

$$S_{landing} = 5\left(\frac{W}{S}\right)\left(\frac{1}{\sigma C_{Lmax}}\right) + S_a \quad [12]$$

Where W is the takeoff weight, S the wing area, σ the density ratio and S_a which represents the obstacle-clearance distance. The first term of the above equation represents the ground roll to absorb the kinetic energy at touchdown speed and is represented as S_r. Therefore

$$S_r = 5\left(\frac{W}{S}\right)\left(\frac{1}{\sigma C_{Lmax}}\right) \quad [13]$$

Using the value of stalling speed provided in Jane's UAV [120] the approach speed can be calculated assuming:

$$V_{stall} = 1.2V_a \quad [14]$$

where V_a is the approach speed.

Since the necessary lift should be equal to the aircraft's weight the lift equation can be used to calculate the approach C_L.

$$L = \frac{1}{2}\rho V^2 S C_L \text{ if } L = W$$

$$=> W = \frac{1}{2}\rho V^2 S C_L \quad [15]$$

The above procedure enables the calculation of S_r. Substituting the respective values into equation [12] and using S_a= constant (for simplicity) provides an initial estimate of $S_{landing}$.

The results show that the 18% increase in C_{Lmax} achieved by implementing a 10% Krueger flap, translates to approximately a 10% or 40m decrease in the required landing distance, while by implementing a 5% flap the respective decrease is 8% or approximately 30m.

Using the same formula but assuming constant $S_{landing}$ the increase of 18% in the lift coefficient translates to an 18% increase in the aircraft's weight or 60% increase to its payload. (Similarly, if the 5% flap is implemented the respective increase in the payload is 45%).

To obtain a more accurate value of $S_{landing}$ for the Hermes 450 however, the value of S_a must first be calculated. This can be accomplished from the calculation of the glide angle γ.

9.3.2 Glide angle estimate

The expression for the glide angle γ is given by:

$$\tan\ \gamma = \frac{C_D}{C_L} \text{ or } \tan\ \gamma = \frac{1}{L/D} \quad [16]$$

Using the value of stalling speed given in Table 9 for the Hermes 450 and substituting in equation [14] the value of the approach speed can be calculated as:

$$V_{stall} = 1.2V_a => V_a = \frac{V_{stall}}{1.2} = \frac{21.6}{1.2} = 18\ m/s \quad [17]$$

Substituting the above value in the equation for lift (eq [15]) and using L=W the required lift coefficient for landing ($C_{L\mathit{landing}}$) can be obtained.

For W=450Kg (max weight) => $C_{L\mathit{landing}} = 0.33$

From the experimental and numerical results, it can be seen that this value of C_L is achieved at $\alpha = 0^o$ for the plain Clark Y aerofoil. Similar values of C_L can also be obtained between $\alpha = 0^o$ and 1^o when either the 5% or 10% flap is deployed.

Using the values of L/D obtained at $C_L = 0.33$ the glide angle γ can be calculated (for the different configurations), and these are summarised in Table 10 below for Re = $1x10^6$.

δ(^{o})	**Glide angle γ(^{o})**
Clark Y	≈2^o
5% Flap, 50^o	≈8^o
10% Flap, 110^o	≈18^o

Table 10: Summary of glide angles for the different configurations at Re=$1x10^6$ and α=0^o.

A simple translation of the available and calculated data in terms of landing distances and glide angles for the HERMES 450 UAV, indicates that the implementation of the flap provides steeper angles and shorter landing distances. The results summarised in Table 10, show an increase of approximately nine times of the glide angle with the 10% flap case for the above UAV and four times for the 5% flap.

9.3.3 Glide Path characteristics and Landing Distance Calculation

The above values of γ can be used to calculate S_a and therefore a more accurate value for $S_{landing}$. Assuming a fixed obstacle of 10m height and a 2m clearance above it (see Figure 154 below), it can be seen that when the UAV descents for landing at the lowest glide angle, it will cover the longest distance along the ground (obstacle-clearance distance S_a) before actual touchdown. The variation in S_a between the different configurations at $Re=1x10^6$, is illustrated in Figure 155, which shows that implementation of the flap can lead to a decrease in the obstacle-clearance distance S_a of approximately 73% or 90% when the 5% flap or 10% flap is deployed respectively.

From the relationship of glide angle γ, it is obvious that the configuration will perform better and will achieve lower S_a distances when the L/D ratio is small. The value of (L/D) also determines the minimum glide angle which is obtained at $(L/D)_{max}$. This value would be approximately 1^o for the Hermes 450. The minimum value for ground roll (S_r) is achieved at C_{Lmax}.

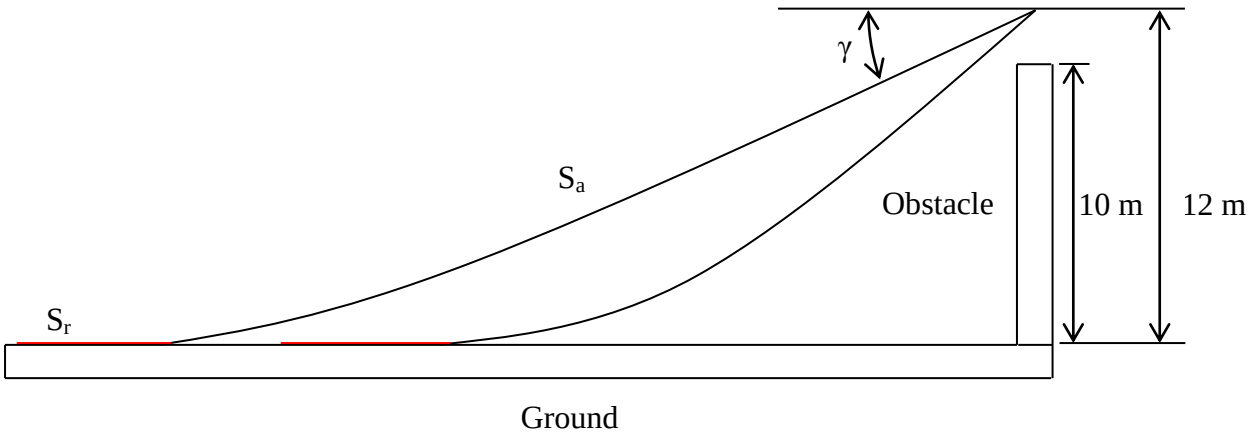

Figure 154: Represents schematic estimates of the total landing distances for different configurations.

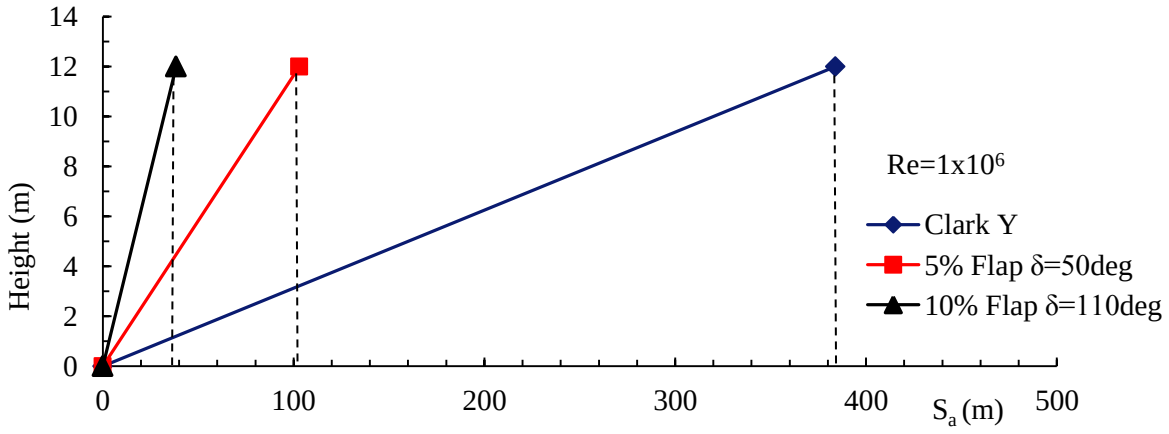

Figure 155: Height Vs Obstacle clearance distance, for the Clark Y and flap configurations, at Re=1x10^6.

Using equation [12] and substituting the values for C_{Lmax} and S_a a more accurate value of the total landing distance ($S_{landing}$) can be obtained. Figure 156, shows the variation of $S_{landing}$ with flap deflection angle. The dotted line represents the value of the baseline Clark Y model with no flap. The 5% flap shows improved aerodynamic characteristics at low flap deflection angles, while the 10% flap shows better and enhanced performance at higher flap deflection angles. In general, the 10% flap performs slightly better for all flap deflection angles. It is clearly evident that both flap configurations show significant improvements in comparison to the baseline Clark Y case.

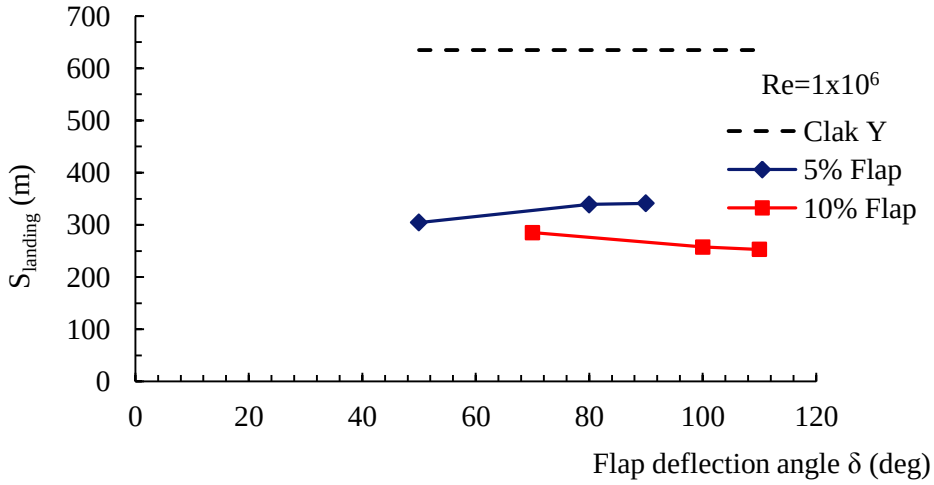

Figure 156: $S_{landings}$ vs flap deflection angle δ, for the Clark Y and flap configurations, at Re=1x10^6.

The value of $S_{landing}$ for a descent from 12m height is illustrated Figure 157. The best aerofoil-flap combination for each case is presented and it can be seen, that with the flap deployed a decrease of approximately 50% and 60% in $S_{landing}$ can be achieved with the 5% flap and 10% flap configurations respectively, in comparison to the baseline Clark Y case. This is a very significant decrease considering the limited amount of available runway for the landing of UAVs in a war zone. It can also be said however, that with successful implementation of the flap, the configuration can also attain higher gliding angles which can lead to enhanced manoeuvrability and better obstacle avoidance capabilities.

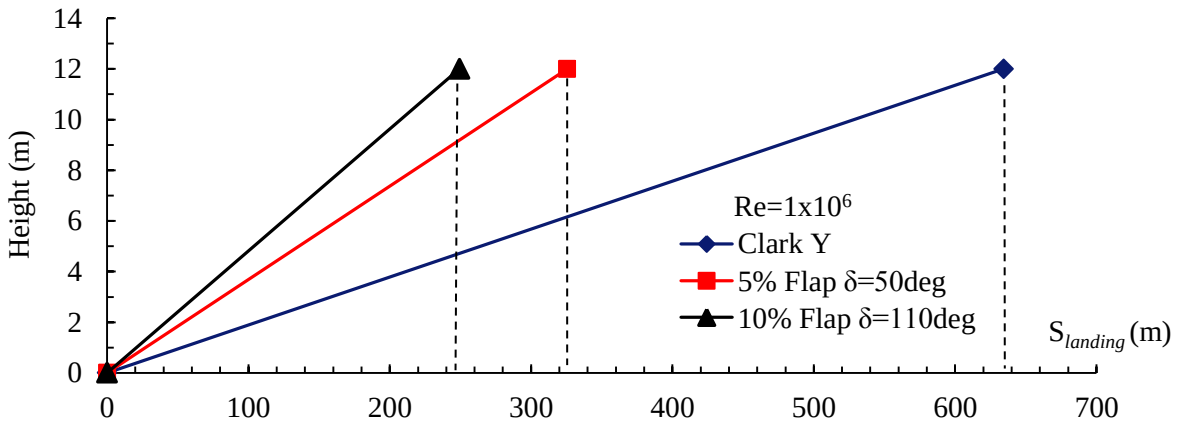

Figure 157: $S_{landing}$ distances, for the Clark Y and flap configurations from constant altitude at Re=1x10^6.

It must be noted that similar performance benefits were observed at all Reynolds numbers and for the rest of the configurations (with 5% flap at $\delta=80^o$ and 90^o, and with 10% flap at $\delta=70^o$ and 100^o) examined. In this chapter however, only the best cases are presented. Also it should be noted, that the effect of flap angle δ on the glide angle γ is $\pm 1^o$. The effect of Re is not significant since the variation of the L/D ratio at the different Reynolds numbers and $\alpha=0^o$ was very small (less than 5%) for all cases examined.

From the above but also the analyses performed in earlier chapters it can be seen that, the aerodynamic ratios of L/D as well as $C_L^{(3/2)}/C_D$, play a very significant role in the performance of a UAV. The successful implementation of a Krueger flap shows that such devices can reduce landing distances, increase endurance and improve manoeuvrability and glide angle characteristics.

9.4 Effect on Endurance

Analysis of the experimental and numerical results showed that, the aerodynamic characteristics of an aerofoil and leading edge flap configuration are superior to those of a plain aerofoil, especially the values of lift to drag ratio and maximum lift coefficient. The potential benefits on endurance and range of such improvements were previously discussed in more detail, in Chapter 7. It was shown that the use of a Krueger flap can increase the endurance of a UAV by approximately 61% to 66% with the 10% flap and 56% to 65% with the 5% flap by increasing $(C_L^{3/2}/ C_D)_{max}$.

Implementation of the flap on the UAV will produce improved performance during the takeoff and landing and could enhance endurance. This could lead to longer missions, which will enable the UAV to stay longer on air as well as offer better fuel economy.

9.5 Flap Design Proposals

To determine the moment created by the flap a similar configuration of the wing platform as that of the Hermes 450 may be considered. Assuming an equally distributed load through the span of the flap, then the 2D moment can be converted into 3D by multiplying by the span of the wing. Furthermore, to consider a flap deployment mechanism, the flap moment as previously discussed is calculated about the rotation point of the flap, which coincides with the centre of the leading edge radius and varies in magnitude according to the angle of attack α, flap deflection angle δ and Reynolds number.

Different mechanisms have been considered involving speed loaded pulleys, torsion springs, and servomechanisms to deploy the flap. It is important to define the operating range at which the flap needs to be deployed, for example if the flap is required to deploy at the UAVs maximum speed the moments acting on it would be significantly higher (in some case up to ten times higher) than if its only required during descent from cruising speed.

Various flap deployment designs have been examined and a brief description of each is presented along with comments regarding their implementation.

9.6 Spring Loaded Design

After establishing the moment characteristics of the aerofoil and flap configurations initially a simple spring loaded design was considered which is illustrated in Figure 158.

Assuming that this system is locked in a spring loaded mode in the retracted position it could simply deploy when released. This could be accomplished by a simple solenoid plunger type lock/release mechanism. If deployment would be for landing purposes only, this might be sufficient with reloading performed manually prior to each take off. If to be used during any other flight condition however, another mechanism would be required for retracting purposes. As such there are available part winding/unwinding servo motors which could both retract as well as deploy the spring loaded system as required.

9.7 Servomotor Design

A Servo motor proposed design is illustrated in Figure 159. As previously mentioned the required Reynolds numbers at which the flap would be expected to deploy would affect the magnitude of the deployment moment. Considering the worst case scenario, the servo motor would have to negotiate approximately 20 Nm of torque at Re = 1.6×10^6, with the 10% flap. Ideally one servo could be employed to deploy the flap as one piece. This however, might be difficult since servos producing such torques are large in size and would be hard to house in the wing. Five smaller servos could therefore be used producing 4.5 Nm torque each, which could deploy the flap as one assembly or in segments. Example of such a servo motor is the HS-M7990TH by: “Hitec” with specifications and dimensions summarised in Table 11.

Model	HS-M7990TH
Dimensions (mm)	44.0 x 22.0 x 40.0
Weight (kg)	0.0765
Speed (sec)	0.17
Torque (N.m)	4.4
Max Rotation	180^{o}

Table 11: Servo motor Specs

9.8 Linear Actuator Design

A design utilising a linear actuator is also presented. Linear actuators are larger and heavier but they can negotiate higher loads. Typical characteristics of such an actuator are presented in Table 12. In contrast with the servo motor mechanism only one such actuator of this type would be necessary for the flap to deploy. It can be seen from Figure 160 that the linear actuator would have to be able to also rotate about a pivot point to allow the flap to deploy.

Model	M10
Dimensions (mm)	159.0 x 55.0 x 34.0
Weight (kg)	0.4 to 0.55
Speed (sec)	0.25 to 0.22 mm/s
Load (N)	Up to 500
Travel Length	Up to 100mm*Adjustable

Table 12: Linear actuator Specs.

Both servo motor and linear actuator designs offer similar benefits since they could both control the rate of deployment as well as the flap deflection angle δ. If the flap is required to deploy only during takeoff and landing, at low Reynolds numbers, then servo actuators would be suited for the application as they are smaller, lighter and can perform just as well. If however, the flap is required to deploy at maximum speeds as well, then either mechanisms

might be used. The design utilising the linear actuator might offer a simpler installation since only one system would then be needed.

In summary, the servo motor operated design would provide better control over both deployment and retraction phases of the flap. The spring loaded system might be lighter than any of the above mentioned, however, an additional retraction mechanism would be required to bring the system back to its initial position. If the device would be needed only during the landing phase of the flight and not during takeoff then a spring system might be the simplest to apply. Such design configuration could manually be returned to its stowed loaded position where the spring would be loaded manually when the UAV is grounded.

9.9 Flap Deployment Mechanism Activation and Control

It was initially believed that the location of the stagnation point could be used as a mechanism for the deployment of the flap. After observing the Cp distribution around the Clark Y aerofoil at the different angles of attack (see Figure 166 to Figure 179, APPENDIX F) however, it was observed that the location of the stagnation point does not significantly change. Other methods however, such as using the altitude, velocity and/or angle of attack may therefore be used, for example:

A pitot - static probe on either side of the UAV could provide readings for the dynamic and static pressures. From these values the velocity and altitude of the UAV could be obtained. The pitot - static system could be connected with a *Digital Air Data Computer* (DADC) and automatic deployment could then be enabled based on altitude and/or speed via the DADC.

A similar system could be used utilising an angle of attack meter where the flap could deploy based on the angle of attack α or glide angle γ. A static pressure based angle of attack meter can be utilised to activate the mechanism at the required angle of attack. These meters can simply be attached to the high pressure side of the wing and they are readily available off-the-shelf.

A combination of the two above mentioned systems could also be implemented. The flap would thus automatically deploy with a sudden change in the angle of attack and/or altitude.

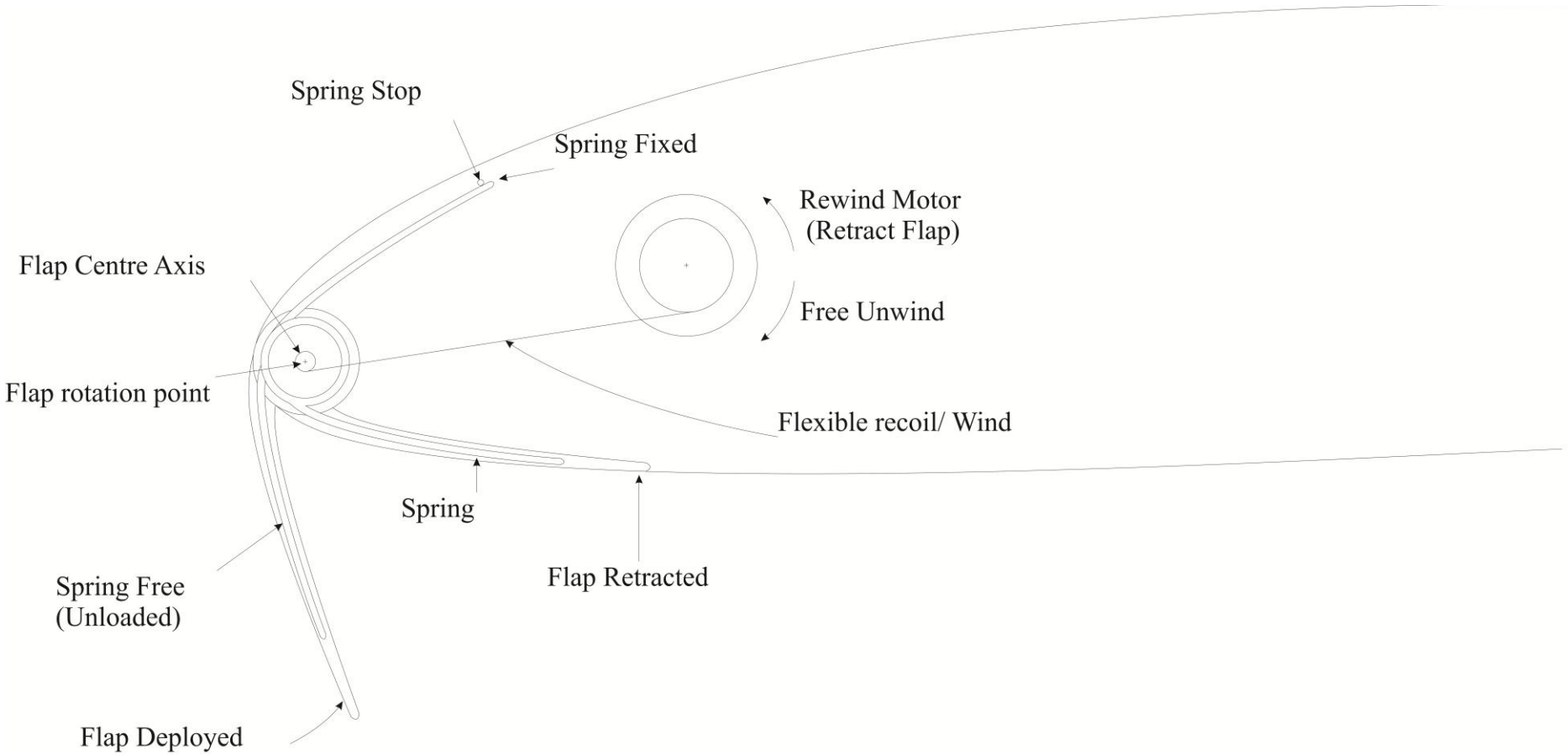

Figure 158: A simple spring loaded leading edge flap design.

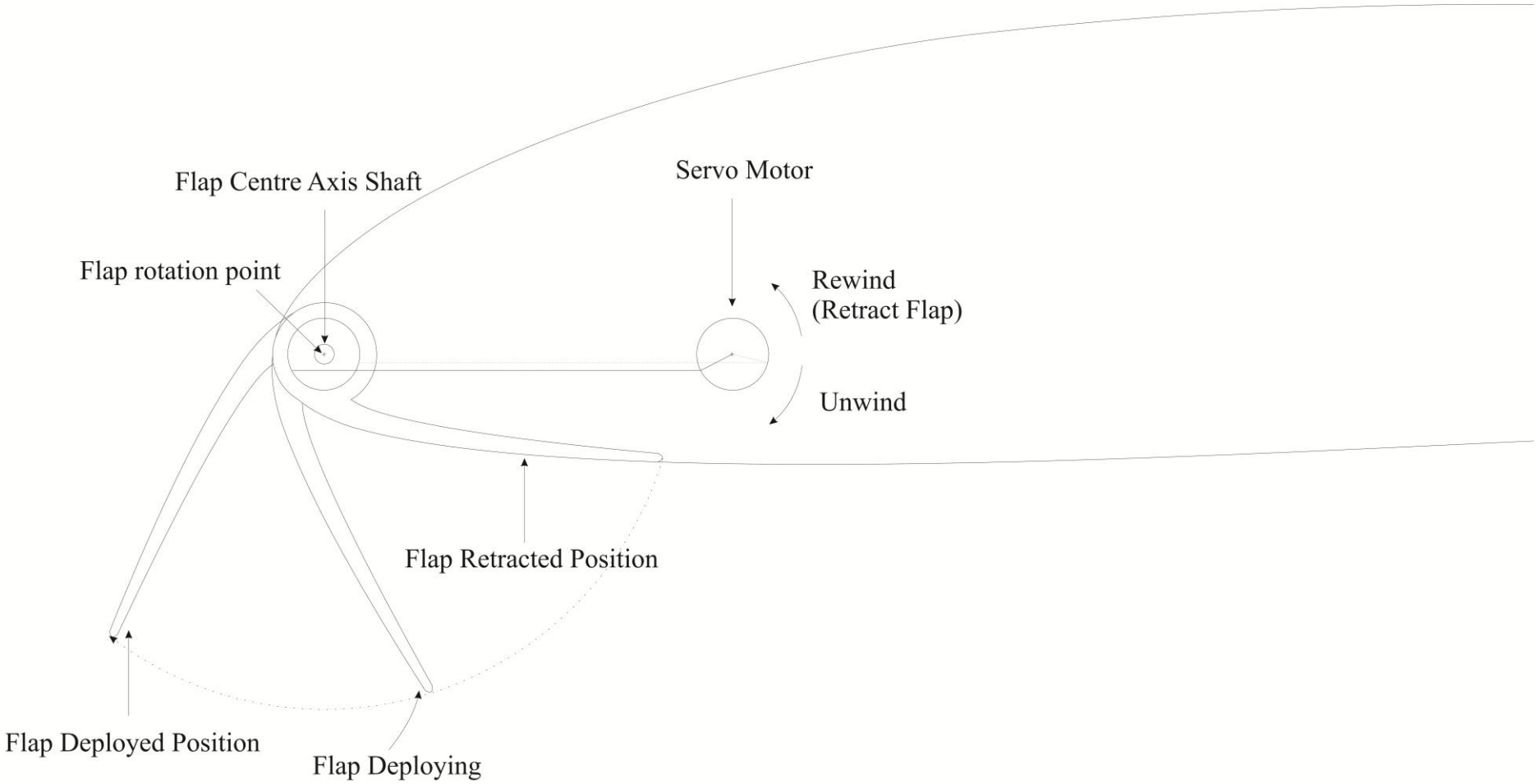

Figure 159: A Servo motor operated configuration schematic design.

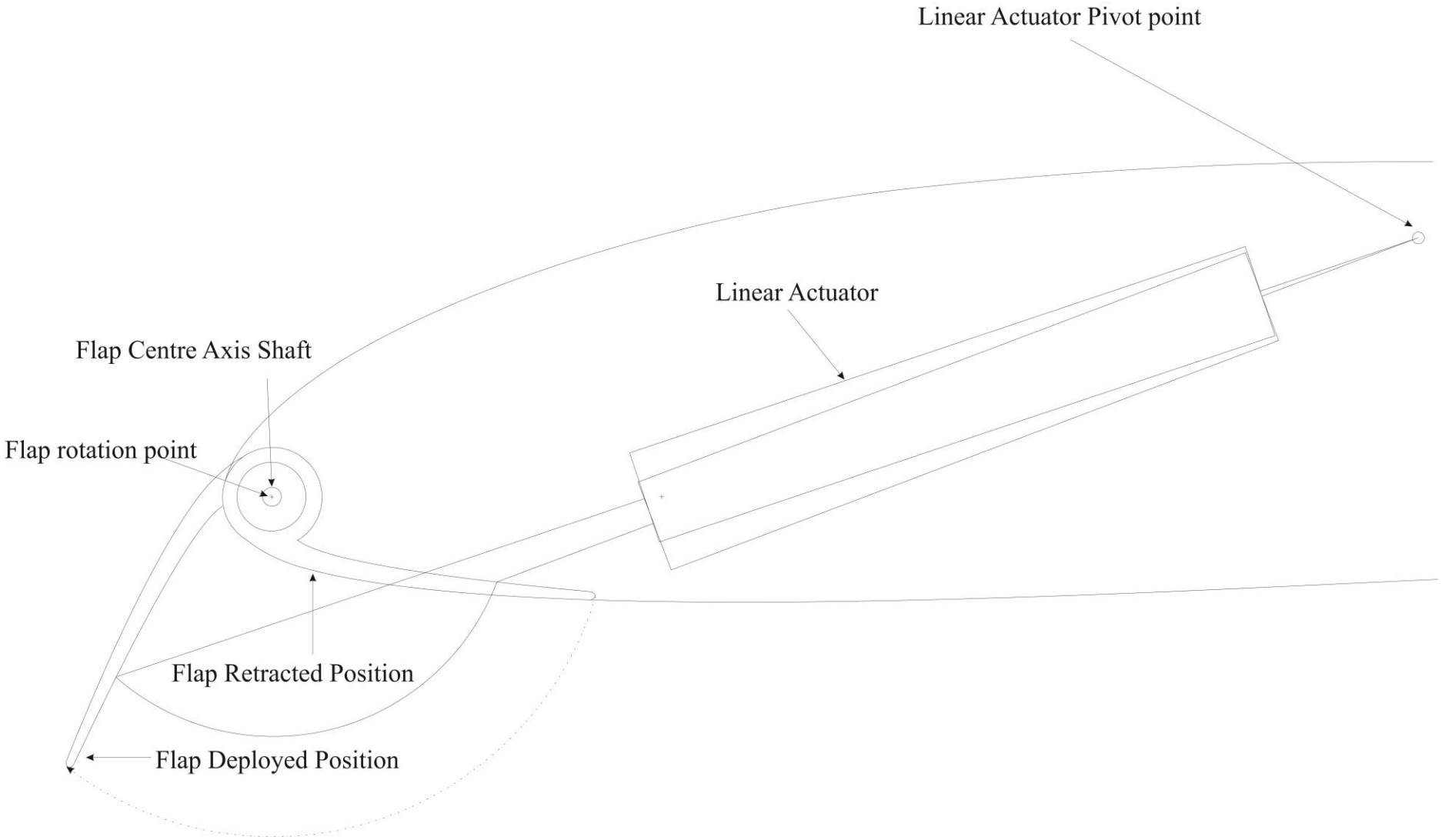

Figure 160: A linear actuator operated configuration schematic design.

Chapter 10. Conclusions and Recommendations

10.1 Conclusions

Experimental and numerical analyses were performed to evaluate the aerodynamic performance of two Krueger flaps applied to a plain Clark Y aerofoil. Two dimensional experiments were conducted in the Cranfield 8x6 ft wind tunnel to establish the aerodynamic forces acting in such configurations. This chapter presents a summary of the important conclusions drawn from the above numerical and experimental study. The work has shown that the Krueger flap positively increases the value of lift coefficient especially at the lower Reynolds number regime and high angles of attack.

An initial wind tunnel flow visualisation test showed that the flow was fully turbulent. The rough surface near the leading edge of the aerofoil-flap configuration as well as the discontinuity of the surface contour due to the implementation of the flap led to an early transition of the flow. The almost identical values of C_L and C_D obtained from the experimental analysis from configurations with and without transition strip also provide evidence to support the statement that the flow was fully turbulent.

Each Krueger flap configuration achieved its maximum ΔC_L at different flap deflection angles δ. An opposite trend was observed in the values of C_{Lmax} between the two flap configurations. The 10% flap achieved maximum lift characteristic at $\delta = 110^o$ and showed an increase in performance as δ increased. The 5% flap yielded the opposite results. This configuration achieved its maximum ΔC_L at $\delta = 50^o$ and its performance decreased thereafter. The C_L plots for the 10% flap, revealed an increase in the maximum lift coefficient between 15% - 18% at a stall angle α between 16^o to 17^o, and flap deflection angle of $\delta = 110^o$, for all three Re numbers. Similarly at $\delta = 100^o$ the increase in the maximum lift, was between 11% - 12%. No significant increase in C_L for $\delta = 70^o$ was observed.

In the case of the 5% flap the corresponding increase in the C_{Lmax} values was between 14% - 15% at a stall angle α between 15^o to 16^o and flap deflection angle $\delta = 50^o$ between 11% - 12% for $\delta = 80^o$ and close to 8% at $\delta = 90^o$. The maximum lift coefficient values were obtained at smaller angles of attack than the 10% flap.

The effect of a transition strip was also examined in the experimental procedure and the results showed that no significant difference was observed with the variation of Reynolds number. Configurations with transition strip appear to achieve increases of 0.02-0.04 of the C_{Lmax} at low Reynolds numbers.

In addition the effect of the step formed during the deployment of the flaps was examined. It was shown that the configurations without the step (step smoothed over) produced significantly better lift coefficient results, especially at high angles of attack, which indicates the importance of a smooth leading edge geometry between the aerofoil and the flap contour. Configurations without the step demonstrated an increase in the C_{Lmax} value of up to 0.15.

Validated CFD results have shown promising Krueger characteristics with C_L increases of up to 18% over a conventional no flap configuration, and delayed separation by up to 2^o for the 10% flap configuration, and up to 12% and 2^o for the 5% flap configuration.

The experimental and numerical results indicated, that with both flap configurations, the flap deployment angle δ increased the angle of attack at which the flap became effective decreased.

Results from the numerical study showed the importance of the mesh density in establishing the aerodynamic performance of the aerofoil especially at high angles of attack. Also it was shown that the performance of the k-ω SST model was superior to the Spalart - Allmaras. A comparison of the numerical results with the experimental wind tunnel results, appear to confirm these findings.

Although the 2D numerical model was successful in predicting the lift coefficient characteristics of the configurations, the model was less reliable and proved to be inadequate in predicting the drag coefficient. In addition to the inability of the numerical analysis to accurately predict the drag coefficient, it is believed that the drag values obtained from the experimental part are slightly higher than what was expected, mainly due to the aerofoil and end-plate flow interactions.

It was observed that the ΔM with increasing α was negative in all cases where the magnitude of the $\Delta M/\alpha$ gradient increased with increasing δ as well as increasing Reynolds number. A pseudo-linear relationship exists between the moment M and angle of attack α. Both flaps follow the same relationship with the 10% flap achieving higher values of moments through the deployment phase.

The Hermes 450 UAV was chosen as an example for this project for Krueger flap application, since its operational Reynolds number range is within the boundaries of the ones also employed in this thesis. If the leading edge flaps were implemented on this UAV the benefits for the 10% flap would be, 18% increase in lift which translates to approximately 10% or 40m decrease in S_r, while the respective S_r decrease for the 5% flap case would be 8% or approximately 30m. Alternatively, at a constant S_r, the increase of 18% in the lift coefficient, by implementing a 10% flap, translates to an 18% increase to the aircraft's weight or 60% increase to its payload. Similarly, if the 5% percent flap is implemented the respective increase in the payload is 45%.

The value of $S_{landing}$ for a descent from 12m height with the flap deployed, is reduced by approximately 50% or 60% for the 5% flap or 10% flap configurations respectively, in comparison to the baseline Clark Y case. This is a very significant decrease, considering the limited amount of runway length available for landing a UAV, especially in war time conditions.

The aerofoil-flap configuration can also achieve higher gliding angles, which can lead to enhanced manoeuvrability and better obstacle avoidance capabilities. The implementation of the flap on a UAV such as the Hermes 450, may result in increases of approximately nine times in the glide angle with the 10% flap or four times with the 5% flap. This is particularly important in rough and mountainous environments such as often observed in war zones where a UAV might have to land as soon as possible to avoid possible detection and/or attack.

It has also been shown that implementation of the flap significantly increases the $(C_L^{3/2}/C_D)_{max}$ of an aerofoil-flap configuration, thus also increasing its endurance. Results from the experimental analysis indicate a max increase of 61% may be achieved with the 10% flap at $\delta=110^o$ and Re $=0.6x10^6$, between the baseline Clark Y model and the aerofoil-flap configurations. Likewise CFD results show an analogous increase of 66% in these characteristics. The corresponding increase for the 5% flap configuration is 56% and 65% for the experimental and numerical analyses respectively.

It was observed that, the 5% flap gives slightly better $(L/D)_{max}$ whereas the 10% flap produces slightly higher values of C_{Lmax}.

Overall, the results obtained from this study indicate the potential benefits of employing a leading edge flap. It has been shown that successful implementation can lead to significant increases in glide angle, endurance and manoeuvrability as well as decrease in the landing distance requirements.

10.2 Recommendations

Although the benefits from the implementation of leading edge devices, such as Krueger flaps are evident, their applicability depends strongly upon completion of further and more in-depth studies so as to increase the knowledge, understanding and confidence on such systems. For example, it has been shown that the aerodynamic characteristics of configurations incorporating such devices closely depend on the chord of the leading edge flap. Although two individual flaps have been examined in detail in this project, with a wealth of data gathered, additional investigation of flaps of other chord lengths will certainly further enhance the knowledge and appreciation of the characteristics, benefits, applicability, and better endow for design and actual use of such devices.

Due to time limitations the flaps were investigated at what were believed to be the optimum flap deflection angles. These positions were in fact obtained by considering and combining previous experimental. It would therefore, be important to repeat this procedure for different flap deflection angles so as to validate such relationships. In addition this extended examination, would provide a fuller and more comprehensive set of data of the aerodynamic characteristics, forces and moments acting on such systems.

During the experimental process it was observed that a step formed between the flap and the aerofoil, when the first was deployed, altered the aerodynamic characteristics of the aerofoil-flap configuration. An experimental procedure using similar configurations with different aerofoil sections could provide a better understanding about this phenomenon and its repeatability. At the same time perhaps a design study could look into the individual section and coupling geometries with the aim to minimise the step and produce a more smooth contour arrangement.

Overall, a more particular and detailed design process could provide a more efficient and optimised design. Ideally the proposed flap mechanism designs should be manufactured and tested under similar conditions. This should enable more precise investigation, comparisons,

correlations and optimisation to be made which may determine the applicability and actual selection, refinement and implementation of such systems.

A good agreement between the experimental and numerical lift coefficients has been observed. There were significant problems however, in predicting the drag coefficient with the same degree of accuracy for most cases. It has been mentioned in the thesis that factors such as the presence of the end - plates in the wind tunnel could have affected the accuracy of the results. Combining this with the inability of the turbulence models to accurately predict the drag, a precise estimation of the true value of drag was not possible. Further work, perhaps using more complex CFD methods, such as large eddy simulation (LES), may offer improved predictions of drag and allow further study and understanding of possible unsteady phenomena generated by the flap configuration.

As mentioned before initial flow visualisation tests showed that the flow was fully turbulent. A fully turbulent CFD model was thus used. It is believed however, that it might be beneficial to run transitional simulations as well as a more detailed flow visualisation test, in the wind tunnel. The flow visualisation tests could lead to a better understanding of the boundary behaviour and could help justify the differences observed in drag.

References

[1] Steinbuch, M., and Shepshelovich, M., "Development of High Altitude Long Endurance Airfoils", 42nd Aerospace Sciences Meeting and Exibit, Reno, NV, 5-8 January, 2004.

[2] Liebeck, R.H., "Subsonic Airfoil Design", Applied Computational Aerodynamics, Progress in Astronautics and Aeronautics, Vol. 125, 1990.

[3] Drela, M., "Elements of Airfoil Design Methodology", Applied Computational Aerodynamics, Progress in Astronautics and Aeronautics, Vol. 125, 1990.

[4] Drela, M., "Newton Solution of Coupled Viscous-Inviscid Multi-Element Airfoil Flow", AIAA 90-1470, AIAA Fluid Dynamics, Plasmodynamics and Laser Conference, Seattle, WA, June 1990.

[5] Steinbuch M., Marcus B. and Shepshelovich M., "Development of UAV Wings - Subsonic Designs". 41st Aerospace Sciences Meeting and Exhibit, Reno, NV, 6-9 January, 2003.

[6] N. Alexander., and Shepshelovich. M "Development of High-Lift UAV Wings" 24th Applied Aerodynamics Conference 5 - 8 June 2006, San Francisco, California

[7] Steinbuch, M. and Shepshelovich, M., "Development of UAV Wings – Transonic Designs", 43rd Aerospace Sciences Meeting and Exhibit, Reno, NV, January 10-13, 2005.

[8] Koss, D., Steinbuch, M., and Shepshelovich, M., "Development of Two-Element NLF Airfoils for Long Endurance Flight", 35th Aerospace Meeting and Exibit, January 6-10, Reno, Nevada, 1997.

[9] Gharib, M, Prespective: The experimentalist and the problem of turbulence in the age of supercomputers. Journal of Fluids Engineering 118: 233-242, 1996.

[10] C.P. van Dam, The aerodynamic design of multi-element high-lift systems for transport airplanes Progress in Aerospace Sciences 38 (2002) 101–144.

[11] Rudolph PKC. High-lift systems on commercial subsonic airliners, NASA CR 4746, September 1996.

[12] Meredith P. Viscous phenomena affecting high-lift systems and suggestions for future CFD development. High-Lift System Aerodynamics, AGARD CP 515, September 1993. p. 19-1–19-8.

[13] D.J. Butter, Recent Progress on Development and Understanding of High-Lift-Systems, AGARD-CP 365, 1984.

[14] Harry L., Morgan, High – Lift Flaps for Natural Flow Airfoils, NASA, N88-23739

[15] Daniel Reckzeh, Aerodynamic design of the high-lift-wing for a Megaliner aircraft, Aerospace Science and Technology 7 (2003) 107–119

[16] Niu MCY., Airframe structural design. Hong Kong, Conmilit Press Ltd., 1988. p. 303–357

[17] John W. Smith, Wilton P. Lock, and Gordon A. Payne, Variable-Camber Systems Integration and Operational Performance of the AFTI/F-111 Mission Adaptive Wing NASA Technical memorandum 4370, April 1992.

[18] Preliminary Design Department of the Boeing Commercial Airplane Company: Assessment of Variable Camber for Application to Transport Aircraft. NASA CR-158930, 1980.

[19] http://www.dfrc.nasa.gov/gallery/photo/index.htm

[20] http://www.airliners.net/

[21] McIntosh W, Wimpress JK., Prediction and analysis of the low speed stall characteristics of the Boeing 747, Aircraft Stalling and Buffeting, AGARD LS 74, February 1975.

[22] Nield BN, An overview of the Boeing 777 high-lift aerodynamic design, Aeronaut J 1995;99:361–71.

[23] V.M Bakhtian, H. Babinsky, A.L.R Thomas and G.K. Taylor, The low Reynolds Number Aerodynamics of Leading Edge Flaps, AIAA 2007-662, 45th AIAA Aerospace Science Meeting and Exhibit, Reno, Nevada, 8-11 January

[24] Carruthers, A., Taylor, G. K., Walker, S. M., and Thomas, A. L. R., Use and function of a Leading Edge Flap on Wings of Eagles, 45th AIAA Aerospace Science and Exhibit, Reno, NV, 8-11January 2007.

[25] Hertel, H., Structure Form Movement, Reinhold Publishing Corporation, New York, 1963.

[26] Azuma, A., Okamoto, M., and Yasuda, K., Aerodynamic Characteristics of Wings at Low Reynolds Number, Fixed and Flapping Wing Aerodynamics for Micro Air Vehicle Applications, edited by T. J. Mueller, Vol. 195 of Progress in Astronautics and Aeronautics, chap. 17, AIAA, 2001, pp. 341-398.

[27] Azuma, A., The Biokinetics of Flying and Swimming, Springer-Verlag, Tokyo, 1992.

[28] W. Krueger, Systematic wind tunnel measurements on a laminar aerofoil with nose flap. M.A.P Volkenrode Ref: MAP – VG 123 – 224T, 1946.

[29] W. Krueger, The nose flap as a means for increasing the maximum lift of high-speed aeroplanes. M.A.P Volkenrode Ref: MAP – VG 87 – 25T, 1946.

[30] W. Krueger, Systematic wind-tunnel measurements on a laminar aerofoil with nose flap. M.A.P Volkenrode Ref: MAP – VG 123 – 224T, 1946.

[31] W. Krueger, Systematic wind-tunnel measurements on a laminar wing with nose flap, NACA-TM-1119, 1947.

[32] Fullmer, Felicien F, Two-dimensional wind-tunnel investigation of the NACA 641-012 airfoil equipped with two types of leading-edge flap. NACA-TN-1277, 1947.

[33] Fullmer, Felicien F, Two-dimensional wind-tunnel investigation of an NACA 64 -009 airfoil equipped with two types of leading-edge flap. NACA-TN-1624, 1947.

[34] Williams, A. L, A new and less complex alternative to the Handley Page slat (Northrop Corp., Aircraft Div., Hawthorne, CA), Journal of Aircraft 1986 0021-8669 vol.23 no.3 (200-206).

[35] Lissaman, P. B. S., Low-Reynolds-Number Airfoils Annual Review of Fluid Mechanics, 15, 223-39, 1983

[36] J. D. Jacob, On the Fluid Dynamics of Adaptive Airfoils, Proceedings of 1998 ASME International Mechanical Engineering Congress and Exposition, 15-20 November, Anaheim, CA, USA.

[37] Shepshelovich, M., "Aerodynamic Concept of IAI Long Endurance UAV". 44th Israel Annual Conference on Aerospace Sciences, 25-26 February, 2004

[38] Shepshelovich, M., "UAV Wing Design – a New Challenge", International Seminar – Aero India 2005, Bangalore, India, 7-9 February 2005.

[39] Nagel, A., and Shepshelovich, M., "The concept of High-Lift, Mild Stall Wing". 24th International Congress of the Aeronautical Sciences, Yohogama, Japan, 29August - 03 September, 2004.

[40] Koss, D., and Shepshelovich, M., "Design and Experimantal Evaluation of Two-element, High-Lift/Low-Drag, Long Endurance Airfoil", 35th Israel Annual Conference on Aerospace Sciences, February, 1995.

[41] Koss, D., Steinbuch, M. and Shepshelovich, M., "Design and Experimental Evaluation of High-Lift, Mild-Stall Airfoil", 12th AIAA Applied Aerodynamics Conference, June 1994.

[42] Marchman III and T. D. Werme, Clark –Y Airfoil Performance at Low Reynolds Number J. FAIAA 22nd Aerospace Sciences Meeting, January 9-12, 1984 Reno, Nevada.

[43] Fred E. Weick and Joseph A. Shortal, The Effect of Multiple Fixed Slots and a Trailing – Edge Flap on the Lift and Drag of a Clark Y Airfoil, NACA Report No. 427, 1932.

[44] Abe Silverstein, Scale Effect on Clark Y Airfoil Characteristics From N.A.C.A Full-Scale Wind-Tunnel Test, NACA No. 502.

[45] Fred E. Weick and Carl J. Wenzinger, The Characteristics of Clark Y Wing Model Equipped With Several Forms of Low-Drag Fixed Slots, NACA Report No 407, 1932.

[46] Fred E. Weick and Millard J Bamber, Wind Tunnel Tests of a Clark Y wing with a Narrow Auxiliary Airfoil in Different Positions NACA Report 428, 1932.

[47] Wenzinger, Carl J., and Shortal, Joseph., The Aerodynamic Characteristics of a Slotted Y Wing as Affected by the Auxiliary Airfoil Position, NACA T.R. No 400, 1931.

[48] Wood, Donald H., Test of Large Airfoils in the Propeller Research Tunnel, Including Two with Corrugated Surfaces, NACA T.R. No 336, 1929.

[49] Stack, John. Test in the Variable Density Wind Tunnel to Investigate the Effects of Scale and Turbulence on Airfoil Characteristics, NACA T.N No 364, 1931

[50] Garrick, I.E., Determination of the Theoretical Pressure Distribution for Twenty Airfoils, NACA T.R. No 465, 1933

[51] Nagel, A., and Shepshelovich, M., "Development of High Lift, Mild Stall Airfoils". 43rd Israel Annual Conference on Aerospace Sciences, 19-20 February, 2003.

[52] Bertin, J.J. and Cummings, R.M. (2009) Aerodynamics for Engineers, 5th edn, Pearson Education Ltd, London.

[53] Nagel, A., and Shepshelovich, M., "Wing Concepts for Tactical UAV". 45th Israel Annual Conference on Aerospace Sciences, 23-24 February, 2005.

[54] Alexander Nagel and Misha Shepshelovich "The Concept Of High Lift, Mild Stall Wing" 24th International Congress Of The Aeronautical Science 2004, Engineering Center, Israel Aircraft Industries.

[55] McMasters J.H., Henderson M.L., "Low-Speed, Single-Element Airfoil Synthesis", Boeing Commercial Airplane Co., MPA Symposium, 1978.

[56] Abbott I.H. and Von Doenhoff A.E., "Theory of Wing Sections", Dover Publications Inc., N.Y., 1959.

[57] Althaus D. and Wortmann F.X., "Stuttgarter Profilkatalog", Wieweg & Sohn, Brounschweig, 1981.

[58] Maghmer M.D. and Somers D.M., "Design and Experimental Results for a High-Altitude, Long- Endurance Airfoil", Aircraft, vol. 26, No. 2, 1989.

[59] John D. Anderson, Jr Computational Fluid Dynamics, The Basics With Applications McGraw-Hill International Editions, Mechanical Engineering Series, ISBN 0-07-113210-4.

[60] Roy P. Koomullil and Bharat K. Soni, Hybrid Grid Generation for CFD Applications, NSF Engineering Research Centre, Mississippi State University.

[61] Jonathon A. Shaw, Hybrid Grids, Handbook of Grid Generation CRC Press, Boca Raton, London, New York, Washington, D.C. ISBN 0-8493-2687-7, pp. 23-1 – 23-18.

[62] H. K. Versteeg & W. Malalasekera, An Introduction To Computational Fluid Dynamics, The Finite Volume Method, Prentice Hall, ISBN 0-582-21884-5.

[63] FLUENT and GAMBIT User's Guide, 2006, Fluent Inc, Lebanon, New Hampsiare, USA. ISBN??

[64] Ronit K. Singha, M. Rafiuddin Ahmed, Mohammad Asid Zullah, Young-Ho Lee, Design of a low Reynolds number airfoil for small horizontal axis wind turbines, Renewable Energy International Journal 42, page 66-76.

[65] Sugavanam, A. and Wu, J. C., Numerical study of separated turbulent flow over airfoils. AZAA J., 1982, 20, 4,464-471. See also AIAA Paper 80-1441.

[66] Rumsey, C. L., Thomas, J. L., Warren, G. P. and Liu, G. C., Upwind Navier-Stokes solutions for separated periodic flows. AZAA J., 1987, 25, 4, 535-541. See also AI& Paper 86-0247.

[67] Tzabiras, G., Dimas, A. and Loukakis, T., A numerical method for the calculation of incompressible steady separated flows around aerofoils. Znt. J. Num. Meth. Fluids, 1986, 6, 799-809.

[68] Kogan, A. and Migemi, S., The calculation of incompressible separated turbulent boundary layers. Inr. J. Num. Meth. Fluids, 1990, 11, 39-56.

[69] Chevallier, G., Prevision du decrochage de profils d'aile par resolution des equations de Navier-Stokes moyennees. These de Doctorat ENSAE, 1994

[70] Lien, F. S. and Leschziner, M. A., Modelling ZD separation from a high lift aerofoil with a non-linear eddy-viscosity model and second-moment closure. Aero. J.. 1995, 125-144.

[71] E. Guilmineau, J. Piquet and P. Queutey., Tow-Dimensional Turbulent viscous Flow simulations past Airfoils at fixed incidence, Computers & Fluids Vol. 26, No. 2, pp. 135-162, 1997

[72] Wolfe, W. P. and Ochs, S. S., "CFD Calculations of S809 Aerodynamic Characteristics," AIAA paper 97-0973.

[73] Wetherill, N.P., Mixed structured and unstructured meshes for aerodynamic flow simulation, Aeronautical Journal, 1990, 94, pp. 111-123.

[74] Joe F. Thompson, Bharat K. Soni Nigel P. Weatherill, Handbook of Grid Generation CRC Press, Boca Raton, London, New York, Washington, D.C. ISBN 0-8493-2687-7.

[75] ANSYS Meshing User's Guide, ANSYS, Inc.

[76] Patrick J. Roache, Verification and Validation in Computational Science and Engineering, Hermosa 1998, ISBN 0913478083.

[77] D. C. Wilcox, Turbulence Modelling for CFD, Second Edition, DWC Industries Inc. La. Canada, California, ISBN 1-928729-10-X.

[78] Christopher L. Rumsey, Susan X. Ying, Prediction of high lift: review of present CFD capability, Progress in Aerospace Sciences 38 (2002) page 145–180.

[79] Stephen B. Pope, Turbulent Flows, Cambridge University Press, ISBN 0521598869.

[80] TH. VON KÁRMÁ, Turbulence and Skin Friction, Journal of Aeronautical Sciences, January 1934, Volume 1.

[81] John D. Anderson, Jr. Introduction To Flight, McGraw-Hill International Edition, Fifth Edition, ISBN 007-123818-2.

[82] Spalart, P. R., Trends in Turbulence Treatments, AIAA Paper 2000-2306, June 2000.

[83] Menter, F. R, Two-equation eddy-viscosity models for engineering applications, AAIA J. Volume 32, pp. 1598-1605, 1994.

[84] Mauro P. Arruda, Fluidic Vector Control of Self – Sustained Oscillatory Cavity Jets, Ph.D. Thesis, Cranfield University, June 2004.

[85] Florian R. Menter, Zonal Two Equation k-ω Turbulence Models for Aerodynamic Flows, AIAA 93-2906, 24th Fluid Dynamics Conference, Orlando, Florida, July 6-9, 1993.

[86] David C. Wilcox Turbulence Modeling: An Overview, AIAA 2001-0724, 39th Aerospace Science Meeting and Exhibit, Reno January 8-11, 2001.

[87] P. R. Spalart and S. R. Allmaras, A One – Equation Turbulence Transport Model for Aerodynamic Flows, AIAA-92-0439, 30th Aerospace Science Meeting & Exhibit Reno, January 6-9, 1992.

[88] Yang, B. and Menq, C., Characterization of contact kinematics and application to the design of wedge dampers in turbomachinery blading, ASME, 97-GT-97.

[89] Wilcox, D. C., Multiscale Model for Turbulent Flows, AIAA Journal, Vol. 26 No 11. November 1988, pp. 1311-1320.

[90] Jones, W. P. and Launder B. E., The Calculation of Low Reynolds Numbers Phenomena with a Two Equation Model of Turbulence, Int. Journal, Heat Mass Transfer, Vol. 16, 1973, pp. 1119-1130

[91] Menter, F. R., Influence of Freestream Values on k-ω Turbulence Model Predictions, AIAA Journal, Vol. 30, No 6, June 1992, pp. 1657-1659.

[92] Menter, F. R., Performance of Popular Turbulence Models For Attached and Separated Adverse Pressure Gradient Flows, AIAA Paper 91-1784, June 1991.

[93] Tuncer Cebeci, Analysis of Turbulent Flows, Second Revised and Expanded Edition, ISBN 0 08 044350 0.

[94] S. E. Rogers, F. R. Menter, P. A. Durbin, Nagi N. Mansour, A Comparison Of Turbulence Models In Computing Multy-Element Airfoil Flows, AIAA-94-0291, 32th Aerospace Science Meeting & Exhibit, Reno, January 10-13, 1994.

[95] W. P. Jones, B. E. Launder, The prediction of laminarization with a two equation model for turbulence, Int. J. Heat Mass Transfer 15, pp. 301-314.

[96] E.G. Tulapurka, Turbulence Models For The Computation of Flow Past Airplanes, Prog. Aerospace Sci, Vol. 33, pp. 71-165, 1997.

[97] Kline S. J., Cantwell B. J., Lilley G. M., eds., 1980-1981 AFOSR-HTTM Stanford Conference on Complex Turbulent Comparison of Computation and Experiment, Stanford University, Stanford, CA, 1981.

[98] Rodi, W. and Scheurer G., Scrutinizing the k-ε Model Under Adverse Pressure Gradient Conditions, Journal Fluids Eng., 108, 1986, pp. 174-179.

[99] Shur M., Strelets, M., Zaikov L., Gulyaev A., Kozlov V. and Secundov A., Comparative numerical testing of one and two equation turbulence models for flows with separation and reattachment, AIAA paper 95-0863, 1995.

[100] Pietro Catalano and Marcello Amato, An evaluation of RANS turbulence modelling for aerodynamic applications, Aerospace Science and Technology 7, pp. 493-509, 2003.

[101] J. E. Bardina, P. G. Huang, T. J. Coakley, Turbulence Modelling Validation Testing and Development, NASA Technical Memorandum 110446, Ames Research Center, April 1997.

[102] Muller, T.J., Jensen, B.J., Aerodynamic Measurements at Low Reynolds Numbers. AIAA 12th Aerodynamic Conference, Williamsburg, Virginia, 1982

[103] Alain Pelletier and Thomas J. Muller, Effect of Endplates on Two – Dimensional Airfoil Testing at Low Reynolds Number. Journal Of Aircraft Vol. 38, November-December 2001 pp. 1056-1059.

[104] P.M. Render, Aerofoil measurements at low Reynolds numbers, CoA Report No 8508, 1985.

[105] Jewel B. Barlow, William H, Rae, JR., Alan Pope, Low-Speed Wind Tunnel Testing, Third Edition, John Wiley & Sons, INC, ISBN 0-471-55774-9.

[106] R.C. Pankhurst & D.W. Holden, Wind Tunnel Technique, Sir Issac Pitman & Sons, LTD, London.

[107] Eastman N. Jacobs, John Stack, Robert M. Pinkerton, Airfoil Pressure Distribution Investigation in the Variable Density Wind Tunnel, NACA Report No. 353.

[108] Ira H. Abbott, Albert E. VON Doenhoff and Louis S. Stivers, Jr Summary of airfoil data, NACA Report No, 824, 1945.

[109] Albert C. Piccirillo, The Clark Y Airfoil: A Historical Retrospective, SAE 2000-01-5517, World Aviation Congress and Exposition, October 2000, San Diego, CA, USA.

[110] Anderson, John D., Jr., A History of Aerodynamics and Its Impact on Flying Machines, Cambridge University Press, Cambridge, UK, 1998

[111] Alain Pelletier and Thomas J. Mueller, Effect of Endplates on Two - Dimensional Airfoil Testing at Low Reynolds Numbers, Journal Of Aircraft Vol.38, No. 6, November – December 2001.

[112] Alain Pelletier and Thomas J. Mueller, Low Reynolds Number Aerodynamics of Low-Aspect-Ratio, Thin/Flat/Cambered-Plate Wings JOURNAL OF AIRCRAFT Vol. 37, No. 5, September–October 2000

[113] Jan Roskam, Chuan-Tau Edward, Airplane Aerodynamics and Performance, Published by DARcorporation, ISBN 1-884885-44-6

[114] Shawn E. Gano, John E. Renaud, Optimize Unmanned Aerial Vehicle With Wing Morphing For Extended Range and Endurance, 9th AIAA/ISSMO Symposium and Exhibit on Multidisciplinary Analysis and Optimization, AIAA-2002-5668

[115] Smith, A. M. O., "High-Lift Aerodynamics," AIAA Journal of Aircraft (37thWright Brothers Lecture), vol. 12, June 1975.

[116] W. Kyle Anderson, Dary L. Bonhaus. Rober McGhee and Betty Walker, Navier-Stokes Computations and Experimental Comparisons for Multielement Airfoil Configuration, NASA Langley research Center.

[117] Anya R. Jones and Holger Babinsky, Leading Edge Flaps at Low Reynolds Numbers, AIAA 2008-424, 46th AIAA Aerospace Science Meeting and Exhibit, Reno, Nevada, 7-10 January.

[118] Woodward, D. S., and Lean, D. E., "Where is High-Lift Today?- A Review of Past UK Research Programmes," Paper presented at AGARD meeting on high-lift aerodynamics. AGARD CP-415, Oct. 1992.

[119] Israeli weapons LTD Citing Internet resources (http://www.israeli-weapons.com/weapons/aircraft/uav/hermes_450/Hermes_450.html)

[120] Jane's Unmanned Aerial Vehicles and Targets. Long-endurance tactical UAV. Hermes 450.

[121] Daniel P. Raymer, Aircraft Design: A Conceptual Approach, Third Edition, AIAA Education Series, ISBN 1-54347-281-3, 1999.

[122] Dr H. Thompson, Aerodynamic lecture handouts 2003,University of Leeds.

[123] B. S. Massey Mechanics Of Fluids Stanley Thornes Publishing 1998 Fifth Edition, ISBN 0-7487-4043-0.

[124] J. Katz, Race Car Aerodynamics, Designing for Speed, Bentley Publishers, ISBN-10: 0-8376-0142-8.

[125] Dr J. Summers: CFD Lecture handouts 2003, University of Leeds.

[126] E. L. Houghton & P.W. Carpenter, Aerodynamics For Engineering Students, Butterworth Heinemann Fifth Edition, ISBN 0-7506-5111-3.

APPENDIX A.
Fluid Dynamics – Background Theory

A.1. Bernoulli's Equation

When an object moves through a fluid (air for this project's purposes) its shape causes the fluid to change direction and speed. Using Newton's first law the change in velocity must be associated with a force. It is to be expected therefore that the pressure of the fluid also would change from point to point [122].

The relationship between these two physical quantities, velocity and pressure is expressed by:

$$P/\rho + V^2/2 = \text{Constant} \qquad [18]$$

where the constant represents the fluid energy level in a given streamline.

Thus considering the change in pressure and velocity from one point in the streamline to the next leads to:

$$P_1/\rho + V_1^2/2 = P_2/\rho + V_2^2/2 \qquad [19]$$

Or for the pressure difference:

$$\Delta P = (V_2^2 - V_1^2)\ \rho/2 \qquad [20]$$

In the case of a symmetric aerofoil moving through air at zero angles of attack ($\alpha = 0^o$) as shown in Figure 161 a velocity and consequently pressure change are expected on the upper and lower surfaces of the aerofoil. However, because of the aerofoil's symmetric nature the

pressure changes on the upper and lower surfaces are equal and opposite therefore no lift results. In addition no pressure drag is expected (since there is no pressure difference) and any value of drag would be due to skin friction instead.

In the cambered aerofoil case as illustrated in Figure 162 however, the velocity of the air on the pressure (lower surface) side is lower than the velocity on the suction (upper surface) side. The obstruction created in the flow due to the aerofoil's increased thickness on the suction side causes the air moving adjacent to it in stream tube A as seen Figure 162 to move out of the way. In doing so, stream tube A is squashed to smaller cross-sectional area. This decrease in the area and the fact that pAV = constant leads to velocity increase around the suction side and consequently a decrease in pressure. Since the aerofoil is designed with positive camber its bottom surface presents less of an obstruction to stream tube B and the flow does not accelerate. As a result, the velocity in stream tube B is less than that in stream tube A. According to Bernoulli's equation (Equation [18]), when velocity increases the pressure decreases therefore the pressure over the suction side of the aerofoil is less than the pressure over the pressure side. This difference in pressure creates an upwards force (lift force).

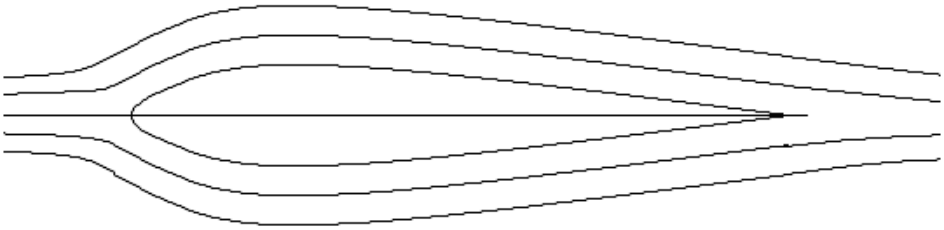

Figure 161: A symmetrical aerofoil at zero angle of attack .

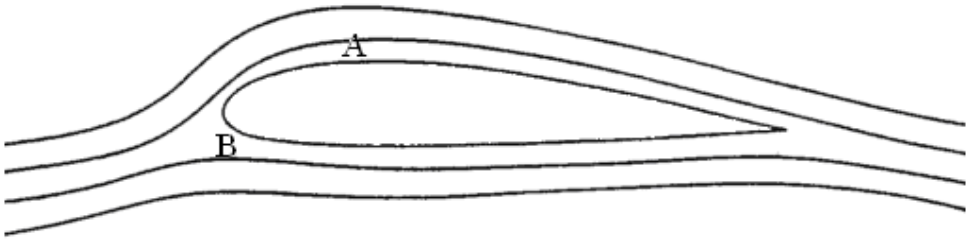

Figure 162: Cambered aerofoil [124].

There is however another way of looking at it and explaining lift [121]. A downwash is created behind the wing caused by the aerofoil camber and angle of attack. Thus the wing has accelerated the air downwards requiring a force to have been applied to the air. An equal and opposite force is therefore applied by the air to the wing according to Newton's law. The downwash momentum in the air adds up to and equals the lift on the wing. According to Raymer [121] both ways of looking at lift are 100% correct. "Lift equals the total downwash momentum imparted on the air" and "lift equals the integrated vertical component of pressures on the wing"

A.2. Viscosity

Viscosity is a measure of resistance to shear in a fluid and is related to the interactions between molecules. The effect of viscosity in a fluid can be demonstrated by the simple example shown in Figure 163 where a viscous fluid is placed between two parallel, solid surfaces.

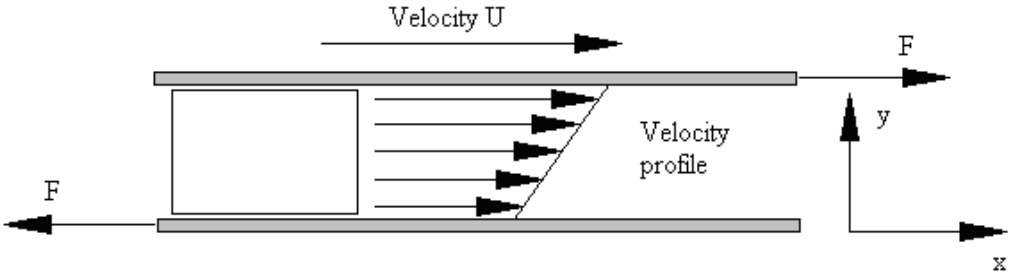

Figure 163: Fluid between two solid surfaces [123].

The lower surface is stationary while the upper surface moves to the right with a constant velocity δu. The molecules in the fluid move in the same direction with the upper surface, but different layers move with different velocities. Due to the no – slip condition the fluid particles adjacent to the two surfaces tend to stick to the solid surfaces and thus maintain a zero relative velocity. This effect gives rise to a velocity gradient between the upper and the lower surfaces as illustrated in Figure 163.

Newton put forward that, for a straight and parallel motion of a given fluid, the tangential stress between two adjoining layers is proportional to the velocity gradient in a direction perpendicular to the layers, that is:

$$\tau = F/A \propto \delta u/\delta y \quad [21]$$

or

$$\tau = \mu \, . \, \delta u/\delta y \quad [22]$$

Where μ is a constant for a particular fluid at a particular temperature. This is known as the coefficient of viscosity or more simply, the viscosity of the fluid. All Newtonian fluids obey the law formalized by $\tau = \mu \, . \, \delta u/\delta y$. Hence Newtonian fluids are fluids whose shear stress at any instance is directly proportional to the applied shear rate (Air is a Newtonian fluid with a constant viscosity of μ = 1.789x10-5 Pa.s) [125].

A.3. Reynolds Number

Reynolds number is a measure of the relative importance of the inertia and viscous terms in the flow (Ratio of Inertia/Viscous terms). Reynolds number is described by the following equation.

$$\text{Re} = (\text{velocity x density x length}) / \text{viscosity} \quad [23]$$

It can be seen that the Reynolds number is large therefore the viscous term is too small when compared to the inertia term. Hence the viscous effects can be assumed to be negligible except near the surface where the boundary layer effects come into existence. This confirms the thin boundary layer theory to be applicable. It is important to note that even if the boundary conditions are steady, it is still possible for the pressure and velocity to vary continuously through time.

A.4. Boundary Layer

There are two fundamental characteristics in a real flow that must be cited prior to discussing boundary layers.

- There is no discontinuity in velocity
- At the solid surface, the fluid velocity relative to the surface is zero (no – slip condition).

As a consequence close to the surface, there is a region in which the velocity rapidly increases from zero and approaches that of the main stream. This is known as the boundary layer region and is illustrated below.

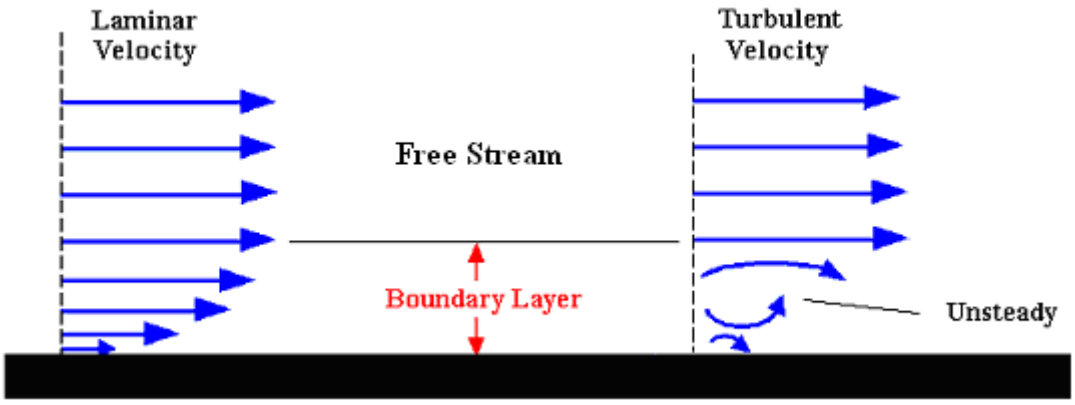

Figure 164: Velocity is zero at surface (no-slip condition).

When a body or object moves through a fluid medium, the molecules of the fluid near the object are disturbed, displaced and forced to move away and around the object. The fluid having originally velocity u_∞ in the direction of the object say a plate (Figure 164) is retarded in the neighbourhood of the surface, and the boundary layer begins at the leading edge of the plate. As increasingly more of the fluid is slowed down the thickness of this layer increases. Hence the boundary layer starts off being fairly thin and laminar at the front of the moving plate, then thickens and becomes quite turbulent. Depending on the value of the Reynolds Number, boundary layers may be either laminar, or turbulent. For lower Reynolds number, the boundary layer is laminar with the streamwise velocity changing uniformly with distance away from the plate, as shown on the left hand side of Figure 164 above. Assuming that a flow is laminar the two physical quantities of interest are the boundary layer thickness δ_b and

shear stress τ_ω at location χ. Formulae for these quantities can be deduced from laminar boundary layer theory. However, the results which have been verified by experiment, are as follows [81]:

$$\delta = \frac{5.2\chi}{\sqrt{\mathrm{Re}_\chi}} \qquad [24]$$

where $\mathrm{Re}_\chi = \rho_\infty V_\infty \chi / \mu_\infty$ as defined by Equation [23].

Equation [24] demonstrates the powerful influence of the Reynolds number Re in aerodynamic calculations. By substituting Re in Equation [24] it follows that $\delta \propto \chi^{0.5}$ that is, the laminar boundary layer grows parabolically.

The local shear stress τ_w is also a function of χ and it can be deduced from:

$$\tau_w = \frac{1}{2} Cf_\chi \rho_\infty V_\infty^2 \qquad [25]$$

were Cf_χ is the skin friction coefficient. The skin friction is dimensionless and is defined as the local shear stress divided by the pressure at the outer edge of the boundary [81].

From boundary layer theory:

$$Cf_\chi = \frac{0.664}{\sqrt{\mathrm{Re}_\chi}} \qquad [26]$$

and the total skin friction coefficient is therefore given as:

$$Cf = \frac{1.328}{\sqrt{\mathrm{Re}_L}} \qquad [27]$$

were the Reynolds number is now based on the total length L.

For higher Reynolds numbers, the boundary layer is characterized by turbulence and the streamwise velocity is unsteady (as shown on the right hand side of Figure 164 above). Turbulence is one of the major unsolved problems in theoretical physics. Knowledge of boundary layer thickness δ_b and shear stress τ_ω therefore rely on experimental results. Such results yield the following approximate formula [81].

$$\delta = \frac{0.37\chi}{\mathrm{Re}_\chi^{0.2}} \qquad [28]$$

It can be seen from Equation [28] that a turbulent boundary layer grows approximately as $\chi^{4/5}$ which is faster than a laminar boundary layer $\chi^{1/2}$.

The local skin friction coefficient for turbulent flow over a flat plate can be approximated by:

$$Cf_\chi = \frac{0.0592}{\mathrm{Re}_\chi^{0.2}} \qquad [29]$$

and the total skin friction coefficient is given approximately as:

$$Cf = \frac{0.074}{\mathrm{Re}_L^{0.2}} \qquad [30]$$

In between there is the transition region. In this region the laminar layer becomes disturbed and the motion within it becomes unstable. The resulting flow irregularities develop into turbulence, causing the thickness of the layer to increase more rapidly over a short length (Figure 164). As previously mentioned a boundary layer is formed around the body and therefore has a similar shape with it. However, sometimes it may separate from the body. This happens because the flow in the boundary layer, relative to the free stream, has very low energy and is therefore more easily driven by changes in pressure. At high angles of attack, flow separation is the cause for wing stall and is discussed in a following section.

Other factors that influence the transition from laminar to turbulent conditions are:

- Surface roughness
- Body forces
- Free stream disturbances
- Pressure gradient

A.5. Flow separation

Flow separation occurs when the air flow does not follow the contours of the body and separates from it. Figure 165 shows the behaviour of a boundary layer in a positive pressure gradient.

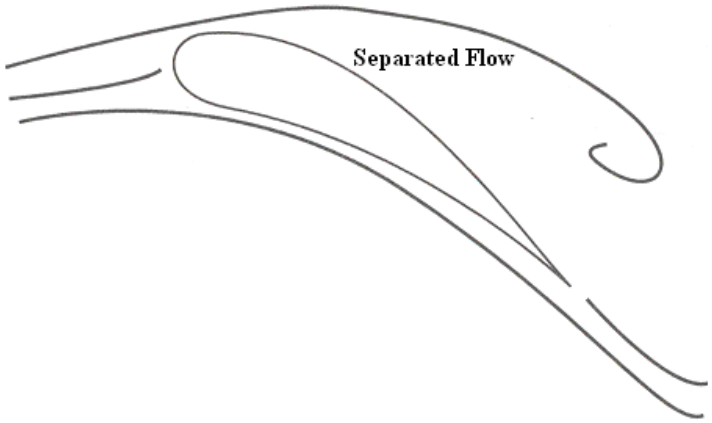

Figure 165: Illustration of separated flow [124].

The variation in pressure along a normal to the surface through the boundary layer thickness is essentially zero, so that the pressure at any point in the mainstream, adjacent to the edge of the boundary layer, is transmitted unaltered through the layer to the surface.

Due to viscosity effects and retarding forces the flow near the boundary of the object will slow down. This slowing down effect will be more pronounced adjacent the surface where the elements are more remote from the accelerating effect, via shearing actions, of the mainstream, so that the successive profile shape in the streamwise direction will change in the manner shown in Figure 165.

Furthermore at point A on the surface of the object, the velocity gradient $(d_u/d_y)_w$ becomes zero. Apart from the change in shape of the profile it is evident that the boundary layer must get thicker rapidly under these conditions in order to satisfy continuity within itself. Downstream of point A the flow adjacent to the surface will be in an upstream direction, so that a circulatory movement, in a plane normal to the surface, takes place near the surface. At point A the momentum of the fluid is insufficient to carry the fluid element further into the region of increased pressure. Hence at this point the air is brought to rest and separates from the surface [126].

The result of separation on the rear half of the aerofoil is to increase the thickness of the wake flow and therefore increase in the pressure drag acting on the aerofoil [126].

A.6. Drag & Lift

When a body (aerofoil or wing) travels through air it experiences two aerodynamic forces, drag and lift.

A.6.1. Drag

Drag is defined as the aerodynamic force that opposes a body's motion in a fluid. Furthermore it is also considered as a measure of the effectiveness of the body to progress through the fluid. It is a mechanical force and is generated by the interaction and contact of a solid body with a fluid.

Drag may be deduced from:

$$D = 0.5 \, . \, C_d \, . \, A \, . \, \rho \, . \, V^2 \qquad [31]$$

Drag is made up by two types of forces:

- Skin friction drag or surface friction drag
- Pressure drag

Skin friction drag is the drag that is generated by the resolved components of the traction due to shear stresses acting on the surface of the body. This traction is due directly to viscosity and acts tangentially at all points on the surface of the body. At each point it has a component aligned with but opposing the undisturbed flow over the whole exposed surface of the body. It could not exist in an invisid flow. As the skin friction is an interaction between a solid and a fluid, the magnitude of the skin friction drag is dependent on the properties of both the solid and fluid. For example for the solid a smooth, waxed and polished surface would produce less skin friction compared to a roughened surface, while for the fluid the magnitude depends on its viscosity and the relative magnitude of the viscous forces to the motion of the flow, expressed as the Reynolds Number.

A.6.2. Lift

Lift is a mechanical force. It is generated by the interaction and contact of a solid body with a fluid. In the case of an aerofoil both the upper and the lower surfaces of the aerofoil contribute to lift generation and it is wrong to neglect the effect of the upper surface. Lift depends on many factors such as the shape of the body, the surface area over which the air flows and the body's inclination to the flow; It also depends on the density of the air, the air's viscosity and compressibility and the square of the velocity. In general, the relationship and interdependence of body shape, inclination, air viscosity, and compressibility is very complex and can be characterized by a single variable called lift coefficient C_l.

The lift coefficient, as a term, is a number used by aerodynamicists to express and model all complex variations of shape, inclination and some flow conditions on lift. The lift coefficient C_l is expressed as:

$$C_L = L / (0.5 . A . \rho . V^2) \qquad [32]$$

The lift coefficient contains the complex dependencies of object shape on lift. For three-dimensional aerofoil (wing), the downwash generated near the wing tips reduces the overall lift coefficient of the wing.

APPENDIX B.

Finite Volume Method

The finite volume method is used by the Fluent solver to arrive at converged solutions.

The finite volume method is described as ‘‘a numerical method for solving partial differential equations that calculates the values of the conserved variables average across the volume’’. The term finite volume refers to the small volume surrounding each node point on a mesh. (It views space as being broken down into a set of volumes each of which surrounds one of the points). In the finite volume method, volume integrals in a partial differential equation containing a divergence term are converted to surface integrals using the ‘‘*divergence theorem’’*. These terms are then evaluated as fluxes at the surface of each finite volume.

The finite volume method has the advantage over finite difference methods in that it does not actually require a structured mesh even though a structured mesh may be used. In addition, the finite volume method is often preferred to other methods due to the fact that boundary conditions may be applied non-invasively. This could be done because the values of the conserved variables are in fact located within the volume element, and not as nodes or surfaces. Furthermore, finite volume methods are particularly powerful in calculations where the mesh moves to track interfaces or shocks and on coarse non-uniform grids in general.

The steps which the finite volume method utilises are [62]:

d) Formal integration of the governing equation(s) of fluid flow over the (finite) cells/control volumes making up the solution domain.
e) Converting the resulting integral equations into a system of algebraic equations by approximating the terms therein, for processes such as convective and diffusive transport by interpolation functions for the face values of the cells/control volumes written in terms of local nodal values.
f) Solution of the algebraic equations.

Fluent uses the finite volume method because it provides a clearer relationship between the numerical algorithm and the underlying physical conservation principle.

For instance, a velocity component (Φ) within a finite control volume may be expressed as a balance between the various processes which tend to increase or decrease it.

Rate of change of		Net flux of Φ due		Net flux of Φ due		Net rate of creation
Φ in the control	=	to convection into	+	to diffusion into	+	of Φ inside the
volume w.r.t time		the control volume		the control volume		control volume [62].

APPENDIX C.

Derivation of y+

The wall y^+ is a non-dimensional number defined as:

$$y^+ = \frac{u_\tau y}{v}$$

Where v is the local kinematic viscosity of the fluid, u_τ is the friction velocity and y is the vertical Distance normal to wall direction.

Unfortunately y^+ is dependent on the friction velocity u_τ which is not known unless the solution of the flow is known. Friction velocity is represented by:

$$u_\tau = \sqrt{\frac{\tau_\omega}{\rho}} \qquad [33]$$

Where τ_ω is the shear stress at the nearest wall grid point. Experimental correlations obtained for simpler flows may therefore be used in order to estimate the values of y and y^+. In the case of an external flow around an aerofoil an appropriate correlation may be given using the formula for the flat plate skin friction coefficient.

$$C_f = 0.074 \times Re_C^{-0.2} \text{ [80]} \qquad [34]$$

Where Re_C is based on the aerofoil's chord c and free steam velocity U_∞.

$$u_\tau = U_\infty \sqrt{\frac{C_f}{2}} \qquad [35]$$

$$y_\tau = \frac{v}{u_\tau} = \frac{v}{U_\infty}\sqrt{\frac{2}{C_f}} \quad [36]$$

$$y = y^+ y_\tau = \ y^+ \frac{v}{U_\infty}\sqrt{\frac{2}{C_f}} \quad [37]$$

$$\frac{y}{C} = y^+ \frac{v}{CU_\infty}\sqrt{\frac{2}{C_f}} = \ y^+ \frac{\sqrt{2}}{Re_C}\frac{1}{\sqrt{0.074}}\ Re_C^{0.1} \quad [38]$$

$$\Longrightarrow \frac{y}{C} = 5.2 \cdot y^+ \cdot Re_C^{-0.9} \quad [39]$$

Rearranging the above equation we have:

$$y = 5.2 \cdot y^+ \cdot Re_C^{-0.9} \cdot C \quad [40]$$

This is the equation used for the calculation of y to obtain the required values of y^+.

APPENDIX D.

Turbulence Model Selection

Among the most frequently used two-equation turbulence models, is the k-ε model which makes use of the turbulent dissipation rate ε as second turbulent scale. This model was proposed in the standard form by Jones and Launder [95] and has been the subject of much research and effort mainly dedicated to the stiffness of the equation ε. The k-ε model is valid when the Reynolds number is high. Whatever the free stream Reynolds number, near a solid boundary, the mean velocity is low, the mean velocity gradient is therefore high and the turbulent velocity fluctuations are damped. Therefore in this region, when deriving the model some, of the assumptions made are violated, for example the terms which represent the diffusion by molecular viscosity are not in fact small by comparison with other terms. Special treatments are therefore required for the near wall region. In aerodynamics, the greatest limitation of the k-ε turbulence model is the lack of sensitivity to adverse pressure gradient [96]. The model significantly overpredicts the shear-stress levels under those conditions, hence delaying or completely preventing flow separation [97]. Rodi [98], attributes this shortcoming to the overprediction of the turbulent length scale in the near wall region.

The k-ω [89] turbulence models are becoming more popular in recent years, as they have been shown to be less stiff, and are more accurate for the boundary layer flows subjected to adverse pressure gradient than the k-ε [77]. The k-ω model does not require any correction near the wall, but is rather sensitive to the freestream conditions [91], while the k-ε model needs to be modified near the wall, but is not so sensitive to freestream conditions. Menter [83], combines the k-ε and k-ω models in such a way that would allow them to be used in regions where they perform the best. Therefore this method uses the k-ω model near the wall, but then switches through a function of F_1 to the k-ε equations away from the wall, with these equations having been transformed to k-ω format. Menter called the new model as “shear stress transport or SST k-ω model”.

The SST model has proved to produce superior results for flows with strong adverse pressure gradients than the results achieved with either the original k-ε or k-ω models [83],[85]. An evaluation of the SST method, as compared with two one-equation models has been presented by Shur et al [99]. The one-equation models are those of their own and that of Spalart-Allmaras. They conclude that for flows over backward and forward facing steps, these models perform significantly better than the standard k-ε model. Its noted however, that none of the models captures all the details of the flow. The SST method is better in the recirculation zone for backward facing step, while the one-equation models are somewhat better in the region downstream of reattachment.

According to Pietro Catalano and Marcello Amato [100], the SST k-ω has provided results similar to the nonlinear k-ε, but being less stiff and computational expensive. The shear stress transport formulation has proved to be effective and important to improve the results. This model has been utilised in an application to compute the drag polar of a three-component aerofoil in high lift conditions up to stall. The aerodynamic coefficients have been reproduced with satisfactory accuracy in the model and predicted the sudden characteristic of the stall presented in the experimental data [100]. In conclusion, the SST k-ω, for the transonic and high–lift flows investigated by Pietro Catalano and Marcello Amato, has shown the best compromise between the physical capabilities and the numerical stiffness.

In published literature, it seems there are disagreements about which model is more accurate between the Wilcox k-ω and the Launder–Sharma k-ε, with the first to be superior in numerical stability to the k-ε model primarily in the viscous sublayer near the wall and the later to give reasonably good results, for free-shear-layer flows with relatively small pressure gradients. For wall bounded flows, the k-ε model gives good agreement with experimental results for zero and small pressure gradients, but is less accurate for large adverse pressure gradients [101]. The predictions of k-ε are insensitive to freestream values of turbulence, in contrast to k-ω which shows sensitivity to small freestream values of ω [101]. Most authors however, judge that for aerodynamic applications, the best overall model is the SST k-ω, followed by the Spalart –Allmaras.

APPENDIX E.

The k-ω SST model

The k-ω SST model was developed by Menter [85],[91],[92], based on the k-ω model of Wilcox and in its conservation form is given by the following equations:

$$\frac{\partial(\rho k)}{\partial t} + \frac{\partial(\rho u_j k)}{\partial x_j} = P - \beta^* \rho \omega k + \frac{\partial}{\partial x_j}\left[(\mu + \sigma_k \mu_t)\frac{\partial k}{\partial x_j}\right]$$

$$\frac{\partial(\rho \omega)}{\partial t} + \frac{\partial(\rho u_j \omega)}{\partial x_j} = \frac{\gamma}{\nu_t} P - \beta \rho \omega^2 + \frac{\partial}{\partial x_j}\left[(\mu + \sigma_\omega \mu_t)\frac{\partial \omega}{\partial x_j}\right] + 2(1-F_1)\frac{\rho \sigma_{\omega 2}}{\omega}\frac{\partial k}{\partial x_j}\frac{\partial \omega}{\partial x_j}$$

The k-ω SST was considered the most suitable for this project since it predicts complex flows involving separation while giving results comparable with the best of the other models for simple flows. The two main characteristic features of this model are:

a) a zonal weighting of model coefficients and

b) a limitation on the growth of the eddy viscosity in rapidly strained flows.

The zonal modelling, uses Wilcox's k-ω model near solid walls and Laurent and Sharma's k-ε model near boundary layer edges and in free shear layers. This switching is achieved with a blending function (F_1) of the model coefficients. The shear stress transport modelling also modifies the eddy viscosity by forcing the turbulent shear stress to be bounded by a constant, times the turbulent kinetic energy inside boundary layers. This modification improves the prediction of flows with strong adverse pressure gradients and separation [93], which implies that it should be more appropriate for this case. This model utilizes the Enhanced Wall Treatment, which determines the near wall region by the use of a fine mesh with $y^+ \approx 1$. Coarser near wall meshes are also accepted provided the value of y^+ does not exceed 4-5 as previously mentioned. To resolve the viscous sub-layer the two-layer zonal model is applied for fine mesh densities. The Enhanced Wall Function (EWF) blends the linear and logarithmic laws by using a function to represent the laminar sub-layer, buffer region and fully turbulent outer region.

APPENDIX F.

Cp plots for a baseline Clark Y at Re = 0.6x10^6 and AOA range of α=0^o to 15^o.

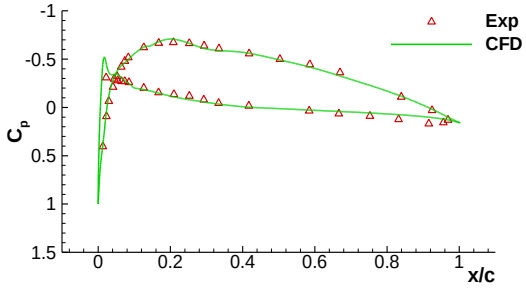

Figure 166. Experimental and numerical C_p plots for a baseline Clark Y at Re=0.6x10^6 and α=0^o.

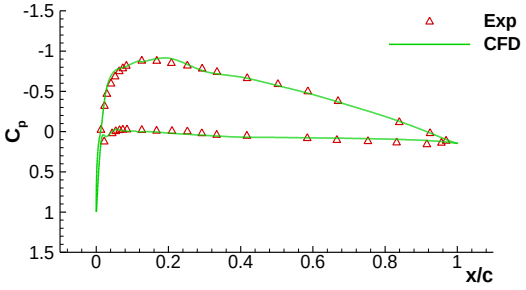

Figure 167. Experimental and numerical C_p plots for a baseline Clark Y at Re=0.6x10^6 and α=2^o.

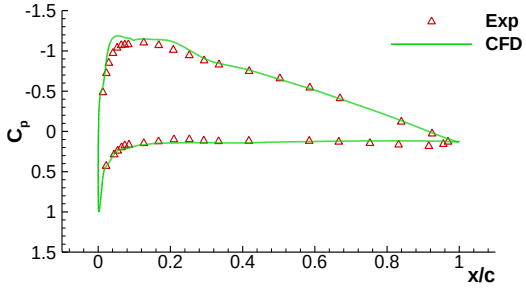

Figure 168. Experimental and numerical C_p plots for a baseline Clark Y at Re=0.6x10^6 and α=4^o.

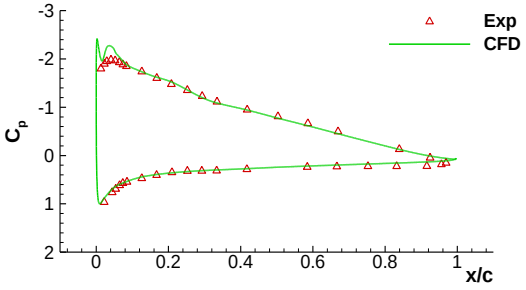

Figure 169. Experimental and numerical C_p plots for a baseline Clark Y at Re=0.6x10^6 and α=8^o.

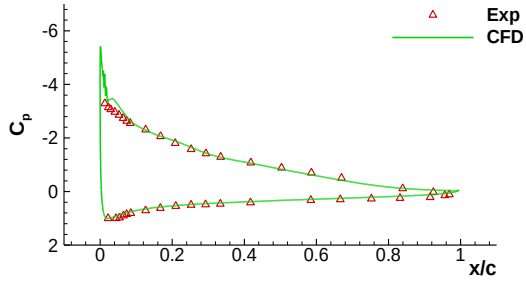

Figure 170. Experimental and numerical C_p plots for a baseline Clark Y at Re=0.6x10^6 and α=12^o.

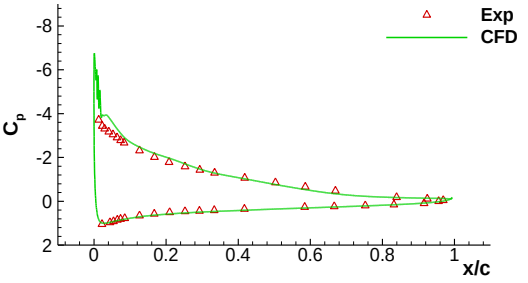

Figure 171. Experimental and numerical C_p plots for a baseline Clark Y at Re=0.6x10^6 and α=14^o.

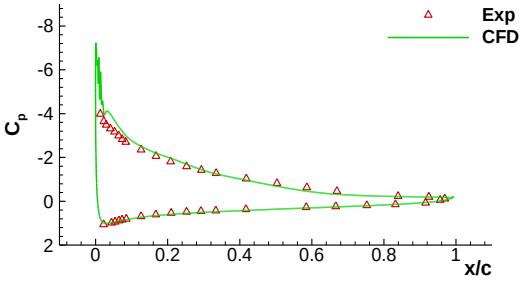

Figure 172. Experimental and numerical C_p plots for a baseline Clark Y at Re=0.6x10^6 and α=15^o.

Cp plots for a baseline Clark Y at Re = 1.6x10^6 and AOA range of α=0^o to 15^o.

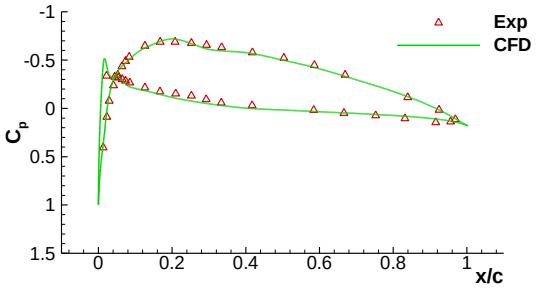

Figure 173. Experimental and numerical C_p plots for a baseline Clark Y at Re=1.6x10^6 and α=0^o.

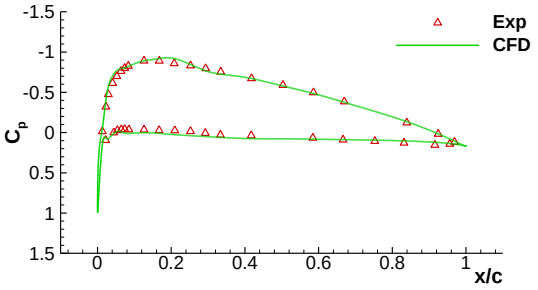

Figure 174. Experimental and numerical C_p plots for a baseline Clark Y at Re=1.6x10^6 and α=2^o.

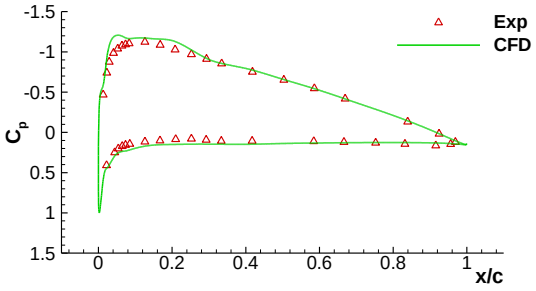

Figure 175. Experimental and numerical C_p plots for a baseline Clark Y at Re=1.6x10^6 and α=4^o.

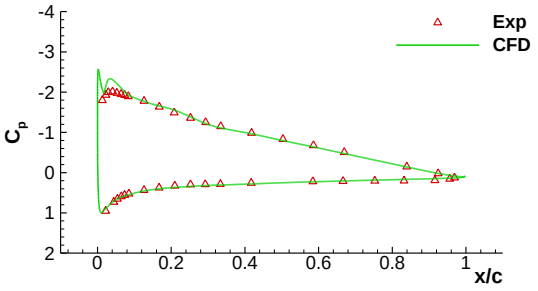

Figure 176. Experimental and numerical C_p plots for a baseline Clark Y at Re=1.6x10^6 and α=8^o.

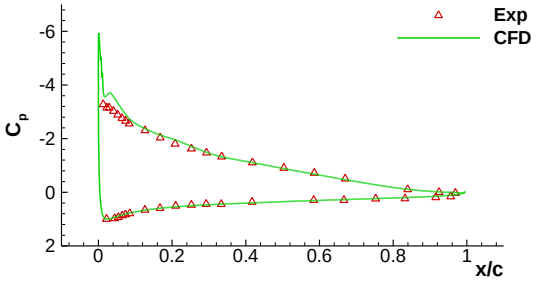

Figure 177. Experimental and numerical C_p plots for a baseline Clark Y at Re=1.6x10^6 and α=12^o.

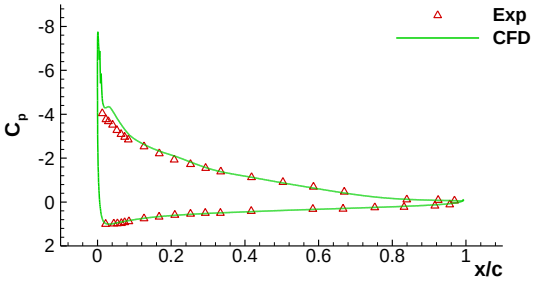

Figure 178. Experimental and numerical C_p plots for a baseline Clark Y at Re=1.6x10^6 and α=14^o.

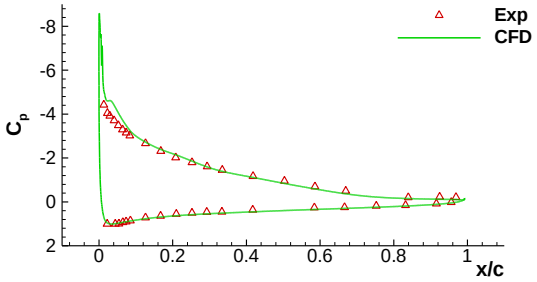

Figure 179. Experimental and numerical C_p plots for a baseline Clark Y at Re=1.6x10^6 and α=15^o.

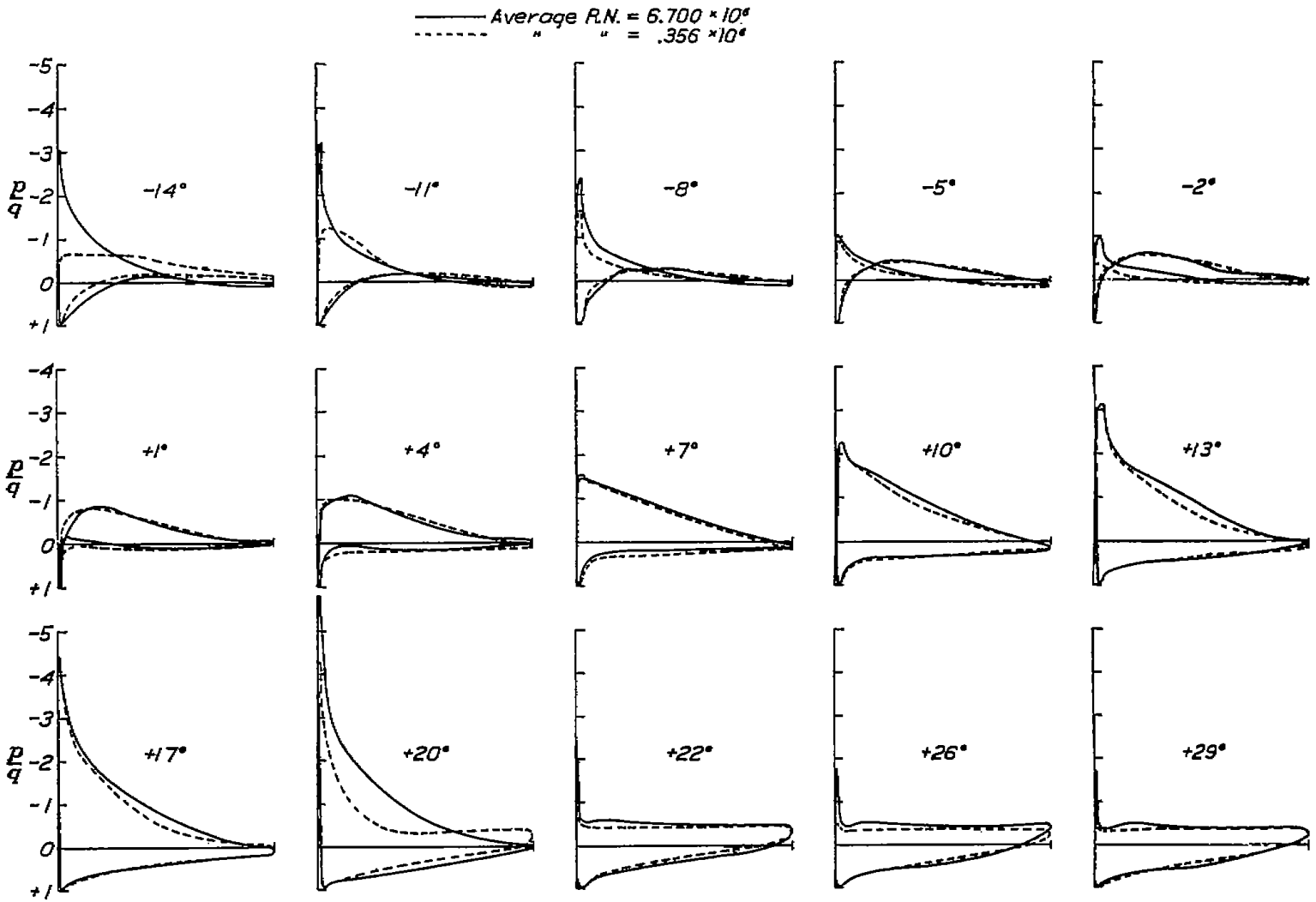

Figure 180: Pressure distribution around a Clark Y at Re=6.7x10^6 and 0.356x10^6 [107].

APPENDIX G.

C_p values with 10% flap at $\delta = 110^o$ and $Re=0.6x10^6$

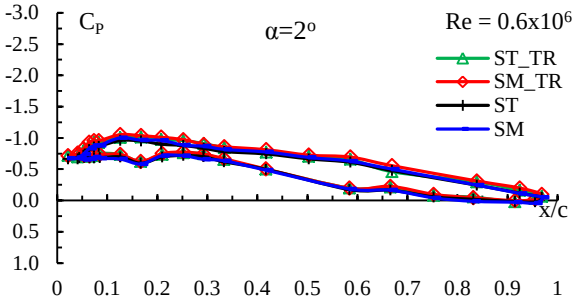

Figure 181. Exp C_p plots for the four configurations examined, with $\delta = 110^o$ at $Re=0.6x10^6$ and $\alpha=2^o$.

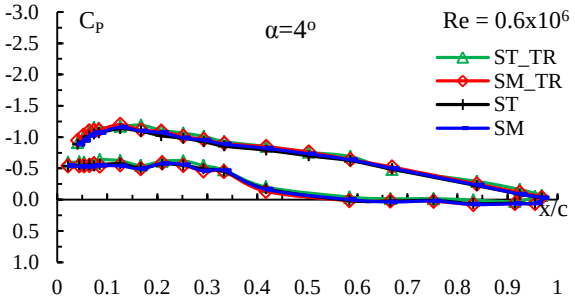

Figure 182. Exp C_p plots for the four configurations examined, with $\delta = 110^o$ at $Re=0.6x10^6$ and $\alpha=4^o$.

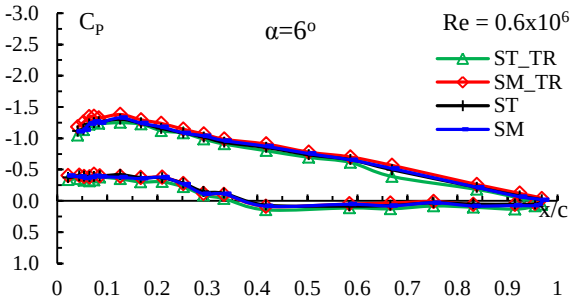

Figure 183. Exp C_p plots for the four configurations examined, with $\delta = 110^o$ at $Re=0.6x10^6$ and $\alpha=6^o$.

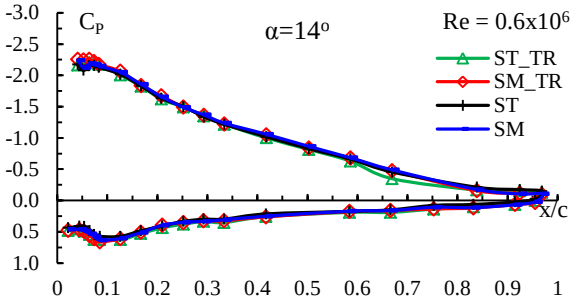

Figure 184. Exp C_p plots for the four configurations examined, with $\delta = 110^o$ at $Re=0.6x10^6$ and $\alpha=14^o$.

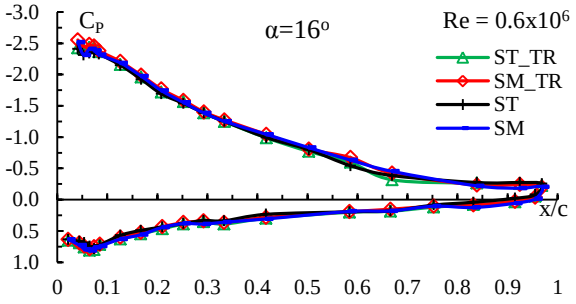

Figure 185. Exp C_p plots for the four configurations examined, with $\delta = 110^o$ at $Re=0.6x10^6$ and $\alpha=16^o$.

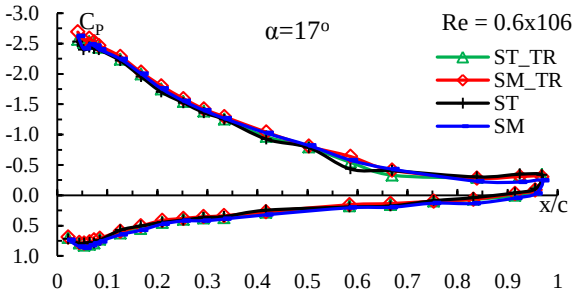

Figure 186. Exp C_p plots for the four configurations examined, with $\delta = 110^o$ at $Re=0.6x10^6$ and $\alpha=17^o$.

Cp values with 10% flap at δ = 110° and Re=1x10^6

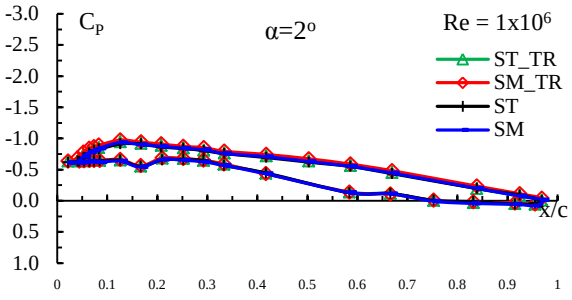

Figure 187. Exp C_p plots for the four configurations examined, with δ = 110° at Re=1x10^6 and α=2°.

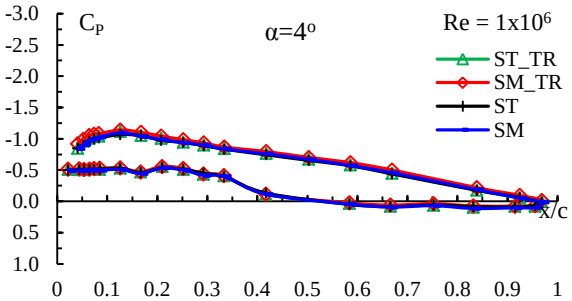

Figure 188. Exp C_p plots for the four configurations examined, with δ = 110° at Re=1x10^6 and α=4°.

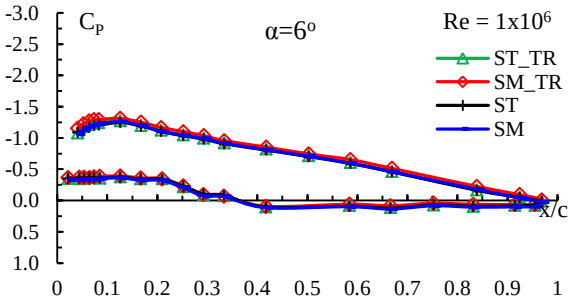

Figure 189. Exp C_p plots for the four configurations examined, with δ = 110° at Re=1x10^6 and α=6°.

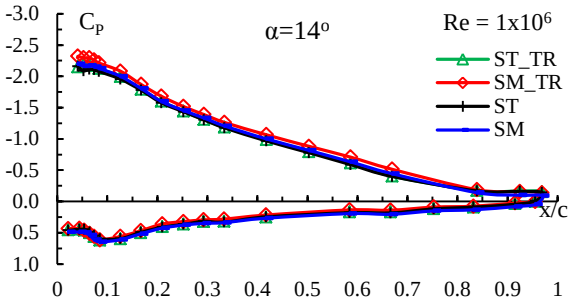

Figure 190. Exp C_p plots for the four configurations examined, with δ = 110° at Re=1x10^6 and α=14°.

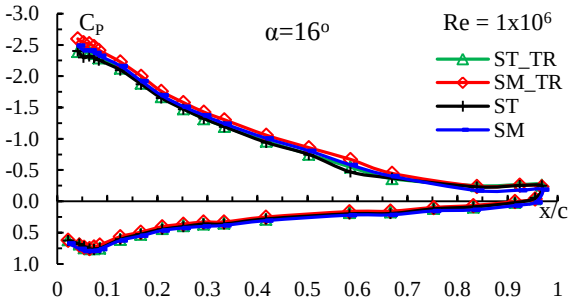

Figure 191. Exp C_p plots for the four configurations examined, with δ = 110° at Re=1x10^6 and α=16°.

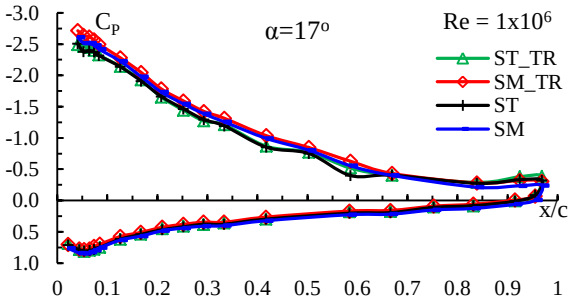

Figure 192. Exp C_p plots for the four configurations examined, with δ = 110° at Re=1x10^6 and α=17°.

Cp values with 10% flap at $\delta = 110^o$ and $Re=1.6x10^6$

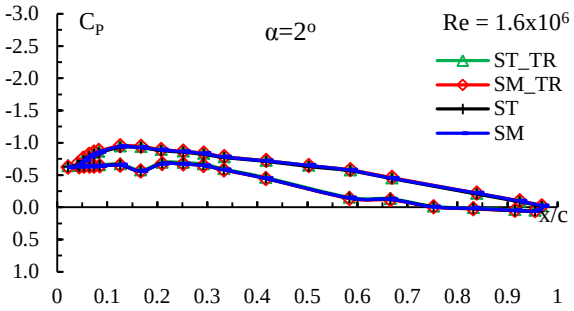

Figure 193. Exp C_p plots for the four configurations examined, with $\delta = 110^o$ at $Re=1.6x10^6$ and $\alpha=2^o$.

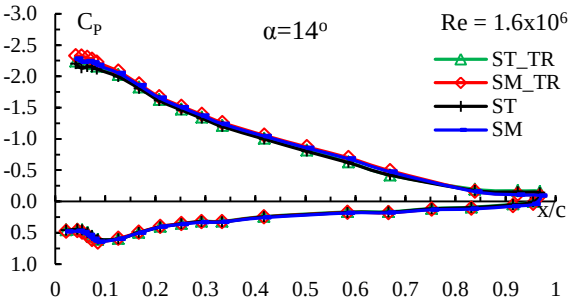

Figure 196. Exp C_p plots for the four configurations examined, with $\delta = 110^o$ at $Re=1.6x10^6$ and $\alpha=14^o$.

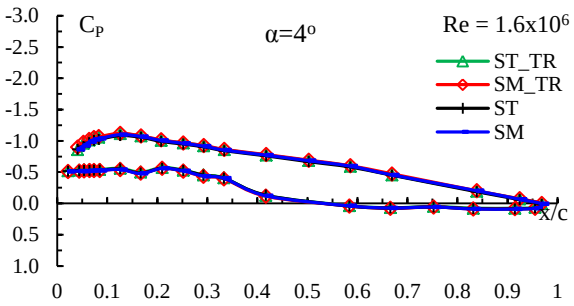

Figure 194. Exp C_p plots for the four configurations examined, with $\delta = 110^o$ at $Re=1.6x10^6$ and $\alpha=4^o$.

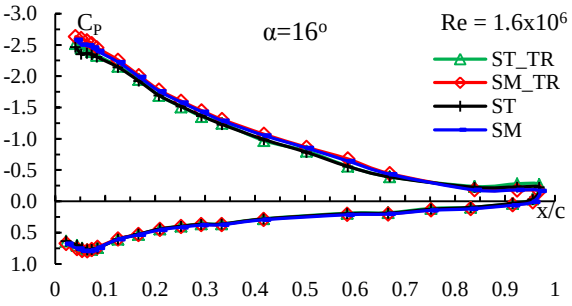

Figure 197. Exp C_p plots for the four configurations examined, with $\delta = 110^o$ at $Re=1.6x10^6$ and $\alpha=16^o$.

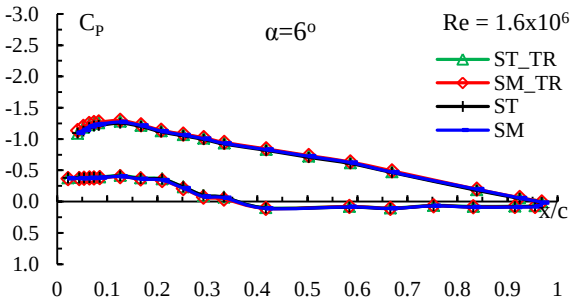

Figure 195. Exp C_p plots for the four configurations examined, with $\delta = 110^o$ at $Re=1.6x10^6$ and $\alpha=6^o$.

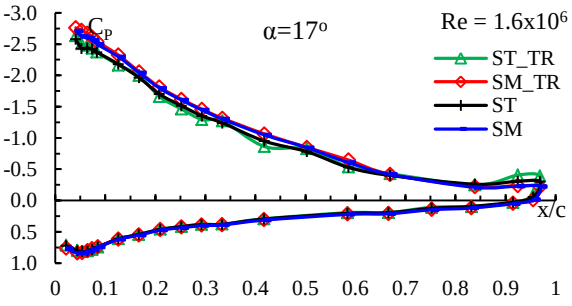

Figure 198. Exp C_p plots for the four configurations examined, with $\delta = 110^o$ at $Re=1.6x10^6$ and $\alpha=17^o$.

Cp values with 5% flap at δ = 50° and Re=0.6x10^6

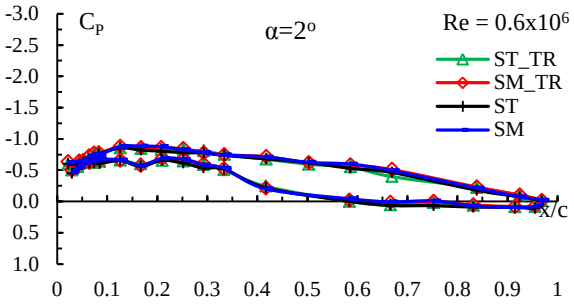

Figure 199. Exp C_p plots for the four configurations examined, with δ = 50° at Re=0.6x10^6 and α=2°.

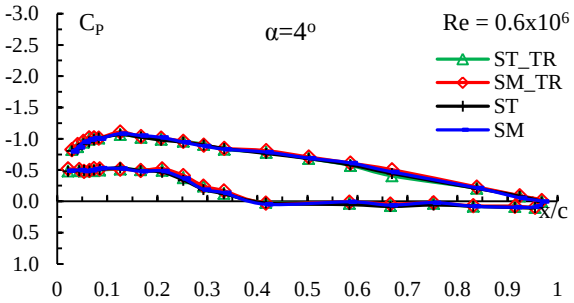

Figure 200. Exp C_p plots for the four configurations examined, with δ = 50° at Re=0.6x10^6 and α=4°.

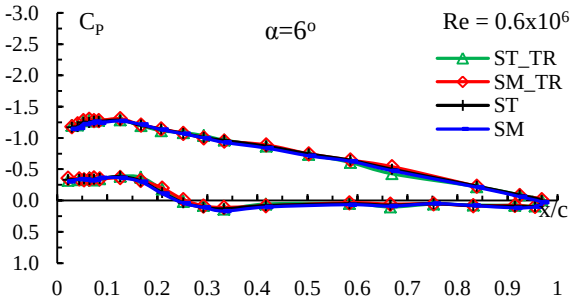

Figure 201. Exp C_p plots for the four configurations examined, with δ = 50° at Re=0.6x10^6 and α=6°.

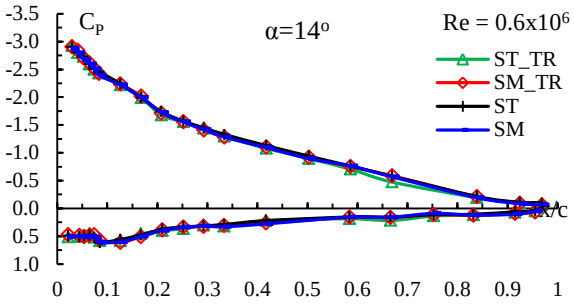

Figure 202. Exp C_p plots for the four configurations examined, with δ = 50° at Re=0.6x10^6 and α=14°.

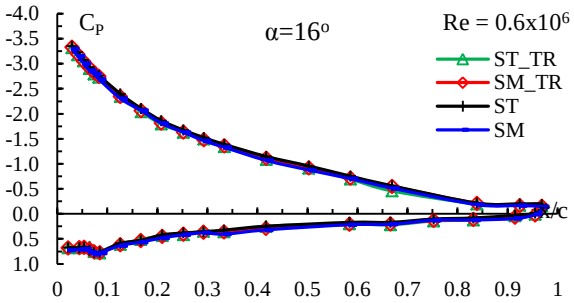

Figure 203. Exp C_p plots for the four configurations examined, with δ = 50° at Re=0.6x10^6 and α=16°.

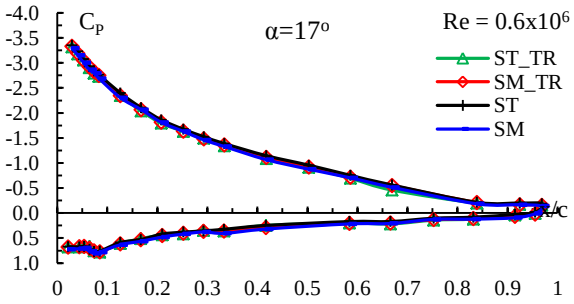

Figure 204. Exp C_p plots for the four configurations examined, with δ = 50° at Re=0.6x10^6 and α=17°.

Cp values with 5% flap at δ = 50° and Re=1x10^6

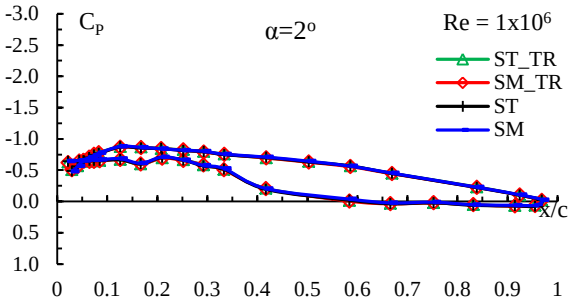

Figure 205. Exp C_p plots for the four configurations examined, with δ = 50° at Re=1x10^6 and α=2°.

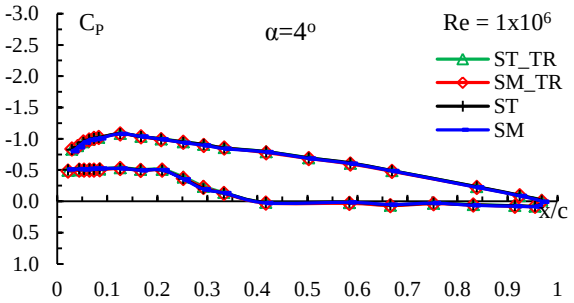

Figure 206. Exp C_p plots for the four configurations examined, with δ = 50° at Re=1x10^6 and α=4°.

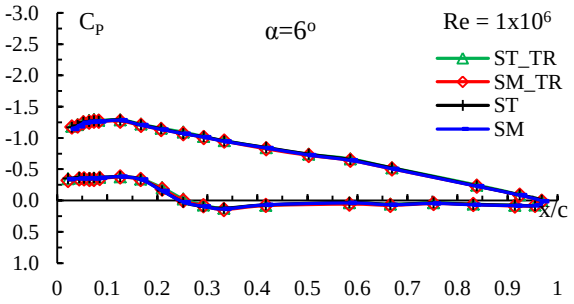

Figure 207. Exp C_p plots for the four configurations examined, with δ = 50° at Re=1x10^6 and α=6°.

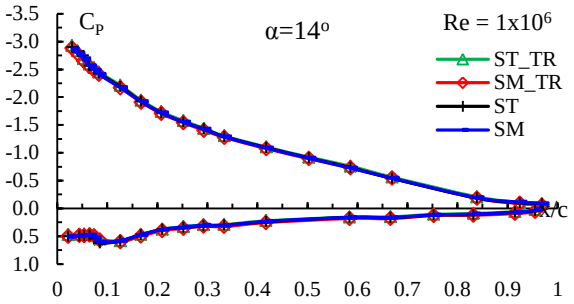

Figure 208. Exp C_p plots for the four configurations examined, with δ = 50° at Re=1x10^6 and α=14°.

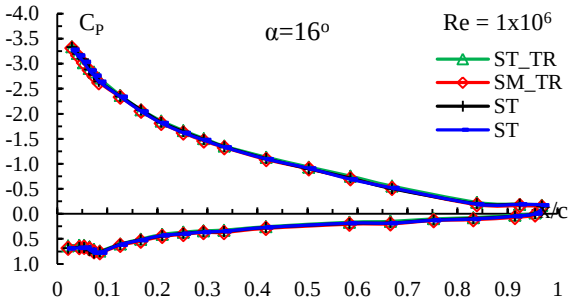

Figure 209. Exp C_p plots for the four configurations examined, with δ = 50° at Re=1x10^6 and α=16°.

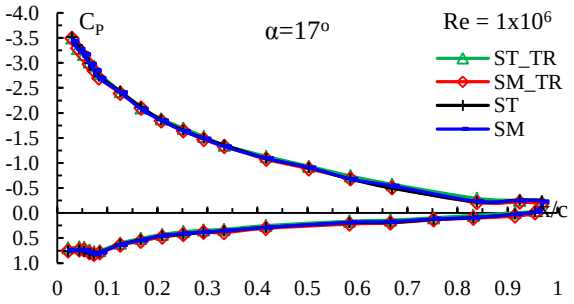

Figure 210. Exp C_p plots for the four configurations examined, with δ = 50° at Re=1x10^6 and α=17°.

Cp values with 5% flap at $\delta = 50^o$ and $Re=1.6x10^6$

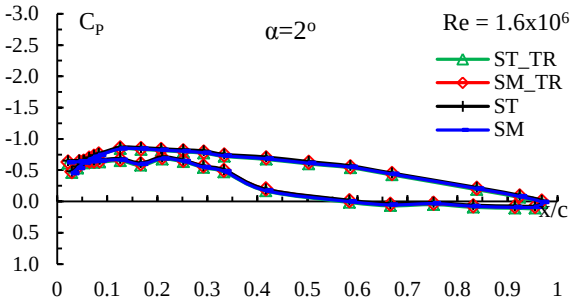

Figure 211. Exp C_p plots for the four configurations examined, with $\delta = 50^o$ at $Re=1.6x10^6$ and $\alpha=2^o$.

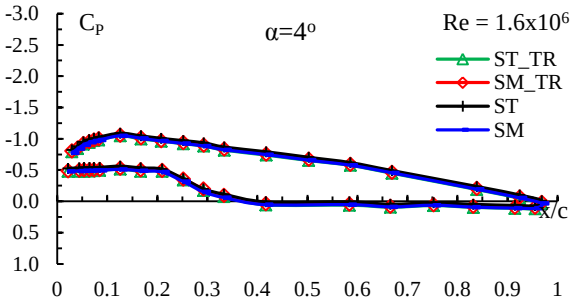

Figure 212. Exp C_p plots for the four configurations examined, with $\delta = 50^o$ at $Re=1.6x10^6$ and $\alpha=4^o$.

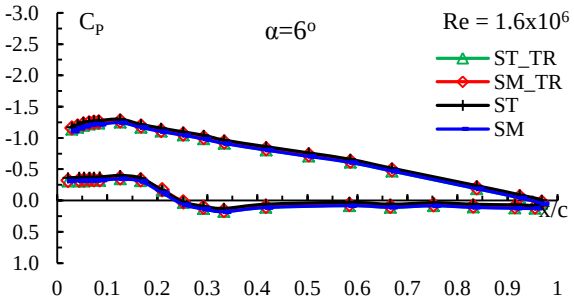

Figure 213. Exp C_p plots for the four configurations examined, with $\delta = 50^o$ at $Re=1.6x10^6$ and $\alpha=6^o$.

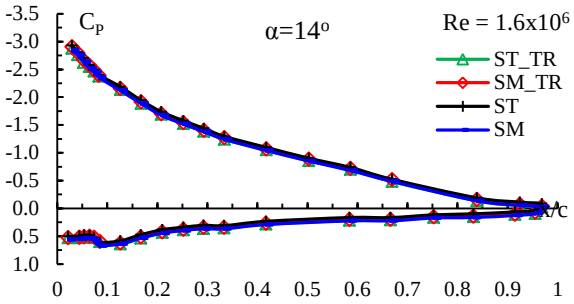

Figure 214. Exp C_p plots for the four configurations examined, with $\delta = 50^o$ at $Re=1.6x10^6$ and $\alpha=14^o$.

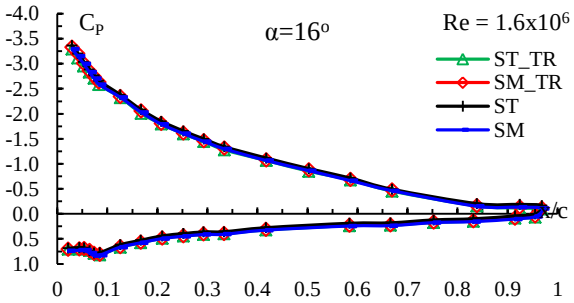

Figure 215. Exp C_p plots for the four configurations examined, with $\delta = 50^o$ at $Re=1.6x10^6$ and $\alpha=16^o$.

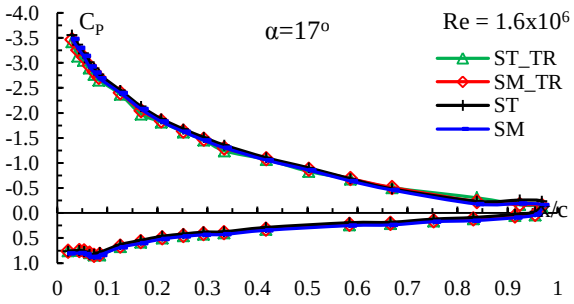

Figure 216. Exp C_p plots for the four configurations examined, with $\delta = 50^o$ at $Re=1.6x10^6$ and $\alpha=17^o$.

APPENDIX H.

Velocity magnitude contours of Clark Y

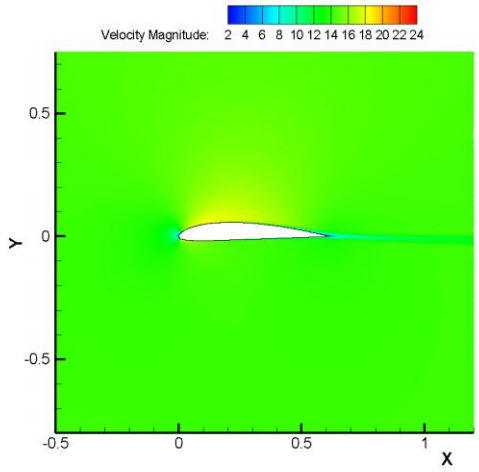

Figure 217: Velocity magnitude contours of Clark Y at $\alpha=0^o$ and Re=0.6x10^6

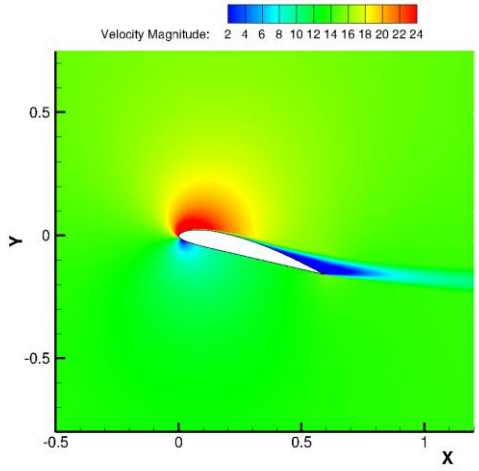

Figure 218: Velocity magnitude contours of Clark Y at $\alpha=15^o$ and Re=0.6x10^6

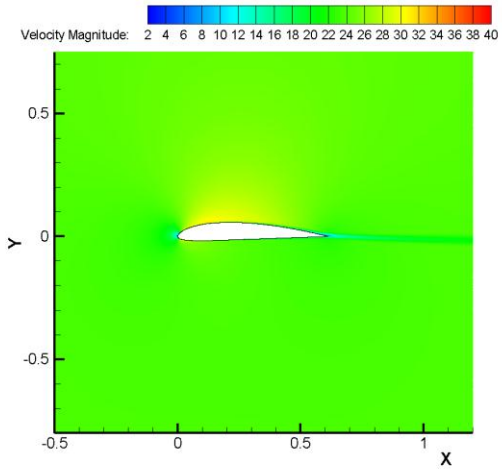

Figure 219: Velocity magnitude contours of Clark Y at $\alpha=0^o$ and Re=1x10^6

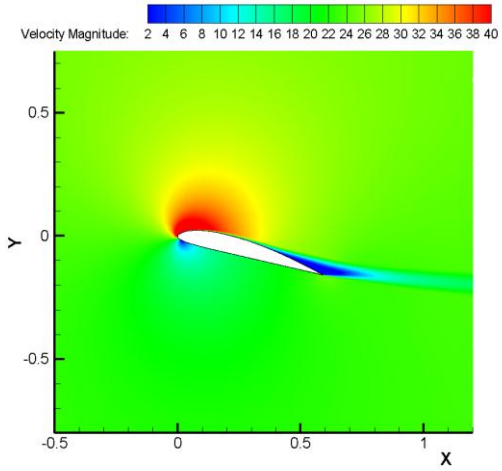

Figure 220: Velocity magnitude contours of Clark Y at $\alpha=15^o$ and Re=1x10^6

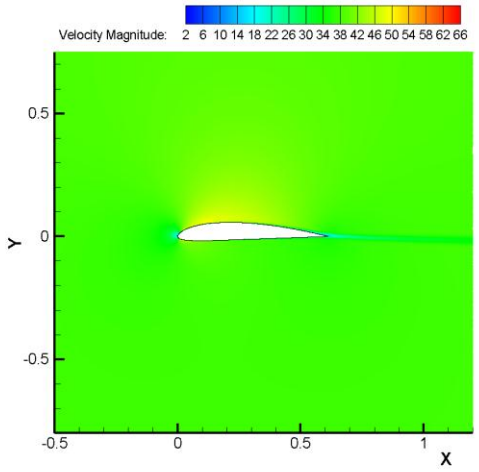

Figure 221: Velocity magnitude contours of Clark Y at $\alpha=0^o$ and Re=1.6x10^6

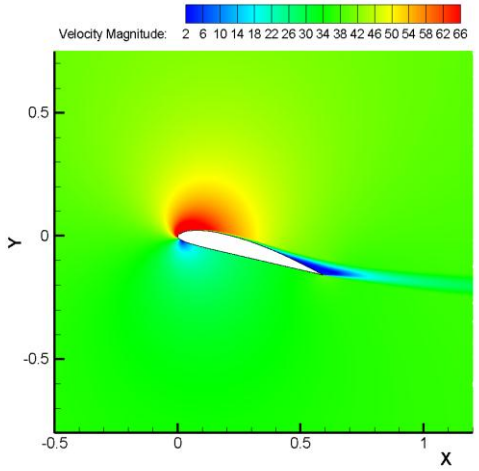

Figure 222: Velocity magnitude contours of Clark Y at $\alpha=15^o$ and Re=1.6x10^6

APPENDIX I.

5% Flap Forces and Moments

Forces 5% flap

The individual components of the force acting on the 5% flap where calculated from the numerical analysis and are presented Figure 223and Figure 224. These figures illustrate the Normal and Horizontal force to the flap. Both trends can be seen to have similar but opposite characteristics. A pseudo-linear relationship describes the behaviour of the forces as was the case for the 10% flap. The gradient of the graphs increases with the Reynolds number indicating a dependency of the behaviour of the force on the value of Re. An increasing trend of the force (F) can be seen with increasing Reynolds number. This is comparable to the 10% flap cases but the magnitudes of the forces are lower. Figure 224 shows the dependency of the force F on the flap deflection angle δ from which it can be seen that with increasing α, the ΔF is positive for the normal force and negative for the horizontal. The maximum forces are obtained at high angles of attack and reach values of approximately 30 N for $\delta = 90^{o}$ and Re $1x10^{6}$. A design envelop can be attained from the graphs to provide a working frame for the design of a passive design. The point on intersection between the two lines is where the flap starts to act positively in the value of C_L.

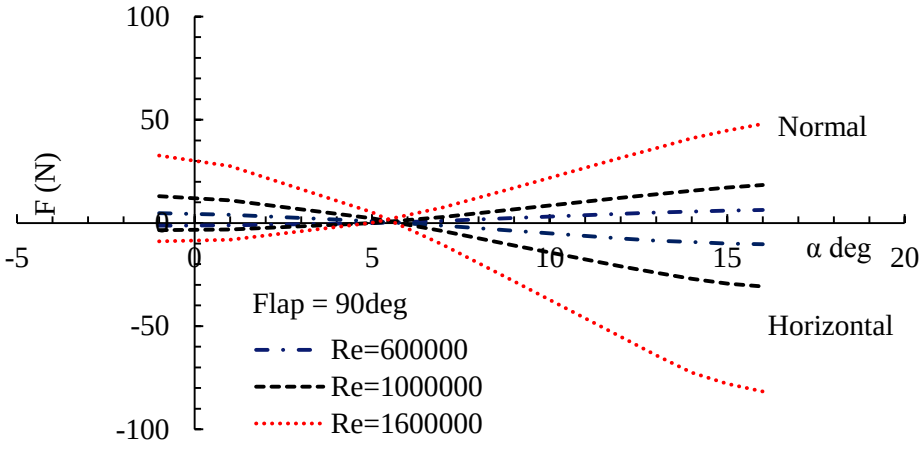

Figure 223: Force on a 5% flap with δ=90° at three Reynolds numbers.

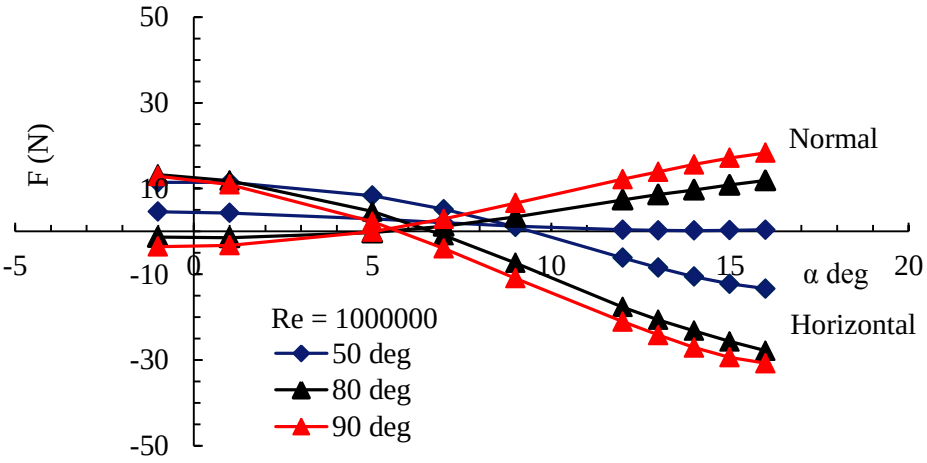

Figure 224: Force on a 5% flap with variable δ at Re = 1x10^6.

Moments 5% flap

The moments for the 5% flap are illustrated in Figure 225 and Figure 226. Similarly as in the case of the 10% flap it can be seen that the ΔM with increasing α is negative in all cases where the magnitude of the ΔM/α gradient increases with increasing δ. The magnitudes of the moments observed in this case are smaller than the 10% flap case. Figure 227 shows a further plot of M vs δ for a series of α which illustrates the pseudo-linear relationship that exists.

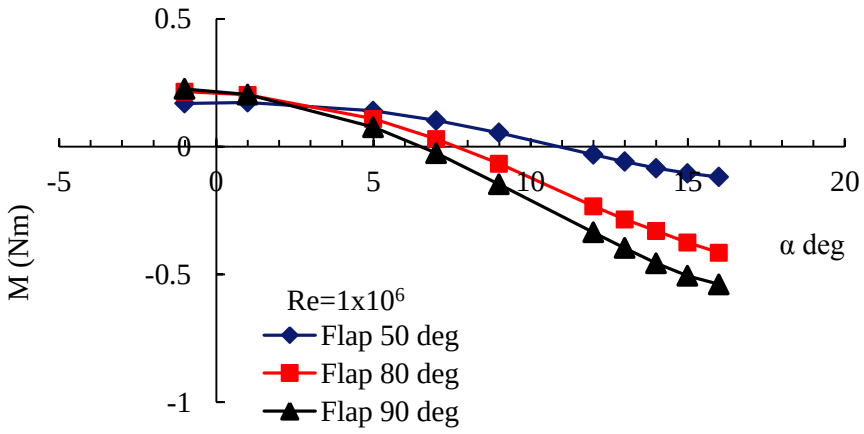

Figure 225: Moment (M) plots for Re = 1x10^6 over the range of flap angles and angles of attack for the 5% flap.

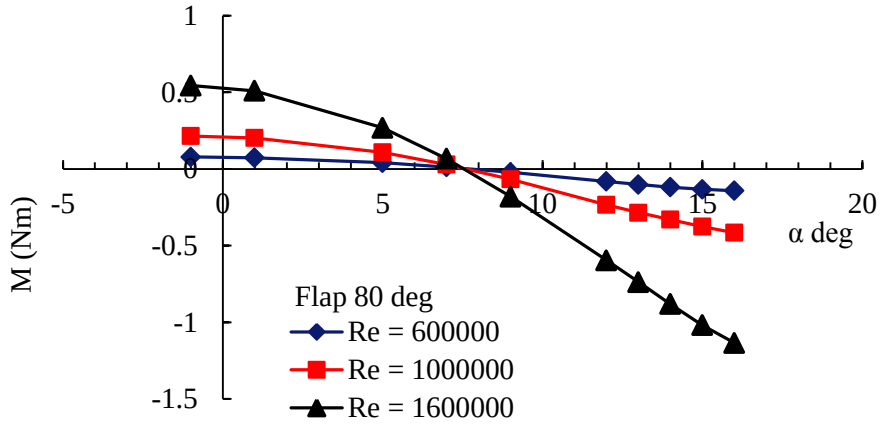

Figure 226: Moment (M) over a range of Re numbers for the 5% flap at δ=80°.

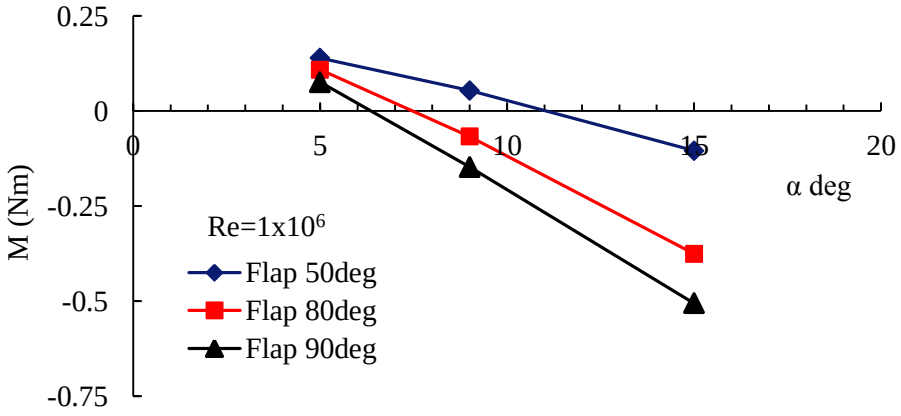

Figure 227: Moment (M) for δ =50°, 80° and 90° for Re number 1x10^6 and fixed α for the 5% flap.

APPENDIX J.

Velocity magnitude contours of 10% flap configuration

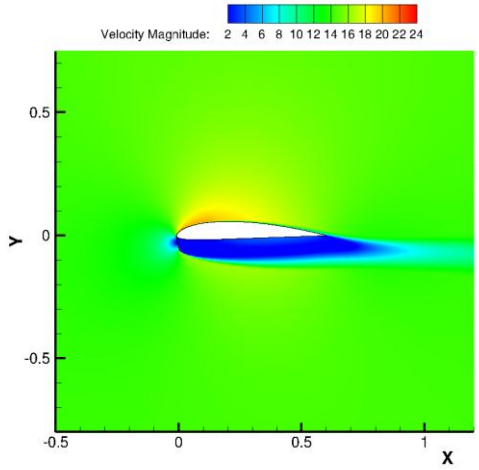

Figure 228: Velocity magnitude contours of 10% flap configuration at α=0^o, δ=70^o & Re=0.6x10^6

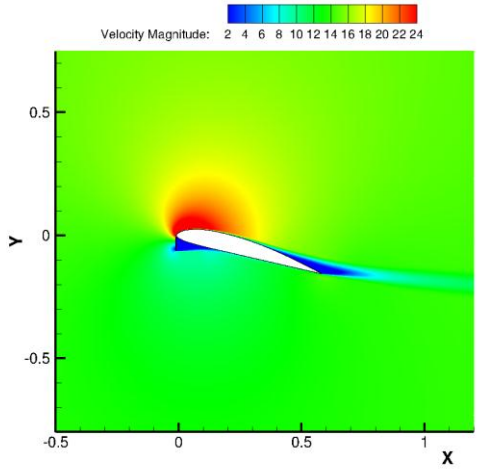

Figure 229: Velocity magnitude contours of 10% flap configuration at α=15^o, δ=70^o & Re=0.6x10^6

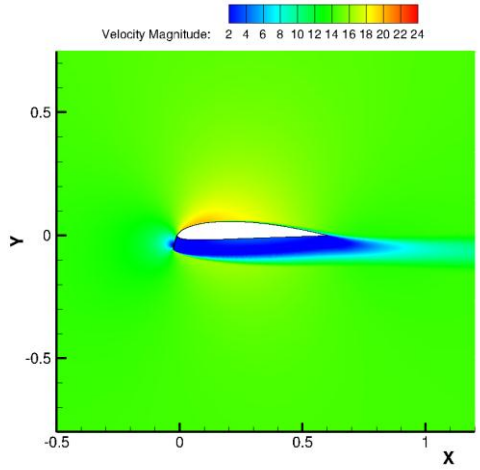

Figure 230: Velocity magnitude contours of 10% flap configuration at α=0^o, δ=100^o & Re=0.6x10^6

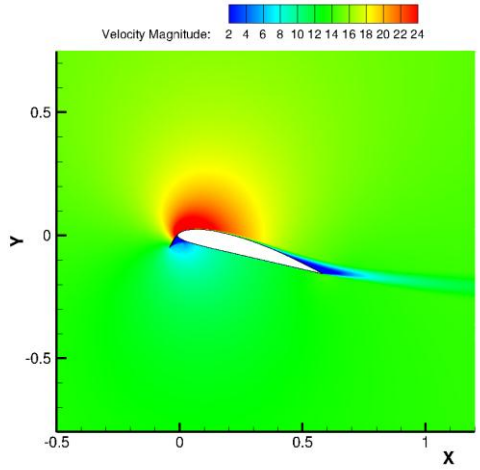

Figure 231: Velocity magnitude contours of 10% flap configuration at α=15^o, δ=100^o & Re=0.6x10^6

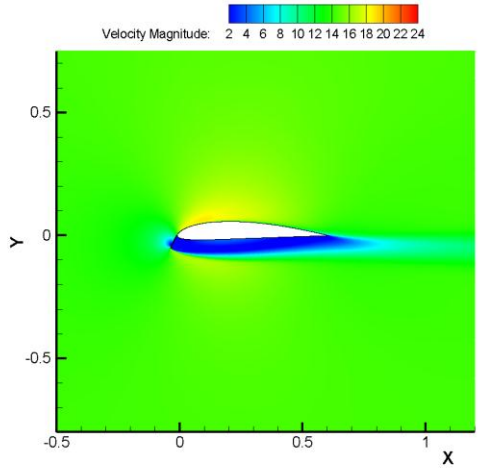

Figure 232: Velocity magnitude contours of 10% flap configuration at α=0^o, δ=110^o & Re=0.6x10^6

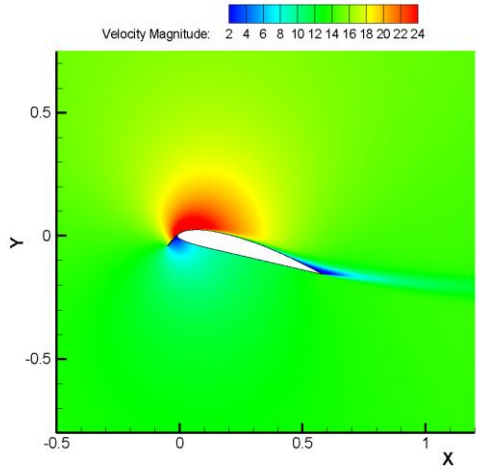

Figure 233: Velocity magnitude contours of 10% flap configuration at α=15^o, δ=110^o & Re=0.6x10^6

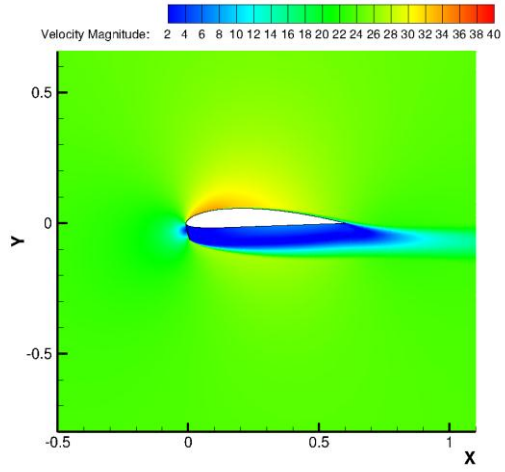

Figure 234: Velocity magnitude contours of 10% flap configuration at α=0^o, δ=70^o & Re=1x10^6

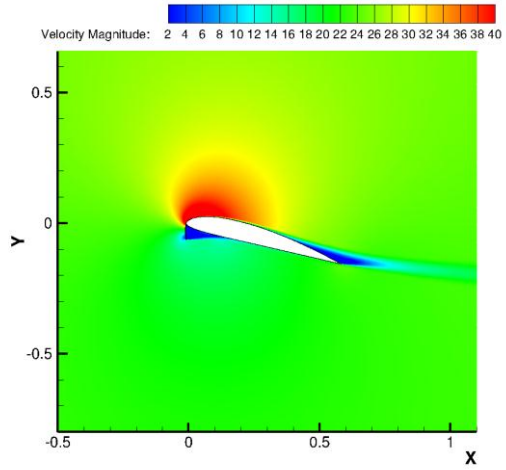

Figure 235: Velocity magnitude contours of 10% flap configuration at α=15^o, δ=70^o & Re=1x10^6

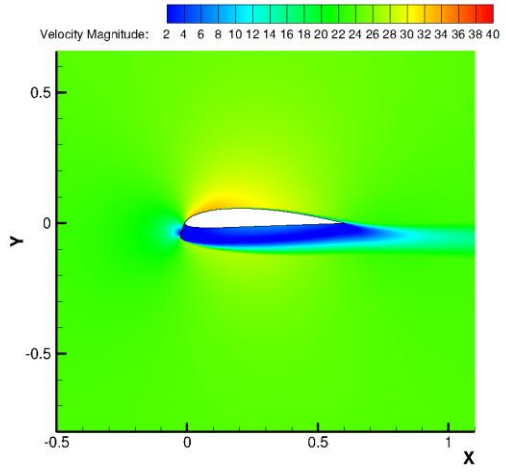

Figure 236: Velocity magnitude contours of 10% flap configuration at α=0^o, δ=100^o & Re=1x10^6

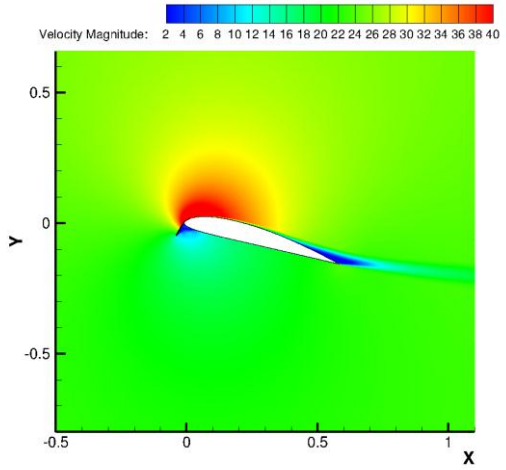

Figure 237: Velocity magnitude contours of 10% flap configuration at α=15^o, δ=100^o & Re=1x10^6

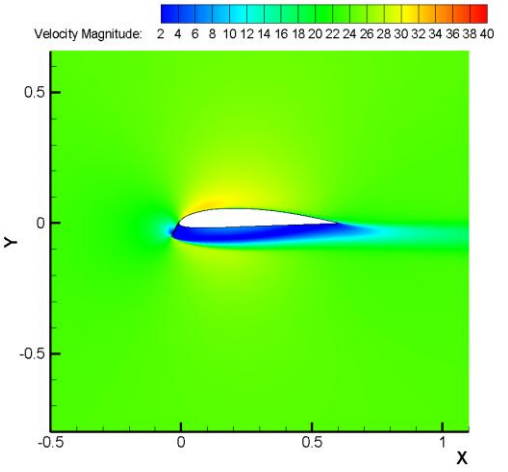

Figure 238: Velocity magnitude contours of 10% flap configuration at α=0^o, δ=110^o & Re=1x10^6

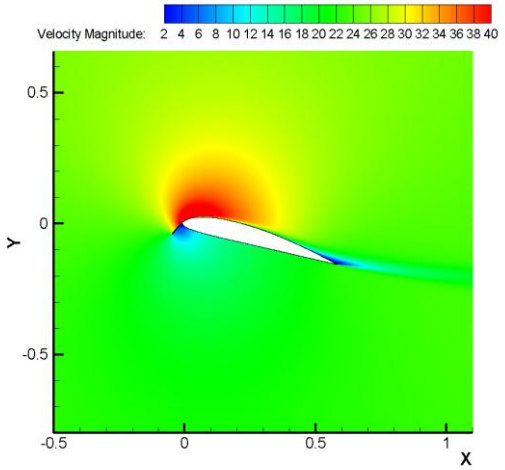

Figure 239: Velocity magnitude contours of 10% flap configuration at α=15^o, δ=110^o & Re=1x10^6

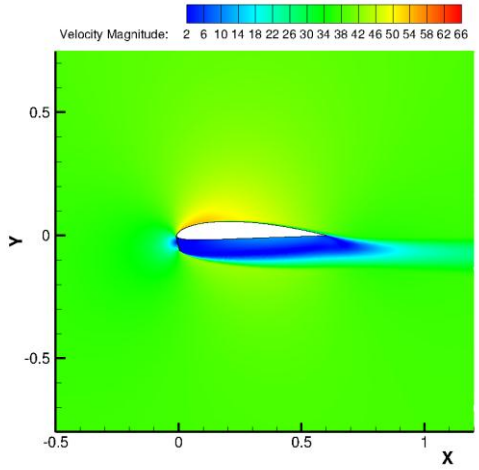

Figure 240: Velocity magnitude contours of 10% flap configuration at α=0^o, δ=70^o & Re=1.6x10^6

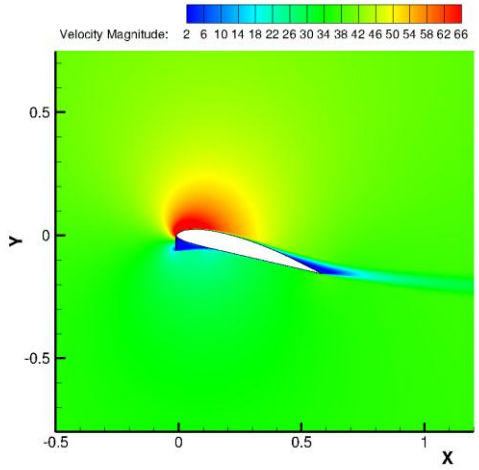

Figure 241: Velocity magnitude contours of 10% flap configuration at α=15^o, δ=70^o & Re=1.6x10^6

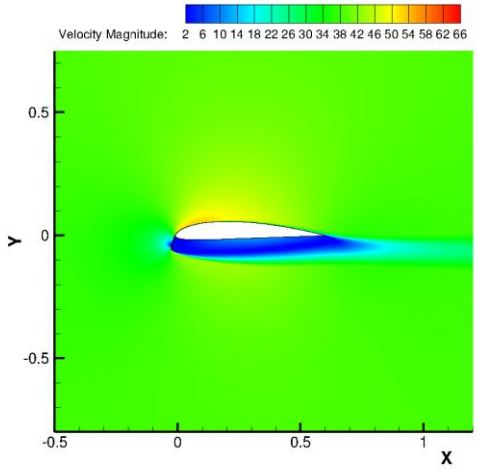

Figure 242: Velocity magnitude contours of 10% flap configuration at α=0^o, δ=100^o & Re=1.6x10^6

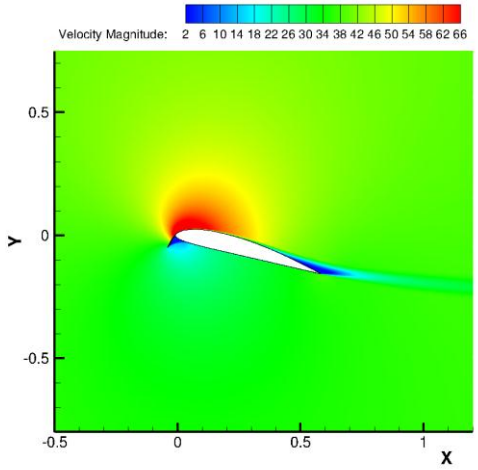

Figure 243: Velocity magnitude contours of 10% flap configuration at α=15^o, δ=100^o & Re=1.6x10^6

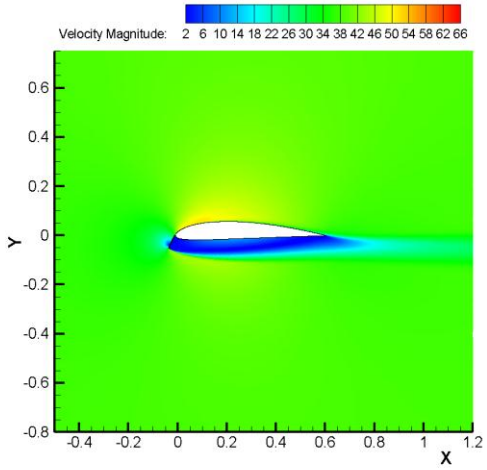

Figure 244: Velocity magnitude contours of 10% flap configuration at α=0^o, δ=110^o & Re=1.6x10^6

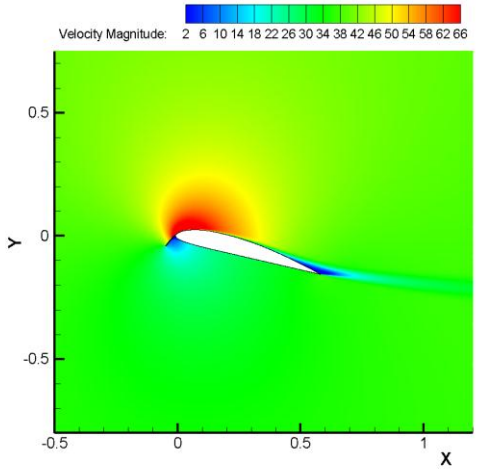

Figure 245: Velocity magnitude contours of 10% flap configuration at α=15^o, δ=110^o & Re=1x10^6